

**UCLA**

**UCLA Electronic Theses and Dissertations**

**Title**

Design and applications of novel computational methods for the study of quantum properties of emergent nanomaterials and biomolecules

**Permalink**

<https://escholarship.org/uc/item/0q5924xt>

**Author**

Agarwal, Shivang

**Publication Date**

2024

Peer reviewed|Thesis/dissertation

UNIVERSITY OF CALIFORNIA

Los Angeles

Design and applications of novel computational methods for the study of quantum  
properties of emergent nanomaterials and biomolecules

A dissertation submitted in partial satisfaction  
of the requirements for the degree  
Doctor of Philosophy in Electrical & Computer Engineering

by

Shivang Agarwal

2024

© Copyright by  
Shivang Agarwal  
2024

## ABSTRACT OF THE DISSERTATION

Design and applications of novel computational methods for the study of quantum properties of emergent nanomaterials and biomolecules

by

Shivang Agarwal

Doctor of Philosophy in Electrical & Computer Engineering

University of California, Los Angeles, 2024

Professor Kang Lung Wang, Co-Chair

Professor Amartya Sankar Banerjee, Co-Chair

We discuss the formulation and use of computational first principles-based methods to study the electronic structure and quantum properties of novel nanomaterials and biomolecules. A helical symmetry-adapted spectral framework, HelicES, is developed for the electronic structure calculation of quasi-one-dimensional structures with imposed or intrinsic twists. Such structures, including nanotubes and nanoribbons, have the potential to exhibit fascinating electronic, optical, and transport properties. We explore the convergence properties of our method, and assess its accuracy by comparison against reference finite difference, transfer matrix method and plane-wave results. Next, we introduce a pseudo-spectral representation of the Laplacian in helical coordinates, which lays down the path towards incorporating self consistency within HelicES by enabling an efficient evaluation of the electrostatic potential. Here too, we provide a comparison between our method and other conventional methods used for the evaluation of this Newtonian potential, such as Ewald summations. Then, in a slightly different line of work involving quantum properties of biomolecules, we present a

detailed and comprehensive study on calcium phosphate clusters, most notably, the calcium phosphate trimer (Posner molecule). First, we use *ab initio* methods to examine the structural ensemble of these clusters. This is essential to then calculate the phosphorus nuclear spin state lifetimes in these molecules, in light of the claim that these spin states in pairs of Posner molecules might be extremely long-lived. Our work, however, conclusively proves that the Posner molecule does not maintain long-lived spin states. Lastly, realizing that many of the frameworks developed and discussed in this work have poor (cubic) scaling with respect to the system size, we also discuss the development of a generalised machine learning framework to overcome this intrinsic limitation of density functional theory (DFT) calculations. We showcase the utility of the uncertainty quantification-enabled method to systems beyond the reach of conventional DFT calculations, i.e. those with millions of atoms. We end with a brief discussion on the ongoing and future applications of our work which may find uses in the study and discovery of novel nanomaterials.

The dissertation of Shivang Agarwal is approved.

Benjamin S. Williams

Robert N. Candler

Daniel Kattnig

Amartya Sankar Banerjee, Committee Co-Chair

Kang Lung Wang, Committee Co-Chair

University of California, Los Angeles

2024

Dedicated to my family

## TABLE OF CONTENTS

<b>1</b>	<b>Introduction . . . . .</b>	<b>1</b>
<b>2</b>	<b>HelicES: A symmetry-adapted spectral electronic structure method . . . . .</b>	<b>9</b>
2.1	Formulation . . . . .	9
2.1.1	Description of physical system and computational problem . . . . .	9
2.1.2	The helical coordinate system and transformation of Schrödinger's equation . . . . .	12
2.1.3	Basis set and discretization . . . . .	15
2.2	Numerical Implementation . . . . .	24
2.2.1	Wave function storage: reciprocal and real space considerations . . . . .	24
2.2.2	Imposition of kinetic energy cutoff . . . . .	26
2.2.3	$\eta$ -space discretization and parallelization . . . . .	27
2.2.4	Fast basis transforms . . . . .	28
2.2.5	Eigensolvers and preconditioning . . . . .	37
<b>3</b>	<b>Application of HelicES to quasi-one-dimensional nanostructures . . . . .</b>	<b>39</b>
3.1	Simulations and Results . . . . .	39
3.1.1	Computational platform . . . . .	39
3.1.2	Convergence studies . . . . .	40
3.1.3	Accuracy studies . . . . .	43
3.1.4	Comments on computational efficiency and timing studies . . . . .	48
3.1.5	Application to the study of the electromechanical response of nanotubes . . . . .	50



3.2	Concluding remarks . . . . .	52
<b>4</b>	<b>The solution of the Poisson problem for twisted geometries . . . . .</b>	<b>53</b>
4.1	Theoretical background . . . . .	56
4.2	Formulation . . . . .	60
4.2.1	The radial Poisson ODE . . . . .	60
4.2.2	Charge distribution setup . . . . .	63
4.2.3	Evaluating boundary conditions . . . . .	66
4.3	Reduction in computational complexity and algorithms . . . . .	68
4.4	Results . . . . .	75
4.4.1	Computational platform . . . . .	75
4.4.2	Convergence and accuracy studies . . . . .	76
4.4.3	Calculation of the electrostatic interaction energy . . . . .	79
4.5	Concluding remarks . . . . .	81
<b>5</b>	<b>The Posner molecule: Importance and structural ambiguity . . . . .</b>	<b>83</b>
5.1	Background and the claim of a biological neural qubit . . . . .	83
5.2	Computational methodology . . . . .	85
5.3	The structural ensemble of calcium phosphate clusters . . . . .	86
5.3.1	Calcium phosphate monomers . . . . .	87
5.3.2	Calcium phosphate dimers . . . . .	87
5.3.3	Calcium phosphate trimers (Posner molecule) . . . . .	89
<b>6</b>	<b>Nuclear spin coherence lifetimes in calcium phosphate clusters . . . . .</b>	<b>103</b>
6.1	Computational methodology . . . . .	105

6.2	Setting up the spin Hamiltonian . . . . .	106
6.2.1	Intramolecular dipole-dipole interactions between $^{31}\text{P}$ nuclear spins . . . . .	108
6.3	Calculation and evolution of the singlet state . . . . .	109
6.3.1	Calculation of concurrence . . . . .	110
6.4	Application of the framework to the Posner molecule . . . . .	110
6.5	Exploratory calculations on calcium phosphate dimers . . . . .	119
6.6	The effect of the number of coupled nuclear spins on the spin dynamics of a system . . . . .	124
6.7	Calculations on the calcium phosphate monomer . . . . .	127
6.8	Concluding remarks . . . . .	128
<b>7</b>	<b>Electronic structure prediction of multi-million atom systems . . . . .</b>	<b>130</b>
7.1	Introduction . . . . .	130
7.2	Computational Framework . . . . .	133
7.2.1	<i>Ab Initio</i> Molecular Dynamics . . . . .	133
7.2.2	Machine learning map for charge density prediction . . . . .	135
7.2.3	Atomic neighborhood descriptors . . . . .	135
7.2.4	Selection of optimal set of descriptors . . . . .	136
7.2.5	Bayesian Neural Network . . . . .	137
7.2.6	Uncertainty quantification . . . . .	139
7.2.7	Transfer Learning using multi-scale data . . . . .	140
7.2.8	Postprocessing of ML predicted electron density . . . . .	142
7.3	Machine learning predictions . . . . .	142
7.3.1	Error Estimation . . . . .	144

7.3.2	Uncertainty quantification . . . . .	150
7.3.3	Computational efficiency gains and confident prediction for very large system sizes . . . . .	155
7.3.4	Reduction of training data generation cost via transfer learning . . . .	158
7.4	Discussions . . . . .	160
<b>8</b>	<b>Conclusion and future directions . . . . .</b>	<b>163</b>
	<b>References . . . . .</b>	<b>165</b>

## LIST OF FIGURES

2.1	Examples of the type of nanostructures that can be investigated using the computational framework presented in this work. Helical and cyclic symmetry parameters associated with the geometries of the structures are shown. . . . .	11
2.2	The helical coordinate system represented as constant surfaces of the parameters $r, \theta_1, \theta_2$ (the twist parameter $\alpha$ is nonzero here). . . . .	13
2.3	The computational mesh represented in simulation space using helical coordinates ( <u>left</u> ), and physical space using Cartesian coordinates ( <u>right</u> ). The slanted walls of the fundamental domain $\mathcal{D}$ in physical space ( <u>right</u> ) arise due to possibly arbitrary values of twist associated with the system. . . . .	14
2.4	Variation of the normalized time for basis transforms plotted against the basis set size. Both axes are logarithmic. Straight lines were fit using the average of the forward and inverse transform times in each case. . . . .	30
2.5	Pictorial representation of the workings of the fast angular 2D inverse Fourier transform (Algorithm 2) . . . . .	32
2.6	Pictorial representation of the workings of the fast angular 2D forward Fourier transform (Algorithm 4). ‘Scale’ indicates dividing the result of the 2D FFT by $(N_{\theta_1} N_{\theta_2})$ . . . . .	35
2.7	Effect of the Teter-Payne-Allan preconditioner [1] on LOBPCG [2] iterations for diagonalizing the discretized Hamiltonian in HelicES. An untwisted (6,6) armchair carbon nanotube (Mayer pseudopotentials [3]) has been used, and the residual associated with the 2 <sup>nd</sup> eigenvalue for $\eta = 0, \nu = 0$ as been monitored. For clarity, the residual for every 10 <sup>th</sup> iteration has been plotted. Without preconditioning, the number of iterations required to reach a given convergence threshold tends to dramatically increase as the basis set grows larger. . . . .	38

3.1	Convergence of the first three non-degenerate eigenvalues of an armchair (16, 16) carbon nanotube with a twist parameter of $\alpha = 0.002$ using HelicES (both with and without the energy cutoff mask implemented) and a finite difference method (FDM), i.e., Helical DFT [4, 5]. The mesh size of the FDM decreases from 0.7 Bohrs to 0.4 Bohrs (in steps of 0.05 Bohrs) as the full Hamiltonian size varies from 30, 744 to 157, 440. The sparsity factor for the FDM Hamiltonian was 0.0055. The reference eigenvalues were taken to be the ones using an energy cutoff of 40 Ha for HelicES and a mesh spacing of 0.10 Bohr for Helical DFT. The $\eta = 0, \nu = 0$ case (“gamma point”) is considered here. Note that the errors in the eigenvalues, for different eigenvalues, differ by $\mathcal{O}(10^{-4})$ or less in the FDM case, which makes them indistinguishable in the plot above. . . . .	41
3.2	Convergence of the electronic band energy, the Valence Band Maximum (VBM) eigenvalue, the Conduction Band Minimum (CBM) eigenvalue, and the band gap, with respect to the energy cutoff, in the HelicES code. An armchair (16, 16) carbon nanotube with a twist parameter of $\alpha = 0.002$ has been investigated. The reference values were generated using an energy cutoff of 40 Ha. . . . .	42
3.3	Convergence of the band energy and electron density of a (16, 16) armchair carbon nanotube with a twist parameter of $\alpha = 0.002$ . The reference value was taken to be from a calculation with 45 $\eta$ -points . . . . .	42
3.4	Comparison of band diagrams for a twisted (16, 16) armchair carbon nanotube (diameter = 2.726 nm) with twist parameter of $\alpha = 0.002$ , generated using HelicES and the FDM based Helical DFT code [5, 4]. The green shaded region in the structure on the right is the fundamental domain used in HelicES, while the green arrow denotes the $\mathbf{e}_z$ axis. . . . .	45

3.5	Comparison of band diagrams for a (5,5) armchair carbon nanotube (diameter = 0.851 nm) generated using HelicES and a transfer-matrix technique [3]. The dashed green box in the plot represents the region of the band diagram over which the reference data was available for comparison. The green shaded region in the structure on the right is the fundamental domain used in HelicES and the green arrow denotes the $\mathbf{e}_z$ axis. . . . .	46
3.6	Comparison of band diagrams for a (10,0) zigzag carbon nanotube (diameter = 0.983 nm) generated using HelicES and a transfer-matrix technique [3]. The dashed green box in the plot represents the region of the band diagram over which the reference data was available for comparison. The green shaded region in the structure on the right is the fundamental domain used in HelicES and the green arrow denotes the $\mathbf{e}_z$ axis. . . . .	47
3.7	Comparison of band diagrams for a hydrogen passivated armchair graphene nanoribbon generated using HelicES and a plane-wave technique [6, 7]. The green shaded region in the structure on the right is the fundamental domain used in HelicES and the green arrow denotes the $\mathbf{e}_z$ axis. . . . .	47
3.8	Comparison of band diagrams for a hydrogen passivated, $\langle 100 \rangle$ oriented silicon nanowire generated using HelicES and a plane-wave technique [6, 7]. The dashed green box in the plot represents the region of the band diagram over which the reference data was available for comparison. The green shaded region in the structure in the middle is the fundamental domain used in HelicES, with the green arrow denoting the $\mathbf{e}_z$ axis. The right image shows a top view of the structure (i.e., looking down along $\mathbf{e}_z$ ). . . . .	48
3.9	Band diagram for an armchair graphene nanoribbon with a twist parameter of $\alpha = 0.02$ (corresponding to a rate of twist $\beta = 16.9^\circ$ per nanometer) generated using HelicES. The green shaded region in the structure on the right is the fundamental domain used in HelicES. The green arrow denotes the $\mathbf{e}_z$ axis. . . . .	50

3.10	Band gap trend as the twist parameter $\alpha$ is varied for a (16, 16) armchair carbon nanotube. Results from HelicES (empirical pseudopotentials) and the Helical DFT code (self consistent calculations with ab initio pseudopotentials and atomic relaxation effects included [4, 5]) are both shown. . . . .	51
4.1	The figure on the left represents a few layers of a twisted (10,10) armchair carbon nanotube with the fundamental domain shown ( $\mathfrak{N} = 10$ ). The fundamental domain, over which the Hartree potential is to be computed, is represented in physical space using Cartesian coordinates on the right. The slanted walls of the fundamental domain $\mathcal{D}$ in physical space arise due to possibly arbitrary values of twist associated with the system. For the points beyond $r = R$ , we include boundary conditions into our framework via helical Ewald sums. The red shaded area represents the points where we apply pole conditions in our FD stencil to accommodate $r < 0$ . . . . .	59
4.2	A flowchart of the mixed spectral – finite-difference based numerical method developed in this study. The (neutral) charge density, $g(\theta_1, \theta_2, r)$ , is first transformed into 2D reciprocal space along the angular directions. The resultant field, $G_{m,n}(r)$ , acts as the RHS of the ODE. The boundary conditions, $v(\theta_1, \theta_2, r)$ , are obtained from the evaluation of the potential exerted by $g(\theta_1, \theta_2, r)$ at the boundary points. This too is then transformed into the 2D reciprocal space. The ODE solver outputs the Hartree potential, $P_{m,n}(r)$ , in the 2D reciprocal space. The complete potential, $V_H(\theta_1, \theta_2, r)$ over $\mathcal{D}$ is then obtained via an angular 2D inverse Fourier transform. . . . .	64

4.3	Setting up the compensating pseudocharges for a (6,6) armchair carbon nanotube. Only a slice of the nanotube has been depicted for ease of visualization. Here, the blue spheres represent the carbon atoms, and the translucent blue sphere encompassing each atom is the nuclear pseudocharge density. The red translucent spheres represent the artificial compensating electronic charge density. Note how none of the charge densities overlap — a necessary condition as outlined in [8]. . . . .	65
4.4	The time taken to calculate the full Hartree potential over $\mathcal{D}$ using different methods for a (6,6) CNT with $\alpha = 0.004$ , $\mathfrak{N} = 6$ . An energy cutoff of 120 Ha was used, and the FD order used was 12. All times are in seconds. Note that the bar plots have been stacked in reverse chronological order for ease of visualization (i.e., for instance, for the Spectral-FD case, the actual chronological order is the evaluation of the Ewald kernel, its usage, and then the ODE solver). . . . .	69
4.5	Pictorial representation of generating the FD stencil for an order of $n_0 = 8$ , as outlined in Algorithm 10. The variables $h, n_r$ , and $c_1$ are taken from Algorithm 10 as well. The term $d(i)$ represents the $i^{\text{th}}$ diagonal term in the stencil. The entries above the diagonal (in dark blue) are cut off at the end (shaded area) due to boundary conditions, whereas the entries below the diagonal (in purple) are cut off at the start due to pole conditions. . . . .	75
4.6	The difference in left hand side and the right hand side of the eigenvalue equation (Eq. 4.24) for different harmonics of the eigenfunction. The plot on the bottom right shows the ratio of the left hand side to the right hand side for values of $r$ where the eigenfunction is non-zero. The spikes occur in the immediate vicinity of the zeroes of the eigenfunction. In each case, the basis set maxima were set to $M_{\text{max}} = 20, N_{\text{max}} = 50, K_{\text{max}} = 300$ which are high enough to avoid any errors creeping in due to coarseness of the mesh. A FD order of 4 was used, with $n_r = 2N_r$ (consistent with the results in Fig. 4.9). . . . .	77



- 4.7 Convergence in the  $L^2$  norm per electron, calculated as  $\frac{1}{N_e} \times \sqrt{\int_{\mathcal{D}} (V - V_{\text{ref}})^2 2\pi\tau r dr d\theta_1 d\theta_2}$ , and  $L^1$  norm per electron, calculated as  $\frac{1}{N_e} \times \int_{\mathcal{D}} |V - V_{\text{ref}}| 2\pi\tau r dr d\theta_1 d\theta_2$ , with respect to different basis set maxes for the Gaussian pseudocharge distribution [9]. Here  $N_e$  is the number of electrons in  $\mathcal{D}$ . In each case, the other two basis set maxima were held constant at  $M_{\text{max}} = 30, N_{\text{max}} = 75, K_{\text{max}} = 300$ . The method was tested on a 6,6 carbon nanotube with  $\alpha = 0.004, \mathfrak{N} = 6$ . The reference,  $V_{\text{ref}}$ , was calculated using the analytical expression in Eq. 4.21 with a basis set size corresponding to  $M_{\text{max}} = 30, N_{\text{max}} = 75, K_{\text{max}} = 300$ . . . . . 78
- 4.8 Convergence in the  $L^2$  norm per electron, calculated as  $\frac{1}{N_e} \times \sqrt{\int_{\mathcal{D}} (V - V_{\text{ref}})^2 2\pi\tau r dr d\theta_1 d\theta_2}$ , and  $L^1$  norm per electron, calculated as  $\frac{1}{N_e} \times \int_{\mathcal{D}} |V - V_{\text{ref}}| 2\pi\tau r dr d\theta_1 d\theta_2$ , with respect to different basis set maxes for the pseudocharge distribution introduced in [8]. Here  $N_e$  is the number of electrons in  $\mathcal{D}$ . In each case, the other two basis set maxima were held constant at  $M_{\text{max}} = 30, N_{\text{max}} = 75, K_{\text{max}} = 300$ . The method was tested on a 6,6 carbon nanotube with  $\alpha = 0.004, \mathfrak{N} = 6$ . The reference,  $V_{\text{ref}}$ , was calculated using the analytical expression in Eq. 4.21 with a basis set size corresponding to  $M_{\text{max}} = 30, N_{\text{max}} = 75, K_{\text{max}} = 300$ . . . . . 79
- 4.9 Convergence in the  $L^2$  norm per electron, calculated as  $\frac{1}{N_e} \times \sqrt{\int_{\mathcal{D}} (V - V_{\text{ref}})^2 2\pi\tau r dr d\theta_1 d\theta_2}$ , between the Hartree potential as evaluated analytically (from Eq. 4.21) and as evaluated by our psuedo-spectral method with respect to the finite difference order for a (6,6) armchair carbon nanotube with a twist of  $\alpha = 0.004$ , and  $\mathfrak{N} = 6$ . We show convergence across 3 different values of  $n_r$ , and for 3 different sizes of the basis set. . . . . 80
- 4.10 The behaviour of the electrostatic interaction energy as a function of the twist parameter,  $\alpha$ , for a (6,6) carbon nanotube,  $\mathfrak{N} = 6$ . The basis set size chosen was  $M_{\text{max}} = 15, N_{\text{max}} = 30, K_{\text{max}} = 125$ . The FD order was 4, with  $n_r = N_r$ , consistent with the observations from Fig. 4.9. We see an expected quadratic behaviour, consistent with prior works [10]. . . . . 81

5.1	A calcium phosphate monomer exhibiting the expected $D_{3h}$ molecular point group symmetry. The result was obtained using DL POLY, Quantum ESPRESSO, and Q-Chem, and is consistent with previous studies. The blue, purple, and red spheres represent Ca, P, and O atoms respectively. . . . .	87
5.2	Some calcium phosphate dimer relaxed geometries obtained in our study. The methodology to obtain these structures was based on the results of Kanzaki et al.	88
5.3	(a) The scheme used for creating over 10,000 structures by rotating the phosphate units and scaling all the coordinates with respect to central atom. The blue, purple, and red spheres represent Ca, P, and O atoms respectively. (b) Percentage occurrence of each point group symmetry after <i>ab initio</i> structural relaxation of over 10,000 initial structures (DFT with B3LYP hybrid functional and 6-311G(d,p) basis set). . . . .	91
5.4	The eight different structures that were used as starting geometries for dynamical simulations of the PM. The labels ( <b>A–H</b> ) used in the manuscript are stated. . .	93
5.5	Comparison between the IR spectra of the structural configuration <b>E</b> and <b>G</b> used in this study, and of that obtained by Swift et al. [11]. . . . .	93
5.6	Time persistence of symmetries and the associated frequency of occurrence of each symmetry for two different starting configurations over a dynamical run. In the above figure, (a) and (c) represent the data for configuration <b>C</b> , whereas (b) and (d) represent data for configuration <b>H</b> . Note that (a) and (b) represent the data at $T = 298K$ , and thus some additional symmetries which were observed at $T = 315K$ are not present in these plots. . . . .	96

5.7	The energy spread of the dynamical runs for each of the starting configurations listed in Fig. 5.4 represented by kernel density estimations in the form of vertical violin plots. The blue dots represent the energy of the time-average structure over the entire dynamical run, and the red dot represents the energy of the time-average structure of that subset of the high symmetry phase that is present for the longest continuous duration. The point-group symmetry of the averages is indicated next to the symbols. The semi-transparent overlays on each of the violin plots represent the energy distribution for the entire high symmetry phase. The most stable high symmetry phase for each of the cases were $\mathbf{D}_{2h}$ , $\mathbf{D}_{2h}$ , $\mathbf{C}_{2h}$ , $\mathbf{D}_{2h}$ , $\mathbf{C}_{2h}$ , $\mathbf{D}_{2h}$ , $\mathbf{D}_{2h}$ , and $\mathbf{D}_{2h}$ , respectively. Dots missing from the graph were found at energies higher than the scale of the figure. The plot also shows the mean and standard deviation of the energy spread within the representations of probability density functions in the form of white boxes. The energies reported are within the numerical accuracy of the method and basis set used. [12, 13] . . .	99
5.8	(a), (c), (e) Eigenvalues resulting from PCA over a single dynamical run for configurations $\mathbf{E}$ , $\mathbf{D}$ , and $\mathbf{B}$ respectively. (b), (d), (f) Difference between the most dominant eigenmode and the time-average structure of the corresponding dynamical run. . . . .	101
6.1	A pair of $^{31}\text{P}$ nuclei, namely the pair labeled (0,0), entangled and initialized in the singlet state in two separate but identical Posner molecules. The separation between the molecules, although arbitrary, is large enough for intermolecular interactions between the $^{31}\text{P}$ nuclear spins to be negligible. The entanglement between the nuclear spins has been depicted by a dotted line. . . . .	104

6.2	Illustration of the methodology for obtaining different configurations for spin dynamics calculations, starting from the AIMD structures presented in Ref. [14]. Here, we only show the type of structures obtained from one AIMD simulation (out of the eight that were performed). Overall, our approach gave us 102 unique structures. The graph on the left shows the evolution of the molecular point-group symmetry during a dynamic simulation of a transition-state structure of the Posner molecule. . . . .	111
6.3	The short-lived nature of the singlet probability and concurrence for the Posner molecule, shown for three representative structures. Insets show zoomed in regions of the plots. (a) and (d) correspond to the structure with the longest-lived singlet state — a $k$ -means structure with $D_{2h}$ symmetry; (b) and (e) correspond to the energetically most stable structure with no symmetry in our dynamical study [14]; (c) and (f) are the average singlet probability and concurrence for all 102 structures considered. Contrary to previous studies [11, 15, 16], the plots above suggest that the system is not suitable for quantum information processing at biologically relevant time scales. . . . .	113
6.4	The first and last instances of the singlet probability crossing the threshold of $1/2$ . The number of structures for each case, with different scales, has been represented on the $x$ -axis. Note that the $y$ -axes have different scales. A total of 102 structures have been considered, obtained from methods depicted in Fig. 6.2. The 50% quantile line has been shown in each case, and confirms that a majority of the structures are unable to maintain the singlet state for more than a second.	114
6.5	Transfer of entanglement between nuclear spin pairs in a Posner molecule. The 6 nuclear spins in each Posner are indexed from 0 through 5. . . . .	116

6.6	The symmetry of the molecule does not seem to play a major role in maintaining entanglement in the system, and Posner molecules generally have short entanglement lifetimes ( $< 1$ s) irrespective of their point-group symmetry. The marker size in each plot is proportional to the number of data points at the location, whereas darker areas represent overlapping of markers. . . . .	117
6.7	A comparison of the singlet probabilities for two $S_6$ structures — $\mathcal{A}$ , taken from Ref. [16], and $\mathcal{B}$ , taken from Ref. [11] — with coupling constants as reported in Ref. [11] and as calculated in our study. . . . .	118
6.8	Singlet probabilities for the six stable dimer structures explored in our previous study [14]. Long-lived singlet states are observed irrespective of the symmetry of the dimer, unlike the Posner molecule, potentially making it more suitable for quantum information processing. For clarity, the plots (a) through (f) have been arranged in decreasing order of the stability of the dimer structure . . . . .	120
6.9	Transfer of entanglement between nuclear spin pairs in a tricalcium biphosphate dimer with a $C_2$ point-group symmetry. The 4 nuclear spins in each dimer are indexed from 0 through 3. The notation $ij$ corresponds to spin pair comprising of the $i^{th}$ spin in the first dimer molecule, and the $j^{th}$ spin in the second dimer molecule. . . . .	123
6.10	The entanglement yield monotonically decreases with the number of coupled nuclear spins. Note that the error bars and the data on the $S_4$ and $S_6$ – symmetric dimer and Posner structures respectively show that for individual structures, a different set of coupling constants result in different yields for a given number of $^{31}\text{P}$ atoms. . . . .	125
6.11	Singlet probability for the calcium phosphate monomer . . . . .	127

7.1	Convergence of error with respect to the number of descriptors, shown for aluminum. The blue line shows the convergence with respect to $N_{\text{set I}}$ , while the other three lines show convergence with respect to $N_{\text{set II}}$ . The optimal $N_{\text{set I}}$ and $N_{\text{set II}}$ are obtained where their test RMSE values converge. . . . .	137
7.2	Comparison of (a) error and (b) training data generation time between models with and without transfer learning for aluminium (left) and SiGe (right) systems.	141
7.3	Overview of the present Machine Learning (ML) model. The first step is the training data generation via <i>ab initio</i> simulations shown by the arrow at the top. The second step is to generate atomic neighborhood descriptors $\mathbf{x}(i)$ for each grid point, $i$ , in the training configurations. The third step is to create a probabilistic map (Bayesian Neural Network with DenseNet like blocks consisting of skip connections) from atomic neighborhood descriptors $\mathbf{x}(i)$ to the charge density at the corresponding grid point $\rho(i)$ . The trained model is then used for inference which includes (i) descriptor generation for all grid points in the query configuration, (ii) forward propagation through the Bayesian Neural Network, and (iii) aggregation of the point-wise charge density $\rho(i)$ to obtain the charge density field $\rho$ . . . . .	143
7.4	1372 atom aluminum simulation cell at 631 K. Electron densities (a) calculated by DFT and (b) predicted by ML. The two-dimensional slice of (b) that has the highest mean squared error, as calculated by (c) DFT and predicted by (d) ML. (e) Corresponding absolute error in ML with respect to DFT. (f) - (h) Magnified view of the rectangular areas in (c) - (e) respectively. The unit for electron density is $e\text{Bohr}^{-3}$ , where $e$ denotes the electronic charge. . . . .	146

7.5	512 atoms $\text{Si}_{0.5}\text{Ge}_{0.5}$ simulation cell at 2300 K. Electron densities (a) calculated by DFT and (b) predicted by ML. The two-dimensional slice of (b) that has the highest mean squared error, as calculated by (c) DFT and predicted by (d) ML. (e) Corresponding absolute error in ML with respect to DFT. The unit for electron density is $e \text{ Bohr}^{-3}$ , where $e$ denotes the electronic charge. . . . .	146
7.6	Electron density contours for aluminum systems with localized and extended defects — Left: calculated by DFT, Right: predicted by ML. (a) (Top) Mono-vacancy in 256 atom aluminum system, (Bottom) Di-Vacancy in 108 atom aluminum system, (b) (1 1 0) plane of a perfect screw dislocation in aluminum with Burgers vector $\frac{a_0}{2}[110]$ , and line direction along $[110]$ . The coordinate system was aligned along $[1\bar{1}2]-[\bar{1}11]-[110]$ , (c) (Top) (0 1 0) plane, (bottom) (0 0 1) plane of a $[001]$ symmetric tilt grain boundary ( $0^\circ$ inclination angle) in aluminum, (d) Edge dislocation in aluminum with Burgers vector $\frac{a_0}{2}[110]$ . The coordinate system was aligned along $[110]-[\bar{1}11]-[1\bar{1}2]$ and the dislocation was created by removing a half-plane of atoms below the glide plane. The unit for electron density is $e \text{ Bohr}^{-3}$ , where $e$ denotes the electronic charge. . . . .	147
7.7	Electron density contours and absolute error in ML for SiGe systems with (a-c) Si double vacancy defect in 512 atom system (d-f) Ge single vacancy defect in 216 atom system. Densities (a,d) calculated by DFT, (b,e) predicted by ML, and (c,f) error in ML predictions. Note that the training data for the above systems did not include any defects. The unit for electron density is $e \text{ Bohr}^{-3}$ , where $e$ denotes the electronic charge. . . . .	148

- 7.8 A comparison of the accuracy in the prediction of the charge density (in terms of the  $L^1$  norm per electron between  $\rho^{\text{DFT}}$  and  $\rho^{\text{scaled}}$ ), and the error (in Ha/atom) in the ground state total energy computed using  $\rho^{\text{DFT}}$  and  $\rho^{\text{scaled}}$ , for Al (left), and SiGe (right) systems.  $\rho^{\text{scaled}}$  is the scaled ML predicted electron density as given in Eq. 7.6. We observe that the errors are far better than chemical accuracy, i.e., errors below 1 kcal mol<sup>-1</sup> or 1.6 milli-Hartree atom<sup>-1</sup>, for both systems, even while considering various types of defects and compositional variations. Note that for Si<sub>x</sub>Ge<sub>1-x</sub>, we chose  $x = 0.4, 0.45, 0.55, 0.6$ . . . . . 149
- 7.9 The energy curve with respect to different lattice parameters for a  $2 \times 2 \times 2$  (left) and  $3 \times 3 \times 3$  (right) supercell of aluminum atoms. Overall, we see excellent agreement in the energies (well within chemical accuracy). The lattice parameter (related to the first derivative of the energy plot) calculated in each case agrees with the DFT-calculated lattice parameter to  $\mathcal{O}(10^{-2})$  Bohr or better (i.e., it is accurate to a fraction of a percent). The bulk modulus calculated (related to the second derivative of the energy plot) from DFT data and ML predictions agree to within 1%. For the  $3 \times 3 \times 3$  supercell, the bulk modulus calculated via DFT calculations is 76.39 GPa, close to the experimental value of about 76 GPa [17]. The value calculated from ML predictions is 75.80 GPa. . . . . 152
- 7.10 Uncertainty quantification for 1372 atom aluminum system. (a) ML prediction of the electron density, (b) Epistemic Uncertainty (c) Aleatoric Uncertainty (d) Total Uncertainty shown along the dotted line from the ML prediction slice. The uncertainty represents the bound  $\pm 3\sigma_{total}$ , where,  $\sigma_{total}$  is the total uncertainty. The unit for electron density is e Bohr<sup>-3</sup>, where e denotes the electronic charge. 153



7.11	Uncertainty quantification for $\text{Si}_{0.4}\text{Ge}_{0.6}$ system. (a) ML prediction of the electron density, (b) Epistemic Uncertainty (c) Aleatoric Uncertainty (d) Total Uncertainty shown along the dotted line from the ML prediction slice. The uncertainty represents the bound $\pm 3\sigma_{total}$ , where, $\sigma_{total}$ is the total uncertainty. The unit for electron density is $e \text{ Bohr}^{-3}$ , where e denotes the electronic charge. . . . .	153
7.12	Uncertainty quantification for a 256 atom aluminum system with a mono vacancy defect. (a) ML prediction of the electron density shown on the defect plane, (b)) Epistemic uncertainty (c) Aleatoric uncertainty d) Uncertainty shown along the black dotted line from the ML prediction slice. The uncertainty represents the bound $\pm 3\sigma_{total}$ , where, $\sigma_{total}$ is the total uncertainty. Note that the model used to make the predictions in (a-d) is not trained on the defect data, as opposed to the model used for (e), where defect data from the 108 atom aluminum system was used to train the model. The uncertainty and error at the location of the defect reduce with the addition of defect data in the training, as evident from (d) and (e). The unit for electron density is $e \text{ Bohr}^{-3}$ , where e denotes the electronic charge. . . . .	154
7.13	Computational time comparison between DFT calculations and prediction via trained ML model. (Top) Aluminum, (Bottom) SiGe. The DFT calculations scale $\mathcal{O}(N_a^3)$ with respect to the system size (number of atoms $N_a$ ), whereas, the present ML model scales linearly (i.e., $\mathcal{O}(N_a)$ ). The time calculations were performed using the same number of CPU cores and on the same system (Perlmutter CPU). . . . .	156
7.14	Prediction of electronic structure for aluminum system containing $\approx 4.1$ million atoms. The unit for electron density is $e \text{ Bohr}^{-3}$ , where e denotes the electronic charge. . . . .	157

7.15 Prediction of electronic structure for $\text{Si}_{0.5}\text{Ge}_{0.5}$ system containing $\approx 1.4$ million atoms. The unit for electron density is $e \text{ Bohr}^{-3}$ , where $e$ denotes the electronic charge. . . . .	158
7.16 Models with Transfer Learning (TL) and without Transfer Learning (Non-TL) for aluminium (left) and SiGe (right): (a) Root mean square error (RMSE) on the test dataset and (b) Computational time to generate the training data. In the case of aluminum, the TL model is trained using 32 and 108 atom data. For SiGe, the TL model was trained using 64 and 216 atom data. In the case of aluminum, the non-TL model is trained using 108 atom data. Whereas, in the case of SiGe, the non-TL model is trained using 216 atom data. . . . .	159

## LIST OF TABLES

3.1	Accuracy of the HelicES code while studying finite systems (green arrow denotes the $\mathbf{e}_z$ axis). Reference data was generated using RSDFT [18], a finite difference method (FDM) based MATLAB code. The last two columns show the maximum differences in the eigenvalues and the band energy per atom computed using the two methods. . . . .	44
5.1	The point group symmetries for each of the structures in Fig. 5.4, their formation energies, as well as the point group symmetries displayed by each configuration during a dynamical simulation/evolution over 22.8 ps. In comparison, the formation energy for a monomer calcium phosphate was calculated to be $-84.244$ eV. The listed formation energies of all trimer configurations are lower than three times this value. . . . .	95
6.1	The $J$ -coupling constants for each of the 6 dimer structures considered in this study. All values are in Hz. The coordinates of the $^{31}\text{P}$ atoms corresponding to subscripts $a, b, c, d$ are shown in Table 6.2. . . . .	121
6.2	The coordinates of the $^{31}\text{P}$ atoms corresponding to each figure in Fig. 6.8 . . . .	121

7.1	<p>Accuracy of the ML predicted electron density in terms of the <math>L^1</math> norm per electron, calculated as <math>\frac{1}{N_e} \times \int_{\Omega}  \rho^{\text{scaled}}(\mathbf{r}) - \rho^{\text{DFT}}(\mathbf{r})  d\mathbf{r}</math>, for various test cases for an FCC aluminum bulk system (<math>N_e</math> is the number of electrons in the system). Also shown in the table are errors in the different energies as computed from <math>\rho^{\text{scaled}}</math>. The test data set for post-processing was chosen such that it covered examples from all system sizes, configurations, and temperatures. For calculating the relevant energies, <math>\rho^{\text{scaled}}</math> was used as the initial guess for the electron density, and a single Hamiltonian diagonalization step was performed. Energies were then computed. . . . .</p>	150
7.2	<p>Accuracy of the ML predicted electron density in terms of <math>L^1</math> norm per electron, calculated as <math>\frac{1}{N_e} \times \int_{\Omega}  \rho^{\text{scaled}}(\mathbf{r}) - \rho^{\text{DFT}}(\mathbf{r})  d\mathbf{r}</math>, for various test cases for <math>\text{Si}_{0.5}\text{Ge}_{0.5}</math> (<math>N_e</math> is the number of electrons in the system). Also shown in the table are errors in the different energies as computed from <math>\rho^{\text{scaled}}</math>. The test data set for post-processing was chosen such that it covered examples from all system sizes and temperatures. For calculating the relevant energies, <math>\rho^{\text{scaled}}</math> was used as the initial guess for the electron density, and a single Hamiltonian diagonalization step was performed. Energies were then computed. For <math>\text{Si}_x\text{Ge}_{1-x}</math>, we used <math>x = 0.40, 0.45, 0.55, 0.60</math>. . . . .</p>	151
7.3	<p>A comparison between the calculated lattice parameter and the bulk modulus for aluminum using <math>\rho^{\text{ML}}</math> and <math>\rho^{\text{DFT}}</math> (DFT values in parentheses). We observe that the predicted lattice parameter closely matches the value given by DFT calculations. The “true” optimized lattice parameter for Al, using a fine k-space mesh, is found to be 7.5098 Bohr while experimental values are about 7.6 Bohr [19]). The ML predicted value of the bulk modulus matches the DFT value very closely, which itself is very close to the experimental value of approximately 76 GPa [17], at room temperature. . . . .</p>	151

## ACKNOWLEDGMENTS

I would like to take this opportunity to thank everyone who has helped me and inspired me throughout my academic endeavours. Notably, I would like to thank my advisor, Prof. Amartya S. Banerjee, who not only gave me the opportunity to work in an interesting area of research but who was also a great role model for me. I very much appreciate his unwavering support through some difficult and uncertain times, as well as the freedom and confidence I received from him during the entirety of my doctoral studies. Under his guidance, my journey has been fun and fulfilling. I have learnt from him much more than what is presented in this thesis, and for that I am truly grateful.

I would like to thank my committee members, Prof. Kang Wang, Prof. Benjamin Williams, Prof. Robert Candler, and Prof. Daniel Kattnig, for their feedback and suggestions. I would also like to specially thank Prof. Daniel Kattnig for his invaluable contributions and guidance to the works done in collaboration with him.

I also acknowledge support from grant DE-SC0023432 funded by the U.S. Department of Energy, Office of Science. This research used resources of the National Energy Research Scientific Computing Center, a DOE Office of Science User Facility supported by the Office of Science of the U.S. Department of Energy under Contract No. DE-AC02-05CH11231, using NERSC awards BES-ERCAP0025205, BES-ERCAP0025168, and BES-ERCAP0028072. A lot of the simulations in this work were also performed on the Hoffman2 cluster at UCLA's Institute for Digital Research and Education (IDRE).

Last but definitely not least, I would also like to thank my parents for giving me the opportunity to pursue such an enriching academic path, and for always pushing me to be the best version of myself. I would not be here without them.

## VITA

- 2015-2019 Bachelor of Technology (B. Tech.) in Electrical Engineering with Honors in Materials Science and Engineering, Indian Institute of Technology, Gandhinagar
- 2019 Award for Outstanding Research in B. Tech.
- 2019-2021 Master of Science in Electrical Engineering, University of California, Los Angeles

## PUBLICATIONS

- Agarwal, S., Aiello, C. D., Kattnig, D. R., & Banerjee, A. S. (2021). The dynamical ensemble of the posner molecule is not symmetric. *The Journal of Physical Chemistry Letters*, 12(42), 10372-10379.
- Aiello, C. D., Abendroth, J. M., Abbas, M., Afanasev, A., Agarwal, S., Banerjee, A. S., ... & Wang, Q. H. (2022). A chirality-based quantum leap. *ACS nano*, 16(4), 4989-5035.
- Agarwal, S., Kattnig, D. R., Aiello, C. D., & Banerjee, A. S. (2023). The Biological Qubit: Calcium Phosphate Dimers, Not Trimers. *The Journal of Physical Chemistry Letters*, 14(10), 2518-2525.
- Agarwal, S., & Banerjee, A. S. (2024). Solution of the Schrödinger equation for quasi-one-dimensional materials using helical waves. *Journal of Computational Physics*, 496, 112551.

Yu, H. M., Sharma, S., Agarwal, S., Liebman, O., & Banerjee, A. S. (2024). Carbon Kagome nanotubes—quasi-one-dimensional nanostructures with flat bands. *RSC advances*, 14(2), 963-981.

Pathrudkar, S., Thiagarajan, P., Agarwal, S., Banerjee, A. S., & Ghosh, S. (2024). Electronic structure prediction of multi-million atom systems through uncertainty quantification enabled transfer learning. (*accepted to npj Computational Materials*)

# CHAPTER 1

## Introduction

Low dimensional materials have been intensely investigated in the past few decades due to their remarkable electronic, optical, transport and mechanical characteristics [20, 21]. The properties of these materials often provide sharp contrasts with the bulk phase, and have led to various technological applications, including e.g., new kinds of sensors, actuators and energy harvesting devices [22, 23, 24, 25, 26, 27]. Quasi-one-dimensional materials — which include nanotubes, nanoribbons, nanowires, nanocoils, as well as miscellaneous structures of biological origin [28, 29] — are particularly interesting in this regard. This is due to the unique electronic properties that emerge as a result of the availability of a single extended spatial dimension in these structures [30, 31, 32, 33], the possibility that they are associated with ferromagnetism, ferroelectricity, and superconductivity [34, 35, 36, 37], and the fact that the behavior of these materials may be readily modulated via imposition of mechanical deformation modes such as torsion and/or stretching. [5, 38, 39]. Quasi-one-dimensional materials have also been investigated as hardware components for computing platforms — both conventional [40, 41] and quantum [42]. The applications of such materials in the latter case are connected to anomalous transport (the Chiral Induced Spin Selectivity effect [43]) and exotic electronic states [44] that can be observed in such systems.

Given the importance of quasi-one-dimensional materials, it is highly desirable to have available computational methods that can efficiently characterize the unique electronic properties of these systems. However, conventional electronic structure calculation methods — based e.g. on plane-waves [45, 46] — are generally inadequate in handling them. This is



a result of the non-periodic symmetries in the atomic arrangements of such materials. As a result of these symmetries, the single particle Schrödinger equation associated with the electronic structure problem exhibits special invariances [4, 47], which plane-waves, being intrinsically periodic, are unable to handle. For example, ground state plane-wave calculations of a twisted nanoribbon (see Fig. 2.1a) will usually involve making the system artificially periodic along the direction of the twist axis — thus resulting in a periodic supercell containing a very large number of atoms, as well as the inclusion of a substantial amount of vacuum padding in the directions orthogonal to the twist axis, so as to minimize interactions between periodic images. Together, these conditions can make such calculations extremely challenging even on high performance computing platforms, if not altogether impractical. There have been a few attempts to treat quasi-one-dimensional materials using Linear Combination of Atomic Orbitals (LCAO) based techniques [48, 49, 50, 51, 52, 53]. However, such methods suffer from basis incompleteness and superposition errors [54, 55, 56], which can make it difficult to obtain systematically convergent and improvable results.

In view of these limitations of conventional methods, a series of recent contributions has explored the use of real space techniques to study quasi-one-dimensional materials and their natural deformation modes [4, 5, 57, 58]. Specifically, this line of work incorporates the helical interaction potentials present in such systems using *helical Bloch waves* and employs higher order finite differences to discretize the single particle Schrödinger equation in *helical coordinates*. While this technique shows systematic convergence, and has enabled the exploration of various fascinating electromechanical properties, it also has a number of significant drawbacks. First, due to the curvilinearity of helical coordinates, the discretized Hamiltonian appearing in these calculations is necessarily non-Hermitian [59, 60]. This complicates the process of numerical diagonalization and makes many of the standard iterative eigensolvers [61] unusable. Second, the discretized equations have a coordinate singularity along the system axis which restricts the use of the methods to tubular structures and prevents important nanomaterials such as nanowires and nanoribbons from being studied. The presence of the

singularity also tends to ill condition the discretized Hamiltonian, which further restricts the applicability of the method to systems in which the atoms lie far enough away from the system axis (e.g. larger diameter nanotubes). Finally, while the finite difference approach does allow for the simulation of materials with twist (intrinsic or applied), the sparsity pattern of the discretized Hamiltonian worsens upon inclusion of twist, making simulations of such systems significantly more burdensome.

In this work we formulate and implement a novel computational technique that remedies all of the above issues and allows one to carry out systematic numerical solutions of the Schrödinger equation, as it applies to quasi-one-dimensional materials and structures. The technique presented here can be thought of as an analog of the classical plane-wave method, and is similar in spirit to the spectral scheme for clusters presented in [62]. Like the classical plane-wave method, a single parameter (the kinetic energy cutoff) dictates the overall quality of solution of our numerical scheme. We present a derivation of the basis functions of our method — called *helical waves* (or *twisted waves*) — as eigenfunctions of the Laplacian under suitable boundary conditions. We describe how helical waves may be used to discretize the symmetry adapted Schrödinger equation for quasi-one-dimensional materials, and how matrix-free iterative techniques can be used for diagonalization. A key feature of our technique is the handling of convolution sums through the use of fast basis transforms, and we describe in detail how these transforms are formulated and implemented. We also discuss various other computational aspects, including the choice of eigensolvers and preconditioners, and the handling of oscillatory radial integrals that appear in our method. We have implemented these techniques into a MATLAB [63] package called HelicES (**H**elical **E**lectronic **S**tructure), which we use for carrying out demonstrative electronic structure calculations of various quasi-one-dimensional materials. We also present results related to the convergence, computational efficiency and accuracy properties of our method, while using finite difference, transfer matrix and plane-wave methods for reference data.

We remark that our technique has connections with methods presented in earlier work

concerning electronic structure calculations in cylindrical geometries [64, 65, 66, 67, 68], but is more general in that the use of helical waves automatically allows both chiral (i.e., twisted) and achiral (i.e., untwisted) structures to be naturally handled. Additionally, some of these earlier studies have employed the strategy of setting up of the discretized Hamiltonian explicitly and then using direct diagonalization techniques, which scales in a significantly worse way (both in memory and computational time) compared to the transform based matrix-free strategies adopted by us. We also note in passing that the basis functions presented here appear to be scalar versions of twisted wave fields explored recently in the x-ray crystallography [69, 70] and elastodynamics [71, 72] literature.

Often, at the heart of such methods is the problem of evaluation of Newtonian potentials, that can be reformulated in terms of scalar Poisson equations [73]. We propose here a mixed spectral – finite-difference based numerical method for solving the Poisson problem for twisted geometries. Our computational method relies on expressing the governing equations in helical coordinates, and then using fast Fourier transforms along two coordinate directions, while incorporating finite differences along the third. The coordinate singularity at the origin is handled using suitable pole conditions [74, 75, 76]. Radial boundary conditions consistent with the decay of electrostatic potentials are naturally incorporated in our method, and the technique can also take advantage of cyclic symmetries that may be present in the problem. We demonstrate systematic convergence properties of the method and discuss issues governing its overall accuracy. We also present performance comparisons between our method and alternates based on helical Ewald sums [10] and analytical solutions (when available), and demonstrate orders of magnitude gains. We showcase the utility of our method in electronic structure calculations of one-dimensional nanomaterials, especially as they are subjected to twisting deformations. This lays down much of the groundwork for incorporating self consistency within the helical waves framework developed in our works.

In addition to the above, and in line with the theme of computational methods to study emergent nanomaterials and biomolecules, we extend our efforts towards the study of Posner

Molecules (PMs) [77]. The PM (calcium phosphate trimer,  $\text{Ca}_9(\text{PO}_4)_6$ ), was first hypothesized to exist in the bone mineral hydroxyapatite [77], and has since been identified as the structural unit of amorphous calcium phosphate [78]. Its aggregation is thought to underpin bone growth [79, 80, 81, 82]. Although the Posner molecule is yet to be unambiguously experimentally observed in an isolated form, its biochemical relevance has long been recognized. In recent years, Fisher and co-workers have suggested that pairs of isolated Posner molecules could act as “neural qubits” by harboring long-lived entangled spin states amongst the twelve  $^{31}\text{P}$  nuclei [11, 15, 83]. This has been hypothesized to facilitate long-range quantum-correlated release of  $\text{Ca}^{2+}$  ions in pre-synaptic neurons and thus, to potentially give rise to correlated post-synaptic neuron firing [15].

Central to the above-mentioned proposal is the supposed  $S_6$ -symmetric arrangement of the molecule, wherein a rotational axis of symmetry allows the binding and unbinding of Posner molecules to act as a “pseudospin” entangler for the nuclear spin states [11, 15]. However, through an extensive series of first principles simulations, we demonstrate [14] that the Posner molecule does not exhibit the required symmetry and instead exists as a dynamical ensemble of predominantly low-symmetry clusters. Given that all prior works [11, 16], until now, have considered the  $S_6$ -symmetric structure of the Posner molecule to make theoretical predictions on the entanglement times of the nuclear spin states and for examining the viability of the molecule as a potential biomolecular qubit, here, we explore if, and for how long,  $^{31}\text{P}$  nuclear spin coherences can be maintained for the multiple asymmetric configurations found in our work.

While our studies above were fruitful, we were often limited on the size of the structures that we could simulate and the accuracy of those simulations. This is due to the inherent cubic scaling of KS-DFT with respect to the number of atoms in the simulation cell. Most *ab initio* frameworks — which forms the bulk of the computational methodologies used in this study — are subject to similar limitations. To address this challenge, a number of different approaches, which vary in their computational expense and their range of applicability, have

been proposed over the years. Such techniques generally avoid explicit diagonalization of the Kohn-Sham Hamiltonian in favor of computing the single particle density matrix [84]. Many of these methods are able to scale linearly with respect to the system size when bulk insulators or metals at high temperatures are considered [84, 85, 86, 87, 88], while others exhibit sub-quadratic scaling when used for calculations of low-dimensional materials (i.e., nanostructures) [89, 90]. Contrary to these specialized approaches, there are only a handful of first-principles electronic structure calculation techniques that operate universally across bulk metallic, insulating, and semiconducting systems, while performing more favorably than traditional cubic scaling methods (especially, close to room temperature). However, existing techniques in this category, e.g. [91, 92], tend to face convergence issues due to aggressive use of density matrix truncation, and in any case, have only been demonstrated for systems containing at most a few thousand atoms, due to their overall computational cost. Keeping these developments in mind, a separate thread of research has also explored reducing computational wall times by lowering the prefactor associated with the cubic cost of Hamiltonian diagonalization, while ensuring good parallel scalability of the methods on large scale high-performance computing platforms [93, 94, 95, 96]. In spite of demonstrations of these and related methods to study a few large example problems (e.g. [97, 98, 99]), their routine application to complex condensed matter systems, using modest, everyday computing resources appears infeasible.

An attractive alternative path to overcoming the cubic scaling bottleneck of KS-DFT — one that has found much attention in recent years — is the use of Machine Learning (ML) models as surrogates [100, 101]. Indeed, a significant amount of research has already been devoted to the development of ML models that predict the energies and forces of atomic configurations matching with KS-DFT calculations, thus spawning ML-based interatomic potentials that can be used for molecular dynamics calculations with ab initio accuracy [102, 103, 104, 105, 106, 107]. Parallely, researchers have also explored direct prediction of the ground state electron density via ML models trained on the self-consistent electron density

obtained from KS-DFT simulations [108, 109, 110, 111, 112, 113]. This latter approach is particularly appealing, since, in principle, the ground state density is rich in information that goes well beyond energies and atomic forces, and such details can often be extracted through simple post-processing steps. Development of ML models of the electron density can also lead to electronic-structure-aware potentials, which are likely to overcome limitations of existing Machine Learning Interatomic Potentials, particularly in the context of reactive systems [114, 115]. Having access to the electron density as an intermediate verifiable quantity is generally found to also increase the quality of ML predictions of various material properties [108, 116], and can allow training of additional ML models. Such models can use the density as a descriptor to predict specific quantities, such as defect properties of complex alloys [117, 118] and bonding information [119]. Two distinct approaches have been explored in prior studies to predict electron density via Machine Learning, differing in how they represent the density – the output of the machine learning model. One strategy involves representing the density by expanding it as a sum of atom-centered basis functions [120, 121]. The other involves predicting the electron density at each grid point in a simulation cell. Both strategies aim to predict the electron density using only the atomic coordinates as inputs. While the former strategy allows for a compact representation of the electron density, it requires the determination of an optimized basis set that is tuned to specific chemical species. It has been shown in [120] that the error in the density decomposition through this strategy can be reduced to as low as 1%. In contrast, the latter strategy does not require such optimization but poses a challenge in terms of inference - where the prediction for a single simulation cell requires inference on thousands of grid points (even at the grid points in a vacuum region). The former strategy has shown good results for molecules [120] while the latter has shown great promise in density models for bulk materials especially metals [110, 122, 112].

In this work, we use the latter approach and propose a machine-learning model that accurately predicts the ground state electron density of bulk materials at any scale, while quantifying the associated uncertainties. Once trained, our model significantly outperforms

conventional KS-DFT-based computations in terms of speed. To address the high cost of training data generation associated with KS-DFT simulations of larger systems — a key challenge in developing effective ML surrogates of KS-DFT — we adopt a transfer learning (TL) approach [123]. Thus, our model is first trained using a large quantity of cheaply generated data from simulations of small systems, following which, a part of the model is retrained using a small amount of data from simulations of a few large systems. This strategy significantly lowers the training cost of the ML model, without compromising its accuracy.

## CHAPTER 2

# HelicES: A symmetry-adapted spectral electronic structure method

### 2.1 Formulation

In this section, we describe our formulation of our spectral electronic structure framework for quasi-one-dimensional materials with arbitrary twists. We first lay out the notation used in the rest of the paper. In what follows,  $\mathbf{e}_x$ ,  $\mathbf{e}_y$ ,  $\mathbf{e}_z$  will denote the standard orthonormal basis of  $\mathbb{R}^3$ . Position vectors will be typically denoted using boldface lower case letters (e.g.,  $\mathbf{p}$ ) and rotation matrices using boldface uppercase (e.g.,  $\mathbf{Q}$ ). The atomic unit system of  $m_e = 1$ ,  $\hbar = 1$ ,  $\frac{1}{4\pi\epsilon_0} = 1$  will be used throughout the paper, unless otherwise mentioned. Cartesian and cylindrical coordinates will be typically denoted as  $(x, y, z)$  and  $(r, \vartheta, z)$  respectively. The  $\times$  sign will be reserved for denoting dimensions of matrices (e.g. using  $M \times N$  to denote the dimensions of a matrix with  $M$  rows and  $N$  columns), while  $*$  will be used to explicitly denote multiplication by or in between scalars, vectors and matrices.

#### 2.1.1 Description of physical system and computational problem

We consider a quasi-one-dimensional nanostructure of infinite extent aligned along  $\mathbf{e}_z$  (see Fig. 2.1). We assume the structure to be of limited extent along  $\mathbf{e}_x$  and  $\mathbf{e}_y$ . Let the atoms of the structure have coordinates:

$$\mathcal{S} = \{\mathbf{p}_1, \mathbf{p}_2, \mathbf{p}_3, \dots : \mathbf{p}_i \in \mathbb{R}^3\}. \quad (2.1)$$



Quasi-one-dimensional structures in their undeformed states, or while being subjected to natural deformation modes such as extension, compression or torsion, can often be described using helical (i.e., screw transformation) and cyclic symmetries [4, 5, 29, 47]. Accordingly, we may identify a finite subset of atoms of the structure with coordinates:

$$\mathcal{P} = \{\mathbf{r}_1, \mathbf{r}_2, \mathbf{r}_3, \dots, \mathbf{r}_M : \mathbf{r}_i \in \mathbb{R}^3\}, \quad (2.2)$$

and a corresponding set of symmetry operations:

$$\mathcal{G} = \left\{ \Upsilon_{\zeta, \mu} = (\mathbf{R}_{(2\pi\zeta\alpha + \mu\Theta)} | \zeta\tau\mathbf{e}_z) : \zeta \in \mathbb{Z}, \mu = 0, 1, \dots, \mathfrak{N} - 1 \right\}, \quad (2.3)$$

such that:

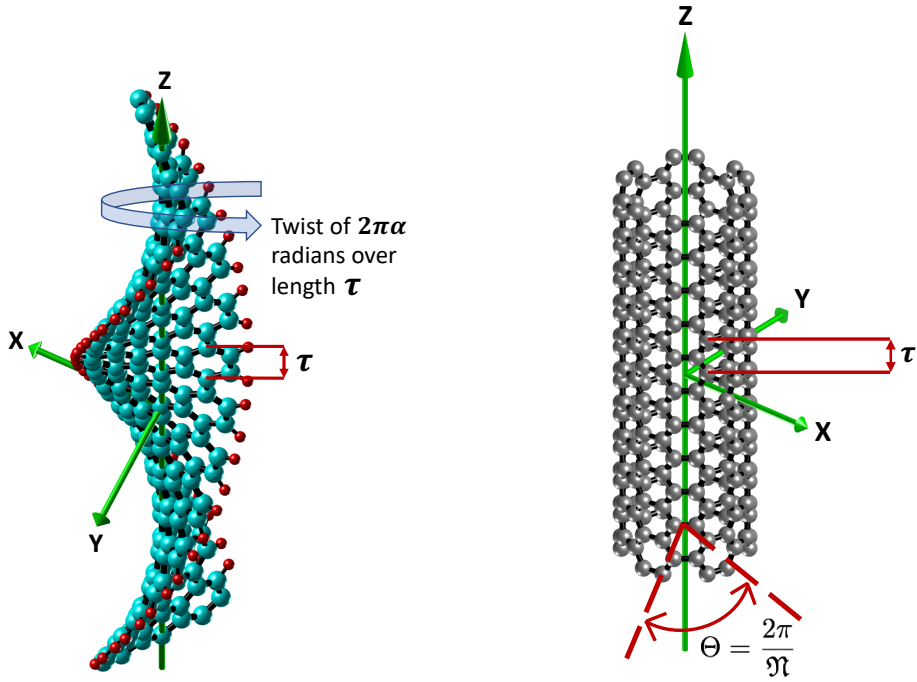
$$\mathcal{S} = \bigcup_{\substack{\zeta \in \mathbb{Z} \\ \mu=0,1,\dots,\mathfrak{N}-1}} \bigcup_{i=1}^M \mathbf{R}_{(2\pi\zeta\alpha + \mu\Theta)} \mathbf{r}_i + \zeta\tau\mathbf{e}_z. \quad (2.4)$$

Here, the  $\Upsilon_{\zeta, \mu}$  are symmetry operations of the structure — specifically, each  $\Upsilon_{\zeta, \mu}$  is an isometry whose action on an arbitrary point  $\mathbf{x} \in \mathbb{R}^3$  (denoted as  $\Upsilon_{\zeta, \mu} \circ \mathbf{x}$ ) is to rotate it by the angle  $2\pi\zeta\alpha + \mu\Theta$  about  $\mathbf{e}_z$ , while simultaneously translating it by  $\mu\tau$  about the same axis. The natural number  $\mathfrak{N}$  is related to cyclic symmetries in the nanostructure about the axis  $\mathbf{e}_z$ , with  $\Theta = 2\pi/\mathfrak{N}$  denoting the cyclic symmetry angle. The quantity  $\tau$  is the pitch of the screw transformation part of  $\Upsilon_{\zeta, \mu}$ , the parameter  $\alpha$  takes values  $0 \leq \alpha < 1$ , and  $\beta = 2\pi\alpha/\tau$  captures the rate of twist (imposed or intrinsic) in the structure. The case  $\alpha = 0$  usually represents achiral or untwisted structures (see Fig. 2.1).

The electronic properties of a quasi-one-dimensional material under study can be investigated by calculating the spectrum of the single particle Schrödinger operator:

$$\mathfrak{H} = -\frac{1}{2}\Delta + V(\mathbf{x}), \quad (2.5)$$

associated with the system. Determination of the spectrum in an efficient manner, especially for realistic quasi-one-dimensional nanomaterials serves as the primary computational problem of interest in this work. Here,  $V(\mathbf{x})$  represents the “effective potential” as perceived by



(a) A twisted nanoribbon

(b) An armchair nanotube

Figure 2.1: Examples of the type of nanostructures that can be investigated using the computational framework presented in this work. Helical and cyclic symmetry parameters associated with the geometries of the structures are shown.

the electrons. The potential can be computed through self-consistent means (for example, as part of Density Functional Theory calculations [4, 5]), or through the use of empirical pseudopotentials [124, 125], as done here. Due to the presence of global structural symmetries, the potential is expected to obey:

$$V(\mathbf{x}) = V(\Upsilon_{\zeta, \mu} \circ \mathbf{x}), \forall \Upsilon_{\zeta, \mu} \in \mathcal{G}. \quad (2.6)$$

As a consequence of the quasi-one-dimensional nature of the system, and the above symmetry conditions, the eigenstates of the Hamiltonian can be characterized in terms of Helical Bloch

waves [4, 47]. Specifically, solutions of the Schrödinger equation:

$$\left(-\frac{1}{2}\Delta + V(\mathbf{x})\right)\psi = \lambda\psi, \quad (2.7)$$

can be labeled using band indices  $j \in \mathbb{N}$ , and symmetry adapted quantum numbers  $\eta \in [-\frac{1}{2}, \frac{1}{2})$ ,  $\nu \in \{0, 1, 2, \dots, \mathfrak{N} - 1\}$ . Moreover, these solutions obey the following condition for any symmetry operation  $\Upsilon_{\zeta, \mu} \in \mathcal{G}$ :

$$\psi_j(\Upsilon_{\zeta, \mu} \circ \mathbf{x}; \eta, \nu) = e^{-2\pi i \left(\zeta\eta + \frac{\mu\nu}{\mathfrak{N}}\right)} \psi_j(\mathbf{x}; \eta, \nu). \quad (2.8)$$

The above relation can be used to reduce the computational problem of determining the eigenstates of the Schrödinger operator over all of space, to a fundamental domain or symmetry-adapted unit cell.

Since the structures considered here have limited spatial extent in the  $\mathbf{e}_x - \mathbf{e}_y$  plane, so does the computational unit cell. We denote the maximum radial coordinate of the points in the computational domain as  $R$ . Then, this region of space (see Fig. 2.3) can be parametrized in cylindrical coordinates as:

$$\mathcal{D} = \left\{ (r, \vartheta, z) : 0 \leq r \leq R, \frac{2\pi\alpha z}{\tau} \leq \vartheta \leq \frac{2\pi\alpha z}{\tau} + \Theta, 0 \leq z \leq \tau \right\}. \quad (2.9)$$

Due to the decay of the wavefunctions in the radial direction [126, 127], it is often appropriate to enforce Dirichlet boundary conditions on the surface  $r = R$ , as done here. In practice, the value of  $R$  can be chosen so as to ensure a sufficient amount of vacuum exists between the structure under study and this lateral boundary surface [4, 57].

### 2.1.2 The helical coordinate system and transformation of Schrödinger's equation

For computational purposes, it is useful to utilize a coordinate system that describes the computational domain  $\mathcal{D}$ , and the quasi-one-dimensional system's symmetries more naturally. To this end, we employ helical coordinates [47, 128, 129] in this work (Fig. 2.2). For

a point  $\mathbf{p} \in \mathbb{R}^3$  with Cartesian coordinates  $(x_{\mathbf{p}}, y_{\mathbf{p}}, z_{\mathbf{p}})$ , cylindrical coordinates  $(r_{\mathbf{p}}, \vartheta_{\mathbf{p}}, z_{\mathbf{p}})$ , and helical coordinates  $(\theta_{1\mathbf{p}}, \theta_{2\mathbf{p}}, r_{\mathbf{p}})$ , the following relations hold:

$$\begin{aligned} r_{\mathbf{p}} &= \sqrt{x_{\mathbf{p}}^2 + y_{\mathbf{p}}^2}, \quad \theta_{1\mathbf{p}} = \frac{z_{\mathbf{p}}}{\tau}, \\ \theta_{2\mathbf{p}} &= \frac{1}{2\pi} \arctan 2(y_{\mathbf{p}}, x_{\mathbf{p}}) - \alpha \frac{z_{\mathbf{p}}}{\tau} = \frac{\vartheta_{\mathbf{p}}}{2\pi} - \alpha \frac{z_{\mathbf{p}}}{\tau}. \end{aligned} \quad (2.10)$$

Regardless of the amount of twist or cyclic symmetries present in the system, the fundamental domain  $\mathcal{D}$  (eq. 2.9) can be conveniently expressed as a cuboid in helical coordinates, i.e.,

$$\mathcal{D} = \{(\theta_1, \theta_2, r) : 0 \leq \theta_1 \leq 1, 0 \leq \theta_2 \leq \frac{1}{\mathfrak{N}}, 0 \leq r \leq R\}. \quad (2.11)$$

Thus, it is easier to setup a computational mesh over the fundamental domain using helical coordinates. Moreover, the action of the symmetry operations  $\Upsilon_{\zeta, \mu} \in \mathcal{G}$  is to simply result in translations of the helical coordinates: if  $\mathbf{p} \in \mathbb{R}^3$  has helical coordinates  $(\theta_{1\mathbf{p}}, \theta_{2\mathbf{p}}, r_{\mathbf{p}})$ , then  $\Upsilon_{\zeta, \mu} \circ \mathbf{p}$  has helical coordinates  $(\theta_{1\mathbf{p}} + \zeta, \theta_{2\mathbf{p}} + \frac{\mu}{\mathfrak{N}}, r_{\mathbf{p}})$ . In particular, this implies that

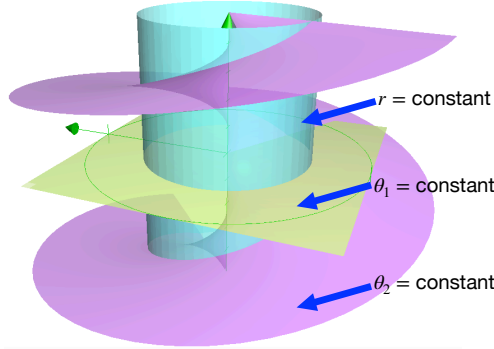


Figure 2.2: The helical coordinate system represented as constant surfaces of the parameters  $r, \theta_1, \theta_2$  (the twist parameter  $\alpha$  is nonzero here).

a function that is group invariant may be represented over the computational domain by means of periodic boundary conditions along the  $\theta_1$  and  $\theta_2$  directions.

Next, we formulate the governing equations, i.e., Helical-Bloch wave form of Schrodinger's equation over the fundamental domain using helical coordinates. To this end, we first note

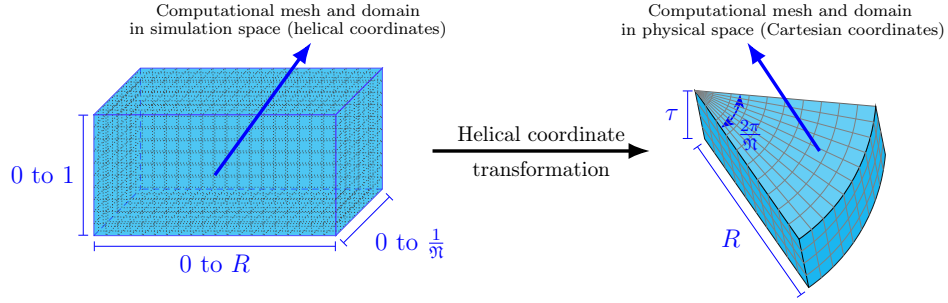


Figure 2.3: The computational mesh represented in simulation space using helical coordinates (left), and physical space using Cartesian coordinates (right). The slanted walls of the fundamental domain  $\mathcal{D}$  in physical space (right) arise due to possibly arbitrary values of twist associated with the system.

that:

$$\begin{aligned}
 -\frac{1}{2}\Delta\psi_j + V\psi_j = & -\frac{1}{2}\left[ (\psi_j)_{rr} + \frac{1}{r}(\psi_j)_r + \frac{1}{\tau^2}(\psi_j)_{\theta_1\theta_1} - \frac{2\alpha}{\tau^2}\psi_{\theta_1\theta_2} \right. \\
 & \left. + \frac{1}{4\pi^2}\left(\frac{1}{r^2} + \frac{4\pi^2\alpha^2}{\tau^2}\right)(\psi_j)_{\theta_2\theta_2} \right] + V\psi_j = \lambda_j\psi_j
 \end{aligned} \tag{2.12}$$

Then, we recast eq. 2.8 to imply that the wavefunctions admit the following Helical Bloch ansatz [5]:

$$\psi_j(\theta_1, \theta_2, r; \eta, \nu) = e^{-i2\pi(\eta\theta_1 + \nu\theta_2)}\phi_j(\theta_1, \theta_2, r; \eta, \nu). \tag{2.13}$$

Here,  $\eta \in [-\frac{1}{2}, \frac{1}{2})$ ,  $\nu \in \{0, 1, 2, \dots, \mathfrak{N} - 1\}$ , and the auxiliary functions  $\phi_j(\theta_1, \theta_2, r; \eta, \nu)$  are group invariant. In particular, this implies that these functions obey the conditions:

$$\begin{aligned}
 \phi_j(\theta_1, \theta_2, r; \eta, \nu) &= \phi_j(\theta_1 + 1, \theta_2, r; \eta, \nu) \\
 \phi_j(\theta_1, \theta_2, r; \eta, \nu) &= \phi_j(\theta_1, \theta_2 + \frac{1}{\mathfrak{N}}, r; \eta, \nu).
 \end{aligned} \tag{2.14}$$

Substituting eq. 2.13 into the Schrödinger equation above (eq. 2.12) and after some algebra, we arrive at:

$$\begin{aligned}
 \left[ -\frac{1}{2}\Delta\phi_j - \left( \frac{2\pi^2}{\tau^2} \left\{ \nu\alpha(2\eta - \nu\alpha) - \eta^2 \right\} - \frac{\nu^2}{2r^2} \right) \phi_j - \frac{2i\pi}{\tau^2}(\nu\alpha - \eta)(\phi_j)_{\theta_1} \right. \\
 \left. - 2i\pi \left[ \frac{\alpha}{\tau^2}(\eta - \nu\alpha) - \frac{\nu}{4\pi^2 r^2} \right] (\phi_j)_{\theta_2} + V\phi_j \right] = \lambda_j\phi_j.
 \end{aligned} \tag{2.15}$$

This serves as the governing equation for the computational method in this work. It needs to be discretized and solved over the fundamental domain along with the enforcement of periodic boundary conditions in the  $\theta_1$  and  $\theta_2$  directions (eq. 2.14), and the imposition of wavefunction decay in the radial direction, i.e.:

$$\phi_j(\theta_1, \theta_2, r = R; \eta, \nu) = 0. \quad (2.16)$$

Note that due to eq. 2.6, the effective potential in helical coordinates,  $V(\theta_1, \theta_2, r)$ , also obeys conditions of the form outlined in eq. 2.14, although it is generically not expected to obey the decay conditions similar to eq. 2.16.

### 2.1.3 Basis set and discretization

We now discuss discretization of the governing equations using helical waves. First, we derive the basis set that we use in this work. In analogy to the classical plane-wave method [45, 46], the basis functions in our scheme are eigenfunctions of the Laplacian. However, instead of periodic boundary conditions obeyed by planewaves, we consider boundary conditions resulting from invariance under helical and cyclic symmetries. The calculation presented below is based on similar results in [47], while a vector version of this calculation appears in [69, 70] in the context of x-ray diffraction patterns of twisted nanomaterials.

Let  $F(\theta_1, \theta_2, r)$  be a basis function expressed in helical coordinates. Then, invariance under helical and cyclic symmetries implies that this function must be periodic in  $\theta_1$  with a period of 1, and also periodic in  $\theta_2$  with a period of  $\frac{1}{\mathfrak{N}}$ . Assuming  $F(\theta_1, \theta_2, r)$  is separable, we characterize the dependence of the function on  $\theta_1$  and  $\theta_2$  through Fourier modes (i.e., complex exponentials), and write:

$$F_{m,n,k}(\theta_1, \theta_2, r) = e^{i2\pi(m\theta_1 + n\mathfrak{N}\theta_2)} \xi(r). \quad (2.17)$$

Here  $\xi(r)$  is a purely radial function that possibly depends on  $m, n, k$ , and incorporates

normalization constants. The Laplacian of the above function in the helical coordinates is:

$$\begin{aligned} \Delta F_{m,n,k} = & \xi_r e^{i2\pi(m\theta_1+n\mathfrak{N}\theta_2)} + \frac{1}{r} \xi_{rr} e^{i2\pi(m\theta_1+n\mathfrak{N}\theta_2)} - \frac{4\pi^2 m^2}{\tau^2} F_{m,n,k} \\ & + \frac{8\alpha\pi^2 n m \mathfrak{N}}{\tau^2} F_{m,n,k} - \left( \frac{1}{r^2} + \frac{4\pi^2 \alpha^2}{\tau^2} \right) n^2 \mathfrak{N}^2 F_{m,n,k}, \end{aligned} \quad (2.18)$$

which can be rewritten as:

$$\Delta f_{m,n,k} = e^{i2\pi(m\theta_1+n\mathfrak{N}\theta_2)} \left[ \xi_{rr} + \frac{1}{r} \xi_r \right] - F_{m,n,k} \left[ \frac{n^2 \mathfrak{N}^2}{r^2} + \frac{4\pi^2}{\tau^2} (m - \alpha n \mathfrak{N})^2 \right]. \quad (2.19)$$

Now, imposing the condition that  $f_{m,n,k}$  is an eigenfunction of the Laplacian, i.e.,

$$-\Delta F_{m,n,k} = \lambda_{m,n,k}^0 F_{m,n,k}, \quad (2.20)$$

we get:

$$\begin{aligned} -e^{i2\pi(m\theta_1+n\mathfrak{N}\theta_2)} \left[ \xi_{rr} + \frac{1}{r} \xi_r \right] + e^{i2\pi(m\theta_1+n\mathfrak{N}\theta_2)} \left[ \frac{n^2 \mathfrak{N}^2}{r^2} + \frac{4\pi^2}{\tau^2} (m - \alpha n \mathfrak{N})^2 \right] \xi \\ = \lambda_{m,n,k}^0 e^{i2\pi(m\theta_1+n\mathfrak{N}\theta_2)} \xi, \end{aligned} \quad (2.21)$$

which simplifies to:

$$\xi_{rr} + \frac{1}{r} \xi_r - \xi \left[ \frac{n^2 \mathfrak{N}^2}{r^2} - \lambda_{m,n,k}^0 + \frac{4\pi^2}{\tau^2} (m - \alpha n \mathfrak{N})^2 \right] = 0. \quad (2.22)$$

Denoting  $\xi_{m,n}^2 = \frac{4\pi^2}{\tau^2} (m - \alpha n \mathfrak{N})^2$  and performing the change of variables:

$$\tilde{r} = r \sqrt{\lambda_{m,n,k}^0 - \gamma_{m,n}^2}, \quad \xi(r) = \tilde{\xi}(\tilde{r}), \quad (2.23)$$

we see that the above equation reduces to:

$$\tilde{r}^2 \tilde{\xi}_{\tilde{r}\tilde{r}} + \tilde{r} \tilde{\xi}_{\tilde{r}} + (\tilde{r}^2 - n^2 \mathfrak{N}^2) \tilde{\xi} = 0. \quad (2.24)$$

This is simply Bessel's equation [130, 131] in  $\tilde{\xi}(\tilde{r})$ . Since  $n\mathfrak{N}$  is real, the general solution of this equation can be expressed in terms of ordinary Bessel functions of the first and second kind as:

$$\tilde{\xi}(\tilde{r}) = A J_{n\mathfrak{N}}(\tilde{r}) + B Y_{n\mathfrak{N}}(\tilde{r}). \quad (2.25)$$

To evaluate the constants  $A$  and  $B$ , we need to invoke boundary and normalization conditions. Since the wavefunctions are expected to be finite valued at the origin ( $r = 0$ ), and Bessel functions of the second kind approach infinity near 0, we conclude that  $B = 0$ . Furthermore, since the wavefunctions obey Dirichlet boundary conditions on the lateral surface of the computational domain ( $r = R$ ), so should the basis functions used to discretize them. Hence, we obtain:

$$\xi\left(R\sqrt{\lambda_{m,n,k}^0 - \gamma_{m,n}^2}\right) = A J_{n\mathfrak{N}}\left(R\sqrt{\lambda_{m,n,k}^0 - \gamma_{m,n}^2}\right) = 0. \quad (2.26)$$

This implies that  $R\sqrt{\lambda_{m,n,k}^0 - \gamma_{m,n}^2}$  must be a root of the the ordinary Bessel function of the first kind. Denoting the  $k^{\text{th}}$  root ( $k = 1, 2, \dots$ ) of the Bessel function of order  $p$ , as  $b_k^p$ , we see that:

$$b_k^{n\mathfrak{N}} = R\sqrt{\lambda_{m,n,k}^0 - \gamma_{m,n}^2}, \quad (2.27)$$

from which, it follows that:

$$\lambda_{m,n,k}^0 = \left(\frac{b_k^{n\mathfrak{N}}}{R}\right)^2 + \left[\frac{2\pi}{\tau}(m - \alpha n\mathfrak{N})\right]^2. \quad (2.28)$$

Thus, we have:

$$\xi(r) = A J_{n\mathfrak{N}}\left(\frac{b_k^{n\mathfrak{N}}}{R}r\right). \quad (2.29)$$

Finally, to determine the constant  $A$ , we apply the orthonormality condition between two distinct basis functions  $F_{m,n,k}$  and  $F_{m',n',k'}$ :

$$\langle F_{m,n,k}, F_{m',n',k'} \rangle_{\mathcal{L}^2(\mathcal{D})} = \delta_{m,m'} \delta_{n,n'} \delta_{k,k'}. \quad (2.30)$$

This requires that:

$$\begin{aligned} A^2 \int_0^1 e^{i2\pi(m-m')\theta_1} d\theta_1 \times \int_0^{\frac{1}{\mathfrak{N}}} e^{i2\pi\mathfrak{N}(n-n')\theta_2} d\theta_2 \\ \times \int_0^R J_{n\mathfrak{N}}\left(\frac{b_k^{n\mathfrak{N}}}{R}r\right) J_{n'\mathfrak{N}}\left(\frac{b_{k'}^{n'\mathfrak{N}}}{R}r\right) 2\pi\tau r dr = \delta_{m,m'} \delta_{n,n'} \delta_{k,k'}. \end{aligned} \quad (2.31)$$



Due to the properties of complex exponentials and Bessel functions, we note that this condition is readily satisfied for distinct basis functions (i.e., when any of the conditions  $m \neq m'$ ,  $n \neq n'$ ,  $k \neq k'$  hold). For the case  $m = m'$ ,  $n = n'$ ,  $k = k'$ , we arrive at:

$$\frac{2\pi\tau A^2}{\mathfrak{N}} \int_0^R J_{n\mathfrak{N}}^2 \left( \frac{b_k^{n\mathfrak{N}} r}{R} \right) r dr = 1, \quad (2.32)$$

i.e.,

$$\frac{2\pi\tau A^2}{\mathfrak{N}} \frac{R^2}{2} J_{n\mathfrak{N}+1}^2 (b_k^{n\mathfrak{N}}) = 1. \quad (2.33)$$

Thus it follows that the normalization constant:

$$A = \sqrt{\frac{\mathfrak{N}}{\pi\tau}} \frac{1}{R J_{n\mathfrak{N}+1} (b_k^{n\mathfrak{N}})}, \quad (2.34)$$

and that:

$$\xi(r) \equiv \xi_{n,k}(r) = \sqrt{\frac{\mathfrak{N}}{\pi\tau}} \frac{1}{R J_{n\mathfrak{N}+1} (b_k^{n\mathfrak{N}})} J_{n\mathfrak{N}} \left( \frac{b_k^{n\mathfrak{N}} r}{R} \right). \quad (2.35)$$

Hence, the basis functions in our method have the form:

$$F_{m,n,k}(\theta_1, \theta_2, r) = \sqrt{\frac{\mathfrak{N}}{\pi\tau}} \frac{1}{R J_{n\mathfrak{N}+1} (b_k^{n\mathfrak{N}})} e^{i2\pi(m\theta_1 + n\mathfrak{N}\theta_2)} J_{n\mathfrak{N}} \left( \frac{b_k^{n\mathfrak{N}} r}{R} \right). \quad (2.36)$$

Note that if the computational domain were an annular cylinder (as employed in [4, 5]), instead of the solid cylinder considered here, the boundary conditions on the radial part of the wavefunction would be expected to change. For Dirichlet boundary conditions applied to the inner and outer walls of such an annular cylinder — often employed in simulations of large diameter nanotubes — Bessel functions of both kinds would be involved (i.e.,  $A, B \neq 0$  in eq. 2.25) and the zeros of the cross products of Bessel functions [132] would be required.

With the knowledge of the above basis set, we can now discuss the strategy to discretize our governing equations. In what follows, we will usually suppress the dependence of  $\phi_j(\theta_1, \theta_2, r; \eta, \nu)$  on the band index ( $j$ ) for the sake of simplicity of notation. Denoting the

basis functions as  $F_{m,n,k}(\theta_1, \theta_2, r)$  in helical coordinates, we write:

$$\begin{aligned}\phi(\theta_1, \theta_2, r) &= \sum_{(m,n,k) \in \Gamma} \hat{\phi}_{m,n,k} F_{m,n,k}(\theta_1, \theta_2, r) \\ &= \sum_{(m,n,k) \in \Gamma} \hat{\phi}_{m,n,k} c_{m,n,k} e^{i2\pi(m\theta_1 + n\mathfrak{N}\theta_2)} J_{n\mathfrak{N}}\left(\frac{b_k^{n\mathfrak{N}} r}{R}\right).\end{aligned}\quad (2.37)$$

Here,  $\hat{\phi}_{m,n,k}$  are the expansion coefficients,  $J_{n\mathfrak{N}}(\cdot)$  denotes Bessel functions of the first kind of order  $n\mathfrak{N}$ , while  $b_k^{n\mathfrak{N}}$  denote the zeros of the Bessel functions. The basis function normalization constants  $c_{m,n,k}$  are:

$$c_{m,n,k} = \sqrt{\frac{\mathfrak{N}}{\pi\tau}} \frac{1}{R J_{n\mathfrak{N}+1}(b_k^{n\mathfrak{N}})}.\quad (2.38)$$

The set  $\Gamma$  denotes triplets of integers  $(m, n, k)$  such that  $m \in [-M_{\max}, M_{\max}]$ ,  $n \in [-N_{\max}, N_{\max}]$  and  $k \in [1, K_{\max}]$ . The basis set size is  $\mathcal{L} = (2M_{\max} + 1) * (2N_{\max} + 1) * K_{\max}$ , i.e., it grows as  $\mathcal{O}(M_{\max} N_{\max} K_{\max})$  in terms of the discretization sizes along the  $\theta_1, \theta_2, r$  directions. By design, the basis functions are orthonormal, i.e.:

$$\langle F_{m,n,k}, F_{m',n',k'} \rangle_{\mathcal{L}^2(\mathcal{D})} = \delta_{m,m'} \delta_{n,n'} \delta_{k,k'},\quad (2.39)$$

and they satisfy:

$$-\Delta F_{m,n,k} = \lambda_{m,n,k}^0 F_{m,n,k}, \quad \lambda_{m,n,k}^0 = \left(\frac{b_k^{n\mathfrak{N}}}{R}\right)^2 + \left|\frac{2\pi}{\tau}(m - \alpha n\mathfrak{N})\right|^2.\quad (2.40)$$

The above condition implies that the kinetic energy part of the single particle Schrödinger operator is diagonalized in this basis.

Consistent with the literature, we will refer to the representation of a function in terms of its expansion coefficients (i.e.,  $\hat{\phi}_{m,n,k}$  in the above) as its *reciprocal space representation*. Furthermore, we will refer to the representation of the function in terms of its values on a discrete set of grid points as its *real space representation*. If the basis functions are also available on these same grid points, the real and reciprocal space representations of the function can be connected via eq. 2.37.

For common systems of interest, the number of basis functions required for discretizing the governing equations can number in the tens or hundreds of thousands (See Section 3). Thus, it can become infeasible to explicitly store the discretized Hamiltonian. This scenario is also encountered in the classical plane-wave method for bulk systems [45, 46], and can be addressed by working with the discretized Hamiltonian implicitly, and using iterative, matrix-free diagonalization techniques to compute the eigenstates [61, 133]. For adopting such strategies, we need to be able to compute action of the Hamiltonian on an arbitrary vector, such as the wavefunction, as represented in our basis set. To this end, we consider a vector  $\phi \in \text{Span}\{F_{m,n,k} : (m,n,k) \in \Gamma\}$ , substitute eq. 2.37 into eq. 2.15, and use eq. 2.40, to arrive at:

$$\begin{aligned} \left(-\frac{1}{2}\Delta + V\right)\phi &= \frac{1}{2} \sum_{\Gamma} \hat{\phi}_{m,n,k} \lambda_{m,n,k}^0 F_{m,n,k} - a(\alpha, \tau, \eta, \nu) \phi - b(\alpha, \tau, \eta, \nu) \phi_{\theta_1} \\ &\quad - c(\alpha, \tau, \eta, \nu) \phi_{\theta_2} + \frac{\nu^2}{2r^2} \phi + \frac{i\nu}{2\pi r^2} \phi_{\theta_2} + V\phi = \lambda\phi, \end{aligned} \quad (2.41)$$

which further simplifies to:

$$\begin{aligned} &\frac{1}{2} \sum_{\Gamma} \hat{\phi}_{m,n,k} \lambda_{m,n,k}^0 F_{m,n,k} - a(\alpha, \tau, \eta, \nu) \sum_{\Gamma} \hat{\phi}_{m,n,k} f_{m,n,k} \\ &- b(\alpha, \tau, \eta, \nu) \sum_{\Gamma} \hat{\phi}_{m,n,k} (i2\pi m) F_{m,n,k} - c(\alpha, \tau, \eta, \nu) \sum_{\Gamma} \hat{\phi}_{m,n,k} (i2\pi n \mathfrak{N}) F_{m,n,k} \\ &+ \frac{\nu^2}{2} \sum_{\Gamma} \hat{\phi}_{m,n,k} \frac{F_{m,n,k}}{r^2} + \frac{i\nu}{2\pi} \sum_{\Gamma} \hat{\phi}_{m,n,k} \left(\frac{i2\pi n \mathfrak{N}}{r^2}\right) F_{m,n,k} + V(r, \theta_1, \theta_2) \sum_{\Gamma} \hat{\phi}_{m,n,k} F_{m,n,k} \\ &= \lambda \sum_{\Gamma} \hat{\phi}_{m,n,k} F_{m,n,k}. \end{aligned} \quad (2.42)$$

The constants  $a, b, c$  in the above are as follows:

$$\begin{aligned} a(\alpha, \tau, \eta, \nu) &= \frac{2\pi^2}{\tau^2} \left\{ \nu\alpha(2\eta - \nu\alpha) - \eta^2 \right\}, \\ b(\alpha, \tau, \eta, \nu) &= \frac{2i\pi}{\tau^2} (\nu\alpha - \eta), \quad c(\alpha, \tau, \eta, \nu) = \frac{2i\pi\alpha}{\tau^2} (\eta - \nu\alpha). \end{aligned} \quad (2.43)$$

The action of the Hamiltonian on the vector  $\phi$  is simply the left hand side of eq. 2.42 above. We observe that due to orthonormality of the basis set, the first four terms on the left hand

side are easily handled in reciprocal space. Specifically, the second term is simply a scaling of the input vector  $\phi$  with the factor  $a(\alpha, \tau, \eta, \nu)$ , while the other three terms can be evaluated as element-wise product operations (Matlab operation  $.*$ ). Thus, these terms can all be evaluated at a cost that scales linearly with the basis set size. The last term on the left hand side is associated with action of the effective potential  $V(\mathbf{x})$  on the wavefunction vector. If the expansion coefficients of the potential are available as:

$$V(\theta_1, \theta_2, r) = \sum_{(\tilde{m}, \tilde{n}, \tilde{k}) \in \Gamma} \hat{V}_{\tilde{m}, \tilde{n}, \tilde{k}} F_{\tilde{m}, \tilde{n}, \tilde{k}}(\theta_1, \theta_2, r), \quad (2.44)$$

then the expansion coefficients of  $V(\mathbf{x})\phi(\mathbf{x})$  can be computed as:

$$\begin{aligned} & \left\langle V(\theta_1, \theta_2, r) \phi(\theta_1, \theta_2, r), F_{m', n', k'}(\theta_1, \theta_2, r) \right\rangle_{\mathcal{L}^2(\mathcal{D})} \\ &= \left\langle \left( \sum_{\Gamma} \hat{V}_{\tilde{m}, \tilde{n}, \tilde{k}} F_{\tilde{m}, \tilde{n}, \tilde{k}}(\theta_1, \theta_2, r) \right) \left( \sum_{\Gamma} \hat{\phi}_{m, n, k} F_{m, n, k}(\theta_1, \theta_2, r) \right), F_{m', n', k'}(\theta_1, \theta_2, r) \right\rangle_{\mathcal{L}^2(\mathcal{D})} \\ &= \left\langle \left( \sum_{\Gamma} \sum_{\Gamma} \hat{V}_{\tilde{m}, \tilde{n}, \tilde{k}} \hat{\phi}_{m, n, k} F_{\tilde{m}, \tilde{n}, \tilde{k}}(\theta_1, \theta_2, r) F_{m, n, k}(\theta_1, \theta_2, r) \right), F_{m', n', k'}(\theta_1, \theta_2, r) \right\rangle_{\mathcal{L}^2(\mathcal{D})} \\ &= \sum_{\Gamma} \sum_{\Gamma} \hat{V}_{\tilde{m}, \tilde{n}, \tilde{k}} \hat{\phi}_{m, n, k} \langle F_{\tilde{m}, \tilde{n}, \tilde{k}} F_{m, n, k}, F_{m', n', k'} \rangle_{\mathcal{L}^2(\mathcal{D})}. \end{aligned} \quad (2.45)$$

There are two problems with the above evaluation strategy. First, the time complexity of the procedure scales in a cubic manner with respect to the basis set size, i.e.,  $O(M_{\max}^3 N_{\max}^3 K_{\max}^3)$ . Moreover, if the coupling coefficients:

$$\begin{aligned} & \langle F_{\tilde{m}, \tilde{n}, \tilde{k}} F_{m, n, k}, F_{m', n', k'} \rangle_{\mathcal{L}^2(\mathcal{D})} = c_{\tilde{m}, \tilde{n}, \tilde{k}} c_{m, n, k} c_{m', n', k'}^* \int_0^1 e^{i2\pi(m+\tilde{m}-m')\theta_1} d\theta_1 \\ & \times \int_0^{\frac{1}{\mathfrak{N}}} e^{i2\pi\mathfrak{N}(n+\tilde{n}-n')\theta_2} d\theta_2 \int_0^R J_{n\mathfrak{N}}\left(\frac{b_k^n \mathfrak{N} r}{R}\right) J_{n'\mathfrak{N}}\left(\frac{b_{k'}^{n'} \mathfrak{N} r}{R}\right) J_{\tilde{n}\mathfrak{N}}\left(\frac{b_{\tilde{k}}^{\tilde{n}} \mathfrak{N} r}{R}\right) 2\pi\tau r dr, \end{aligned} \quad (2.46)$$

are to be calculated and stored ahead of time for easier evaluation of eq. 2.45, the memory complexity of the procedure would also scale cubically with the basis set size. By making use of the fact that the coupling coefficients are non-zero only for  $m + \tilde{m} = m'$  and  $n + \tilde{n} = n'$ , their evaluation, storage and application to eq. 2.45, can be somewhat simplified. Despite this, the overall complexity still continues to be cubic in the basis set size in both memory

and time. Second, the potential  $V(\mathbf{x})$  is generally not expected to be equal to zero at  $r = R$  and may be slowly decaying due to long range electrostatics effects. Hence, it is inappropriate to express this quantity in terms of helical waves obeying Dirichlet boundary conditions.

Both of the above issues can be remedied by adopting a pseudospectral evaluation strategy [62, 134, 135, 136, 137], as we now describe. This is related to the observation that if  $V(\mathbf{x})$  and  $\phi(\mathbf{x})$  are available in real space, as functions sampled at a common set of grid points, the product  $\chi(\mathbf{x}) = V(\mathbf{x})\phi(\mathbf{x})$  can be evaluated with a cost proportional to the size of the grid. Thereafter, the function  $\chi(\mathbf{x})$  can be directly expanded in terms of helical waves to yield:

$$\widehat{\chi}_{m',n',k'} = \left\langle V(\theta_1, \theta_2, r) \phi(\theta_1, \theta_2, r), f_{m',n',k'}(\theta_1, \theta_2, r) \right\rangle_{\mathcal{L}^2(\mathcal{D})}. \quad (2.47)$$

Since  $\chi(\mathbf{x})$  obeys Dirichlet boundary conditions and inherits all symmetries of the group  $\mathcal{G}$ , its expansion using helical waves is appropriate. To put this strategy into practice however, we need access to fast basis transforms so that functions expressed in reciprocal space (i.e., as expansion coefficients) and real space (i.e., on the grid), may be readily interconverted. We describe the formulation and implementation of such transform routines in Sections 2.2.4.1 and 2.2.4.2. The overall computational cost of this strategy is the sum total of the costs of the forward and inverse transforms, and the cost of carrying out the real space product. Theoretically, the transforms described here scale in a manner that is slightly worse than the basis set size. However, as we show later, in practice they scale more favorably, in a sub-linear manner (see Fig. 2.4). Furthermore, the real space grid size is usually a constant multiple of the basis set size, leading to the overall cost of the pseudospectral method scaling in a manner that is close to the first power of this quantity ( $= \mathcal{O}(M_{\max}N_{\max}K_{\max}^2)$ ). The memory complexity is also reduced and scales as the basis set size itself, i.e.,  $\mathcal{O}(M_{\max}N_{\max}K_{\max})$ .

Finally, we discuss the evaluation of the fifth and the sixth terms on the left hand side of eq. 2.42. The fifth term, i.e.,

$$\ell(\theta_1, \theta_2, r) = \frac{\nu^2}{2} \sum_{\Gamma} \hat{\phi}_{m,n,k} \frac{F_{m,n,k}}{r^2}, \quad (2.48)$$

satisfies  $\ell(\theta_1, \theta_2, r = R) = 0$  and invariance under  $\mathcal{G}$ , since it is a finite linear combination of terms which individually obey these conditions. Thus, the expansion coefficients are:

$$\begin{aligned}
\widehat{\ell}_{m',n',k'} &= \left\langle \ell(\theta_1, \theta_2, r), F_{m',n',k'}(\theta_1, \theta_2, r) \right\rangle_{L^2(\mathcal{D})} \\
&= \frac{\nu^2}{2} \sum_{\Gamma} \widehat{\phi}_{m,n,k} \int_0^1 \int_0^{\frac{1}{\mathfrak{N}}} \int_0^R \frac{F_{m,n,k} F_{m',n',k'}^*}{r^2} 2\pi\tau r \, dr \, d\theta_2 \, d\theta_1 \\
&= \nu^2 \pi \tau \sum_{\Gamma} \widehat{\phi}_{m,n,k} c_{m,n,k} c_{m',n',k'}^* \left[ \int_0^1 e^{i2\pi(m-m')\theta_1} d\theta_1 \times \right. \\
&\quad \left. \int_0^{\frac{1}{\mathfrak{N}}} e^{i2\pi\mathfrak{N}(n-n')\theta_2} d\theta_2 \int_0^R \frac{J_{n\mathfrak{N}}\left(\frac{b_k^{\mathfrak{N}} r}{R}\right) J_{n'\mathfrak{N}}\left(\frac{b_{k'}^{\mathfrak{N}} r}{R}\right)}{r^2} r \, dr \right] \\
&= \frac{\nu^2}{R^2} \sum_{k=1}^{K_{\max}} \widehat{\phi}_{m',n',k} \frac{1}{J_{n'\mathfrak{N}+1}\left(\frac{b_k^{\mathfrak{N}}}{R}\right) J_{n'\mathfrak{N}+1}\left(\frac{b_{k'}^{\mathfrak{N}}}{R}\right)} \int_0^R \frac{J_{n'\mathfrak{N}}\left(\frac{b_k^{\mathfrak{N}} r}{R}\right) J_{n'\mathfrak{N}}\left(\frac{b_{k'}^{\mathfrak{N}} r}{R}\right)}{r^2} r \, dr. \quad (2.49)
\end{aligned}$$

In the above, we have made use of the orthonormality of the complex exponentials in the  $\theta_1$  and  $\theta_2$  directions. We may rewrite eq. 2.49 as:

$$\widehat{\ell}_{m',n',k'} = \frac{\nu^2}{R^2} \sum_{k=1}^{K_{\max}} \widehat{\phi}_{m',n',k} \mathcal{I}(n', k, k'), \quad (2.50)$$

with:

$$\mathcal{I}(n', k, k') = \frac{1}{J_{n'\mathfrak{N}+1}\left(\frac{b_k^{\mathfrak{N}}}{R}\right) J_{n'\mathfrak{N}+1}\left(\frac{b_{k'}^{\mathfrak{N}}}{R}\right)} \int_0^1 \frac{J_{n'\mathfrak{N}}\left(\frac{b_k^{\mathfrak{N}} q}{R}\right) J_{n'\mathfrak{N}}\left(\frac{b_{k'}^{\mathfrak{N}} q}{R}\right)}{q^2} q \, dq. \quad (2.51)$$

Thus, if the quantities  $\mathcal{I}(n', k, k')$  are known ahead of time, the coefficients  $\ell_{m',n',k'}$  can be readily evaluated at a cost of  $\mathcal{O}(M_{\max} N_{\max} K_{\max}^2)$ , i.e., quite close to the overall basis set size, and similar in computational complexity to the evaluation of the potential term. Since  $\mathcal{I}(n', k, k')$  is problem independent (e.g., it has no dependence on  $R$ ,  $\alpha$ ,  $\tau$  or the potential  $V(\mathbf{x})$ ), we may evaluate and store it as a table for a large range of values of  $n, k$  and  $k'$ . During program execution, this table of values may be loaded into memory, and each  $\ell_{m',n',k'}$  can be evaluated as a vector dot product (eq. 2.50), after accessing the necessary values of  $\mathcal{I}(n', k, k')$ . As for the evaluation of the  $\mathcal{I}(n', k, k')$  values themselves, we may use the

recurrence relation [130]:

$$\frac{2\kappa}{q} J_\kappa(q) = J_{\kappa-1}(q) + J_{\kappa+1}(q), \quad (2.52)$$

to rid the integrand in eq. 2.51 of it's denominator, and obtain a pair of oscillatory integrals. We may then compute these by using Gauss-Jacobi quadrature as outlined in [138].

In an analogous manner, the sixth term on the left hand side of eq. 2.42, i.e.,

$$\frac{i\nu}{2\pi} \sum_{\Gamma} \hat{\phi}_{m,n,k} (i2\pi n' \mathfrak{N}) \int_0^1 \int_0^{\frac{1}{\mathfrak{N}}} \int_0^R \frac{F_{m,n,k} F_{m',n',k}^*}{r^2} 2\pi \tau r dr d\theta_2 d\theta_1, \quad (2.53)$$

can be simplified to:

$$= \frac{i\nu}{\pi R^2} \sum_{k=1}^{K_{\max}} \left( \hat{\phi}_{m',n',k} * i2\pi n' \mathfrak{N} \right) \mathcal{I}(n', k, k'). \quad (2.54)$$

With the quantities  $\mathcal{I}(n', k, k')$  available, the above can be evaluated in a manner similar to the evaluation of the fifth term, at a computational cost of  $\mathcal{O}(M_{\max} N_{\max} K_{\max}^2)$ . The key difference is that instead of the vector  $\{\hat{\phi}_{m,n,k}\}_{(m,n,k) \in \Gamma}$ , we need to consider an alternate one with entries  $\{i2\pi n' \mathfrak{N} \hat{\phi}_{m,n,k}\}_{(m,n,k) \in \Gamma}$ . However, this modified vector is already available as part of evaluation of the fourth term on the left hand side of eq. 2.42, and therefore, it can be reused.

## 2.2 Numerical Implementation

We have implemented the above computational strategies into a MATLAB [63] package called HelicES (**H**elical **E**lectronic **S**tructure). To ensure efficiency, our code heavily relies on vectorization features of MATLAB. Various details of our implementation are as follows.

### 2.2.1 Wave function storage: reciprocal and real space considerations

For any quantity in reciprocal space, there are three indices  $m, n, k$  associated with each expansion coefficient, making the collection of coefficients a three-dimensional object of dimensions  $(2M_{\max} + 1) \times (2N_{\max} + 1) \times K_{\max} = \mathcal{L}$ . However, it is easier for linear algebra

operations to have these coefficients stacked up as vector in  $\mathbb{C}^{\mathcal{L}}$ . To achieve this, we adopt the following mapping between  $(m, n, k) \in \Gamma$  and the linear index  $\mathbf{i} \in \{1, 2, \dots, \mathcal{L}\}$ :

$$\mathbf{i}(m, n, k) = (m + M_{\max}) * (2N_{\max} + 1) * K_{\max} + (n + N_{\max}) * K_{\max} + k. \quad (2.55)$$

With this, a collection of  $N_s$  wavefunctions can be stored as a complex matrix of dimensions  $\mathcal{L} \times N_s$ .

For real space representation, the number of grid points to be chosen along each helical coordinate  $\theta_1, \theta_2$  is dictated by the accuracy of the basis transforms (see Section 2.2.4). We choose to work with Fourier nodes along the  $\theta_1$  and  $\theta_2$  directions and denote the corresponding number of grid points as  $N_{\theta_1}$  and  $N_{\theta_2}$  respectively. Along the radial direction, we choose  $N_r$  Gauss-Jacobi nodes [139] over the interval  $[0, R]$ . This has the advantage that the coordinate singularity at the origin is automatically avoided. In order to accommodate non-linearities and to reduce aliasing errors [62, 140], we typically choose  $N_{\theta_1} = 4 * M_{\max} + 1$ ,  $N_{\theta_2} = 4 * N_{\max} + 1$  and  $N_r = 4 * K_{\max}$ . These choices generally allow transforms to be evaluated accurately up to machine precision. With this setup, quantities such as the wavefunction are available in real space over a three-dimensional grid (i.e., the tensor product grid resulting from the one-dimensional grids along the individual coordinate directions), and each grid point is indexed via  $\mathbf{i} \in \{1, 2, \dots, N_{\theta_1}\}$ ,  $\mathbf{j} \in \{1, 2, \dots, N_{\theta_2}\}$  and  $\mathbf{k} \in \{1, 2, \dots, N_r\}$ . For storage, we stack this three dimensional representation into a complex column vector of size  $N_{\theta_1} * N_{\theta_2} * N_r$ , for which we use the following ordering:

$$\mathbf{j}(\mathbf{i}, \mathbf{j}, \mathbf{k}) = (\mathbf{i} - 1) * N_r * N_{\theta_2} + (\mathbf{j} - 1) * N_r + \mathbf{k}. \quad (2.56)$$

Since the memory requirement for storage of each wavefunction in real space is much higher than storing it in reciprocal space, we typically avoid storing real space versions of all  $N_s$  wave functions simultaneously.



### 2.2.2 Imposition of kinetic energy cutoff

In conventional plane-wave calculations, it is common to specify a *kinetic energy cutoff*, i.e., a limit on the  $H^1$  Sobolev norm of the plane-waves to be used for discretization [46, 141]. Once a suitable periodic unit cell has been identified, this criterion automatically provides a recipe for calculating the number of planewaves along each of the Cartesian axes, and in turn, the dimensions of the underlying real space grid to be used for Fast Fourier Transforms (FFTs). In a similar vein, we may wish to retain only helical waves with kinetic energies below a pre-specified cutoff in our calculation, since this has the advantage that the basis set limits  $M_{\max}$ ,  $N_{\max}$ , and  $K_{\max}$  get specified automatically in proportion to the computational domain's geometry parameters. At the gamma point ( $\eta = 0, \nu = 0$ ) for example, the kinetic energy cutoff criterion requires that all helical waves  $f_{m,n,k}$ , with  $m, n, k$  values satisfying:

$$\frac{1}{2}\lambda_{m,n,k}^0 = \frac{1}{2} \left[ \left( \frac{b_k^{n\mathfrak{N}}}{R} \right)^2 + \left| \frac{2\pi}{\tau} (m - \alpha n \mathfrak{N}) \right|^2 \right] \leq E_{\text{cut}}, \quad (2.57)$$

be included in our calculations. In our implementation, we first determine the largest absolute values of integers  $m, n$  and the largest natural number  $k$  consistent with eq. 2.57. We set the basis set limits  $M_{\max}$ ,  $N_{\max}$ , and  $K_{\max}$  accordingly. The real space grids used for carrying out fast transforms (described below) are chosen based on these quantities. Within these  $(2M_{\max} + 1) * (2N_{\max} + 1) * K_{\max}$  helical waves, however, not every combination of  $m, n, k$  would satisfy the kinetic energy criterion. To remedy this, we create a *masking vector* to exclusively retain helical waves which satisfy eq. 2.57, in various operations of interest (such as the Hamiltonian times wavefunction products). Based on the linear ordering for reciprocal space storage outlined in eq. 2.55, we may express the masking vector as:

$$\begin{aligned} \mathcal{M}_{i(m,n,k)} &= 1, \text{ for } \frac{1}{2}\lambda_{m,n,k}^0 \leq E_{\text{cut}} \\ &= 0, \text{ otherwise.} \end{aligned} \quad (2.58)$$

Element-wise multiplication of a given vector with the masking vector results in only kinetic energy limited helical waves being retained in the calculation. We implement the above

strategy at each  $\eta, \nu$  point (with the expression for the kinetic energy modified appropriately) to impose the kinetic energy cutoff in HelicES.

### 2.2.3 $\eta$ -space discretization and parallelization

As described earlier, to obtain the helical Bloch states (eq. 2.8), i.e., solutions to the single electron problem with a symmetry adapted potential (eq. 2.6), the single electron Hamiltonian has to be diagonalized for every  $\eta \in [-\frac{1}{2}, \frac{1}{2})$  and  $\nu \in \{0, 1, 2, \dots, \mathfrak{N} - 1\}$ . To make this calculation feasible, we sample  $\eta$  over a discrete set  $\{\eta_b\}_{b=1}^{N_\eta} \subset [-\frac{1}{2}, \frac{1}{2})$ . The specific choice of the values  $\eta_b$  is based on the Monkhorst-Pack scheme [142]. This procedure akin to “k-point sampling” in conventional periodic codes [45]. With this choice, the Hamiltonian needs to be diagonalized at  $N_{\mathcal{K}} = N_\eta \times \mathfrak{N}$  points, and integrals in  $\eta$  can be calculated via quadrature:

$$\int_{-\frac{1}{2}}^{\frac{1}{2}} p(\eta) d\eta \approx \sum_{b=1}^{N_\eta} w_b p(\eta_b). \quad (2.59)$$

Here,  $\{w_b\}_{b=1}^{N_\eta}$  are the Monkhorst-Pack quadrature weights and are uniformly equal to  $1/N_\eta$ . Integrals of the above kind appear, for example, while computing the electronic band energy, or the electron density from helical Bloch states [4, 5].

If the single electron Hamiltonian does not include magnetic fields — as is the case here, time reversal symmetry allows further reduction in the number of  $\eta, \nu$  points at which the Hamiltonian has to be diagonalized [57, 143]. Specifically, it holds that for any  $\eta \in [-\frac{1}{2}, \frac{1}{2})$  the helical Bloch states and the associated electronic bands obey:

$$\left. \begin{aligned} \psi_j(\mathbf{x}; \eta, \nu) &= \overline{\psi_j(\mathbf{x}; -\eta, \mathfrak{N} - \nu)} \\ \lambda_j(\eta, \nu) &= \lambda_j(-\eta, \mathfrak{N} - \nu) \end{aligned} \right\} \text{for } \nu \in \{0, 1, 2, \dots, \mathfrak{N} - 1\}, \quad (2.60)$$

and:

$$\left. \begin{aligned} \psi_j(\mathbf{x}; \eta, 0) &= \overline{\psi_j(\mathbf{x}; -\eta, 0)} \\ \lambda_j(\eta, 0) &= \lambda_j(-\eta, 0) \end{aligned} \right\} \text{for } \nu = 0. \quad (2.61)$$

Overall, this reduces the number of discrete points in reciprocal space by a factor of 2.

Since the diagonalization problem arising from distinct sets of  $\eta, \nu$  values are independent of one another, they can be dealt with in an embarrassingly parallel manner. In our implementation, we have used MATLAB’s Parallel Computing Toolbox (specifically, the `parfor` function) to carry out this parallelization.

#### 2.2.4 Fast basis transforms

Since our strategy for carrying out Hamiltonian matrix-vector products involves fast basis transforms, we now elaborate on various aspects of the implementation of such operations within the HelicES code. To arrive at fast transforms, we exploit the separability of the basis functions into radial and  $\theta_1, \theta_2$  dependence. This allows us to make use of quadrature along the radial direction, and subsequently, efficient two-dimensional fast Fourier transforms (FFTs) along the  $\theta_1, \theta_2$  directions for each radial grid point, or for each radial basis function. Since the radial part of the basis functions consists of Bessel functions, we have also investigated the use of Hankel and discrete Bessel transforms [144, 145, 146]. However, we found that the quadrature approach adopted here resulted in better performance for the basis set sizes considered, consistent with some earlier studies [147].

In what follows,  $O_{M \times N}$  is used to denote a zero matrix of size  $M \times N$ . The typical real space grid point for sampling a function will be denoted as  $(\theta_1^i, \theta_2^j, r^k)$ , with  $i \in \{1, 2, \dots, N_{\theta_1}\}$ ,  $j \in \{1, 2, \dots, N_{\theta_2}\}$  and  $k \in \{1, 2, \dots, N_r\}$ . We will use the MATLAB commands `ifft2` and `fft2` to denote two-dimensional fast inverse and forward Fourier Transforms respectively [63]. Additionally, we will use the MATLAB commands `ifftshift` and `fftshift` to denote rearrangements of Fourier transform coefficients related to shifting of zero frequency components to matrix center [63]. Finally, we will use the MATLAB ‘:’ (colon) operator notation to denote array/matrix indices with regular increments. Thus,  $i : k : j$  will denote indices starting at  $i$ , incremented by  $k$  and ending at  $j$ ,  $i : j$  will denote the indices  $i, i + 1, i + 2, \dots, j - 1, j$ , and simply ‘:’ will denote all indices along a particular matrix dimension.

### 2.2.4.1 Fast Inverse Basis Transform

Given the expansion coefficients  $\{\hat{g}_{m,n,k}\}_{(m,n,k)\in\Gamma}$ , a naive way of implementing the inverse basis transform would be to calculate each basis function  $\{F_{m,n,k}\}_{(m,n,k)\in\Gamma}$  at every grid point  $(\theta_1^i, \theta_2^j, r^k)$ , and to then evaluate the sum:

$$g(\theta_1^i, \theta_2^j, r^k) = \sum_{\Gamma} \hat{g}_{m,n,k} F_{m,n,k}(\theta_1^i, \theta_2^j, r^k). \quad (2.62)$$

The computational complexity of this ‘‘naive inverse transform’’ can be easily seen to be  $\mathcal{O}(M_{\max} N_{\theta_1} N_{\max} N_{\theta_2} K_{\max} N_r)$ , which simplifies to  $\mathcal{O}(M_{\max}^2 N_{\max}^2 K_{\max}^2)$ . The constant involved in the latter estimate can be seen to be quite large based on the discussion in Section 2.2.1. To remedy this situation, we express the basis functions as in 2.1.3, i.e.,  $F_{m,n,k}(\theta_1, \theta_2, r) = e^{i2\pi(m\theta_1+n\mathfrak{N}\theta_2)} \xi_{n,k}(r)$  and also rewrite the eq. 2.62 as:

$$\begin{aligned} g(\theta_1^i, \theta_2^j, r^k) &= \sum_{m=-M_{\max}}^{M_{\max}} \sum_{n=-N_{\max}}^{N_{\max}} \sum_{k=1}^{K_{\max}} \hat{g}_{m,n,k} e^{i2\pi(m\theta_1^i+n\mathfrak{N}\theta_2^j)} \xi_{n,k}(r^k) \\ &= \sum_{m=-M_{\max}}^{M_{\max}} \sum_{n=-N_{\max}}^{N_{\max}} e^{i2\pi(m\theta_1^i+n\mathfrak{N}\theta_2^j)} \left( \sum_{k=1}^{K_{\max}} \hat{g}_{m,n,k} \xi_{n,k}(r^k) \right). \end{aligned} \quad (2.63)$$

Since the quantity in parentheses is independent of the basis function index  $k$ , we may rewrite the above as:

$$\begin{aligned} g(\theta_1^i, \theta_2^j, r^k) &= \sum_{m=-M_{\max}}^{M_{\max}} \sum_{n=-N_{\max}}^{N_{\max}} e^{i2\pi(m\theta_1^i+n\mathfrak{N}\theta_2^j)} G_{m,n}(r^k) \\ \text{with : } G_{m,n}(r^k) &= \sum_{k=1}^{K_{\max}} \hat{g}_{m,n,k} \xi_{n,k}(r^k). \end{aligned} \quad (2.64)$$

Thus, if the quantities  $G_{m,n}(r^k)$  are known, calculation of the inverse basis transform amounts to computing an inverse two-dimensional fast Fourier transform at each radial grid point  $r^k$ . Additionally, we observe that at each radial grid point  $r^k$ ,  $G_{m,n}(r^k)$  can be expressed as a vector dot product between two  $K_{\max}$  dimensional vectors, i.e.,  $\{\hat{g}_{m,n,k}\}_{k=1}^{K_{\max}}$  and  $\{\xi_{n,k}(r^k)\}_{k=1}^{K_{\max}}$ . In fact, by grouping the evaluation of  $G_{m,n}(r^k)$  for different grid points together, the above operation may be expressed as the product of a  $N_r \times K_{\max}$  matrix with a  $K_{\max}$  dimensional vector, which allows for the use of Level-2 BLAS [148] operations. If the radial part

of the basis functions (i.e.,  $\xi_{n,k}(r^k)$ ) are available ahead of time, the above steps provide a convenient recipe of computing the inverse basis transforms with computational complexity  $\mathcal{O}(M_{\max}N_{\max}K_{\max}(K_{\max} + \log(M_{\max}) + \log(N_{\max})))$ , a significant improvement over the naive algorithm discussed earlier. We outline the overall steps of our implementation in Algorithms 1 and 2 below, and also illustrate some key aspects through Fig. 2.5.

In Fig. 2.4 we compare the naive and fast inverse transforms as implemented in HelicES. The starting vectors  $\{\hat{g}_{m,n,k}\}_{(m,n,k)\in\Gamma}$  were randomly chosen for the tests. The results from these two methods always agreed with each other to machine precision, guaranteeing consistency of the implementations. However, consistent with the discussion above, the computational time for the naive transforms is found to scale in a quadratic manner with the basis set size, while for the fast transforms, it is close to being linear. The fact that the observed scaling of our fast transform implementation is actually *sublinear*, is almost certainly related to our use of machine optimized linear algebra and Fourier transform routines as available within MATLAB.

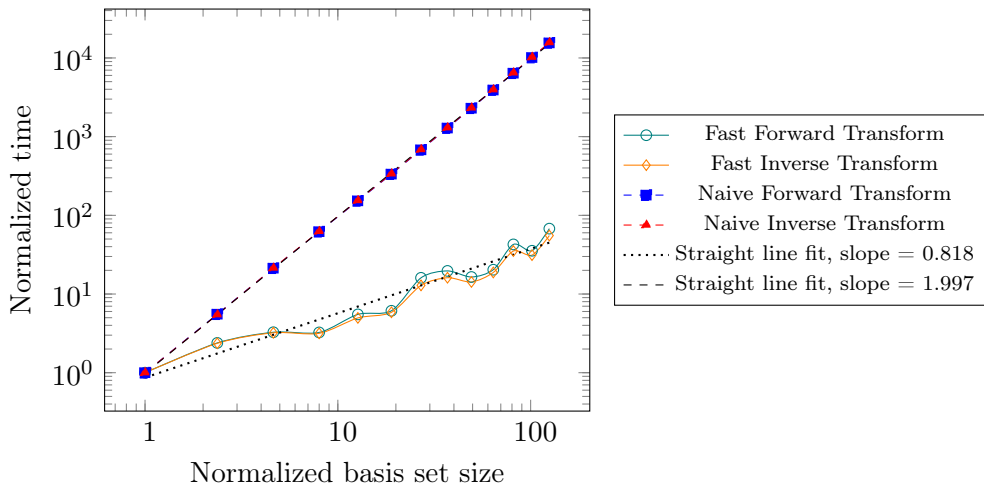


Figure 2.4: Variation of the normalized time for basis transforms plotted against the basis set size. Both axes are logarithmic. Straight lines were fit using the average of the forward and inverse transform times in each case.

---

**Algorithm 1: Fast Inverse Basis Transform**

---

**Input:** The vector of expansion coefficients  $\{\hat{g}_{m,n,k}\} \in \mathbb{C}^{\mathcal{L}}$

**Prerequisite:** The radial basis functions sampled on the grid  $\{r^k\}_{k=1}^{N_r}$ ,

i.e., for each integer  $n \in [-N_{\max}, N_{\max}]$ , the matrix:

$$\mathfrak{R}_n = \begin{pmatrix} \xi_{n,1}(r^1) & \cdots & \xi_{n,K_{\max}}(r^1) \\ \vdots & \ddots & \vdots \\ \xi_{n,1}(r^{N_r}) & \cdots & \xi_{n,K_{\max}}(r^{N_r}) \end{pmatrix}$$

---

Initialize  $g = O_{N_r N_{\theta_1} N_{\theta_2} \times 1}$ ,  $G = O_{(2M_{\max}+1)(2N_{\max}+1)N_r \times 1}$

Initialize  $i, j, p = 1$

**for**  $m, n \in \Gamma$  **do**

    Calculate  $G(i : i + N_r - 1) = \mathfrak{R}_n * \hat{g}_{m,n,k}(j : j + K_{\max} - 1)$

$i = i + N_r$

$j = j + K_{\max}$

**end**

**for**  $p \leq N_r$  **do**

    Set  $\hat{v} = G(p : N_r : \text{end})$

$g(p : N_r : \text{end}) = \text{AngularInverseTransform}(\hat{v})$

**end**

**Result:** The inverse basis transform  $g(\theta_1, \theta_2, r)$  of the vector  $\{\hat{g}_{m,n,k}\}$

---

---

**Algorithm 2: AngularInverseTransform**

---

(Fast Angular 2D Inverse Fourier Transform)

**Input:** Vector  $\hat{v} \in \mathbb{C}^{(2M_{\max}+1) \times (2N_{\max}+1)}$

Initialize  $\mathcal{W} = O_{N_{\theta_1} \times N_{\theta_2}}$  // **Note:**  $N_{\theta_1} = 4M_{\max} + 1$ ,  $N_{\theta_2} = 4N_{\max} + 1$

Reshape  $\hat{v}$  into a matrix  $\mathcal{V} \in \mathbb{C}^{(2N_{\max}+1) \times (2M_{\max}+1)}$

$\mathcal{W}(N_{\max} + 1 : 3N_{\max} + 1, M_{\max} + 1 : 3M_{\max} + 1) = \mathcal{V}$

$\mathcal{U} = \text{ifft2}(\text{ifftshift}(\mathcal{W}))$

Scale  $\mathcal{U} = \mathcal{U} * (N_{\theta_1} * N_{\theta_2})$

Reshape  $\mathcal{U}$  into a column vector  $v \in \mathbb{C}^{N_{\theta_1} * N_{\theta_2}}$

**Result:** The angular inverse Fourier transform  $v(\theta_1, \theta_2)$  of the vector  $\hat{v}$

---

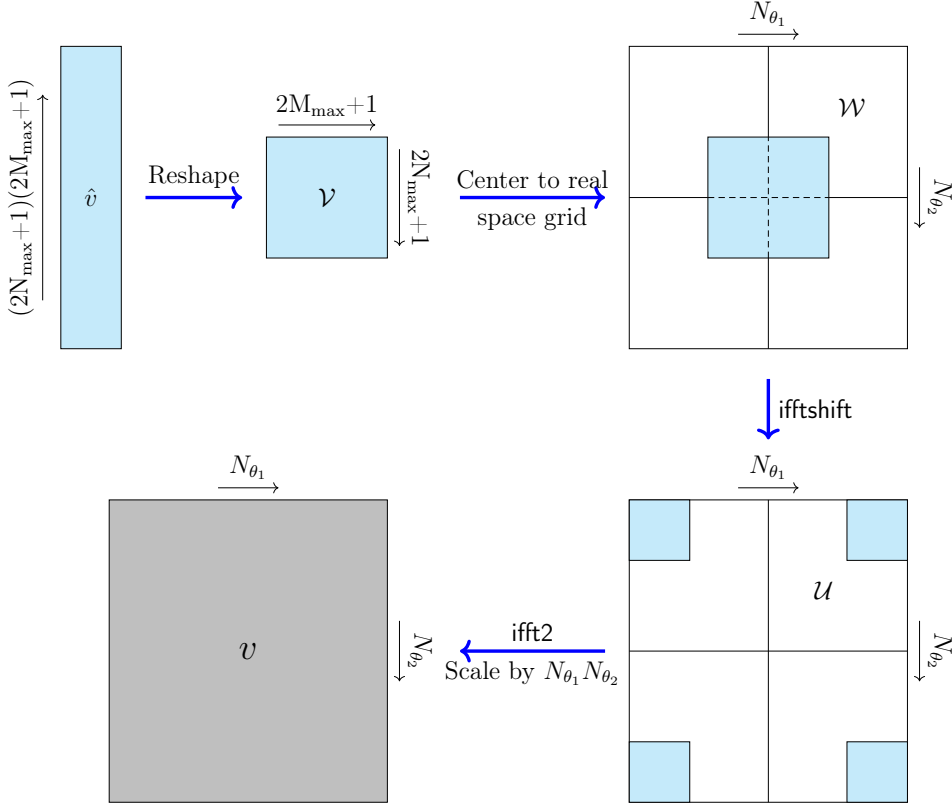


Figure 2.5: Pictorial representation of the workings of the fast angular 2D inverse Fourier transform (Algorithm 2)

#### 2.2.4.2 Fast Forward Basis Transform

We now discuss the implementation of forward basis transforms within HelicES. Given a function  $g(\theta_1, \theta_2, r)$ , the forward basis transform is defined as:

$$\hat{g}_{m,n,k} = \langle g, F_{m,n,k} \rangle_{\mathcal{L}^2(\mathcal{D})} = \int_0^1 \int_0^{\frac{1}{9\pi}} \int_0^R g(\theta_1, \theta_2, r) F_{m,n,k}^*(\theta_1, \theta_2, r) 2\pi\tau r dr d\theta_2 d\theta_1. \quad (2.65)$$

With  $F_{m,n,k}$  and  $g$  both sampled on the real space grid, this can be approximated via quadrature as:

$$\hat{g}_{m,n,k} \approx 2\pi\tau * \left( \sum_{i=1}^{N_{\theta_1}} \sum_{j=1}^{N_{\theta_2}} \sum_{k=1}^{N_r} g(\theta_1^i, \theta_2^j, r^k) e^{-i2\pi(m\theta_1^i + n\mathfrak{N}\theta_2^j)} \xi_{n,k}(r^k) \omega_r^k \omega_{\theta_1}^i \omega_{\theta_2}^j \right). \quad (2.66)$$

Here, the quadrature weights along the  $\theta_1, \theta_2$  directions are constants, i.e.,  $\omega_{\theta_1}^i = 1/N_{\theta_1}$  and  $\omega_{\theta_2}^j = 1/(\mathfrak{N}N_{\theta_2})$ , due to the use of Fourier nodes (i.e., trapezoidal rule). The radial weights  $\{\omega_r^k\}_{k=1}^{N_r}$  correspond to Gauss-Jacobi quadrature. We can see that like the case of the inverse transforms, a naive implementation of the above expression will lead to a computational complexity of  $\mathcal{O}(M_{\max}^2 N_{\max}^2 K_{\max}^2)$ . Instead, we deal with the evaluation of this expression along the  $\theta_1, \theta_2$  directions simultaneously at each radial grid point using 2D FFTs, and then perform quadrature in the radial direction. Thus, we compute:

$$H_{m,n}(r^k) = \frac{1}{N_{\theta_1} N_{\theta_2}} * \left( \sum_{i=1}^{N_{\theta_1}} \sum_{j=1}^{N_{\theta_2}} g(\theta_1^i, \theta_2^j, r^k) e^{-i2\pi(m\theta_1^i + n\mathfrak{N}\theta_2^j)} \right), \quad (2.67)$$

followed by:

$$\hat{g}_{m,n,k} = \frac{2\pi\tau}{\mathfrak{N}} * \left( \sum_{k=1}^{N_r} H_{m,n}(r^k) \xi_{n,k}(r^k) \omega_r^k \right). \quad (2.68)$$

The radial quadratures in the above expression can be conveniently cast in terms of Level-2 BLAS [148] operations if the radial basis functions scaled by the corresponding quadrature weights (i.e.  $\{\omega_r^k \xi_{n,k}(r^k)\}_{k=1}^{K_{\max}}$ ) are available as a matrix ahead of time. We outline the steps of our implementation in Algorithms 3 and 4 below, and illustrate key aspects in Figure 2.6.



---

**Algorithm 3:** Fast Forward Basis Transform

---

**Input:** Real space representation of function  $\{g(\theta_1^i, \theta_2^j, r^k)\} \in \mathbb{C}^{N_r N_{\theta_1} N_{\theta_2}}$

**Prerequisite:** The radial basis functions sampled on the grid  $\{r^k\}_{k=1}^{N_r}$ , scaled by the corresponding quadrature weights i.e., for each integer  $n \in [-N_{\max}, N_{\max}]$ , the following matrix:

$$\mathfrak{D}_n = \begin{pmatrix} \omega_r^1 \xi_{n,1}(r^1) & \cdots & \omega_r^{N_r} \xi_{n,1}(r^{N_r}) \\ \vdots & \ddots & \vdots \\ \omega_r^1 \xi_{n,K_{\max}}(r^1) & \cdots & \omega_r^{N_r} \xi_{n,K_{\max}}(r^{N_r}) \end{pmatrix}$$

---

Initialize  $\hat{g} = O_{\mathcal{L} \times 1}$ ,  $H = O_{N_r \times (2M_{\max}+1)(2N_{\max}+1)}$

Initialize  $i, j, p = 1$

**for**  $p \leq N_r$  **do**

    Set  $u = g(p : N_r : \text{end})$

$H(p, :) = \text{AngularForwardTransform}(u)$

**end**

**for**  $m, n \in \Gamma$  **do**

    Calculate  $\hat{g}(i : i + K_{\max} - 1) = \mathfrak{D}_n * H(:, j)$

$i = i + K_{\max}$

$j = j + 1$

**end**

Scale  $\hat{g} = (2\pi\tau/\mathfrak{N}) * \hat{g}$

**Result:** The forward basis transform  $\{\hat{g}_{m,n,k}\}$  of the function  $g(r, \theta_1, \theta_2)$

---

---

**Algorithm 4:** AngularForwardTransform

---

(Fast Angular 2D Forward Fourier Transform)

---

**Input:** Vector containing real space representation of 2D angular function on

    Fourier grid, i.e.,  $\{u(\theta_1^i, \theta_2^j)\} \in \mathbb{C}^{N_{\theta_1} N_{\theta_2}}$

Reshape  $u$  into a matrix  $\mathcal{W} \in \mathbb{C}^{N_{\theta_2} \times N_{\theta_1}}$

$\mathcal{V} = \text{fft2}(\mathcal{W})$

Scale  $\mathcal{V} = (\frac{1}{N_{\theta_1} N_{\theta_2}}) * \mathcal{V}$

$\mathcal{U} = \text{fftshift}(\mathcal{V})$

$\hat{u} = \mathcal{U}(N_{\max} + 1 : 3N_{\max} + 1, M_{\max} + 1 : 3M_{\max} + 1)$

**Result:** The 2D angular Fourier transform  $\{\hat{u}_{m,n}\}$  of the function  $u(\theta_1, \theta_2)$

---

Referring to Fig. 2.4, we see that like the case of the fast inverse basis transforms, our implementation of the fast forward basis transforms scale in a sublinear manner with respect

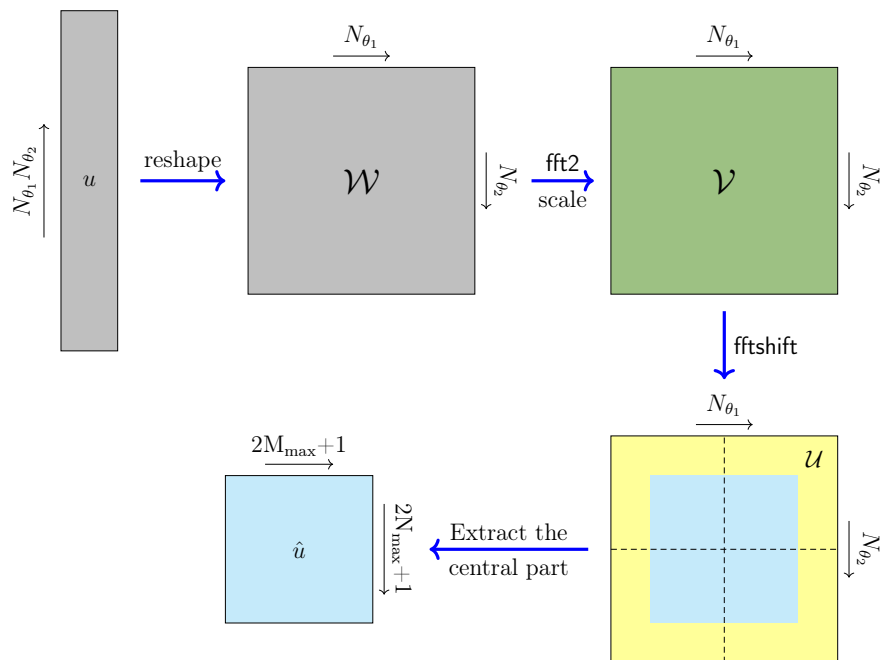


Figure 2.6: Pictorial representation of the workings of the fast angular 2D forward Fourier transform (Algorithm 4). ‘Scale’ indicates dividing the result of the 2D FFT by  $(N_{\theta_1} N_{\theta_2})$

to basis set size increase, although a somewhat worse performance is expected theoretically. In contrast, a naive implementation of the forward transform scales in a quadratic manner with respect to basis set size, although both implementations of the transforms always agree with each other to machine precision.

In practice, the differences between the efficiencies of the fast and the naive transform implementations (both forward and inverse transforms) are not only apparent in terms of their respective scalings with respect to basis set size, but also the actual computational wall times. Indeed, we found that the fast transform implementations can be orders of magnitude faster as compared to the naive ones, even for relatively small basis set sizes. In

Algorithm 5, we outline the steps of calculating the product of the Hamiltonian matrix with a wavefunction vector block by use of the fast transforms, as implemented in HelicES.

---

**Algorithm 5:** Product of Hamiltonian Matrix with a block vector of wavefunctions

---

**Input:** Block of  $N_s$  wavefunctions expressed in reciprocal space, i.e.,  $\hat{X} \in \mathbb{C}^{\mathcal{L} \times N_s}$ , real space representation of local potential  $V(\theta_1, \theta_2, r)$  as a vector  $\mathcal{V} \in \mathbb{C}^{N_{\theta_1} N_{\theta_2} N_r}$ , cyclic k-point  $\nu$  and helical k-point  $\eta$ .

Prerequisites: Indexing function  $\mathbf{i} : \Gamma \rightarrow \{1, 2, \dots, \mathcal{L}\}$  (eq. 2.55),

for each  $n \in [-N_{\max}, N_{\max}]$ , the matrix  $I_n \in \mathbb{R}^{K_{\max} \times K_{\max}}$  with entries

given by  $I_n(k, k') = \mathcal{I}(n, k, k')$  (eq. 2.51),

vector  $\Lambda \in \mathbb{R}^{\mathcal{L}}$  with entries corresponding to eq. 2.40, i.e.,  $\Lambda(\mathbf{i}(m, n, k)) = \lambda_{m,n,k}^0$ ,

vector  $\mathcal{M} \in \mathbb{C}^{\mathcal{L}}$  with entries  $\mathcal{M}(\mathbf{i}(m, n, k)) = i2\pi m$ ,

and vector  $\mathcal{N} \in \mathbb{C}^{\mathcal{L}}$  with entries  $\mathcal{N}(\mathbf{i}(m, n, k)) = i2\pi \eta n$ .

---

Initialize  $a = \frac{2\pi^2}{r^2} \left\{ \nu\alpha (2\eta - \nu\alpha) - \eta^2 \right\}$ ,  $b = \frac{2i\pi}{r^2} (\nu\alpha - \eta)$ ,  $c = \frac{2i\pi\alpha}{r^2} (\eta - \nu\alpha)$

Set  $\hat{Y} = O_{\mathcal{L} \times N_s}$  // Result to be stored in this

**for**  $j \leq N_s$  **do**

$\hat{Z} = \hat{X}(:, j)$  // Work on  $j^{\text{th}}$  wavefunction.

$\hat{P} = \mathcal{M} .* \hat{Z}$

$\hat{Q} = \mathcal{N} .* \hat{Z}$

$\hat{Y}(:, j) = \frac{1}{2} * (\Lambda .* \hat{Z})$

$\hat{Y}(:, j) = \hat{Y}(:, j) - a * \hat{Z} - b * \hat{P} - c * \hat{Q}$

**if**  $\nu \neq 0$  **then**

        Initialize  $i = 1$

**for**  $m, n \in \Gamma$  **do**

$T = \frac{\nu^2}{R^2} * \hat{Z}(i : i + K_{\max} - 1) + \frac{i\nu}{\pi R^2} * \hat{Q}(i : i + K_{\max} - 1)$

$\hat{Y}(i : i + K_{\max} - 1, j) = \hat{Y}(i : i + K_{\max} - 1, j) + I_n * T$

$i = i + K_{\max}$

**end**

**end**

$Z = \text{FastInverseBasisTransform}(\hat{Z})$  // Use Algorithm 1.

$\hat{Y}(:, j) = \hat{Y}(:, j) + \text{FastForwardBasisTransform}(Z .* \mathcal{V})$  // Use Algorithm 3.

**end**

**Result:**  $\hat{Y} \in \mathbb{C}^{\mathcal{L} \times N_s}$ , i.e., the product of the Hamiltonian with  $\hat{X}$  at the given values of  $\eta, \nu$ .

---

### 2.2.5 Eigensolvers and preconditioning

As mentioned earlier, we make use of matrix-free iterative eigenvalue solvers for diagonalization of the discretized Hamiltonian. Within HelicES, we have investigated two different diagonalization strategies for this purpose. The first is based on the Krylov-Schur method as implemented in the MATLAB Eigs function [149, 150, 151]. The second is based on a MATLAB implementation [152] of the Locally Optimal Block Preconditioned Conjugate Gradient (LOBPCG) scheme [2, 153, 154]. LOBPCG requires the use of a preconditioner, for which we have adopted the Teter-Payne-Allan (TPA) recipe [1, 150, 151]. This preconditioner was originally developed in the context of plane-wave calculations of bulk systems, but has also been successfully applied to other spectral methods [62]. During LOBPCG iterations, use of the TPA preconditioner requires the calculation and application of a diagonal matrix  $\mathcal{H} \in \mathbb{R}^{\mathcal{L} \times \mathcal{L}}$  to the residual vector. The entries of the matrix are:

$$\mathcal{H}_{i,j} = \frac{27 + 18 g_i + 12 g_i^2 + 8 g_i^3}{27 + 18 g_i + 12 g_i^2 + 8 g_i^3 + 16 g_i^4} \delta_{i,j}, \quad (2.69)$$

with:

$$g_i = \frac{\text{kinetic energy of basis function } i}{\text{kinetic energy of the residual vector}}. \quad (2.70)$$

As shown in Fig. 2.7, the preconditioner can have quite a dramatic effect on the convergence of the diagonalization procedure, especially as the basis set size (and therefore, the size of the discretized Hamiltonian) is increased. Thus, the benefits of the preconditioner are likely to become more apparent when larger systems and/or harder pseudopotentials are considered. Additionally, this becomes especially important for cases where a very fine discretization of the computational domain is required, such as for the calculation of the Hartree potential within this framework, which will be discussed in later sections (See Chapter 4).

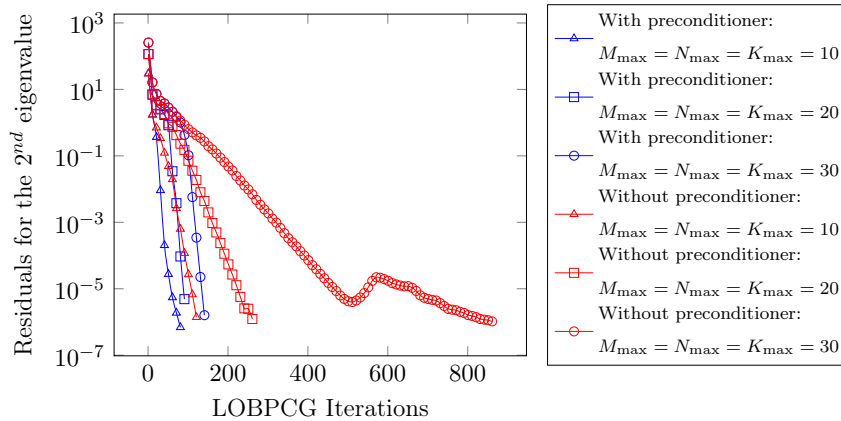


Figure 2.7: Effect of the Teter-Payne-Allan preconditioner [1] on LOBPCG [2] iterations for diagonalizing the discretized Hamiltonian in HelicES. An untwisted (6,6) armchair carbon nanotube (Mayer pseudopotentials [3]) has been used, and the residual associated with the 2<sup>nd</sup> eigenvalue for  $\eta = 0, \nu = 0$  as been monitored. For clarity, the residual for every 10<sup>th</sup> iteration has been plotted. Without preconditioning, the number of iterations required to reach a given convergence threshold tends to dramatically increase as the basis set grows larger.

We found that use of LOBPCG along with the TPA preconditioner generally tends to require longer diagonalization wall times as compared to `Eigs` along with an energy cutoff. Therefore, the latter strategy is adopted for most of the the examples considered in the next section. Implementation of more efficient eigensolvers in HelicES, particularly, ones that work well within self consistent field iterations [94, 155, 156], is the scope of future work.

## CHAPTER 3

# Application of HelicES to quasi-one-dimensional nanostructures

We now present results obtained using HelicES and investigate the convergence and accuracy properties of our implementation. All of our calculations have been carried out using smooth empirical pseudopotentials [3, 6]. We have used the planewave code PETRA [7], as well as two separate MATLAB based finite difference codes to generate reference data for comparison purposes. Specifically, we have employed the helical symmetry adapted finite difference code Helical DFT [4, 5] and the Cartesian grid finite difference code RSDFT [18]. The original versions of these finite difference codes were designed for self consistent field calculations, and were modified to work with the empirical pseudopotentials used in HelicES. We have also carried out comparisons of results obtained from HelicES against data obtained from the literature [3, 6]. We have used the WebPlotDigitizer tool [157] for extracting data from published plots.

### 3.1 Simulations and Results

#### 3.1.1 Computational platform

All simulations involving HelicES were carried out using dedicated desktop workstations (Dell Precision 7920 Tower, iMac, and iMac Pro) or on single nodes of the Hoffman2 cluster at UCLA's Institute for Digital Research and Education (IDRE). The Dell Precision workstation has an 18-core Intel Xeon Gold 5220 processor (24.75 L3 MB cache, 2.2 GHz clock

speed), 256 GB of RAM and 1 TB of SATA Class 20 Solid State Drive (SSD) storage. The iMac has an 8-core Apple M1 processor (12 MB L2 cache, 3.2 GHz clock speed), 16 GB of RAM and a 2 TB Solid State Drive (SSD). The iMac Pro has an 18-core Intel Xeon W processor (24.75 MB L3 cache, 2.3 GHz clock speed), 256 GB of RAM and a 2 TB SSD. Every compute node of the Hoffman2 cluster has two 18-core Intel Xeon Gold 6140 processors (24.75 MB L3 cache, clock speed of 2.3 GHz), 192 GB of RAM and local SSD storage. MATLAB version 9.7.0 (R2019b) was used for the simulations. Parallelization was achieved by use of using MATLAB’s Parallel Computing Toolbox. Reference results generated using Helical DFT [4], RSDFT [18] and PETRA [7] employed the above platforms as well.

### 3.1.2 Convergence studies

Using a twisted armchair carbon nanotube as an example system (Mayer pseudopotentials [3]), we first investigate the convergence properties of HelicES. Considering first the case of eigenvalues of the Hamiltonian at  $\eta = 0, \nu = 0$ , we see in Fig. 3.1 that as the number of basis functions in HelicES is increased, there is a rapid convergence to the reference values, regardless of which eigenvalue is considered. Consistent with earlier results for electronic structure calculations using spectral basis sets [62, 141], HelicES shows a curvature on a log-log scale, indicative of super-polynomial convergence. In contrast, the finite difference method, also shown on the same figure, shows slower, polynomial convergence. This is consistent with earlier findings for finite difference electronic structure calculations using curvilinear coordinates [5, 57]. Furthermore, when the energy cutoff criterion is engaged, HelicES appears to employ noticeably fewer degrees of freedom than the finite difference method (Helical DFT) in reaching the same levels of convergence.

The electronic features of quasi-one-dimensional systems can be characterized by one-dimensional band diagrams [4, 5], and these can be readily calculated for systems of interest using HelicES. As the next step in our studies, we checked the convergence behavior of the code with regard to a few quantities that are associated with the overall features of the one-

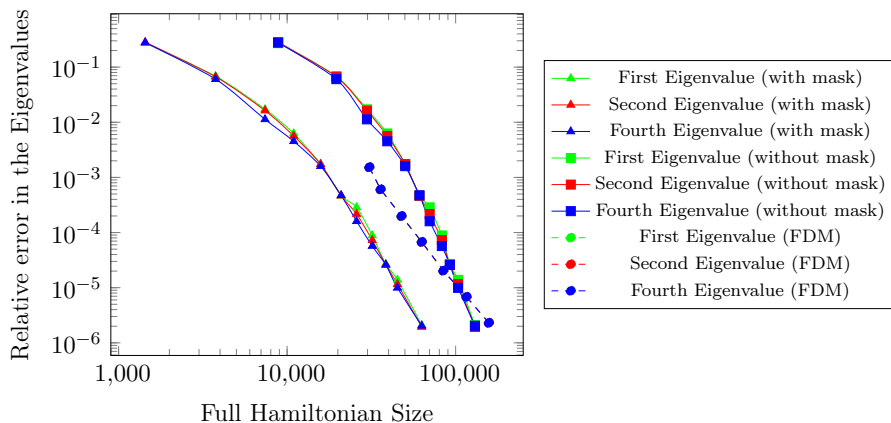


Figure 3.1: Convergence of the first three non-degenerate eigenvalues of an armchair (16, 16) carbon nanotube with a twist parameter of  $\alpha = 0.002$  using HelicES (both with and without the energy cutoff mask implemented) and a finite difference method (FDM), i.e., Helical DFT [4, 5]. The mesh size of the FDM decreases from 0.7 Bohrs to 0.4 Bohrs (in steps of 0.05 Bohrs) as the full Hamiltonian size varies from 30,744 to 157,440. The sparsity factor for the FDM Hamiltonian was 0.0055. The reference eigenvalues were taken to be the ones using an energy cutoff of 40 Ha for HelicES and a mesh spacing of 0.10 Bohr for Helical DFT. The  $\eta = 0, \nu = 0$  case (“gamma point”) is considered here. Note that the errors in the eigenvalues, for different eigenvalues, differ by  $\mathcal{O}(10^{-4})$  or less in the FDM case, which makes them indistinguishable in the plot above.

dimensional band diagram of the aforementioned armchair carbon nanotube system. These include the the electronic band energy — which for an insulating system is simply twice the sum of all occupied state eigenvalues, the valence band maximum eigenvalue, the conduction band minimum eigenvalue and the band gap. As shown in Fig. 3.2, we see that all these quantities, except for the band gap, show monotonic convergence to reference values. We also note that convergence of the band gap is nearly monotonic until the curve enters regions of very high accuracy ( $\mathcal{O}(10^{-6})$  in the figure) and this behavior is likely related to the fact that the band gap is calculated as the difference of two quantities.

Within HelicES, the electronic properties of quasi-one-dimensional systems are also ex-



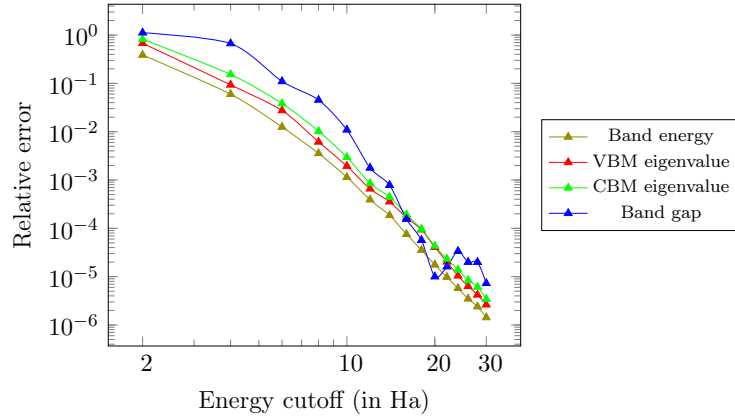


Figure 3.2: Convergence of the electronic band energy, the Valence Band Maximum (VBM) eigenvalue, the Conduction Band Minimum (CBM) eigenvalue, and the band gap, with respect to the energy cutoff, in the HelicES code. An armchair (16,16) carbon nanotube with a twist parameter of  $\alpha = 0.002$  has been investigated. The reference values were generated using an energy cutoff of 40 Ha.

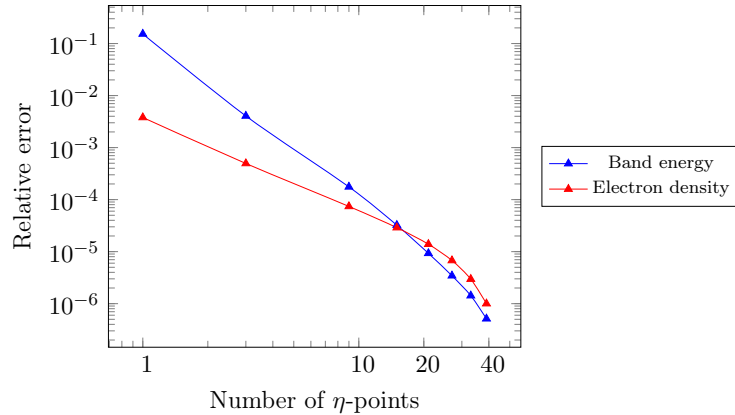


Figure 3.3: Convergence of the band energy and electron density of a (16,16) armchair carbon nanotube with a twist parameter of  $\alpha = 0.002$ . The reference value was taken to be from a calculation with 45  $\eta$ -points

pected to exhibit convergence with respect to the number of points used to discretize the  $\eta$ -space (Section 2.2.3). In Fig. 3.3, we explore the convergence behavior of the electron density (in terms of the  $L^1$  norm per electron) and the electronic band energy for the aforementioned

carbon nanotube system, as the number of  $\eta$  points in the calculation is increased. We see that both the above quantities show excellent convergence. We note that the electron density can be calculated from the wavefunctions  $\phi_j(\theta_1, \theta_2, r; \eta, \nu)$ , and the corresponding electronic occupation numbers  $\varsigma_j(\eta, \nu)$  as:

$$\rho(\theta_1, \theta_2, r) = \frac{2}{\mathfrak{N}} \sum_{j=1}^{N_s} \sum_{b=1}^{N_\eta} \sum_{\nu=0}^{\mathfrak{N}-1} w_b \varsigma_j(\eta_b, \nu) |\phi_j(\theta_1, \theta_2, r; \eta_b, \nu)|^2. \quad (3.1)$$

This requires inverse basis transforms to be carried out on each wavefunction vector, at the end of the diagonalization procedure. We also note from Figs. 3.2, 3.3 that for the Mayer pseudopotential employed in the above calculations, an energy cutoff of 16 Ha and 15  $\eta$ -points are more than sufficient to reach chemical accuracy.

### 3.1.3 Accuracy studies

While the discussion in Section 3.1.2 serves to illustrate the systematic convergence properties of HelicES, it does not address the accuracy or correctness of the converged results produced by the code. Therefore, we now carry out a series of systematic tests and compare the results produced by HelicES against solutions produced by other methods, for a variety of systems.

Our first set of tests compares the results produced by HelicES against those computed through the Finite Difference Method (FDM). For these studies, the Mayer pseudopotential [3] was once again employed and the energy cutoff in HelicES was set at 16 Ha. Reference results using the FDM codes were generated using a mesh spacing of 0.2 Bohr, this being the finest mesh that could be uniformly employed for all systems of interest, within computational resource constraints. We first used the RSDFT code [18] for calculating the electronic structure of a variety of finite (cluster-like) systems. The bound state eigenvalues for these same systems, as calculated by HelicES are compared against RSDFT results in Table 3.1. We see that for these discretization parameters, the agreement between the codes with respect to individual eigenvalues is about  $1.3 \times 10^{-4}$  Ha or better, while the band energies agree to within millihartree range, suggesting excellent accuracy.

Next, we generated the electronic band diagram associated with a deformed quasi-one-dimensional system, namely an armchair nanotube subjected to about  $\beta = 2.95^\circ$  of twist per nanometer. Reference calculations were carried out using the Helical DFT code. Both Helical DFT and HelicES were made to use 21  $\eta$ -points and the Eigs eigensolver in MATLAB. As shown in Figure 3.4, the band diagrams produced by the two codes are virtually identical, once again suggesting the excellent accuracy of HelicES. Overall, these findings illustrate that HelicES adequately addresses many of the the computational bottlenecks in existing methods for the study of electronic properties of quasi-one-dimensional systems, commensurate with its design goals.



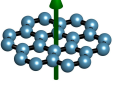
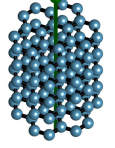
System (# atoms)	Hamiltonian size	Maximum difference in the eigenvalues (in Ha) between HelicES and FDM	Difference in band energy (in Ha/atom) between HelicES and FDM
Carbon dimer (2 atoms) 	HelicES without mask: 148625 HelicES with mask: 96353 FDM: 1030301	$6.0698 \times 10^{-5}$	$5.7475 \times 10^{-5}$
Carbon ring (6 atoms) 	HelicES without mask: 148625 HelicES with mask: 96353 FDM: 8120601	$3.8266 \times 10^{-5}$	$3.7686 \times 10^{-5}$
Carbon disk (24 atoms) 	HelicES without mask: 240096 HelicES with mask: 152556 FDM: 4173281	$7.7064 \times 10^{-5}$	$4.7145 \times 10^{-5}$
Carbon pillar (120 atoms) 	HelicES without mask: 129591 HelicES with mask: 85741 FDM: 8120601	$1.2604 \times 10^{-4}$	$3.7118 \times 10^{-5}$

Table 3.1: Accuracy of the HelicES code while studying finite systems (green arrow denotes the  $\mathbf{e}_z$  axis). Reference data was generated using RSDFT [18], a finite difference method (FDM) based MATLAB code. The last two columns show the maximum differences in the eigenvalues and the band energy per atom computed using the two methods.

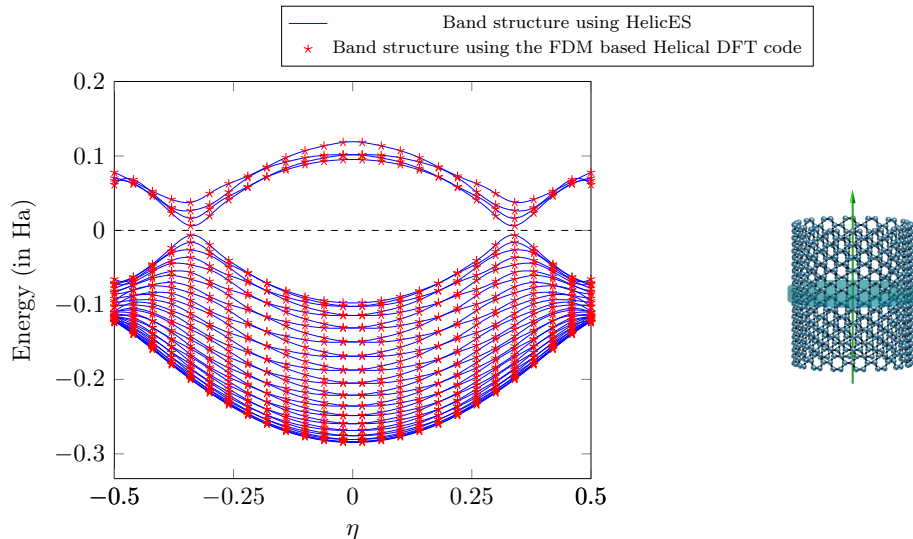


Figure 3.4: Comparison of band diagrams for a twisted (16, 16) armchair carbon nanotube (diameter = 2.726 nm) with twist parameter of  $\alpha = 0.002$ , generated using HelicES and the FDM based Helical DFT code [5, 4]. The green shaded region in the structure on the right is the fundamental domain used in HelicES, while the green arrow denotes the  $\mathbf{e}_z$  axis.

Due to inherent design limitations, the aforementioned FDM codes are unable to simulate quasi-one-dimensional nanostructures which have atoms situated near or along the system axis (e.g. nanoribbons, nanowires or small diameter nanotubes). However, these systems can be conveniently dealt with by HelicES. To carry out accuracy tests for such systems therefore, we compared the band structures calculated by HelicES against those generated through alternate electronic structure calculation techniques. The first of these is based on the transfer matrix method [158, 159, 160], often used in electromagnetics calculations. In Figs. 3.5 and 3.6 we see that the band structure calculated by HelicES is in nearly perfect agreement with results calculated using this technique in [3]. The systems considered here are carbon nanotubes with radii about 0.3 to 0.4 nanometers. For the (5, 5) armchair nanotube, the position of the Dirac cone is correctly predicted to be at  $\eta = \pm\frac{1}{3}$ . Additionally, the

(10,0) zigzag nanotube, the band gap calculated by HelicES is 1.05 eV which is very close to the value of 1.04 eV obtained in [3].

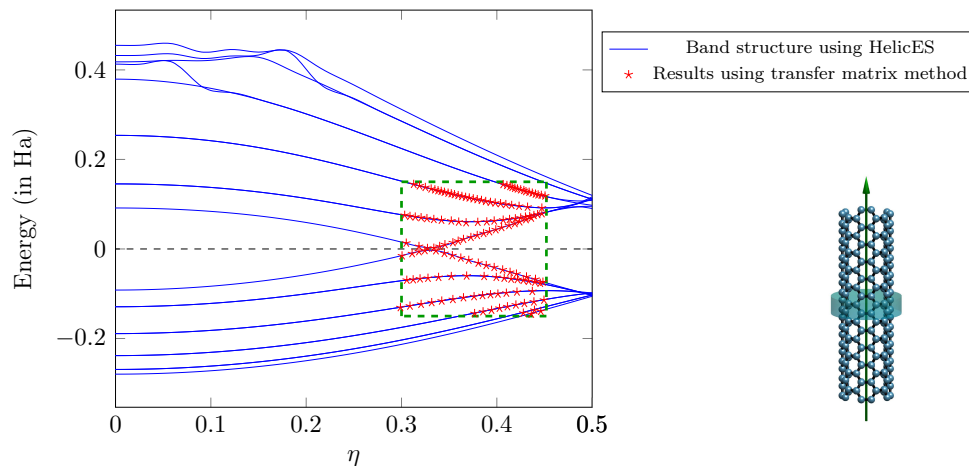


Figure 3.5: Comparison of band diagrams for a (5,5) armchair carbon nanotube (diameter = 0.851 nm) generated using HelicES and a transfer-matrix technique [3]. The dashed green box in the plot represents the region of the band diagram over which the reference data was available for comparison. The green shaded region in the structure on the right is the fundamental domain used in HelicES and the green arrow denotes the  $\mathbf{e}_z$  axis.

Next, we used the PETRA code for studying an armchair graphene nanoribbon, as well as a silicon nanowire oriented along the  $\langle 100 \rangle$  direction. Both these systems were treated using the empirical pseudopotentials developed in [6] and feature hydrogen passivation. Figs. 3.7 and 3.8 show that the overall agreement between HelicES and PETRA is excellent, although some minor variations at the edge of the highest energy band for the nanoribbon case may be observed. This is possibly due to the different boundary conditions being employed by PETRA and HelicES in the directions orthogonal to the ribbon axis. We also note that the band gap for the silicon nanowire calculated by HelicES is 3.82 eV, which is very close to the value of 3.84 eV reported in [6].

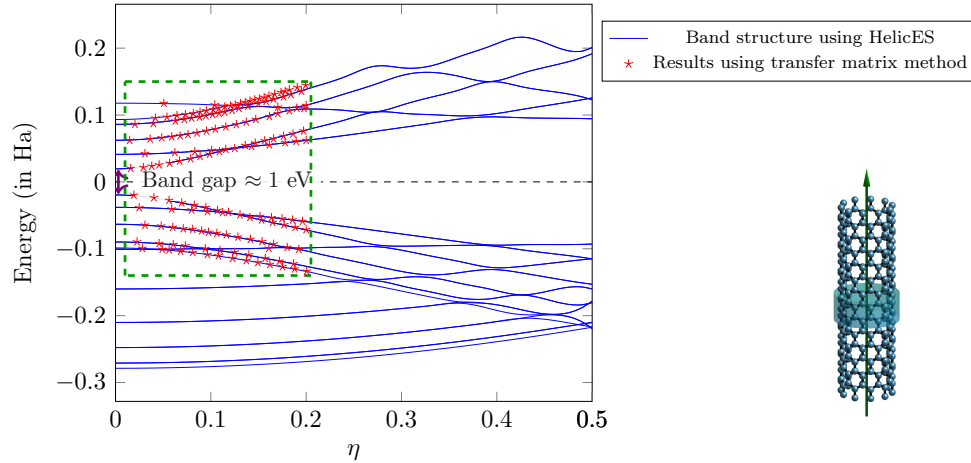


Figure 3.6: Comparison of band diagrams for a (10,0) zigzag carbon nanotube (diameter = 0.983 nm) generated using HelicES and a transfer-matrix technique [3]. The dashed green box in the plot represents the region of the band diagram over which the reference data was available for comparison. The green shaded region in the structure on the right is the fundamental domain used in HelicES and the green arrow denotes the  $\mathbf{e}_z$  axis.

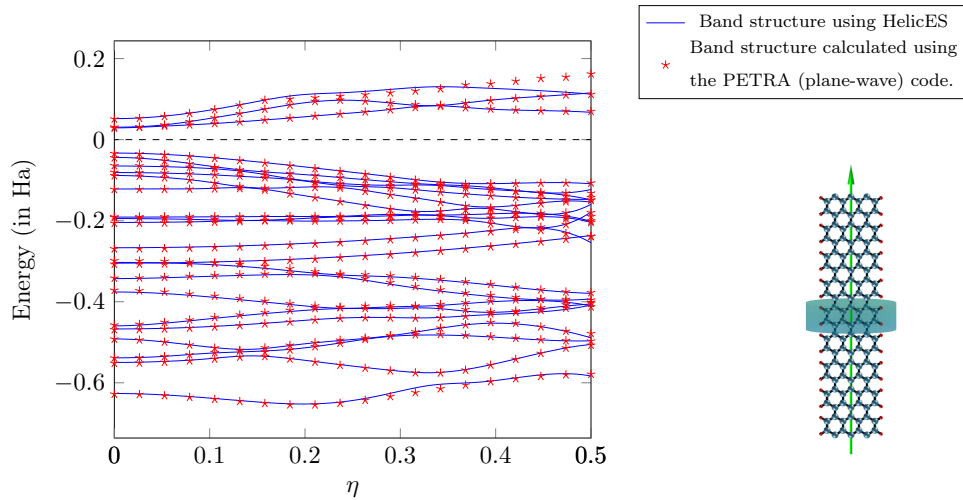


Figure 3.7: Comparison of band diagrams for a hydrogen passivated armchair graphene nanoribbon generated using HelicES and a plane-wave technique [6, 7]. The green shaded region in the structure on the right is the fundamental domain used in HelicES and the green arrow denotes the  $\mathbf{e}_z$  axis.

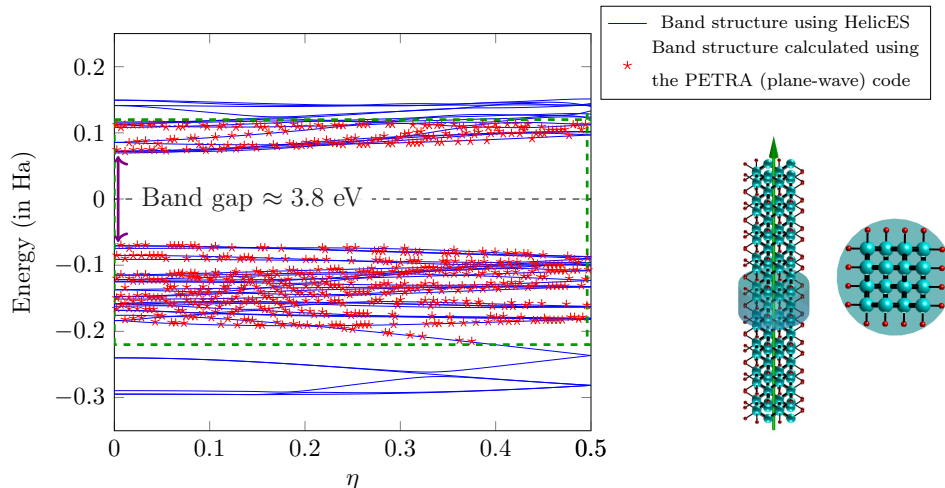


Figure 3.8: Comparison of band diagrams for a hydrogen passivated,  $\langle 100 \rangle$  oriented silicon nanowire generated using HelicES and a plane-wave technique [6, 7]. The dashed green box in the plot represents the region of the band diagram over which the reference data was available for comparison. The green shaded region in the structure in the middle is the fundamental domain used in HelicES, with the green arrow denoting the  $\mathbf{e}_z$  axis. The right image shows a top view of the structure (i.e., looking down along  $\mathbf{e}_z$ ).

### 3.1.4 Comments on computational efficiency and timing studies

We now discuss issues connected to the computational efficiency of HelicES. By design, the code is meant to overcome the computational limitations of prior approaches in modeling quasi-one-dimensional systems. We highlight this aspect of the code by providing timing comparisons between HelicES and other existing methods, for a few systems of interest. We have focused on the Plane-wave Electronic TRANsport (PETRA) code [6, 7, 161] which can model periodic systems, and Helical DFT [4, 5] which models quasi-one-dimensional structures within a finite difference framework. For comparisons with PETRA, we chose a twisted hydrogen-passivated graphene nanoribbon. Note that while realistic values of  $\alpha$  range from 0.0005 to 0.0025 (i.e., less than about  $2.1^\circ$  per nanometer), it is not feasible to use these values in PETRA. This is because to simulate such a system in a typical

plane-wave code like PETRA, we would require  $1/\alpha$  times the number of atoms needed for untwisted geometries (for rational values of  $\alpha$ ). However, the number of atoms required in the fundamental domain in HelicES is independent of the amount of twist. Thus, while a realistic twisted nanoribbon can be studied using only 20 atoms in HelicES, PETRA would require at least 10,000 atoms in the fundamental domain for the same system. Keeping this in mind, we use larger values of  $\alpha = 0.25, 0.2, 0.1$ , and  $0.05$ , so that the simulation and timing data from PETRA could be obtained within reasonable wall times. For both codes, we used the same diagonalization technique. The simulations were carried out on dedicated workstations, or on a single node of the Hoffman2 cluster when larger memory was needed. In our studies, we noted factors of 1.26, 1.84, 3.83, and 12.25 improvement in the total diagonalization wall time of HelicES over PETRA, for  $\alpha = 0.25, 0.2, 0.1$ , and  $0.05$  respectively. Based on the above discussion, we anticipate that the performance gap between HelicES and PETRA, as well as the memory requirements of the latter, will only increase when more realistic values of  $\alpha$  or more complicated unit cells are considered.

Due to the fundamental limitations of plane-wave codes to efficiently represent helical symmetries, it also makes sense to compare HelicES to Helical DFT, since the right symmetries are incorporated into both these codes, although the latter uses finite differences. For this purpose, we studied a twisted (16, 16) armchair carbon nanotube with a diameter of 2.726 nm and a twist parameter of  $\alpha = 0.002$ , and we used 21  $\eta$ -points. As we showed earlier (Section 3.1.3), while the two codes produce nearly identical results, the diagonalization wall time for HelicES was about a factor of 27 lower, and the memory footprint was also significantly less. These observations continue to be true when larger values of the energy cutoff are used in HelicES, with the diagonalization wall time of the code being about a factor of 8 lower than Helical DFT, even when an energy cutoff of 40 Ha is employed.

To finish this discussion on computational advantages of HelicES, we now present a system that cannot be simulated in Helical DFT, and one that will require extensive computational resources in typical periodic finite difference or plane-wave codes — an armchair graphene



nanoribbon with a twist of  $\alpha = 0.02$ . Note that this is still a relatively high value of  $\alpha$ , but was chosen here for a better visual representation of the system. The band diagram of this system is presented in Fig. 3.9. Noticeably, in contrast to the untwisted, passivated nanoribbon presented in Fig. 3.7, this system appears to have a vanishingly small band-gap, indicative of metallic behavior.

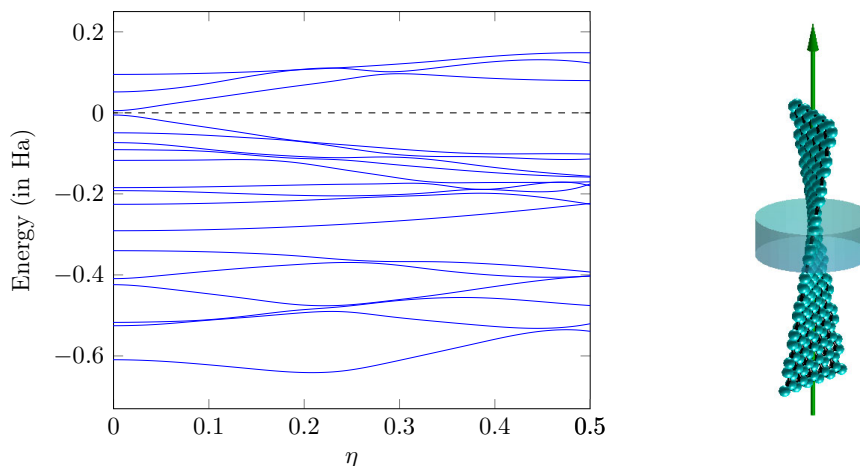


Figure 3.9: Band diagram for an armchair graphene nanoribbon with a twist parameter of  $\alpha = 0.02$  (corresponding to a rate of twist  $\beta = 16.9^\circ$  per nanometer) generated using HelicES. The green shaded region in the structure on the right is the fundamental domain used in HelicES. The green arrow denotes the  $\mathbf{e}_z$  axis.

### 3.1.5 Application to the study of the electromechanical response of nanotubes

Finally, as a demonstration of the utility of the computational method developed here, we study the the electromechanical response of a quasi-one-dimensional nanomaterial as it undergoes deformations. Specifically, we consider a carbon nanotube with a radius of about 1.0 nanometer (an armchair (16, 16) tube), and subject it to twisting. We start from the untwisted structure and increase the rate of applied twist, considering up to about  $\beta = 7.4^\circ$ , in our simulations. Fig. 3.10 shows the variation of the band gap of the material with applied twist. For comparison purposes, results from full self consistent Kohn-Sham

DFT calculations using ab initio Troullier Martins pseudopotentials [162] and Local Density Approximation based exchange correlation [163, 164], are also shown (obtained from [5]). It is well known that upon twisting, armchair nanotubes — which are generally metallic in untwisted form — show metal-to-semiconductor transitions, and that these changes manifest themselves as oscillatory behavior in the band gap [5, 165, 166, 167]. We see from Fig. 3.10 that the results from HelicES do reproduce this qualitative behavior correctly, but the actual response curve is quantitatively different from the first principles data. This is very likely due to the lack of inclusion of atomic relaxation effects in HelicES, as well as the general failure of the Mayer pseudopotential to model scenarios where the carbon atoms do not form a perfect honeycomb lattice — a consequence of the shearing distortions that arise from the applied twist in this case. Therefore, these results strongly suggest the need for building in ab initio pseudopotentials and self consistent iterations into HelicES, which constitutes ongoing work [168].

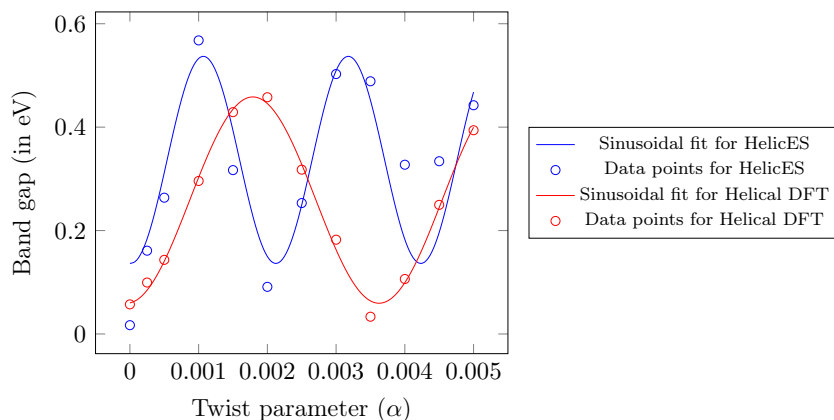


Figure 3.10: Band gap trend as the twist parameter  $\alpha$  is varied for a (16, 16) armchair carbon nanotube. Results from HelicES (empirical pseudopotentials) and the Helical DFT code (self consistent calculations with ab initio pseudopotentials and atomic relaxation effects included [4, 5]) are both shown.

## 3.2 Concluding remarks

In summary, we have presented a novel spectral method for efficiently solving the Schrödinger equation for quasi-one-dimensional materials and structures. The basis functions in our method — helical waves — are natural analogs of plane-waves, and allow systematically convergent electronic structure calculations of materials such as nanowires, nanoribbons and nanotubes to be carried out. We have discussed various mathematical, algorithmic and implementation oriented issues of our technique. We have also used our method to carry out a variety of demonstrative calculations and studied its accuracy, computational efficiency, and convergence behaviors.

We anticipate that the method presented here will find utility in the discovery and characterization of new forms of low dimensional matter. It is particularly well suited for coupling with specialized machine learning techniques [116] and for the multiscale modeling of low dimensional systems [169]. Building self-consistency into the method, so as to enable *ab initio* calculations (e.g. using Hartree-Fock or Kohn-Sham Density Functional Theory [170]) remains the scope of ongoing and future work. An important first step in this direction is the efficient solution of the associated electrostatics problem [10], which will be discussed in detail in Chapter 4. Finally, the full power of some of the techniques described here can be brought to bear upon complex materials problems, once a parallel, efficient, hardware optimized version of HelicES is available. Development of such a code constitutes yet another avenue of ongoing and future work.

## CHAPTER 4

# The solution of the Poisson problem for twisted geometries

The development of mathematical and computational frameworks for the study of matter at the nanoscale has always been an area that has received much attention. Methods such as Hartree-Fock (HF) [171], Density Functional Theory (DFT) [172], and post-HF methods [173, 174, 175] have been instrumental in forming the basis over which some of the other methods were built. One of the most well-established first principles computational methods for electronic structure calculations is the Kohn-Sham Density Functional Theory (KS-DFT) framework [163, 172] which has enabled the prediction and calculation of fundamental material properties with impressive accuracy [45, 176]. Increasingly vast amounts of resources are being allocated for such first principles calculations, and more recently, the predictive power of KS-DFT has been pushed forward further, by the integration of machine learning techniques [116, 100, 101, 177]. KS-DFT owes its success due to striking an appealing balance between generality and computational efficiency, especially when compared to other *ab initio* methods [170]. Because of the *ab initio* nature of this method, it has the ability to be adapted specifically for special systems of interest, thereby increasing its efficiency further.

One particularly interesting family of materials with fascinating electronic, optical and transport properties, that has received much attention recently, are quasi-one-dimensional (1D) materials with intrinsic or applied twist [28, 29]. Consequently, a significant amount of recent effort has been dedicated to study the electronic properties of chiral 1D systems [178, 179, 180, 181, 182] as well as anomalous transport properties associated with such

structures, such as the chiral-induced spin selectivity. Specifically, when studying chiral systems with helical symmetries, it behooves to work in the helical coordinate system to more naturally accommodate for such symmetries. To this effect, we have introduced a spectral framework [138] to target quasi-one-dimensional systems with intrinsic or applied twists, which was discussed in detail in Chapters 2 and 3.

An integral part of many of these calculations is the evaluation of a Newtonian potential arising from a distribution of sources in a twisted geometry. For example, this appears in the evaluation of the electrostatic potential in KS-DFT, as well as evaluation of the exact Hartree-Fock exchange energy. Evaluation of such terms through direct pairwise computations based on Coulomb sums attracts unmanageable computational costs because of the need to include a sufficient number of images for every source point — an issue also present in periodic electronic structure calculations. Moreover, the direct sum is conditionally convergent [183] and has a slow convergence rate [184].

To address this issue in the case of periodic systems, a very well known approach is the use of Ewald summation [185, 186] wherein the conditionally convergent series is split into two independent series — a long range term and a short range term — each of which has a much faster convergence than the original series. This method is exact in the limit of infinite images and, thus, ensures convergence irrespective of the Ewald parameter used to split the initial sum. The evaluation of the short range term is much faster and, as such, the Ewald parameter is chosen to be so small that the short range term can be considered to be a first-order approximation of the potential. However, with unconventional helical symmetries (associated with twisted geometries), the computational efficiency may still suffer because of the need to include more atoms in the fundamental domain. To address this issue, Dumitrica et al. proposed an extension of the classical Ewald summation method to helical geometries [10]. Regardless, the method does have a key limitation in that it scales quadratically with respect to the number of charges in the symmetry-adapted unit cell. This makes it unsuitable for charge distributions where the number of ‘discrete’ point charges can be in the millions —

namely charge distributions associated with computational meshes. Given these challenges, an alternative method is desirable, the most common of which is to obtain the electrostatic Hartree potential by solving the associated Poisson equation [5, 73].

A prominent method that may be used for the solution of the Poisson equation is Finite Differences (FD), wherein the computational real-space domain is discretized, and on which the FD stencil is built. While this method has been successful, it too has inherent issues. The Laplacian is often poorly conditioned and is non symmetric [59, 60]. Moreover, to deal with core singularities, annular geometries befitting tubes have had to be employed. This means that potentially interesting systems such as nanoribbons, nanowires, and nanoflakes can't necessarily be studied.

In this work, we confront the aforementioned issues and formulate a method that obeys the structural symmetries and overcomes core singularities, while also keeping in mind the possibly slow radial decay of the electrostatic potential by incorporating associated boundary conditions (BCs). Furthermore, this method is readily applicable to solutions over meshes and overcomes the difficulties associated with viewing charge distributions as a set of discrete charges at each grid point, as is done in Ewald sums. We alleviate axial singularity issues by using a shifted FD grid — in view of the fact that the singularity is not physical in nature and is only an artifact of the choice of the mesh — and using appropriate pole conditions [74, 75, 76]. Our method is motivated, in part, by recent developments in electronic structure calculations in twisted geometries using helical waves [138], i.e., plane-wave like spectral basis functions. These functions are, by design eigenfunctions of the Laplacian in twisted geometries. However, their direct applications to the current work is not suitable because of the long-ranged nature of the electrostatic potential. Helical waves, on the other hand, are expected to have zero magnitudes everywhere at and beyond the radial boundary by design. Thus, a spectral representation of the electrostatic potential using these helical waves would violate the BCs. Owing to this, we instead use a suitable ansatz that, as we will show, effectively reduces the formalism to the solution of a boundary value problem. While zero

Dirichlet BCs are commonly used [5, 187], these require significant padding and an extension of the fundamental domain which is not desirable. To overcome this issue, here, we evaluate appropriate boundary conditions using a helical Ewald kernel that may be set up only once per simulation. Observing that the Ewald sum is only dependent on the distance between the source and the target allows us to further optimize this calculation and drastically reduce the computational walltime required. We show systematic convergence in the calculation of the Hartree potential with respect to reference analytical solutions for different FD parameters, and also present results pertaining to twisting energies. The evaluation of the electrostatic potential with this method paves the way for incorporating self consistency within our prior work, which could then further optimize the study of interesting systems such as twisted multilayer graphene nanoflakes [188, 189, 190, 191, 192, 193] featuring exotic electronic flat bands.

## 4.1 Theoretical background

In this section, we set up the helical coordinate system and the helical symmetries associated with a quasi-one-dimensional structure. Further details can be found in Chapters 2 and 3. Building on this helical framework, we then focus on the Hartree potential term that features in the single particle Schrödinger equation, taking inspiration from the discussion from the previous section. This will lead us into the mathematical framework in subsequent sections.

As mentioned previously, it is convenient to work in a coordinate system that describes the symmetries of the system more naturally. Motivated by this, we make use of helical coordinates in this work. For a point  $\mathbf{p} \in \mathbb{R}^3$  with Cartesian coordinates  $(x_{\mathbf{p}}, y_{\mathbf{p}}, z_{\mathbf{p}})$ , cylindrical coordinates  $(r_{\mathbf{p}}, \vartheta_{\mathbf{p}}, z_{\mathbf{p}})$ , and helical coordinates  $(\theta_{1\mathbf{p}}, \theta_{2\mathbf{p}}, r_{\mathbf{p}})$ , the following relations hold:

$$\begin{aligned} r_{\mathbf{p}} &= \sqrt{x_{\mathbf{p}}^2 + y_{\mathbf{p}}^2}, \theta_{1\mathbf{p}} = \frac{z_{\mathbf{p}}}{\tau}, \\ \theta_{2\mathbf{p}} &= \frac{1}{2\pi} \arctan 2(y_{\mathbf{p}}, x_{\mathbf{p}}) - \alpha \frac{z_{\mathbf{p}}}{\tau} = \frac{\vartheta_{\mathbf{p}}}{2\pi} - \alpha \frac{z_{\mathbf{p}}}{\tau}. \end{aligned} \tag{4.1}$$

The fundamental domain is then described as:

$$\mathcal{D} = \left\{ (\theta_1, \theta_2, r) : 0 \leq \theta_1 \leq 1, 0 \leq \theta_2 \leq \frac{1}{\mathfrak{N}}, 0 \leq r \leq R \right\}. \quad (4.2)$$

where  $\mathfrak{N}$  denotes the cyclic symmetry of the system, and  $R$  denotes the radial boundary of the fundamental domain. In this setup, the basis functions are given by:

$$\begin{aligned} F_{m,n,k}(\theta_1, \theta_2, r) &= \sqrt{\frac{\mathfrak{N}}{\pi\tau}} \frac{1}{R J_{n\mathfrak{N}+1}\left(\frac{b_k^{n\mathfrak{N}}}{R}\right)} e^{i2\pi(m\theta_1+n\mathfrak{N}\theta_2)} J_{n\mathfrak{N}}\left(\frac{b_k^{n\mathfrak{N}}}{R}r\right) \\ &= c_{m,n,k} R_{n,k}(r) e^{i2\pi(m\theta_1+n\mathfrak{N}\theta_2)}. \end{aligned} \quad (4.3)$$

where  $(m, n, k)$  are triplets of integers such that  $m \in [-M_{\max}, M_{\max}]$ ,  $n \in [-N_{\max}, N_{\max}]$  and  $k \in [1, K_{\max}]$ . The full basis set size is then given by  $\mathcal{L} = (2M_{\max} + 1) * (2N_{\max} + 1) * K_{\max}$ , i.e., it grows as  $\mathcal{O}(M_{\max}N_{\max}K_{\max})$  in terms of the discretization sizes along the  $\theta_1, \theta_2, r$  directions. The number of real space grid points in each direction is denoted by  $N_{\theta_1}, N_{\theta_2}, N_r$  respectively.

The single particle Schrödinger equation, in its most general form, may be expressed as:

$$\left[ -\frac{1}{2}\Delta + v_H(\mathbf{x}) + v_{xc}(\mathbf{x}) + v_{ext}(\mathbf{x}) \right] \psi_i(\mathbf{x}) = H_{KS} \psi_i(\mathbf{x}) = \epsilon_i \psi_i(\mathbf{x}), \quad (4.4)$$

$$v_H(\mathbf{x}) = \int \frac{g(\mathbf{y})}{|\mathbf{x} - \mathbf{y}|} d\mathbf{y}, \quad v_{xc}(\mathbf{x}) = \frac{\delta E_{xc}}{\delta n(\mathbf{x})}, \quad n(\mathbf{x}) = \sum_{i=1}^N |\psi_i(\mathbf{x})|^2 \quad (4.5)$$

Here,  $\psi_i(\mathbf{x})$  are the Kohn-Sham orbitals, and  $g(\mathbf{x})$  is the charge density. A detailed methodology to simplify the above equation in the helical coordinate system using a spectral framework may be found in our previous work. The focus of this work, however, is the Hartree potential term,  $v_H(\mathbf{x})$ .

Assuming that quasi-one-dimensional nanostructures of interest are aligned along the  $\mathbf{e}_z$  direction, we may define a set of symmetry operations:

$$\mathcal{G} = \left\{ \Upsilon_{\zeta,\mu} = \left( \mathbf{R}_{(2\pi\zeta\alpha+\mu\Theta)} \mid \zeta\tau\mathbf{e}_z \right) : \zeta \in \mathbb{Z}, \mu = 0, 1, \dots, \mathfrak{N} - 1 \right\}, \quad (4.6)$$



such that:

$$\mathcal{S} = \bigcup_{\substack{\zeta \in \mathbb{Z} \\ \mu=0,1,\dots,\mathfrak{N}-1}} \bigcup_{i=1}^M \mathbf{R}_{(2\pi\zeta\alpha+\mu\Theta)\mathbf{r}_i} + \zeta\tau\mathbf{e}_z, \quad (4.7)$$

where  $M$  is the total number of atoms in the helical unit cell,  $\mathcal{D}$ . The  $\Upsilon_{\zeta,\mu}$  are symmetry operations of the structure. Under such symmetries, we may rewrite the Hartree potential as:

$$v_H(\mathbf{x}) = \sum_{\Upsilon \in \mathcal{G}} \int_{\mathbf{y} \in \mathcal{D}} \frac{g(\Upsilon \cdot \mathbf{y})}{|\mathbf{x} - \Upsilon \cdot \mathbf{y}|} d\mathbf{y} \quad (4.8)$$

$$g(\mathbf{x}) = \rho(\mathbf{x}) + b(\mathbf{x})$$

where the  $\zeta, \mu$  subscript has been dropped for simplicity. Here,  $\rho(\mathbf{x})$  is the electron charge density and  $b(\mathbf{x})$  is the nuclear charge density at each grid point  $\mathbf{x}$ . Note that in a charge neutral system,  $g(\mathbf{x})$  must integrate to zero over  $\mathcal{D}$ . The potential in Eq. 4.8 may now be evaluated directly using pairwise Coulomb sums, but this procedure is computationally inefficient due to the need for a large number of images ( $\Upsilon$ ), and fine discretization of  $\mathcal{D}$ . While symmetry-adapted helical Ewald sums do provide a better alternative, they too are prohibitively slow due to the presence of  $N_{\theta_1}N_{\theta_2}N_r$  discrete charges. This number can often run into the millions. Although exact in the limit of a sufficiently large number of images, the helical Ewald method scales quadratically with respect to the number of grid points, making this method unsuitable for charge distributions in this work. While we may use Eq. 4.8 in some cases — for instance, for calculating the boundary conditions — the direct evaluation of the Hartree potential over  $\mathcal{D}$  using Eq. 4.8 should be avoided.

An alternate method, as mentioned earlier, is to modify the problem by evaluating the Hartree potential as the solution of the following equivalent Poisson equation:

$$\Delta v_H(\mathbf{x}) = - \sum_{\Upsilon \in \mathcal{G}} \sum_{\mathbf{y} \in \mathcal{D}} 4\pi g(\Upsilon \cdot \mathbf{y}) \quad (4.9)$$

While the equation above can be solved using appropriate FD methods (details of which will be discussed later), we note here that the task at hand is a boundary value problem and that

we still need to evaluate an equation similar to Eq. 4.8 to get said boundary conditions. We have already mentioned why Dirichlet BCs will fail in this case, unless the radial boundary of the fundamental domain is expanded sufficiently such that the electrostatic Hartree potential decays to zero at the boundary. Thus, to make the method computationally efficient and avoid an unnecessary increase in the size of  $\mathcal{D}$ , we must resort to evaluating the BCs explicitly. Evidently, we may now use helical Ewald summations with the benefit that these only need to be calculated at the boundary points instead of the entire fundamental domain. Note that this significantly reduces the number of grid points over which to calculate helical Ewald sums. As will be shown in the following section, due to a suitable choice of an ansatz for the Hartree potential, this could reduce the computational complexity by a scale of  $100^2$ .

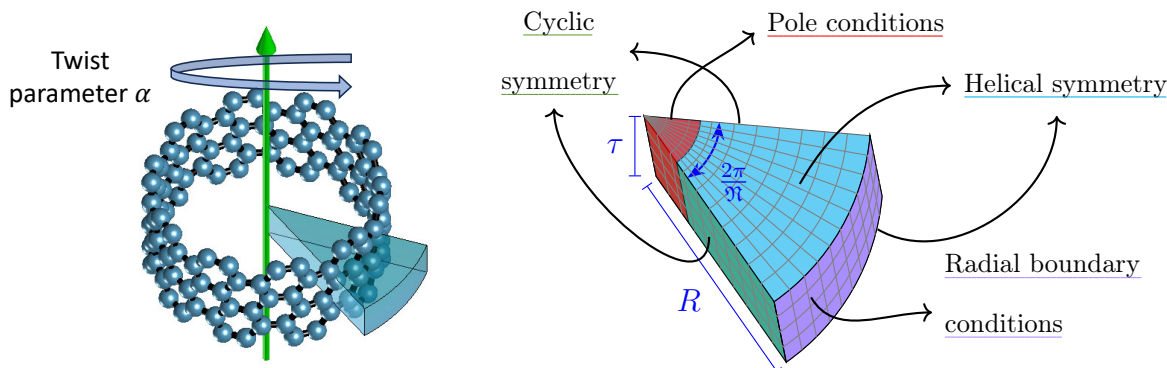


Figure 4.1: The figure on the left represents a few layers of a twisted (10,10) armchair carbon nanotube with the fundamental domain shown ( $\mathfrak{N} = 10$ ). The fundamental domain, over which the Hartree potential is to be computed, is represented in physical space using Cartesian coordinates on the right. The slanted walls of the fundamental domain  $\mathcal{D}$  in physical space arise due to possibly arbitrary values of twist associated with the system. For the points beyond  $r = R$ , we include boundary conditions into our framework via helical Ewald sums. The red shaded area represents the points where we apply pole conditions in our FD stencil to accommodate  $r < 0$ .

## 4.2 Formulation

In this section, we derive, in detail, the method used in this study for the evaluation of the Hartree potential as the solution of Eq. 4.9. We first simplify the Poisson equation to an effective one-dimensional radial Ordinary Differential Equation (ODE) and discuss the framework to solve it. This is followed by a discussion of the set up of the charge neutral distribution as a sum of the electronic and nuclear charge distributions, and finally, a discussion on the evaluation of the boundary conditions wherein we also mention computational complexity and scalability.

### 4.2.1 The radial Poisson ODE

We assume a separable ansatz for the Hartree potential as follows:

$$v_H(\theta_1, \theta_2, r) = \sum_{m,n} P_{m,n}(r) e^{i2\pi(m\theta_1 + n\mathfrak{N}\theta_2)} \quad (4.10)$$

Note again that the separable ansatz cannot be represented in terms of our helical basis functions because the latter are designed to drop to zero at the boundary ( $r = R$ ), which may not necessarily be true for the electrostatic potential. This key observation leads to the inability of our framework to be completely spectral in nature. The total charge density,  $g(\theta_1, \theta_2, r)$ , on the other hand, can be represented in our basis set as follows:

$$g(\theta_1, \theta_2, r) = \sum_{m,n,k} \hat{g}_{m,n,k} c_{m,n,k} R_{n,k}(r) e^{i2\pi(m\theta_1 + n\mathfrak{N}\theta_2)} \quad (4.11)$$

Note here that the total charge density must be computed with a sufficient number of helical images taken into consideration via the symmetry operator,  $\Upsilon$ . Additionally, we observe that  $(\theta_1, \theta_2, r)$  and  $(\theta_1, \theta_2 + \frac{1}{2}, -r)$  represent the same physical grid point, and so, from Eq.

4.10, we have:

$$\begin{aligned}
v_H(\theta_1, \theta_2 + \frac{1}{2}, -r) &= \sum_{m,n} P_{m,n}(-r) e^{i2\pi(m\theta_1 + n\mathfrak{N}\theta_2 + \frac{n\mathfrak{N}}{2})} \\
&= (-1)^{n\mathfrak{N}} \sum_{m,n} P_{m,n}(-r) e^{i2\pi(m\theta_1 + n\mathfrak{N}\theta_2)} \\
P_{m,n}(r) &= (-1)^{n\mathfrak{N}} P_{m,n}(-r)
\end{aligned} \tag{4.12}$$

This is what gives rise to the pole boundary conditions on the left-hand side of the FD stencil, i.e., for  $r < 0$ , as represented in Fig. 4.1. With the above expressions, and with the knowledge that the Laplacian in helical coordinates can be written as [4, 47]:

$$\Delta P = P_{rr} + \frac{1}{r}P_r + \frac{1}{\tau^2}P_{\theta_1\theta_1} - \frac{2\alpha}{\tau^2}P_{\theta_1\theta_2} + \frac{1}{4\pi^2} \left( \frac{1}{r^2} + \frac{4\pi^2\alpha^2}{\tau^2} \right) P_{\theta_2\theta_2} \tag{4.13}$$

where any angular derivatives, i.e. with respect to  $\theta_1$  and  $\theta_2$ , will equate to zero due to the purely radial dependence of  $P_{m,n}(r)$ , we can now rewrite Eq. 4.9 as:

$$\begin{aligned}
\Delta v_H &= e^{i2\pi(m\theta_1 + n\mathfrak{N}\theta_2)} \left[ P_{rr} + \frac{1}{r}P_r \right] - v_H \left[ \frac{n^2\mathfrak{N}^2}{r^2} + \frac{4\pi^2}{\tau^2} (m - \alpha n\mathfrak{N})^2 \right] \\
&= e^{i2\pi(m\theta_1 + n\mathfrak{N}\theta_2)} \left[ P_{rr} + \frac{1}{r}P_r \right] - e^{i2\pi(m\theta_1 + n\mathfrak{N}\theta_2)} P \left[ \frac{n^2\mathfrak{N}^2}{r^2} + \frac{4\pi^2}{\tau^2} (m - \alpha n\mathfrak{N})^2 \right]
\end{aligned} \tag{4.14}$$

for a particular ordered pair  $(m, n)$ . The subscript  $m, n$  from  $P_{m,n}(r)$  has been dropped for simplicity. Thus, we have:

$$\begin{aligned}
e^{i2\pi(m\theta_1 + n\mathfrak{N}\theta_2)} \left[ P_{rr} + \frac{1}{r}P_r \right] - e^{i2\pi(m\theta_1 + n\mathfrak{N}\theta_2)} P \left[ \frac{n^2\mathfrak{N}^2}{r^2} + \frac{4\pi^2}{\tau^2} (m - \alpha n\mathfrak{N})^2 \right] = \\
-4\pi \sum_{m,n,k} \hat{g}_{m,n,k} c_{m,n,k} R_{n,k}(r) e^{i2\pi(m\theta_1 + n\mathfrak{N}\theta_2)}
\end{aligned} \tag{4.15}$$

Taking the inner product of the above with  $e^{i2\pi(m'\theta_1 + n'\mathfrak{N}\theta_2)}$  yields:

$$\left[ P_{rr} + \frac{1}{r}P_r \right] - P \left[ \frac{n'^2\mathfrak{N}^2}{r^2} + \frac{4\pi^2}{\tau^2} (m' - \alpha n'\mathfrak{N})^2 \right] = -4\pi \sum_k \hat{g}_{m',n',k} c_{m',n',k} R_{n',k}(r) \tag{4.16}$$

which can be further simplified to:

$$P_{m',n',rr} + \frac{1}{r}P_{m',n',r} - \left[ \frac{4\pi^2}{\tau^2} (m' - \alpha n'\mathfrak{N})^2 + \frac{(n'\mathfrak{N})^2}{r^2} \right] P_{m',n'} = -4\pi G_{m',n'}(r) \tag{4.17}$$

Note that this equation needs to be solved for every combination of  $(m', n')$ . It is evident that Eq. 4.17 has a singularity at  $r = 0$ . However, as mentioned previously, this can be taken care of by shifting the radial grid such that the point of singularity does not feature as a grid point at all. Thus, we use FD grid such that the  $i^{\text{th}}$  radial node is at  $r_i = (i - \frac{1}{2}) \Delta r$ , where  $\Delta r$  is the FD mesh spacing. As a result, the first radial node occurs at  $\frac{\Delta r}{2}$ . For an ODE of order  $n_0$ , we have:

$$\begin{aligned}
\frac{\delta^2 f(r_i)}{\delta r^2} &= \sum_{p=0}^{n_0} \omega_{p,r}^{\text{second}} (f(r_{i+p}) + f(r_{i-p})) \\
\frac{\delta f(r_i)}{\delta r} &= \sum_{p=1}^{n_0} \omega_{p,r}^{\text{first}} (f(r_{i+p}) - f(r_{i-p})) \\
\omega_{p,r}^{\text{first}} &= \frac{(-1)^{p+1}}{\Delta r p} \frac{(n_0!)^2}{(n_0-p)!(n_0+p)!} = \frac{(-1)^{p+1}(2n_r-1)}{2Rp} \frac{(n_0!)^2}{(n_0-p)!(n_0+p)!} \\
\omega_{p,r}^{\text{second}} &= \frac{2(-1)^{p+1}}{(\Delta r p)^2} \frac{(n_0!)^2}{(n_0-p)!(n_0+p)!} = \frac{(-1)^{p+1}(2n_r-1)^2}{2R^2 p} \frac{(n_0!)^2}{(n_0-p)!(n_0+p)!} \\
\omega_{0,r}^{\text{second}} &= -\frac{1}{\Delta r^2} \sum_{q=1}^{n_0} \frac{1}{q^2} = \frac{(2n_r-1)^2}{4R^2} \sum_{q=1}^{n_0} \frac{1}{q^2}
\end{aligned} \tag{4.18}$$

Thus, from Eq. 4.17, we have:

$$\begin{aligned}
\sum_{p=0}^{n_0} \omega_{p,r}^{\text{second}} (P_{m',n'}(r_{i+p}) + P_{m',n'}(r_{i-p})) + \frac{1}{r_i} \sum_{p=1}^{n_0} \omega_{p,r}^{\text{first}} (P_{m',n'}(r_{i+p}) - P_{m',n'}(r_{i-p})) \\
-\frac{1}{r_i^2} P_{m',n'}(r_i) \left[ n'^2 \mathfrak{N}^2 + \frac{4\pi^2 r_i^2}{\tau^2} (m' - \alpha n' \mathfrak{N})^2 \right] = -4\pi \sum_k G_{m',n',k}(r_i)
\end{aligned} \tag{4.19}$$

At this point, it is worthwhile to note the following. The FD problem is solved on an equispaced grid ( $\frac{\Delta r}{2} \leq r_i < R$ ) consisting of  $n_r$  points. However, the computational radial grid in helical space is setup using  $N_r$  Gaussian nodes that are not equispaced. Thus, the evaluated Hartree potential from Eq. 4.19 needs to be transferred from the FD grid to the radial helical grid by interpolation. Similarly,  $G_{m',n'}(r)$  will also need to be transferred from the helical radial grid on which it is originally evaluated to the FD grid for Eq. 4.19. To avoid interpolation errors for the above, we limit  $n_r$  to within a range dictated by the number of helical radial nodes. Thus, for most cases (unless otherwise mentioned), we use the constraint

$0.5N_r \leq n_r \leq 2N_r$ . This means that increasing  $K_{\max}$  not only increases the number of radial nodes but also increases the number of FD grid points, and subsequently, the accuracy of the FD solver. Unless otherwise specified, we use  $n_r = 2N_r$ . Additionally, because of the radial nature of the ODE and the fact that it needs to be solved for every combination of  $(m', n')$  which span the Fourier space of  $\theta_1, \theta_2$  respectively, there exists the need to perform forward and inverse angular 2D Fourier transforms intermittently. An overview of this can be seen in Fig. 4.2. Details on the numerical implementation of these fast Fourier transforms can be found in our previous work [138].

#### 4.2.2 Charge distribution setup

Our method relies on not just an accurate solution of the ODE, but also on an accurate representation of the RHS in Eq. 4.17. While the electron density,  $\rho(\theta_1, \theta_2, r)$ , is a natural solution of a self-consistent field (SCF) calculation, one still needs an accurate expression for  $b(\theta_1, \theta_2, r)$ , i.e., the nuclear charge density, such that the system is charge neutral. In this work, without loss of generality, we setup the neutral 3-D charge distribution by placing a nuclear pseudocharge  $b(\theta_1, \theta_2, r)$  at each nuclear site, and by placing an equivalent electronic pseudocharge, i.e., *compensating* charge, of  $-b(\theta_1, \theta_2, r)$  at a grid point near the respective nuclear sites. Although this represents an unphysical charge distribution, it is sufficient to test and validate our method as long as charge neutrality is maintained. However, it is vital to avoid overlapping pseudocharge distributions as that can lead to inaccuracies [8]. An example of such a setup of the charge distribution for a carbon nanotube system can be seen in Fig. 4.3. The above strategy, however, limits the softness of the charge distribution, as will be explained in detail in the following paragraphs.

We implement and test our method on two spherically symmetric pseudocharge distri-

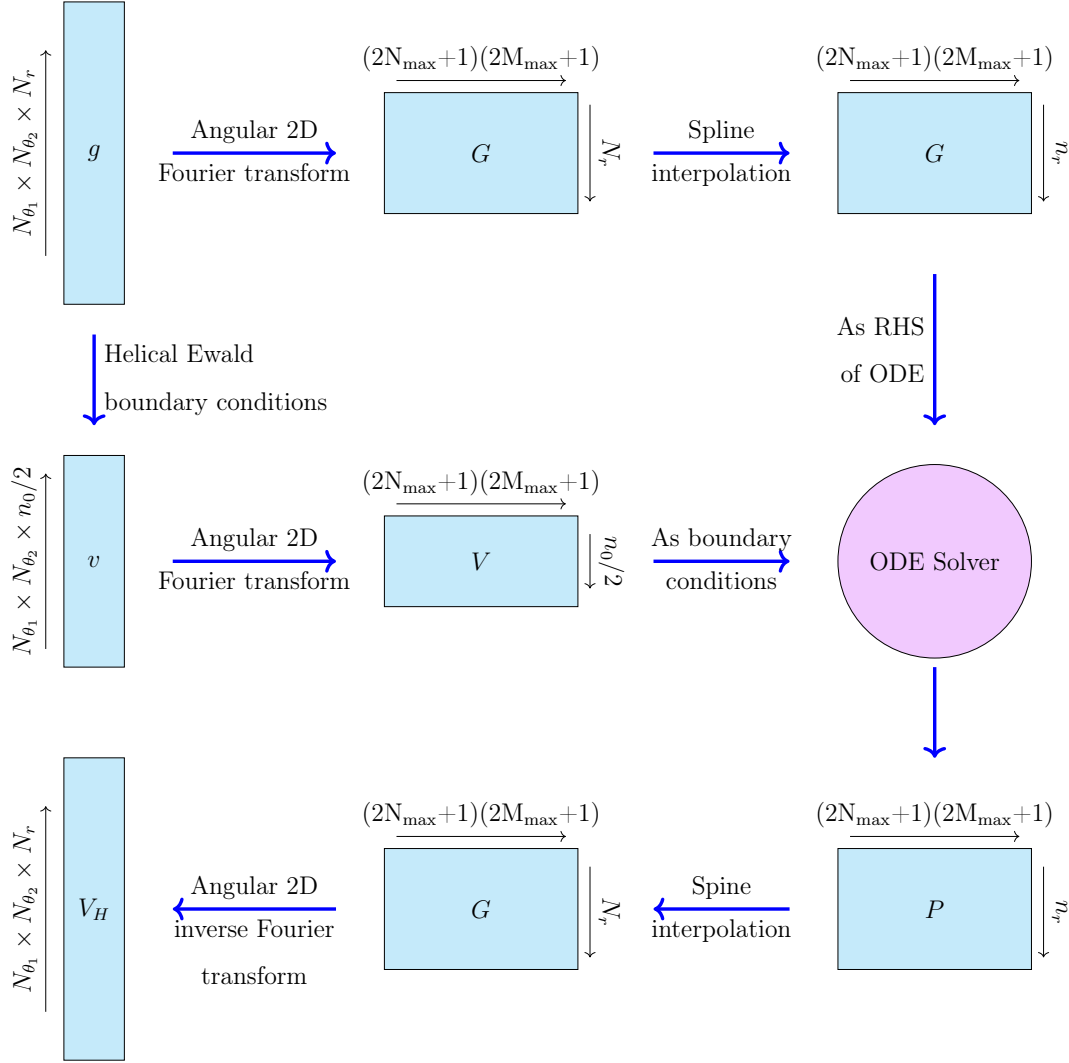


Figure 4.2: A flowchart of the mixed spectral – finite-difference based numerical method developed in this study. The (neutral) charge density,  $g(\theta_1, \theta_2, r)$ , is first transformed into 2D reciprocal space along the angular directions. The resultant field,  $G_{m,n}(r)$ , acts as the RHS of the ODE. The boundary conditions,  $v(\theta_1, \theta_2, r)$ , are obtained from the evaluation of the potential exerted by  $g(\theta_1, \theta_2, r)$  at the boundary points. This too is then transformed into the 2D reciprocal space. The ODE solver outputs the Hartree potential,  $P_{m,n}(r)$ , in the 2D reciprocal space. The complete potential,  $V_H(\theta_1, \theta_2, r)$  over  $\mathcal{D}$  is then obtained via an angular 2D inverse Fourier transform.

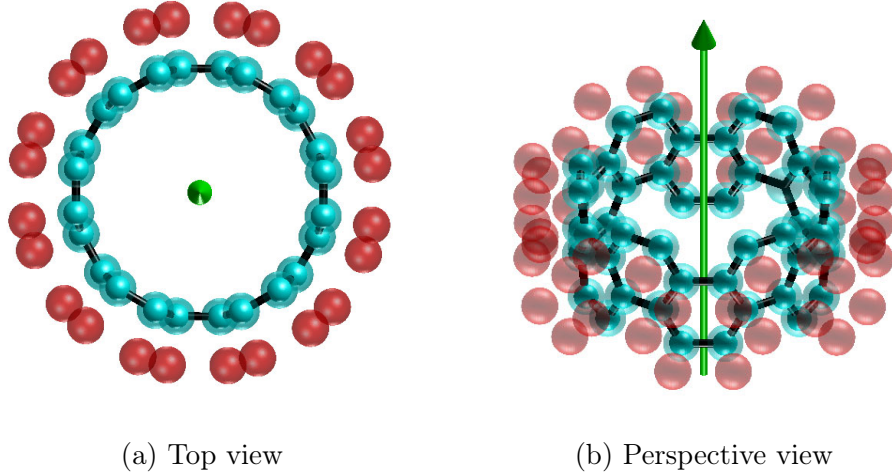


Figure 4.3: Setting up the compensating pseudocharges for a (6,6) armchair carbon nanotube. Only a slice of the nanotube has been depicted for ease of visualization. Here, the blue spheres represent the carbon atoms, and the translucent blue sphere encompassing each atom is the nuclear pseudocharge density. The red translucent spheres represent the artificial compensating electronic charge density. Note how none of the charge densities overlap — a necessary condition as outlined in [8].

butions [8, 9]:

$$\begin{aligned}
 \rho_1(r_s) &= \frac{z}{\pi^{3/2} R_c^3} e^{-\frac{r_s^2}{R_c^2}} \\
 \rho_2(r_s) &= \begin{cases} -21z(r_s - R_c)^3 (6r_s^2 + 3R_c r_s + R_c^2) / 5\pi R_c^8, & r_s \leq R_c \\ 0, & r_s > R_c \end{cases} \quad (4.20)
 \end{aligned}$$

where  $z$  is the nuclear charge and  $R_c$  is the cutoff radius of the pseudocharge distribution. Note that  $r_s$  represents the radial distance in the spherical coordinate system, unlike  $r$ , which represents the axial distance in helical coordinates. The first expression,  $\rho_1(r_s)$ , is a Gaussian distribution and has a relatively long tail. The second expression,  $\rho_2(r_s)$ , on the other hand, is relatively hard and local by design. We note that for  $\rho_1(r_s)$ , the magnitude of the charge drops to zero within machine precision at  $r_s = 6R_c$ . We use this fact to avoid overlapping charge distributions. For instance, if the shortest bond length in the system is  $L$  Bohrs, we



are limited to  $6R_c < 0.5L$  for  $\rho_1(r_s)$ , and  $R_c < 0.5L$  for  $\rho_2(r_s)$ . A notable advantage of using the above pseudocharge distributions is that their respective pseudopotentials are readily available as follows [8, 9]:

$$\begin{aligned}
 V_1(r_s) &= \frac{z}{r_s} \operatorname{erf} \left( \frac{r_s}{R_c} \right) \\
 V_2(r_s) &= \begin{cases} z(9r_s^7 - 30R_c r_s^6 + 28R_c^2 r_s^5 - 14R_c^5 r_s^2 + 12R_c^7) / 5R_c^8, & r_s \leq R_c \\ z/r_s, & r_s > R_c \end{cases} \quad (4.21)
 \end{aligned}$$

where  $\operatorname{erf}$  denotes the error function [194]. This allows us to generate reference analytical answers that serve as the ground truth. Thus, in following sections, we compare the Hartree potential calculated using our pseudo-spectral method using the charge distributions as explained above against the potential as computed using Eq. 4.21.

### 4.2.3 Evaluating boundary conditions

As mentioned earlier, Eq. 4.9 is a boundary value problem, i.e., we need to explicitly calculate the Hartree potential for points outside the fundamental domain,  $\mathcal{D}$ . Note that while the ODE is being solved in one dimension, we require a one-dimensional solution across a 2D reciprocal space spanned by  $(m', n')$ . Thus, the number of points for which these boundary conditions must be evaluated is  $(\frac{n_0}{2}) \times N_{\theta_2} \times N_{\theta_1}$ . Figuratively, this can be seen from Fig. 4.5. While this can be done analytically using the expressions in Eq. 4.21, for a general self consistent calculation, it is not possible to express the potential or the charge distribution in analytical terms. Thus, we resort to computing the potential as expressed in Eq. 4.8 by making use of helical Ewald sums. However, as the computational grid becomes finer, helical Ewald sums — which scale quadratically with respect to the number of grid points — become very expensive to calculate. Thus, there is a pressing need to optimize this calculation.

We tackle this situation by making the following observation. First, we split the Hartree potential into a product of the Ewald kernel  $\left( \sum \frac{1}{|\mathbf{x}-\mathbf{y}|} \right)$  and the charge density. Let  $\mathbf{x}$  ( $\equiv (\theta'_1, \theta'_2, r')$ ) and  $\mathbf{y}$  ( $\equiv (\theta_1^0, \theta_2^0, r^0)$ ) be the target and source locations in helical coordinates

respectively. Then, instead of evaluating the Ewald kernel for every pair of  $\mathbf{x}$  and  $\mathbf{y}$  in a 6D space,  $(\theta'_1, \theta'_2, r', \theta_1^0, \theta_2^0, r^0)$ , we can reduce the evaluation to a 4D space with the help of simple coordinate translations by assuming that, without loss of generalizability, each  $\mathbf{x}$  takes the form  $(0, 0, r')$ . Accordingly, the helical coordinates for each  $\mathbf{y}$  are modified as  $(\theta_1^0 - \theta'_1, \theta_2^0 - \theta'_2, r^0)$ . This works because the Ewald kernel is only dependent on the distance between  $\mathbf{x}$  and  $\mathbf{y}$ , which is invariant under linear coordinate transformations, and can be rigorously shown as follows. We first convert helical coordinates into cylindrical coordinates. Following Eq. 4.1, we have:

$$\vartheta^0 = 2\pi(\alpha\theta_1^0 + \theta_2^0), \quad \vartheta' = 2\pi(\alpha\theta'_1 + \theta'_2), \quad z^0 = \theta_1^0\tau, \quad z' = \theta'_1\tau \quad (4.22)$$

Translating the coordinate system in the  $z$  direction by  $-z'$  and rotating it by  $-\vartheta'$ , we get:

$$\begin{aligned} \vartheta' &\longleftarrow \vartheta - \vartheta' = 0 \\ z' &\longleftarrow z - z' = 0 \\ \vartheta_0 &\longleftarrow \vartheta_0 - \vartheta' = 2\pi(\alpha(\theta_1^0 - \theta'_1) + \theta_2^0 - \theta'_2) \\ z_0 &\longleftarrow z_0 - z' = (\theta_1^0 - \theta'_1)\tau \end{aligned} \quad (4.23)$$

Reverting back to helical coordinates gives us our new source coordinates in helical system as  $(\theta_1^0 - \theta'_1, \theta_2^0 - \theta'_2, r^0)$  and the new target coordinates as  $(0, 0, r')$ . This simple trick eventually reduces the calculation of the helical Ewald kernel from  $(\frac{n_0}{2}) \times N_{\theta_1} \times N_{\theta_2}$  target points to just  $\frac{n_0}{2}$  points. This further elucidates the massive reduction in computational time in working with the Poisson equation rather than evaluating the Hartree potential over  $\mathcal{D}$  in real space. We have reduced the number Ewald sum calculations by a factor of  $2N_r/n_0$ , which is typically around 100. Given the quadratic scaling of Ewald sums, this is an improvement of  $\mathcal{O}(100^2)$ . We may now setup a look-up table for the Ewald kernel covering all possible combinations of source and target pairs in 4D space. This can be done at the start of a self-consistent calculation, i.e., only once for any given simulation. Calculating the Ewald potential for every self-consistent iteration is then simply a matter of accessing the look-up table for a

given grid of shifted source and target locations, and multiplying it by the charge density at that location.

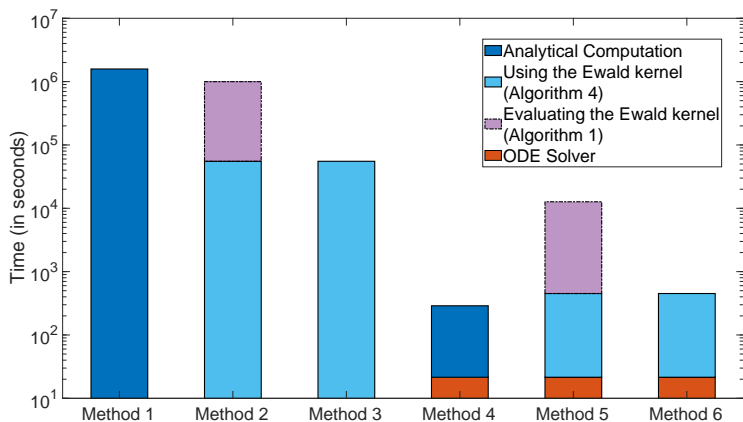
### 4.3 Reduction in computational complexity and algorithms

In this section, we elucidate on the reduced computational complexity of our pseudo-spectral method. First, we briefly discuss the computational complexity of our method, and compare it with a ‘naive’ calculation of the Hartree potential over the fundamental domain. This is followed by a detailed runtime comparison between different methods.

As such, a direct pairwise calculation using the helical Ewald method detailed in this section will have largely a computational complexity of  $\mathcal{O}(K_{\max}^2)$  owing to the quadratic scaling of the Ewald method. The coordinate shifting as described in the previous section will add a further  $\mathcal{O}(M_{\max}^2 N_{\max}^2 K_{\max}^2)$  to the above, albeit with a small prefactor. In contrast, the framework developed in this study uses a combination of FD and fast Fourier transforms, with the helical Ewald method only being called upon for the boundary conditions. The FD part is  $\mathcal{O}(K_{\max})$ , and the fast Fourier transforms combined have a scaling of  $\mathcal{O}(M_{\max} N_{\max} K_{\max} (K_{\max} + \log(M_{\max}) + \log(N_{\max})))$  [138]. The only additional cost is for the evaluation of the boundary conditions, which amounts to  $\mathcal{O}(n_0^2) + \mathcal{O}(M_{\max}^2 N_{\max}^2 n_0^2)$ , both with small prefactors.

Next, we present a direct comparison in the time taken by different methods to compute the same Hartree potential over  $\mathcal{D}$  (see Fig. 4.4). In the analytical method, the potential over  $\mathcal{D}$  is evaluated using analytical expressions as given in Eq. 4.21. In the method titled ‘helical Ewald’, the potential over  $\mathcal{D}$  is calculated using helical Ewald sums by using the Ewald kernel. In the ‘Spectral-FD’ technique, both the methods above are used to calculate the boundary conditions only, and the potential over  $\mathcal{D}$  is then obtained via the ODE solver. We reiterate here that the computation of the Ewald kernel, which is used to evaluate helical Ewald sums, need only be done once per simulation. As such, once precomputed, the wall

time of methods using the kernel can be significantly reduced further, as elucidated in Fig. 4.4.



(a) Timing comparison for different methods

Method	Description
Method 1	Analytical over $\mathcal{D}$
Method 2	Helical Ewald over $\mathcal{D}$
Method 3	Helical Ewald over $\mathcal{D}$ (precomputed kernel)
Method 4	Spectral-FD with analytical BCs
Method 5	Spectral-FD with helical Ewald BCs
Method 6	Spectral-FD with helical Ewald BCs (precomputed kernel)

(b) Methods legend

Figure 4.4: The time taken to calculate the full Hartree potential over  $\mathcal{D}$  using different methods for a (6,6) CNT with  $\alpha = 0.004$ ,  $\mathfrak{N} = 6$ . An energy cutoff of 120 Ha was used, and the FD order used was 12. All times are in seconds. Note that the bar plots have been stacked in reverse chronological order for ease of visualization (i.e., for instance, for the Spectral-FD case, the actual chronological order is the evaluation of the Ewald kernel, its usage, and then the ODE solver).

It is clear that our novel spectral-FD solver using helical Ewald boundary conditions is almost two orders of magnitude faster for realistic simulation parameters, while maintaining low errors, as is shown in the following section. The wall time can be further reduced for lower order of FD because this reduces the number of boundary points in the framework. For instance, and as displayed in Fig. 4.9, we see acceptable values of errors using fourth order FD. Thus, we may be able to reduce the time taken to compute the boundary conditions by a factor of three in Fig. 4.4 by using a lower FD order.

Now, we discuss the mathematical implementation of our framework. In what follows,  $O_{M \times N}$  is used to denote a zero matrix of size  $M \times N$ , and  $I_{M \times N}$  is used to denote a matrix of all ones of size  $M \times N$ . Additionally, the notation  $\{r^k\}_{k=1}^{N_r}$  is used to represent a vector of size  $N_r \times 1$  with entries  $r^k$ , where  $k \in [1, N_r]$ .

---

**Algorithm 6:** Generating the helical Ewald sum kernel

---

**Input:** The helical Ewald sum parameters  $\eta, \zeta, l_{\max}, k_{\max}, p$

**Prerequisites:** The equispaced radial target grid,  $\{r_t^j\}_{j=1}^{n_r}$  and the source coordinates,

$$\left( \{r^k\}_{k=1}^{N_r}, \{\theta_2^n\}_{n=1}^{N_{\theta_2}}, \{\theta_1^m\}_{m=1}^{N_{\theta_1}} \right)$$


---

Initialize  $\mathcal{E} = O_{n_r \times N_r \times N_{\theta_2} \times N_{\theta_1}}$

Calculate  $p$  Gauss-Jacobi radial weights and nodes between 0 and  $\eta$  as  $[t_n, t_w]$

**for**  $i \leq n_r$  **do**

Initialize  $V_L, V_S = O_{N_r \times N_{\theta_2} \times N_{\theta_1}}$

**for**  $n \leq \mathfrak{N} - 1$  **do**

$$\left\{ \theta_2^n \right\}_{n=1}^{N_{\theta_2}} = \left\{ \theta_2^n \right\}_{n=1}^{N_{\theta_2}} + n / \mathfrak{N} \quad // \text{Points skipped due to cyclic symmetries}$$

Create  $G_{3D} \in \mathbb{R}^{N_r \times N_{\theta_2} \times N_{\theta_1}}$ , a 3D grid from the vectors

$$\left\{ r^k \right\}_{k=1}^{N_r}, \left\{ \theta_1^m \right\}_{m=1}^{N_{\theta_1}}, \left\{ \theta_2^n \right\}_{n=1}^{N_{\theta_2}}$$

$V_L = V_L +$  Long range helical Ewald potential between  $(0, 0, r_t^i)$  and  $G_{3D}$

$V_S = V_S +$  Short range helical Ewald potential between  $(0, 0, r_t^i)$  and  $G_{3D}$

**if**  $i = 1$  **then**

$$\left| \begin{array}{l} V_L(\text{end}, 1, 1) = V_L(\text{end}, 1, 1) - 2\sqrt{\frac{\eta}{\pi}} \quad // \mathbf{x} \equiv \mathbf{y} \\ V_S(\text{end}, 1, 1) = 0 \quad // \mathbf{x} \equiv \mathbf{y} \end{array} \right.$$

**end**

**end**

$$\mathcal{E}(i, :, :, :) = V_L + V_S$$

**end**

**Result:** The helical Ewald kernel,  $\mathcal{E} \in \mathbb{R}^{n_r \times N_r \times N_{\theta_2} \times N_{\theta_1}}$ , computed for every target

$$\left( 0, 0, \{r_t^j\}_{j=1}^{n_r} \right) \text{ and source } \left( \{r^k\}_{k=1}^{N_r}, \{\theta_2^n\}_{n=1}^{N_{\theta_2}}, \{\theta_1^m\}_{m=1}^{N_{\theta_1}} \right) \text{ combination}$$


---

Note that Algorithm 6 sets up the helical Ewald kernel for a general radial grid, and, without loss of generality, keeps the  $\theta_1$  and  $\theta_2$  coordinates as 0. When using the algorithm to prepare the kernel for computing boundary conditions, the radial grid is set up as  $\{r_t^j\}_{j=1}^{0.5n_0} \in [R, R + \frac{n_0}{2} \Delta r]$ . Similarly, when generating the kernel for computing the potential directly

over  $\mathcal{D}$ , the grid is set up as  $\{r_t^j\}_{j=1}^{N_r} \in [0, R]$ . However, the grid points must be equispaced to comply with the FD stencil. Details on the helical Ewald algorithms for the short range and long terms can be found in Algorithms 7 and 8.

---

**Algorithm 7:** Short range helical Ewald potential

---

**Input:** The target point  $(\theta'_1, \theta'_2, r_t)$ , the source grid  $G_{3D}$ , and the helical Ewald sum parameters  $\eta, \zeta$

Unpack  $G_{3D}$  as individual vectors  $\{\theta_1^m\}_{m=1}^{N_{\theta_1}}$ ,  $\{\theta_2^n\}_{n=1}^{N_{\theta_2}}$ , and  $\{r^k\}_{k=1}^{N_r}$

$\{\theta_1^m\}_{m=1}^{N_{\theta_1}} = \{\theta_1^m\}_{m=1}^{N_{\theta_1}} + \lambda \quad \forall \lambda \in [\zeta, \zeta] \quad //$  Periodic helical images of  $\mathbf{y}$

Recreate  $G_{3D} \in \mathbb{R}^{N_r \times N_{\theta_2} \times (2\zeta+1)N_{\theta_1}}$

Convert  $G_{3D}$  into a 3D Cartesian grid,  $G_{3D}^{\text{Cart}}$

Convert helical coordinates  $(\theta'_1, \theta'_2, r_t)$  into Cartesian coordinates  $(x', y', z')$

Store distances between  $(x', y', z')$  and  $G_{3D}^{\text{Cart}}$  in  $\mathfrak{D}$

Remove zero values from  $\mathfrak{D} \quad // \mathbf{x} \equiv \mathbf{y}$

$V_S = \frac{1}{\sqrt{\pi}\mathfrak{D}} \cdot * \Gamma(\frac{1}{2}, \eta * \mathfrak{D}^2)$

Reshape  $V_S$  into a  $N_r N_{\theta_2} N_{\theta_1} \times (2\zeta + 1)$  vector and sum across the columns

Reshape  $V_S$  into a  $N_r \times N_{\theta_2} \times N_{\theta_1}$  vector

**Result:** Short range helical Ewald potential,  $V_S \in \mathbb{R}^{N_r \times N_{\theta_2} \times N_{\theta_1}}$ , between  $(\theta'_1, \theta'_2, r_t)$  and  $G_{3D}$

---

---

**Algorithm 8:** Long range helical Ewald potential
 

---

**Input:** The target point  $(\theta'_1, \theta'_2, r_t)$ , the source grid  $G_{3D}$ , the Gauss-Jacobi radial

weights  $(t_w)$  and nodes  $(t_n)$ , and the helical Ewald sum parameters  $l_{max}, k_{max}$

Unpack  $G_{3D}$  as individual vectors  $\theta_1^{\text{grid}} = \{\theta_1^m\}_{m=1}^{N_{\theta_1}}$ ,  $\theta_2^{\text{grid}} = \{\theta_2^n\}_{n=1}^{N_{\theta_2}}$ , and

$$r_{\text{grid}} = \{r^k\}_{k=1}^{N_r}$$

Reshape  $\theta_1^{\text{grid}}$  into a 4D tensor  $\theta_1^{4D} \in \mathbb{R}^{1 \times 1 \times 1 \times N_{\theta_1}}$

Reshape  $\theta_2^{\text{grid}}$  into a 4D tensor  $\theta_2^{4D} \in \mathbb{R}^{1 \times 1 \times N_{\theta_2} \times 1}$

Initialize  $\mathcal{I}^{l \neq 0} = O_{(2l_{max}+1)(2k_{max}+1) \times N_r}$ ,  $\mathcal{I}^{k \neq 0} = O_{(2l_{max}+1)(2k_{max}+1) \times N_r}$

Initialize  $\mathcal{M}^{l \neq 0} = O_{(2l_{max}+1)(2k_{max}+1) \times 1 \times N_{\theta_2} \times N_{\theta_1}}$ ,  $\mathcal{M}^{k \neq 0} = O_{(2l_{max}+1)(2k_{max}+1) \times 1 \times N_{\theta_2} \times N_{\theta_1}}$

Initialize  $c_1, c_2 = 0$ , and set  $E = \exp(-(r_t^2 + r_{\text{grid}}^2) \cdot t_n)$

Set  $A_1 = I_{N_r \times N_{\theta_2} \times N_{\theta_1}} \cdot \left[ \frac{1}{\tau} \sum_p t_{w_p} \cdot \exp\left(\frac{(t_{n_p} \cdot r_t)^2}{t_{n_p}^2}\right) \right]$

Set  $A_2 = \frac{1}{\tau} \cdot \sum_p \frac{1}{t_{n_p}^2} \cdot \text{besseli}(0, 2r_t \cdot r_{\text{grid}} \cdot t_{n_p}) \cdot \exp(-t_{n_p}(r_t^2 + r_{\text{grid}}^2)) \cdot t_{w_p}$

Reshape  $A_2$  as  $A_2 = I_{1 \times N_{\theta_2} \times N_{\theta_1}} \cdot A_2$

**for**  $l \in [-l_{max} : l_{max}]$ ,  $l \neq 0$  **do**

Set  $f_l = \frac{1}{l^2} \cdot \text{besseli}(l, 2r_t \cdot r_{\text{grid}} \cdot t_n) \cdot E$

Set  $h_l = \exp(-2i\pi l((\theta_2^{4D} - \theta'_2) + \alpha(\theta_1^{4D} - \theta'_1))) \cdot \exp(-2i\pi l \alpha(\theta'_1 - \theta_1^{4D}))$

**for**  $k \in [-k_{max} : k_{max}]$  **do**

Increment  $c_1$  by unity

Set  $f = f_l \cdot \exp\left(-\frac{1}{t_n} \cdot \left(\frac{\pi(l\alpha+k)}{\tau}\right)^2\right)$

$\mathcal{I}^{l \neq 0}(c_1, :) = \sum_p f \cdot t_{w_p}$

$\mathcal{M}^{l \neq 0}(c_1, :, :, :) = h_l \cdot \exp(-2i\pi k(\theta'_1 - \theta_1^{4D}))$

**end**

**end**

Set  $A_3$  as sum across all rows of  $\frac{1}{\tau} \cdot (\mathcal{I}^{l \neq 0} \cdot \mathcal{M}^{l \neq 0})$

Set  $f_l = \frac{1}{l^2} \cdot \text{besseli}(0, 2r_t \cdot r_{\text{grid}} \cdot t_n) \cdot E$

**for**  $k \in [-k_{max} : k_{max}]$ ,  $k \neq 0$  **do**

Increment  $c_2$  by unity

$f = f_l \cdot \exp\left(-\frac{1}{t_n} \cdot \left(\frac{\pi k}{\tau}\right)^2\right)$

$\mathcal{I}^{k \neq 0}(c_2, :) = \sum_p f \cdot t_{w_p}$

$\mathcal{M}^{k \neq 0}(c_2, :, :, :) = I_{N_{\theta_2} \times N_{\theta_2}} \cdot \exp(-2i\pi k(\theta'_1 - \theta_1^{4D}))$

**end**

Set  $A_4$  as sum across all rows of  $\frac{1}{\tau} \cdot (\mathcal{I}^{k \neq 0} \cdot \mathcal{M}^{k \neq 0})$

$V_L = A_1 - A_2 + A_3 + A_4$  after removing dimensions of unit length from each

**Result:** Long range helical Ewald potential,  $V_L \in \mathbb{R}^{N_r \times N_{\theta_2} \times N_{\theta_1}}$ , between  $(\theta'_1, \theta'_2, r_t)$

and  $G_{3D}$

---

---

**Algorithm 9:** Helical Ewald sums for boundary points
 

---

**Input:** The source points,  $\{r^k\}_{k=1}^{N_r}$ ,  $\{\theta_1^m\}_{m=1}^{N_{\theta_1}}$ ,  $\{\theta_2^n\}_{n=1}^{N_{\theta_2}}$ , and the target points,

$$\{r^j\}_{j=1}^{0.5n_0}, \{\theta_1^m\}_{m=1}^{N_{\theta_1}}, \{\theta_2^n\}_{n=1}^{N_{\theta_2}}$$

**Prerequisites:** The helical Ewald kernel,  $\mathcal{E}$ , evaluated in Algorithm 6, and the charge

$$\text{density, } g \in \mathbb{R}^{1 \times N_r \times N_{\theta_2} \times N_{\theta_1}}$$


---

Set  $\mathcal{N} = 0.5n_0 N_{\theta_1} N_{\theta_2}$

Initialize  $V_H = O_{\mathcal{N} \times 1}$

Replicate each  $\theta_1^m$  for  $0.5n_0 \times N_{\theta_2}$  instances to get  $\theta_1^{\text{mesh}} \in \mathbb{R}^{\mathcal{N} \times 1}$

Replicate each  $\theta_2^n$  for  $0.5n_0$  instances to get  $\theta_2^{\text{temp}} \in \mathbb{R}^{0.5n_0 N_{\theta_2} \times 1}$

Replicate the whole of  $\theta_2^{\text{temp}}$  for  $N_{\theta_1}$  instances to get  $\theta_2^{\text{mesh}} \in \mathbb{R}^{\mathcal{N} \times 1}$

**for**  $i \leq \mathcal{N}$  **do**

$$\theta_1^s = \{\theta_1^m\}_{m=1}^{N_{\theta_1}} - \theta_1^{\text{mesh}}(i) \quad // \text{Coordinate transformation (see subsection 4.2.3)}$$

$$\theta_2^s = \{\theta_2^n\}_{n=1}^{N_{\theta_2}} - \theta_2^{\text{mesh}}(i) \quad // \text{Coordinate transformation (see subsection 4.2.3)}$$

Map  $\theta_1^s, \theta_2^s$  back into  $\mathcal{D}$ , if needed

$$r^{\text{index}} = i \bmod 0.5n_0$$

**if**  $r^{\text{index}} = 0$  **then**

$$| \quad r^{\text{index}} = 0.5n_0$$

**end**

Find indexing vectors  $\theta_1^{\text{index}}, \theta_2^{\text{index}}$  such that  $\{\theta_1^m\}_{m=1}^{N_{\theta_1}}(\theta_1^{\text{index}}) = \theta_1^s$ , and

$$\{\theta_2^n\}_{n=1}^{N_{\theta_2}}(\theta_2^{\text{index}}) = \theta_2^s$$

$$V_H(i) = \text{sum}(\mathcal{E}(r^{\text{index}}, \cdot, \theta_2^{\text{index}}, \theta_1^{\text{index}}) \cdot * g, \text{ all})$$

Reshape  $V_H$  into  $\mathbb{R}^{0.5n_0 \times N_{\theta_2} \times N_{\theta_1}}$

**end**

**Result:** The Hartree potential,  $V_H \in \mathbb{R}^{0.5n_0 \times N_{\theta_2} \times N_{\theta_1}}$ , computed for every boundary

$$\text{point} \left( \{\theta_1^m\}_{m=1}^{N_{\theta_1}}, \{\theta_2^n\}_{n=1}^{N_{\theta_2}}, \{r^j\}_{j=1}^{0.5n_0} \right)$$


---

After having set up the helical Ewald kernel in the form of a look-up table in Algorithm 6, the potential at a point  $(\theta'_1, \theta'_2, r')$  due to the charge at the point  $(\theta_1^0, \theta_2^0, r^0)$  is given by using the linear coordinate transformation detailed in section 4.2.3, accessing the look-up table, and multiplying the value by the charge at the point  $(\theta_1^0, \theta_2^0, r^0)$ . This process can easily be vectorized, as elucidated in Algorithm 9. In fact, each algorithm has been vectorized in the source coordinate space, allowing the calculation of the potential at a particular target



location due to all source locations in one go.

---

**Algorithm 10:** Poisson ODE

---

**Input:** The FD order,  $n_0$ , and the number of FD grid points,  $n_r$

**Prerequisites:** The FD radial grid,  $r_{\text{FD}}$ , the 2D angular transform of the charge density,  $g_{m,n}(r)$ , over  $\mathcal{D}$ , and the 2D angular transform of boundary conditions,  $V_{m,n}^{\text{BC}}(r)$ , evaluated using helical Ewald sums

---

Initialize  $V_H = O_{n_r \times (2M_{\text{max}}+1)(2N_{\text{max}}+1)}$

**for**  $m' \in [-M_{\text{max}} : M_{\text{max}}]$  **do**

**for**  $n' \in [-N_{\text{max}} : N_{\text{max}}]$  **do**

        Set  $c_1 = (-1)^{n'\mathfrak{N}}$ ,  $c_2 = (n'\mathfrak{N})^2$ ,  $h = 0.5 * n_0$ ,  $\beta = \left[\frac{2\pi}{\tau} (m' - \alpha n'\mathfrak{N})\right]^2$

        Set up spline to interpolate  $g_{m',n'}(r)$  to the FD radial grid,  $g_{m',n'}(r_{\text{FD}})$

$\mathcal{R} = -4\pi g_{m',n'}(r_{\text{FD}}) \in \mathbb{R}^{n_r \times 1}$ , and set  $U, L = O_{n_r \times h}$

        Set up  $\omega_{0,r}^{\text{second}} \in \mathbb{R}$ ,  $\omega_r^{\text{second}} \in \mathbb{R}^{h \times 1}$ , and  $\omega_r^{\text{first}} \in \mathbb{R}^{h \times 1}$  using Eq. 4.18

        Initialize a diagonal matrix  $\mathcal{M}_{n_r \times n_r}$  with diagonal  $\left(2 * \omega_{0,r}^{\text{second}} - \beta - \frac{c_2}{r_{\text{FD}}^2}\right)$

**for**  $i \leq n_r$  **do**

$U(i, :) = \omega_r^{\text{second}} + \frac{\omega_r^{\text{first}}}{r_{\text{FD}}^{(i)}} \quad // \text{ Entries above the diagonal}$

$L(i, :) = \text{flip} \left( \omega_r^{\text{second}} - \frac{\omega_r^{\text{first}}}{r_{\text{FD}}^{(i)}} \right) \quad // \text{ Entries below the diagonal}$

**end**

**for**  $ii \leq n_r$  **do**

            Add entries above and below the diagonal (see Fig. 4.5)

**if**  $ii \leq h$  **then**    //  $r < 0$

                | Implement pole conditions (see Fig. 4.5)

**end**

**end**

        Incorporate boundary conditions,  $V_{m',n'}^{\text{BC}}(r)$ , into the FD stencil  $\mathcal{M}$

        Solve matrix multiplication equation  $\mathcal{M}V_{m',n'}(r_{\text{FD}}) = \mathcal{R}$  to get  $V_{m',n'}(r_{\text{FD}})$

$V_H(:, (m' + M_{\text{max}})(2N_{\text{max}} + 1) + (n' + N_{\text{max}} + 1)) = V_{m',n'}(r_{\text{FD}})$

**end**

**end**

Set up a spline to interpolate  $V_H$  from  $r_{\text{FD}}$  to the computational radial grid,  $\{r^k\}_{k=1}^{N_r}$

Obtain the Hartree potential by performing the 2D inverse angular transform on all

rows of  $V_H$  and reshaping the matrix to  $V_H(\theta_2, \theta_1, r) \in \mathbb{R}^{N_{\theta_2} N_{\theta_1} N_r \times 1}$

**Result:** The Hartree potential,  $V_H(\theta_2, \theta_1, r)$  over  $\mathcal{D}$

---

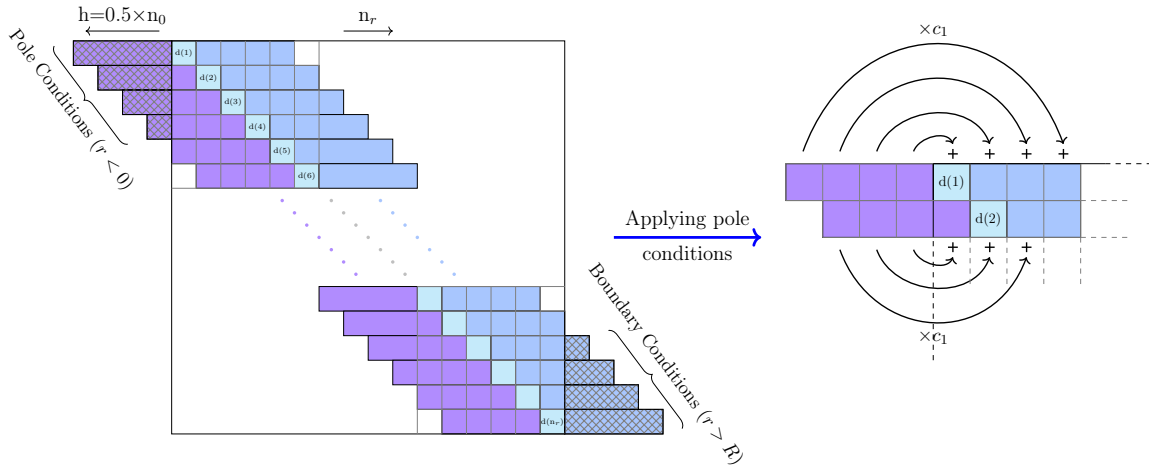


Figure 4.5: Pictorial representation of generating the FD stencil for an order of  $n_0 = 8$ , as outlined in Algorithm 10. The variables  $h$ ,  $n_r$ , and  $c_1$  are taken from Algorithm 10 as well. The term  $d(i)$  represents the  $i^{\text{th}}$  diagonal term in the stencil. The entries above the diagonal (in dark blue) are cut off at the end (shaded area) due to boundary conditions, whereas the entries below the diagonal (in purple) are cut off at the start due to pole conditions.

Having evaluated the Hartree potential at the boundary using Algorithm 9, the potential over  $\mathcal{D}$  is calculated via Algorithm 10 by essentially solving the boundary value problem set up in section 4.2.1.

## 4.4 Results

### 4.4.1 Computational platform

All simulations in this study were carried out using dedicated desktop workstations (Dell Precision 7920 Tower) or on single nodes of the Hoffman2 cluster at UCLA's Institute for Digital Research and Education (IDRE). The Dell Precision workstation has an 18-core Intel Xeon Gold 5220 processor (24.75 L3 MB cache, 2.2 GHz clock speed), 256 GB of RAM and 1 TB of SATA Class 20 Solid State Drive (SSD) storage. Every compute node of the Hoffman2 cluster has two 18-core Intel Xeon Gold 6140 processors (24.75 MB L3 cache, clock speed

of 2.3 GHz), 192 GB of RAM and local SSD storage. MATLAB version 9.7.0 (R2019b) was used for the simulations. Parallelization, wherever possible, was achieved using MATLAB’s Parallel Computing Toolbox.

#### 4.4.2 Convergence and accuracy studies

Before discussing the convergence of the calculated Hartree potential using our method with respect to different simulation parameters, we first showcase the expected behaviour of the Laplacian operator set up in Algorithm 10. We do this by noting that the basis functions are eigenfunctions of the Laplacian operator in helical coordinates [138]. Thus, the eigenvalue equation must be satisfied. This can be represented as:

$$-\Delta F_{m,n,k} = \lambda_{m,n,k}^0 F_{m,n,k}, \quad (4.24)$$

where  $\lambda_{m,n,k}$  is the eigenvalue corresponding to a particular  $(m, n, k)$  harmonic of the eigenfunction  $F_{m,n,k}$ . In Fig. 4.6, we plot the error between the left hand side and the right hand side of Eq. 4.24. For a rigorous analysis, we perform this test for three different harmonics and observe that while the errors in the vectors are low, they increase for higher harmonics. This is to be expected given that the computational grid has been fixed and because aliasing errors may be seen. An additional technique to check the validity of the above equation is to check the ratio of the left hand side to the right hand side. Ideally, one would expect that ratio to be constant, and equal to 1, throughout. We verify that that is indeed the case here, except at zeroes of the eigenfunction, which is to be expected. Thus, we conclude that the FD-based helical Laplacian operator behaves as expected.

With the basis set size,  $\mathcal{L}$ , being defined by three quantities  $(M_{\max}, N_{\max}, K_{\max})$ , it behooves to show systematic convergence of the Hartree potential, as evaluated by our pseudo-spectral method, with respect to each of the three basis set maxes. We demonstrate convergence using both the Gaussian charge distribution [9] as well as the charge distribution developed in [8]. For the Gaussian charge distribution, we consider a (6, 6) carbon nanotube

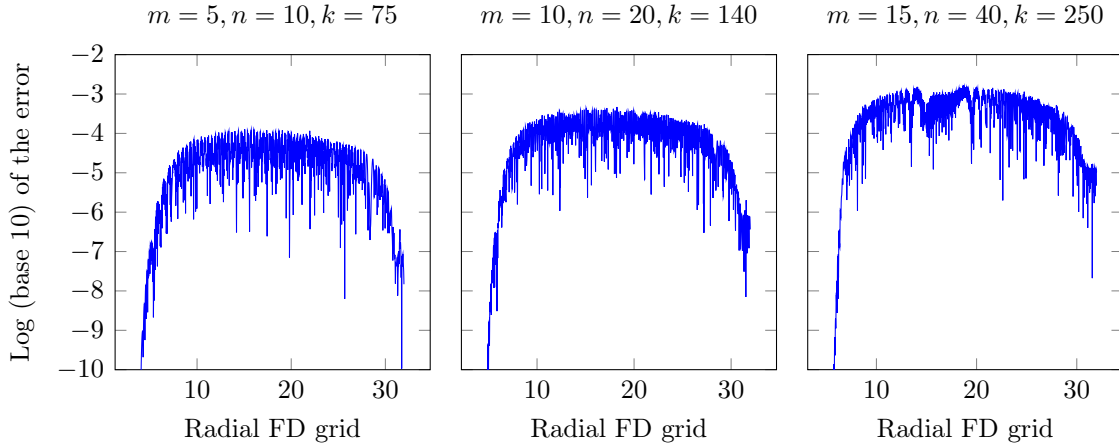


Figure 4.6: The difference in left hand side and the right hand side of the eigenvalue equation (Eq. 4.24) for different harmonics of the eigenfunction. The plot on the bottom right shows the ratio of the left hand side to the right hand side for values of  $r$  where the eigenfunction is non-zero. The spikes occur in the immediate vicinity of the zeroes of the eigenfunction. In each case, the basis set maxima were set to  $M_{\max} = 20$ ,  $N_{\max} = 50$ ,  $K_{\max} = 300$  which are high enough to avoid any errors creeping in due to coarseness of the mesh. A FD order of 4 was used, with  $n_r = 2N_r$  (consistent with the results in Fig. 4.9).

(CNT) with  $\alpha = 0.005$ , whereas for the charge density introduced in [8], we use a (6,6) silicon nanotube with  $\alpha = 0.002$ . In both cases,  $\mathfrak{N} = 6$ .

We observe systematic and monotonic convergence with respect to each of the 3 basis set maxes, as depicted in Fig. 4.7 for a (6,6) armchair carbon nanotube using a Gaussian pseudocharge distribution, and in Fig. 4.8 for an equivalent (6,6) silicon nanotube using the relatively harder pseudocharge distribution introduced in [8]. However, it is interesting to note the slight difference in the convergence trend for the two pseudocharge (and pseudopotential) distributions used in this work. For the Gaussian pseudocharge distribution, the errors are typically higher than the other harder pseudocharge distribution for the same basis set size. However, the trend is reversed at higher values of the basis set size because the convergence in Fig. 4.8 eventually saturates.

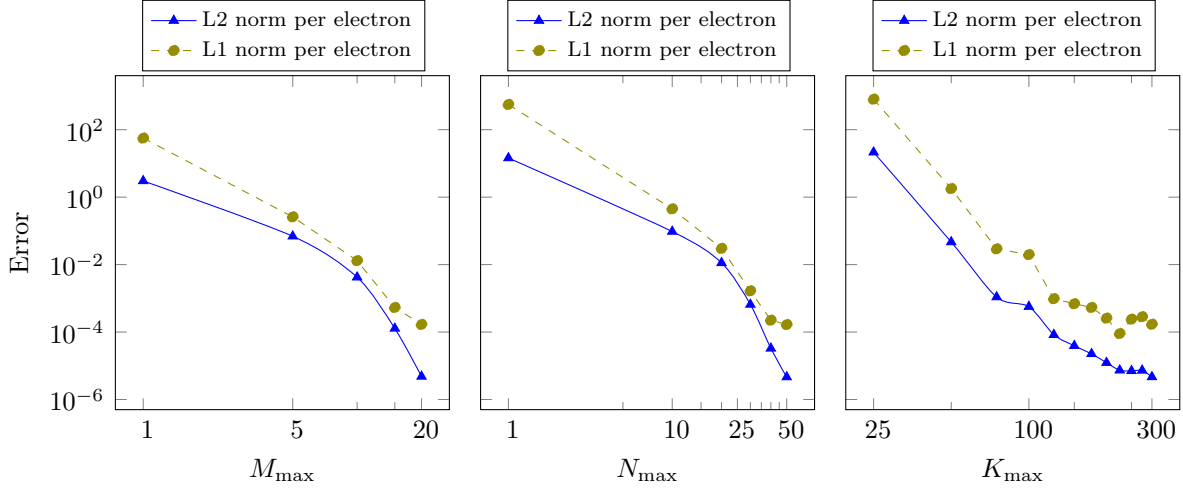


Figure 4.7: Convergence in the  $L^2$  norm per electron, calculated as  $\frac{1}{N_e} \times \sqrt{\int_{\mathcal{D}} (V - V_{\text{ref}})^2 2\pi\tau r dr d\theta_1 d\theta_2}$ , and  $L^1$  norm per electron, calculated as  $\frac{1}{N_e} \times \int_{\mathcal{D}} |V - V_{\text{ref}}| 2\pi\tau r dr d\theta_1 d\theta_2$ , with respect to different basis set maxes for the Gaussian pseudocharge distribution [9]. Here  $N_e$  is the number of electrons in  $\mathcal{D}$ . In each case, the other two basis set maxima were held constant at  $M_{\max} = 30, N_{\max} = 75, K_{\max} = 300$ . The method was tested on a 6,6 carbon nanotube with  $\alpha = 0.004, \mathfrak{N} = 6$ . The reference,  $V_{\text{ref}}$ , was calculated using the analytical expression in Eq. 4.21 with a basis set size corresponding to  $M_{\max} = 30, N_{\max} = 75, K_{\max} = 300$ .

At this point, we could like to note that while our pseudo-spectral method requires relatively high values of the basis set maxes to achieve low errors, we don't necessarily have to use these values for the actual calculation of the electron density. We envision using two sets of basis set maxes — a coarser grid for the computation of the electron density and a much finer grid for the computation of the Hartree potential. Transferring fields from one grid to another is a simple matter of interpolation. This negates the need to use a fine mesh where it may not be required.

Finally, we also perform convergence testing with respect to the FD order, and for multiple values of the number of FD grid points,  $n_r$ . This can be seen in Fig. 4.9 below. It is apparent that the errors saturate irrespective of the size of the basis set, but the level

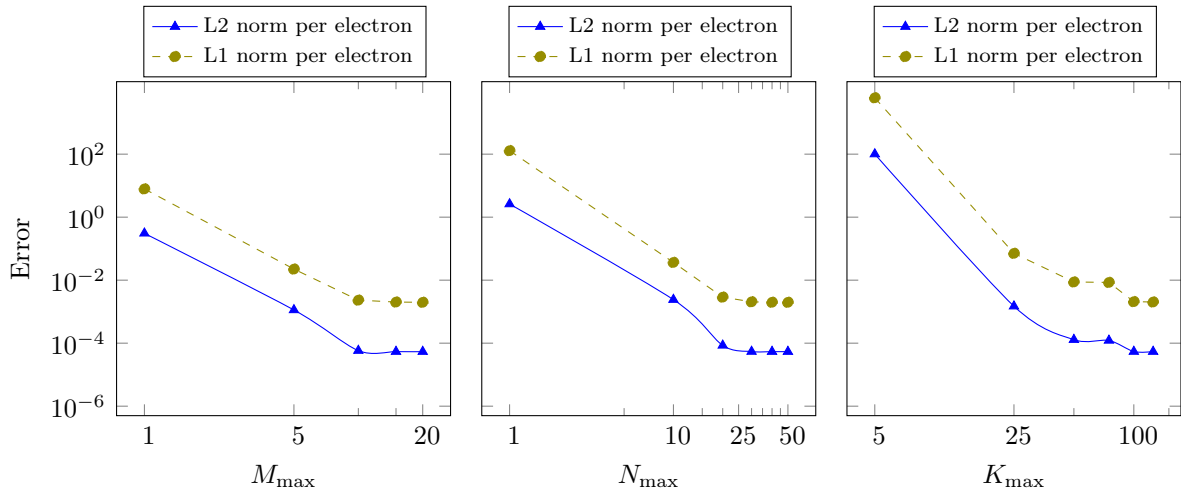


Figure 4.8: Convergence in the  $L^2$  norm per electron, calculated as  $\frac{1}{N_e} \times \sqrt{\int_{\mathcal{D}} (V - V_{\text{ref}})^2 2\pi\tau r dr d\theta_1 d\theta_2}$ , and  $L^1$  norm per electron, calculated as  $\frac{1}{N_e} \times \int_{\mathcal{D}} |V - V_{\text{ref}}| 2\pi\tau r dr d\theta_1 d\theta_2$ , with respect to different basis set maxes for the pseudocharge distribution introduced in [8]. Here  $N_e$  is the number of electrons in  $\mathcal{D}$ . In each case, the other two basis set maxima were held constant at  $M_{\max} = 30$ ,  $N_{\max} = 75$ ,  $K_{\max} = 300$ . The method was tested on a 6,6 carbon nanotube with  $\alpha = 0.004$ ,  $\mathfrak{N} = 6$ . The reference,  $V_{\text{ref}}$ , was calculated using the analytical expression in Eq. 4.21 with a basis set size corresponding to  $M_{\max} = 30$ ,  $N_{\max} = 75$ ,  $K_{\max} = 300$ .

at which they saturate is very much dependent on the basis set size. This, along with the observations from Fig. 4.7 and Fig. 4.8 leads us to conclude that the errors are largely controlled by the basis set maxima and are relatively insensitive to the FD order.

#### 4.4.3 Calculation of the electrostatic interaction energy

Having validated and rigorously tested our method, we now demonstrate its utility for realistic use cases by calculating the energy arising from electrostatic interactions in a system. Here too, two opportunities present themselves. We can calculate the electrostatic interaction energy — obtained as the integral, over  $\mathcal{D}$ , of the Hartree potential and the neutral

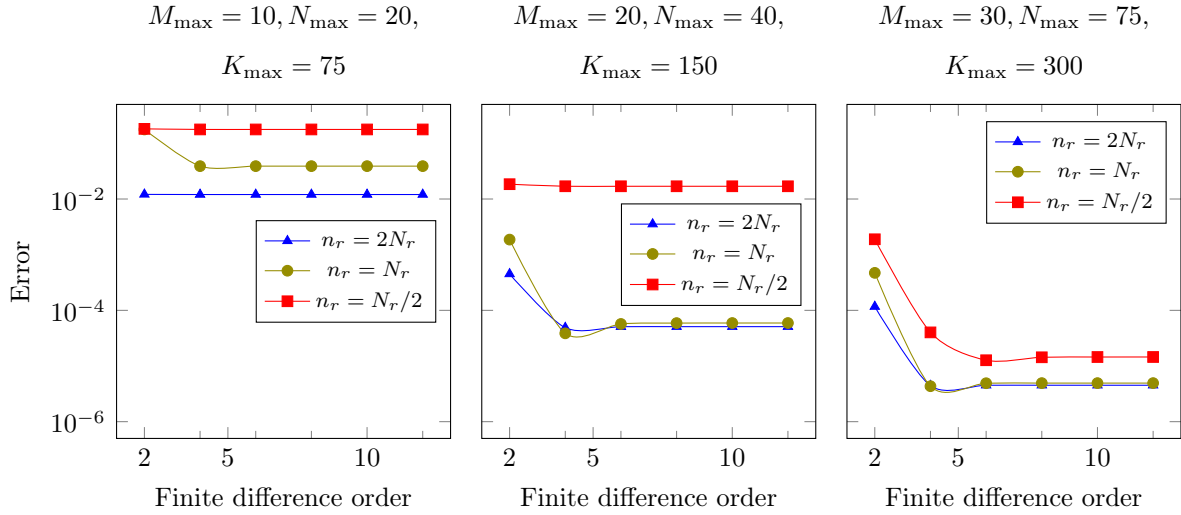


Figure 4.9: Convergence in the  $L^2$  norm per electron, calculated as  $\frac{1}{N_e} \times \sqrt{\int_{\mathcal{D}} (V - V_{\text{ref}})^2 2\pi r dr d\theta_1 d\theta_2}$ , between the Hartree potential as evaluated analytically (from Eq. 4.21) and as evaluated by our pseudo-spectral method with respect to the finite difference order for a (6,6) armchair carbon nanotube with a twist of  $\alpha = 0.004$ , and  $\mathfrak{N} = 6$ . We show convergence across 3 different values of  $n_r$ , and for 3 different sizes of the basis set.

charge density — by using the unphysical setup used in subsection 4.2.2. This results in a parabolic curve wherein the electrostatic interaction energy of the system increases with the twist parameter ( $\alpha$ ), as displayed in Fig. 4.10. Alternatively, the electronic charge density can be computed using an electronic structure code, while the nuclear charge density can be derived from Eq. 4.20. In both cases, once the neutral charge density is obtained, the evaluation of the Hartree potential is done via the method presented in this study. For the latter, we see an inverse parabolic relation with respect to  $\alpha$ . We argue that this may be because the empirical pseudopotential used for the calculation of the electron density [6, 161] may not be compatible with the local pseudopotentials described in Eq. 4.21.

Electrostatic interaction energy using local pseudocharges (Eqs. 4.20, 4.21)

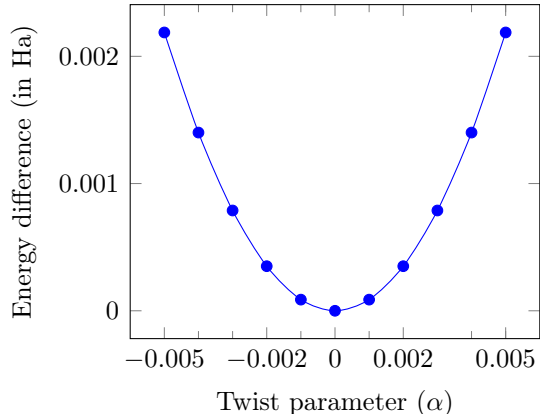


Figure 4.10: The behaviour of the electrostatic interaction energy as a function of the twist parameter,  $\alpha$ , for a (6, 6) carbon nanotube,  $\mathfrak{N} = 6$ . The basis set size chosen was  $M_{\max} = 15$ ,  $N_{\max} = 30$ ,  $K_{\max} = 125$ . The FD order was 4, with  $n_r = N_r$ , consistent with the observations from Fig. 4.9. We see an expected quadratic behaviour, consistent with prior works [10].

## 4.5 Concluding remarks

The above framework for the calculation of the Newtonian potential that features within the KS-DFT equations paves the way to incorporating self consistency within HelicES. The combination of these works is expected to eventually enable full DFT calculations of quasi-one-dimensional materials of interest. A couple of avenues that could be explored include the study of electronic flat bands in twisted graphene nanoflakes, as well as the study of anomalous spin transport phenomenon such as the chiral-induced spin selectivity (CISS) effect. At this point, it is also interesting to note that, since the framework described above is essentially a representation of the Laplacian in helical space, it has the ability to be applied directly for the solution of the one particle Schrödinger equation as an alternate method to what has been discussed in Chapters 2 and 3. Specifically, the Laplacian is expressed pseudo-spectrally wherein we use fast Fourier transforms (FFTs) for the two-dimensional angular



domain but use finite differences in the radial direction. Thus, if the wavefunction too can be expressed in a similar way — i.e., in a 2D reciprocal space for angular dependence, and in a 1D real space for radial dependence — then we could use a variant of Eq. 4.17 (without the RHS) and perform a direct diagonalization preceded by FFTs to compute the wavefunction. A notable advantage of this method over a direct diagonalization of the Laplacian applied to the wavefunction in a fully spectral framework is that the computational cost associated with a one-dimensional numerical quadrature in the radial direction is removed.

## CHAPTER 5

# The Posner molecule: Importance and structural ambiguity

### 5.1 Background and the claim of a biological neural qubit

The calcium phosphate trimer,  $\text{Ca}_9(\text{PO}_4)_6$ , is of special biological interest. First discovered in the bone mineral hydroxyapatite in 1975 by Betts and Posner [77], and henceforth coined as the *Posner molecule* (PM), it is thought to form the structural building block of amorphous calcium phosphate [78]. Its presence in simulated body fluids was confirmed by Onuma and Ito [195], and its aggregation has been hypothesized to underpin bone growth [79, 80, 81, 82]. More recently, it has been proposed that the  $^{31}\text{P}$  nuclear spins within PMs can maintain long-lived entanglement, and that this could play an important role in nervous excitation via synaptic  $\text{Ca}^{2+}$  ion release [11, 15, 83]. These and other studies [16] have subsequently explored PMs as potential “neural qubits”, drawing upon the fact that nuclear spin coherence times associated with these systems have been found to be exceptionally large per theoretical estimates. Such studies have suggested or assumed that the prototypical structure for the PM is one with an  $S_6$  molecular point group symmetry, at least on the average [11]. Furthermore, in the presence of a well-defined rotation axis of the cluster (such as the three-fold  $C_3$  rotational symmetry of the supposed  $S_6$  symmetric cluster), the binding and unbinding of PMs could arguably act as a “pseudospin” entangler of the nuclear spin states of multiple PMs, which is a necessary precondition for the “quantum brain” concept, as suggested in [11].

In the context of the aforementioned mechanism, molecular point group symmetries for PMs are important, because they dictate the form of the spin-spin coupling network. The number of independent components in this network is directly related to the point group symmetry of the structure [196]. Certain molecular symmetries can render the six  $^{31}\text{P}$  nuclei magnetically equivalent (*e.g.*,  $S_6$ ), resulting in a small number of unique scalar ( $J$ ) couplings (*e.g.*, three unique coupling constants for  $S_6$ ) [16]. Understandably, other molecular symmetries could treat groups of  $^{31}\text{P}$  nuclei as distinct, thus, resulting in a larger number of pertinent scalar couplings [197]. As the ability of the system to sustain long-lived spin coherences is starkly related to the asymmetry in the coupling network [198, 199, 200, 201, 202], the spin physics of PMs is inherently linked to the molecule’s point group symmetries. Further, the presence of an inversion center in the PM, as found for  $S_6$ , would render the intra-cluster dipolar coupling block-diagonal in a basis of well-defined parity under exchange of two  $^{31}\text{P}$  nuclei related by inversion. As a consequence, the inclusion of a singlet-polarized diphosphate molecule in such a cluster could generate long-lived spin population differences, spared from fast spin relaxation by the dipolar coupling within the PM.

The structure of the isolated PM is unknown. However, a series of studies [11, 16, 78, 203] suggest a high degree of symmetry, *e.g.*  $S_6$  and beyond, which was later exploited [11] in deriving the molecule’s hypothetical entanglement-driven interaction mechanisms. [16, 204]. That the symmetry of the cluster might in fact be lower, has, on the other hand, been pointed out as early as 2003 in the work of Yin et al. [79], and then later in [204] and [16]. Based on studies of the PM so far, two possibilities ought to be addressed: a) could the molecule exist as a stable entity, *i.e.* corresponding to a minimum on the Potential Energy Surface (PES), of high symmetry that is dominantly populated at physiological temperatures, as motivated by [78, 203], or b) could thermal fluctuations average the molecule’s geometry to an effective structure of high symmetry, *i.e.* of an overall  $S_6$  symmetry, despite the ensemble comprising predominantly low symmetry states, as advocated in [11] ? Ref. [11] reports the energy difference between  $S_6$  and  $C_1$  to be  $0.06 \text{ eV} = 1.53 \text{ meV/atom} = 2.33 k_B T$ ,

while [203] suggests an alternate value of  $0.13 \text{ eV} = 3.33 \text{ meV/atom} = 5.06 k_B T$  between  $S_6$  and  $C_2$ , suggesting that these structures are thermally accessible, thereby highlighting the importance of probing hypothesis b) by studying the dynamical ensemble properties. Indeed, Swift et al. [11], while utilizing the  $S_6$ -symmetry in deriving the specifics of the quantum brain hypothesis, acknowledge the existence of multiple more stable structures of lower symmetries. Moreover, it was understood that they considered non-equilibrated structures, assumed to exist in the average, for their calculations [205]. Naturally, considering a more symmetric yet less stable molecular structure has important implications on its spin properties, and prior works [78, 203, 206] could have suffered from the use of poor basis sets available at the time and the use of molecular force fields rather than *ab initio* methods. Molecular dynamics-based studies [207] using improved force-fields [208, 209] suggest the less symmetric point group  $C_3$  for the molecule as well. Thus, given the conflicting state of the literature on the one the hand, and the importance of the existence of highly symmetric Posner clusters in support of recent quantum biological hypotheses on the other hand, we were prompted to conclusively re-examine the structure of the PM.

Our work [14] conclusively proved that the PM exists as a dynamic ensemble of structures which is largely asymmetric, as will be detailed in later sections (See Section 5.3). However, given that all prior works [11, 16], until now, have considered the  $S_6$ -symmetric structure of the Posner molecule to make theoretical predictions on the entanglement times of the nuclear spin states and for examining the viability of the molecule as a potential biomolecular qubit, here [210], we explore if, and for how long,  $^{31}\text{P}$  nuclear spin coherences can be maintained for the multiple asymmetric configurations found in our work.

## 5.2 Computational methodology

For structural relaxation in our study, we used Quantum ESPRESSO and Q-Chem. Within Quantum ESPRESSO, we used the Standard Solid-State Pseudopotentials library [211, 212]

and the Perdew - Burke - Ernzerhof (PBE) exchange correlation functional. The Broyden - Fletcher - Goldfarb - Shanno (BFGS) algorithm was used for optimization of the structure. A unit cell of more than twice the size of the initial structure was used, and its geometry was subsequently relaxed. The Polarizable Continuum Model (PCM) for solvation was also used to understand the effects of solvation, if any, on structural relaxation of the Posner molecule. We used the conductor-like PCM [213, 214] for solvation with the Switching/Gaussian method. [215]. It was observed that solvation effects do not result in highly symmetric structures either. While working with Q-Chem for *ab initio* molecular dynamics (AIMD) calculations, both PBE and B3LYP exchange-correlation functionals were used, along with a basis set of 6-311G(d,p) for the atomic orbitals, which uses polarized basis functions. Canonical NVT sampling was done using AIMD with the Langevin thermostat. Noting that semi-local density functionals do not capture dispersion interactions properly, we also used dispersion-corrected functionals (the DFT-D3(0) dispersion correction from Grimme et. al. [216]) for some of our simulations. Different self-consistent field (SCF) iteration algorithms, such as Direct Inversion in the Iterative Subspace (DIIS) [217, 218] and Geometric Direct Minimization (GDM) [219] were used. Additionally, Pseudo-Fractional Occupation Number Method (pFON) was used, which is akin to introducing a finite electronic temperature, or smearing, in the system. For completeness, the symmetries were analyzed using two different toolkits, namely VMD and WebMO [220]. No difference in the results was observed.

### 5.3 The structural ensemble of calcium phosphate clusters

Since the PM is a calcium phosphate trimer, we performed initial simulations on the monomer  $\text{Ca}_3(\text{PO}_4)_2$  and dimer  $\text{Ca}_6(\text{PO}_4)_4$  configurations to validate our simulation setup. As detailed below, the symmetry of the optimized monomer structure agreed with previous studies [203, 206]. For the dimer, the work of Kanzaki et al. [206] was followed closely and many of

their structures were replicated. These results gave us confidence to pursue the structural symmetry of the PM.

### 5.3.1 Calcium phosphate monomers

A rough structure of a calcium phosphate monomer was first generated by hand. Once the monomer's structure was optimized using DL POLY [221], Quantum ESPRESSO, and Q-Chem, it always resulted in a structure with a molecular point group symmetry of  $D_{3h}$  as shown in Fig. 5.1. This is in agreement with other studies [203, 206] that have reported the geometry of a stable monomer structure.

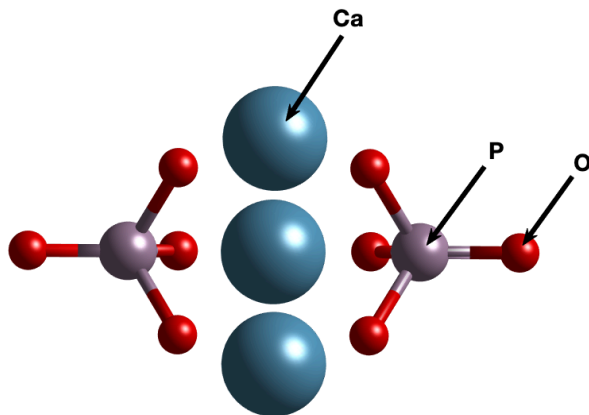


Figure 5.1: A calcium phosphate monomer exhibiting the expected  $D_{3h}$  molecular point group symmetry. The result was obtained using DL POLY, Quantum ESPRESSO, and Q-Chem, and is consistent with previous studies. The blue, purple, and red spheres represent Ca, P, and O atoms respectively.

### 5.3.2 Calcium phosphate dimers

When working with the dimer, which has a slightly more complicated structure than the monomer, some interesting features were observed. Earlier studies [206] have reported multiple possible geometries for the calcium phosphate dimer. To cover all possible geometries

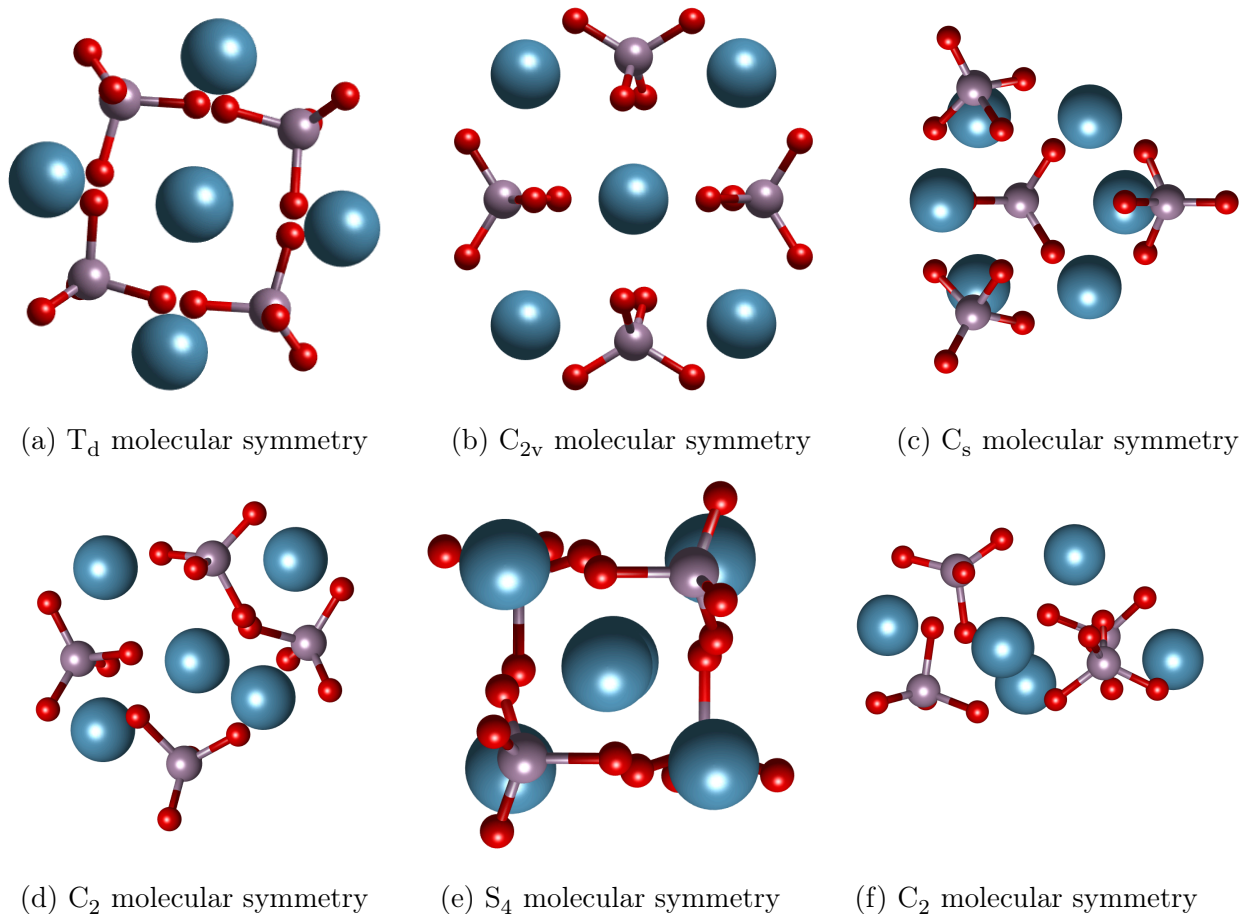


Figure 5.2: Some calcium phosphate dimer relaxed geometries obtained in our study. The methodology to obtain these structures was based on the results of Kanzaki et al.

and starting configurations, we created over 100 initial geometries that were then subjected to structural relaxation. The basic outline of our simulation setup was as follows. We first arrange the atoms in one out of several initial configurations. Based on suggestions in the work by Kanzaki et al. [206], the most common of these was to arrange the calcium atoms and the phosphate groups symmetrically around a cube of appropriate dimensions. The length of the diagonal of this cube effectively describes the approximate diameter of the molecule and thus, the dimensions were chosen accordingly. A large number of starting configurations were then obtained by independently rotating each phosphate group about the

phosphorus atom in steps of  $30^\circ$  while keeping the positions of the phosphorus and calcium atoms fixed. Another route to generating an initial configuration is to arrange the atoms in such a way that it has a structure similar to earlier findings, and to then perturb the structure. Subsequent to structural relaxation, we were able to obtain 6 of the 11 structures that have been reported before [206], with  $C_s$ ,  $C_2$ ,  $T_d$ ,  $C_{2v}$ , and  $D_{2h}$  point group symmetries, as shown in Fig. 5.2. However, Kanzaki et al. reported additional dimer structures that were not found using our methods. This could be because of an incomplete consideration of the structure space of the molecule, as well as the crudeness in the angle of rotation for the phosphate groups. Different starting configurations often led to different optimized final geometries — an artifact that was also later observed when studying the Posner molecule. Thus, we argue that a singular optimal structure does not exist, and that the calcium phosphate dimer possibly exists in a variety of symmetries. At this stage, it is also important to note that the relative energy differences between the structures obtained by us was not the same as have been reported by Kanzaki et al. For instance, even though the  $T_d$  point group symmetry (in agreement with Kanzaki et al.) was found to be the most stable symmetry, the relative energies between that structure and other symmetries differed by about 0.023 eV/atom on average.

### 5.3.3 Calcium phosphate trimers (Posner molecule)

Since the PM is hypothesized to exist in a variety of molecular symmetries [11, 203, 206], we set out to identify symmetric minima on the PES of the molecule. To cover an appreciable portion of the PES of the PM, we used various techniques to set up the initial atomic positions, and different analysis techniques to extract the relevant data, as detailed below.

Firstly, a wide variety of possible structures were created by modifying some of the techniques used in previous studies [206]. A schematic representation of the method can be seen in Fig. 5.3a. All atoms constituting the PM were arranged on a cube of appropriate dimensions. The nine Ca atoms were placed in a body-centred cubic arrangement and



the six  $\text{PO}_4$  groups in a face-centred cubic arrangement. The size of the cube was chosen such that the length of the diagonal was close to  $9\text{\AA}$ , which is the approximate diameter of the PM [11, 16, 222]. Countless configurations of the cluster can be realized by rotating each  $\text{PO}_4$  group around its center. In order to extensively sample the configuration space, the phosphate groups were rotated in steps of  $30^\circ$  in 3 dimensions to create over 2,800 structures. Additionally, the coordinates of the calcium atoms and the  $\text{PO}_4$  groups were scaled with reference to the central Ca atom to account for the possibility of some previously built structures being over-strained. This resulted in over 10,000 viable structures. In all cases, once the molecular structure was optimized using *ab initio* structural relaxation, the resultant configuration had low symmetry, *i.e.*, either  $C_s$ ,  $C_i$ , or no symmetry ( $C_1$ ). Fig. 5.3b shows the distribution of the observed symmetries of the relaxed structures obtained by the described strategy. It is evident that the PES of the PM is dominated by low symmetry structures.

Secondly, the atoms were arranged in relatively high symmetry configurations “by hand” without giving any consideration to the existence and initial stability of the structure, or to the forces on the individual atoms. The rationale was that since none of the previous structures resulted in one of the high-symmetry structures reported in earlier studies, the molecule might instead transition into one of these high-symmetry structures if the starting configuration was constrained in symmetry. Structures with symmetries such as  $S_6$ ,  $T_h$ ,  $C_{3v}$ , and  $D_{3d}$  were constructed. The molecular structures were perturbed slightly from their original symmetries and optimized. However, for all the four above-mentioned symmetries, when subjected to structural relaxation, the molecule failed to retain or increase the point-group symmetry and, instead, tumbled down to a low-symmetry structure –  $C_i$  or  $C_s$  – as was also the case in our previous approach. Structural relaxation with solvent effects included via a Polarizable Continuum Model (PCM) [213, 214] did not result in high-symmetry structures either. Finally, to verify that our results were not an artifact of the particular basis set, exchange correlation functional or simulation software in use, we repeated our calculations

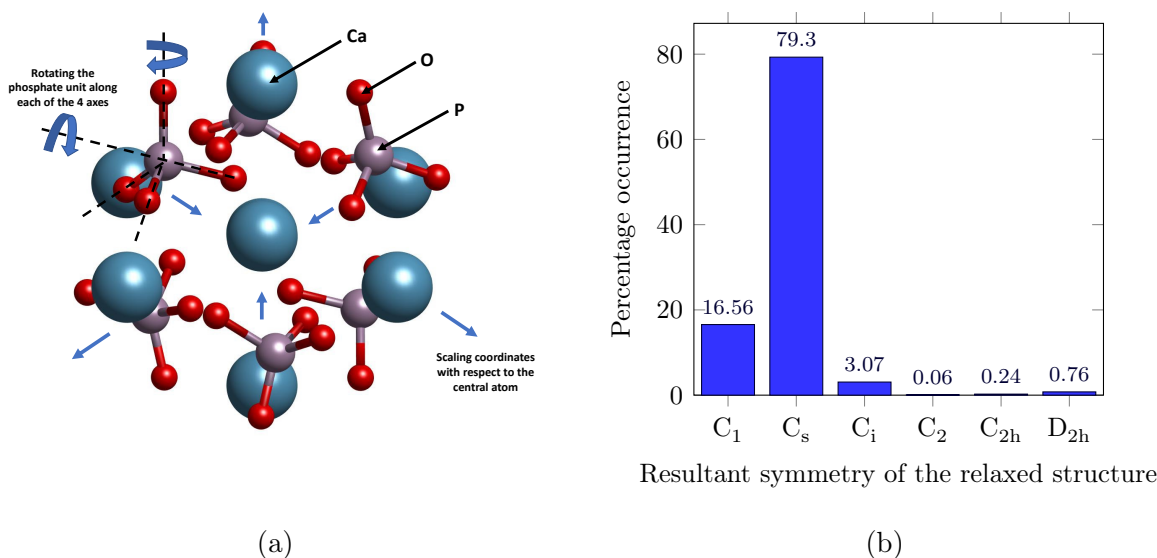


Figure 5.3: (a) The scheme used for creating over 10,000 structures by rotating the phosphate units and scaling all the coordinates with respect to central atom. The blue, purple, and red spheres represent Ca, P, and O atoms respectively. (b) Percentage occurrence of each point group symmetry after *ab initio* structural relaxation of over 10,000 initial structures (DFT with B3LYP hybrid functional and 6-311G(d,p) basis set).

using a semi-local exchange correlation functional and a plane-wave DFT code, and obtained very similar results.

Next, noting that the  $S_6$  symmetry has been so widely discussed and accepted, an  $S_6$  symmetric structure was built using an alternative technique. The phosphate units were considered as rigid tetrahedrals. The force field developed by Demichelis et al. [209] was used to model the atomic interactions. Imposing the  $S_6$  symmetry enables the parameterization of the structure in terms of 10 parameters. Following a symmetry constrained global minimization of the system's energy based on the above parameters, a unique structure was obtained. Using DFT with the B3LYP hybrid functional and a 6-311G(d,p) basis, it was identified as a transition state structure, and subjected to further geometrical relaxation. The optimized structure exhibited a  $C_i$  symmetry – starkly lower in symmetry than the

initial  $S_6$  symmetry. When performed under constrained symmetry, the same *ab initio* geometrical relaxation calculation failed to reach self-consistency. Thus, the optimization of symmetric structures modeled on existing force fields also failed to produce stable structures with low symmetries.

As our exhaustive search using structural relaxation failed to identify symmetric species, we then studied the dynamical properties of eight semi-stable Posner structures by *ab initio* molecular dynamics (AIMD). Starting structures were obtained from the supposedly minimum energy structures in [203], resymmetrized and subjected to *ab initio* structural optimisation (using DFT with the B3LYP hybrid functional and the BP86/Def2TZVPP/W06 basis set). At the end of the relaxation procedure, they had low forces on the atoms (of the order of  $10^{-4}$  eV/Å). However, these structures did not correspond to energy minima, but were transition states of higher order instead. Distorting these structures along the normal modes associated with imaginary frequencies followed by further optimization of these structures resulted in the molecule tumbling to lower symmetries, as did the formation of these structures without the symmetry constraints. We considered the 8 unique molecular structures derived through the above procedure. These, along with the corresponding molecular point group symmetries, as obtained by the Visual Molecular Dynamics (VMD) software [223] are displayed in Fig. 5.4.

We also performed vibrational spectrum calculations on these eight transition state structures, and compared them with an existing spectrum [11] reported in a study that considered the  $S_6$  symmetric structure to be the prototypical structure for the Posner molecule. The results can be seen in Fig. 5.5. The two spectra match closely up to a constant value of shift on the frequency axis. This shows that the structures considered in our study and in the Swift et al. study are quite similar in nature, up to the extent of bond stretching and rotation. However, the replication of the IR spectrum was only found in two cases. Moreover, the similarity in IR spectra is not necessarily translated to a similarity in the spin properties of the corresponding structures.

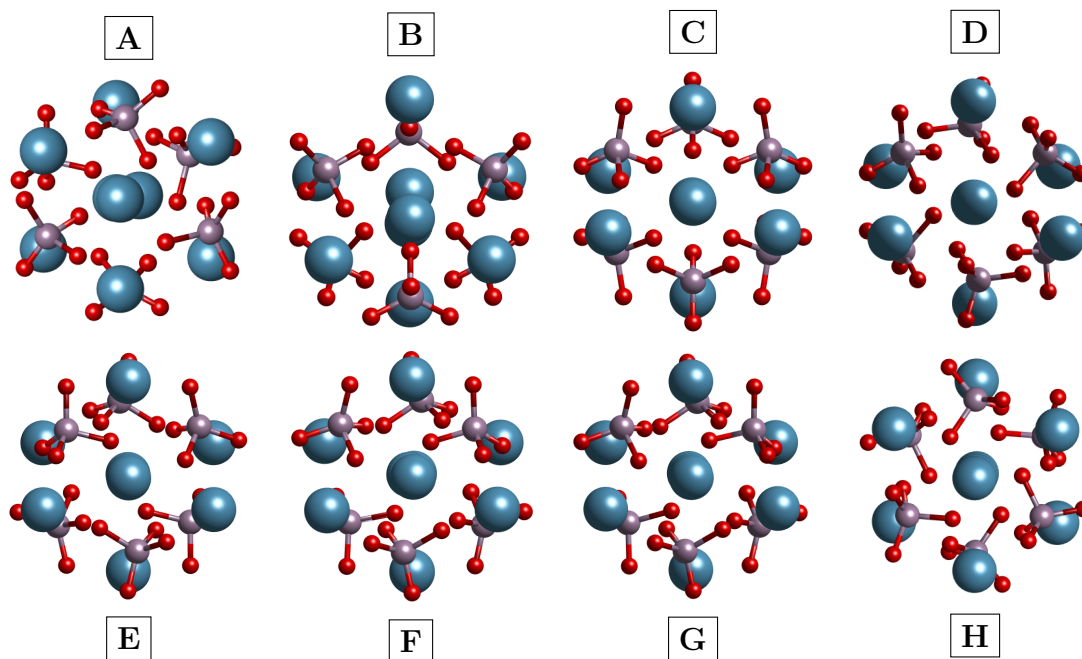


Figure 5.4: The eight different structures that were used as starting geometries for dynamical simulations of the PM. The labels (A–H) used in the manuscript are stated.

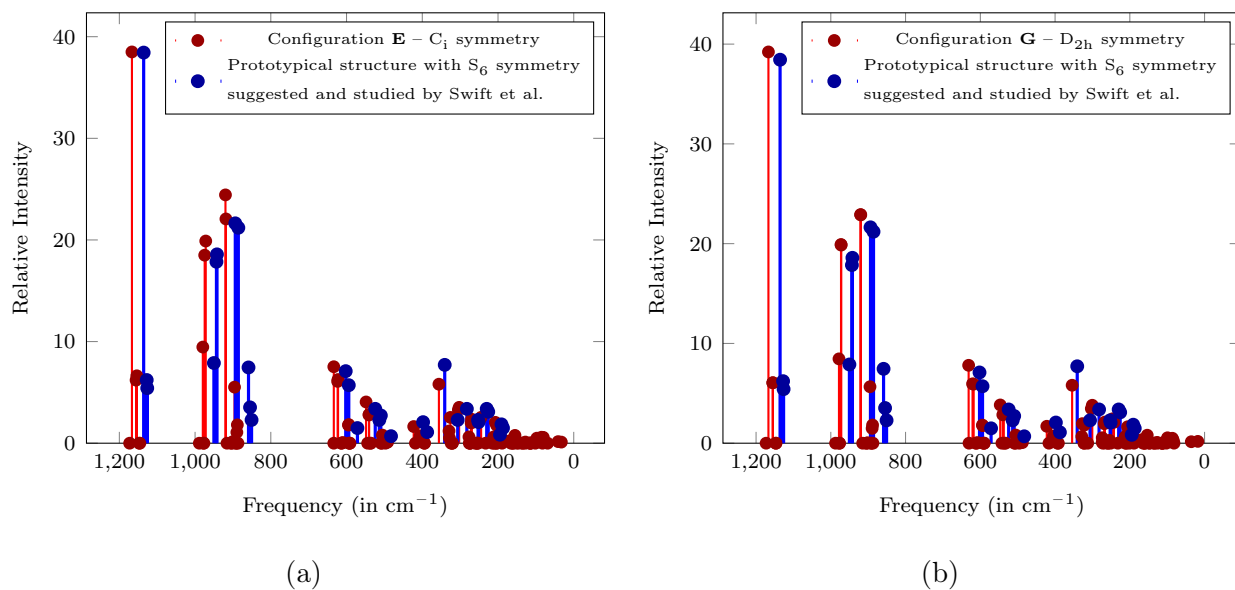


Figure 5.5: Comparison between the IR spectra of the structural configuration E and G used in this study, and of that obtained by Swift et al. [11].

The eight transition state structures were then studied by AIMD using the same basis set and DFT functional as above, at two different temperatures,  $298K$  (room temperature) and  $315K$  (at the higher end of human metabolic temperatures), to see if they maintain their high symmetry or give rise to high-symmetry species in the time average. The molecules were allowed to evolve for a total time of about 24 ps, in which the first 1.2 ps – or the first 5% of the total time – were considered to be the equilibration phase of the molecule, and were not considered for subsequent analyses. Given that the lowest non-zero vibrational frequency mode in Fig. 5.5 (equal to  $100\text{ cm}^{-1}$ ) corresponds to a frequency of 3 THz — or a time scale of 0.334 ps — the above duration of the AIMD simulations were thought to be sufficiently long to allow for adequate structural averaging. The molecule is expected to go through its vibrational relaxation pathways within the time duration considered for our *ab-initio* molecular dynamics simulations. Note further that the energy differences suggested for  $S_6-C_1$ ,  $S_6-C_2$  and  $S_6-C_1$  transitions from Refs. [11, 78, 203] are comparable to the thermal energy. Thus, the transition process is not expected to be a rare event, but is likely to proceed on the timescale of vibrations. Within these assumptions, the studied timescale is certainly sufficient to accommodate the envisaged structural reorganizations. A practical constraint that has to be noted is the balance between accessible simulation timescales and the computational resources consumed, due to the expensive nature of the *ab initio* calculations.

At the end of each of the eight dynamical runs, and at both the above-mentioned temperatures, the PM exhibited either a  $C_s$  or a  $C_1$  point group symmetry. Thus, it was understood that, even if the molecule is forced to exist in a relatively higher symmetry state, as imposed by our method, it will naturally tumble down to one of the lower symmetry states within picoseconds, as is also evident from Table 5.1. This leads us to argue that any stable configuration of the PM is likely to exhibit lower symmetries at room temperature.

Time averages and temporal variations in the molecule’s symmetry were then studied as

Transition structure index	Symmetry prior to the creation of transition structure	Transition structure point group symmetry	Formation energy (in $eV$ ) of the transition structure	Resultant symmetries over dynamical runs
A	$C_s$	$C_s$	-271.660	$C_1, C_2, C_s, D_{2h}$
B	$C_{3v}$	$C_{3v}$	-269.555	$C_1, C_2, C_s, C_{2h}, C_{3v}, D_{2h}$
C	$D_{3d}$	$D_{3d}$	-264.997	$C_1, C_s, C_i, T, C_{2h}, D_{2h}, D_{3d}$
D	$D_{3d}$	$C_{2h}$	-269.551	$C_1, C_s, C_i, T, C_{2v}, C_{2h}, D_{2h}$
E	$S_6$	$C_i$	-271.552	$C_1, C_s, C_i, C_2, T, C_{2h}, D_{2h}$
F	$S_6$	$C_i$	-271.540	$C_1, C_s, C_i, T, C_{2h}, D_{2h}$
G	$S_6$	$D_{2h}$	-271.239	$C_1, C_s, C_i, T, C_{2h}, D_{2h}, O_h$
H	$T_h$	$D_{2h}$	-269.531	$C_1, C_s, C_i, C_2, C_{2v}, C_{2h}, D_{2h}$

Table 5.1: The point group symmetries for each of the structures in Fig. 5.4, their formation energies, as well as the point group symmetries displayed by each configuration during a dynamical simulation/evolution over 22.8 ps. In comparison, the formation energy for a monomer calcium phosphate was calculated to be  $-84.244 eV$ . The listed formation energies of all trimer configurations are lower than three times this value.

it appeared plausible that the molecule might exhibit a symmetric structure in the temporal average. Specifically, we studied the point group symmetries and energies of the  $\mathcal{N} = 9,500$  structures generated during each AIMD run. This allowed us to infer time persistence of the molecule’s symmetry, if present. We observed that the molecule does indeed exhibit a variety of symmetries within the time frame considered, as visualized in Fig. 5.6a and Fig. 5.6b. However, the higher symmetries were observed only fleetingly, i.e. on time scales of the order of 100 fs — too short to be significant, both as an independent species, or to markedly determine the average structure. This supports our claim that the PM prefers to exist in low molecular symmetries. Moreover, as exemplified by Fig. 5.6, we can say that the behavior described above of low symmetry configurations throughout the dynamic evolution

is consistent among all the eight unique structures in Fig. 5.4. For brevity, only details on two of the eight structures has been shown here, but similar results on all the eight structures can be found in [14].

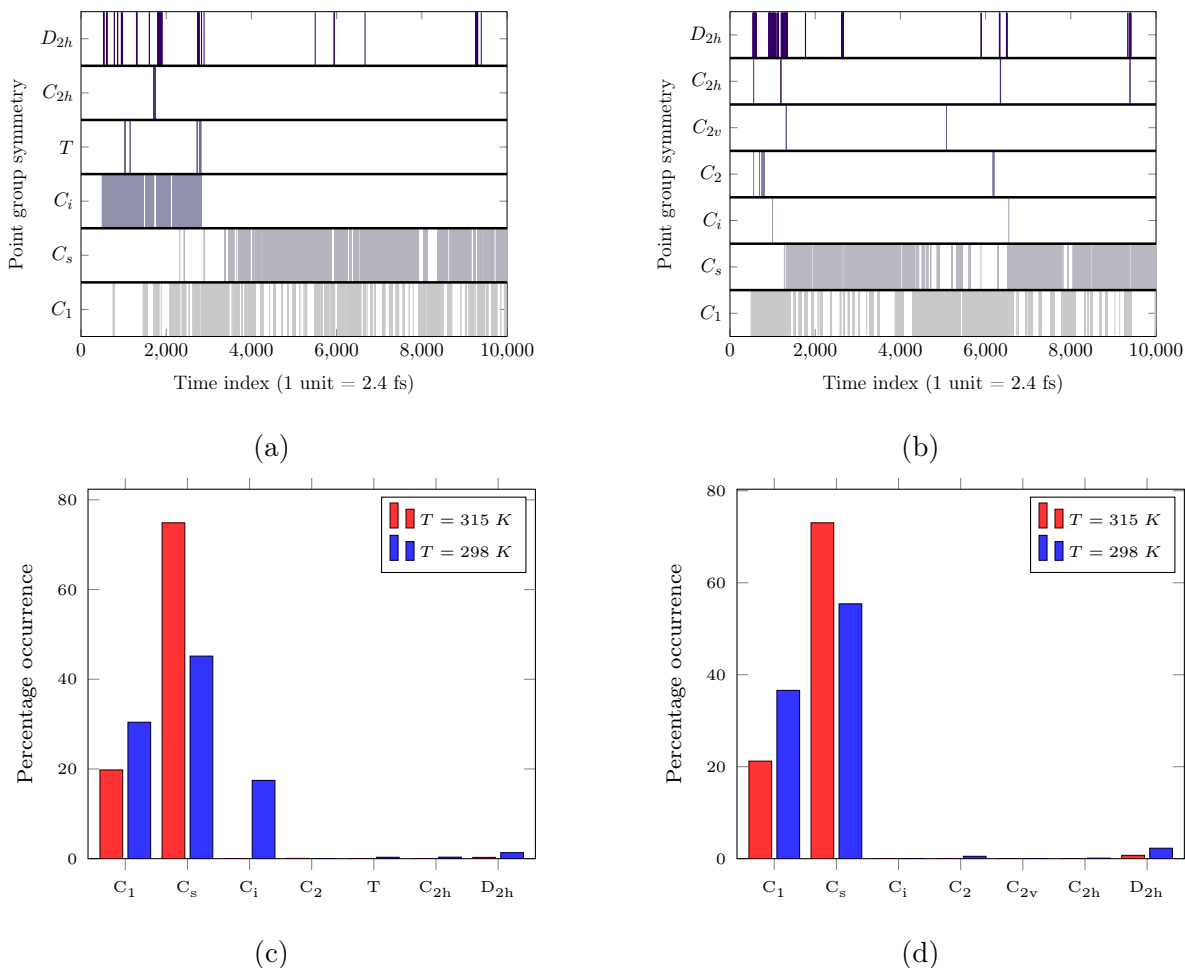


Figure 5.6: Time persistence of symmetries and the associated frequency of occurrence of each symmetry for two different starting configurations over a dynamical run. In the above figure, (a) and (c) represent the data for configuration **C**, whereas (b) and (d) represent data for configuration **H**. Note that (a) and (b) represent the data at  $T = 298 K$ , and thus some additional symmetries which were observed at  $T = 315 K$  are not present in these plots.

Even if the PM exhibits higher symmetries only fleetingly, it may *appear* as a more symmetric structure in the time average. To test this possibility, time-averaged structures

for entire dynamical runs were created and studied. To this end, the translational and rotational motion of the molecule was eliminated via a rigid-body realignment procedure, and the aligned  $\mathcal{N}$  structures averaged. A single point calculation was realized for these time-averaged structures and their energies were compared. In addition to averaging all the  $\mathcal{N}$  structures, an average structure was also obtained for subsets of potentially higher symmetry structures in the dynamic runs, which we define as the most symmetric molecular point group observed in a single dynamical run – e.g.,  $D_{2h}$  for the cases of Fig. 5.6a and Fig. 5.6b. Specifically, the subset of structures chosen for averaging from the entire range of these high-symmetry phases of structures were the longest consecutively occurring group of structures. For instance, in Fig. 5.6b, this would correspond to the group of  $D_{2h}$  structures located just after the 1000<sup>th</sup> time index. Note that we refrained from obtaining an average structure for all of the high-symmetry structures because different high-symmetry structures might have emerged throughout the AIMD runs. Fig. 4 provides a representation of the energy distributions over the AIMD runs together with a comparison of single-point energies and point group symmetries of the time-averaged structures. It can be seen that the energy spread between all averaged structures is relatively small – about 1.36 eV on average. Whenever the  $\mathcal{N}$  intermediate structures were averaged, regardless of the initial configuration of the molecule, the point group symmetry of the averaged structure was either  $C_1$ ,  $C_i$ , or  $C_s$ , which, for the purposes of this study, have been considered as “low symmetries”. Their energies are shown as blue dots. This further reinforces the hypothesis that the PM prefers to exist in lower point group symmetries at any time as well as on average, at biologically relevant temperatures. Additionally, when looking at the energies of only the temporary high-symmetry phases of the PM which, in Fig. 5.7, have been represented by the semi-transparent violin plots overlayed on top of the opaque plots which represent the energies of the entire dynamical run, one can see that the energy of the structures with a higher symmetry is higher than the average energy which agrees with our claim. However, seemingly in contrast to the above observation, we observe that the time-average structure



of the higher symmetry phase can have a lower energy than the time-average structure of the entire dynamical run. This, however, can be explained by the fact that in every studied case, the time-averaging of even a high-symmetry phase yielded a structure with low ( $C_1$  or  $C_s$ ) symmetry. Thus, the lower energy individual structures always possess low symmetries and the data do not invalidate the claim that lower symmetries are preferred. We also mention in passing that we have carried out our point group symmetry analysis using more than one software package (VMD and WebMO [220]) and using different symmetry thresholds as well. However, we obtain similar results. For brevity, these results have not been presented here but can be found in our complete work [14].

Based on the above analyses, we identify the most stable structure of the PM to be the overall time-average structure of the configuration **A**, which can be seen as a blue dot in Fig. 5.7. Notably, the point group symmetry for this structure is  $C_1$ , *i.e.*, no symmetry. At the same time, we reiterate that the PMs possibly exists in an ensemble of structures, and that identifying a singular structure as the dominant PM structure is incorrect. More information about configuration **A** and its atomic coordinates can be found in [14].

With our calculations unable to convincingly point us towards a PM structure with high symmetry, we performed PCA on the data from the dynamical runs. It was expected that, if the molecule exhibits any kind of high symmetry that might have been overlooked in our symmetry analysis methodology, the associated high symmetry structure would show up as one of the dominant eigenmodes of the PCA. However, none of the dominant eigenmodes displayed any kind of high symmetry. In fact, in all cases, the eigenmodes had either a  $C_1$  or a  $C_s$  point group symmetry. Moreover, as can be seen in Fig. 5.8a, Fig. 5.8c, and Fig. 5.8e, each configuration yielded one predominant eigenmode. Similar plots and figures for all dynamical runs can be found in [14]. While the maximum displacement of an atom in this mode from its corresponding position in the time-average structure over the entire dynamical run was small – less than  $0.3\text{\AA}$  – this mode, instead, reflected a more appreciable displacement of the phosphates due to their rotation. Structures corresponding to the first three dominant

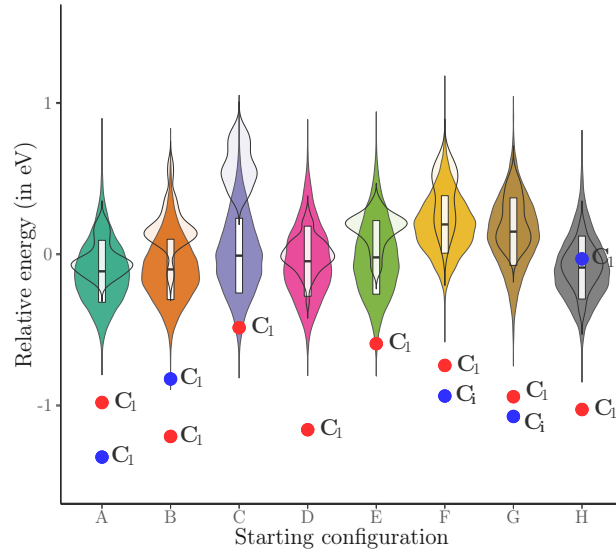


Figure 5.7: The energy spread of the dynamical runs for each of the starting configurations listed in Fig. 5.4 represented by kernel density estimations in the form of vertical violin plots. The blue dots represent the energy of the time-average structure over the entire dynamical run, and the red dot represents the energy of the time-average structure of that subset of the high symmetry phase that is present for the longest continuous duration. The point-group symmetry of the averages is indicated next to the symbols. The semi-transparent overlays on each of the violin plots represent the energy distribution for the entire high symmetry phase. The most stable high symmetry phase for each of the cases were  $D_{2h}$ ,  $D_{2h}$ ,  $C_{2h}$ ,  $D_{2h}$ ,  $C_{2h}$ ,  $D_{2h}$ ,  $D_{2h}$ , and  $D_{2h}$ , respectively. Dots missing from the graph were found at energies higher than the scale of the figure. The plot also shows the mean and standard deviation of the energy spread within the representations of probability density functions in the form of white boxes. The energies reported are within the numerical accuracy of the method and basis set used. [12, 13]

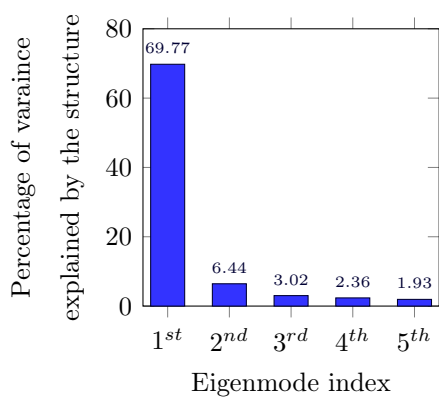
modes did not give way to higher symmetries. The small observed fluctuations, as visualized in Fig. 5.8b, Fig. 5.8d, and Fig. 5.8f as arrows that have been multiplied threefold for clarity, further emphasize that considering an average structure over our dynamical data set was

appropriate. A detailed PCA analysis for all other considered structures is provided in [14].

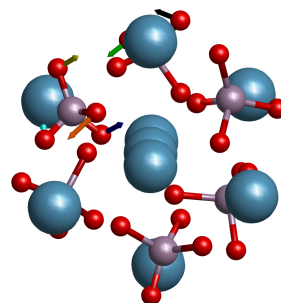
Lastly, we resorted to another powerful data analysis technique, namely  $k$ -means clustering, to identify hidden patterns in the data generated from our dynamical runs that might not have been revealed by our earlier attempts. It was found that, for each of the eight starting configurations, the ideal number of clusters describing our data sets was 2, and that the associated mean structure for each cluster had low point group symmetry –  $C_1$  or  $C_i$ . This further agrees with the data and analyses that have already been presented above, and with our assessment that the PM mostly exists as an ensemble of low-symmetry structures.

Our extensive analysis of the dynamical and structural properties of the Posner molecule suggests that it predominantly exists in low symmetry molecular structures such as  $C_s$ ,  $C_i$  and  $C_1$  at room temperature, as opposed to the results of previous studies suggesting a prototypical  $S_6$  symmetric structure. Moreover, the initial configuration of the molecule often dictates the geometric configurations through which the molecule transitions during a dynamical run. Most of these transition structures exhibit low molecular point group symmetries; the high symmetry phases are found to be present only fleetingly and have thus been assumed to be unimportant. Average structures were also found to be of low symmetry. Our results indicate that that the molecule does not naturally exhibit a three-fold axis of rotation, such as present in  $S_6$ , in vacuum or in a homogenous solvent. We follow this with the calculation of spin-spin coupling constants and spin coherence times for the structures explored by us above in [210] in the following sections.

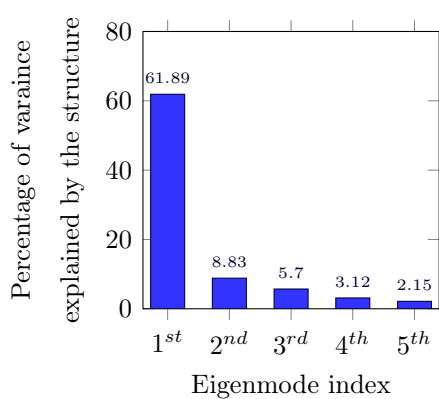
Lastly, we suggest the possibility of experimental verifications of our results. It may well be possible to establish the existence of Posner molecules in simulated body fluids by introducing the constituents at stoichiometric ratios. Imaging techniques such as Dynamic Light Scattering or Transmission Electron Microscopy and NMR spectroscopy could then be applied to observe/study the basic properties of these molecules [15]. However, we believe that more sophisticated techniques, possibly following established quantum optics protocols and using microfluidics, might be needed to assess the possibility of the Posner molecule



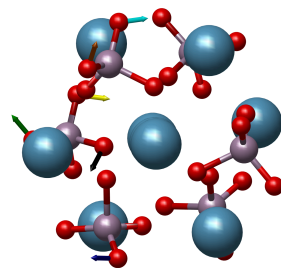
(a)



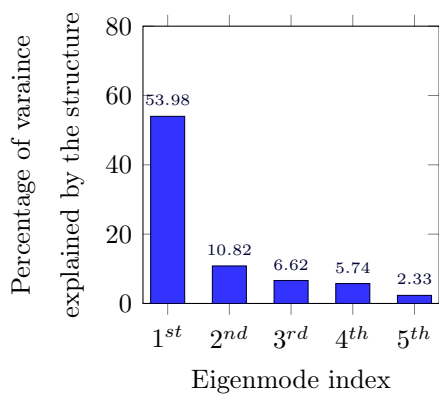
(b)



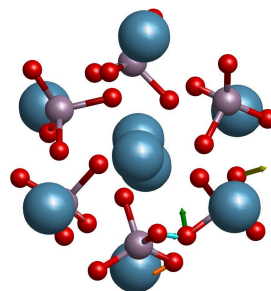
(c)



(d)



(e)



(f)

Figure 5.8: (a), (c), (e) Eigenvalues resulting from PCA over a single dynamical run for configurations **E**, **D**, and **B** respectively. (b), (d), (f) Difference between the most dominant eigenmode and the time-average structure of the corresponding dynamical run.

sustaining  $^{31}\text{P}$  qubit states.

## CHAPTER 6

# Nuclear spin coherence lifetimes in calcium phosphate clusters

With an exhaustive set of structures for the PM, we now turn our attention to if, and how, the asymmetrical nature of the dynamical ensemble of the PM affects nuclear spin coherence lifetimes in pairs of molecules. Keeping Fisher’s original proposal in mind [11, 15], and closely following the work by Player et al. [16], one of the simplest measures to assess the pertinent spin coherences in pairs of PMs or calcium phosphate clusters is the temporal evolution of the (maximally entangled) singlet state for a pair of  $^{31}\text{P}$  nuclei in identical, spatially-separated Posner molecules, with the remaining ten uncorrelated nuclear spins serving as background (see Fig. 6.1). In this arrangement, the evolution of the singlet probability over time serves as a measure of conservation of quantum correlation among the Posner molecules, and can be calculated for a variety of structural configurations of the molecule. Eventually, for the thermalized spin system, the singlet probability will settle down to  $1/4$  — the value expected for a maximally mixed state. A value of the singlet probability greater than  $1/2$  indicates that entanglement is maintained (*i.e.*, a mixed state of singlets and unpolarized triplet states in which more than 50% of the spins are in a singlet state, is entangled) [16]. Additionally, the two-qubit concurrence [16, 224] between the  $^{31}\text{P}$  nuclear spin pairs serves as a direct measure of entanglement. A value of one indicates a maximally entangled state; a value of zero indicates total loss of entanglement. A priori, we expect that the absence of symmetry in the Posner molecule will increase the number of unique scalar spin-spin couplings ( $J$ -couplings) in the coupling network [196, 197] which, as we

explain later, dominate the coherent spin dynamics for this system. A large number of unique coupling constants implies a large number of unique frequencies that characterize the coherent evolution of the singlet probability. In turn, this is expected to accelerate the decay of the singlet probability through destructive interference in our model [16, 198, 199]. Here, we address if this accelerated decay of spin correlation is realized for all structures of the ensemble, and if this is detrimental to the Fisher’s proposal of calcium phosphate-mediated quantum information processing in neurons. Note that our detailed discussion on the link between the symmetry of the Posner molecule and the longevity of the singlet state is motivated by the importance given to the former as a key ingredient for the theory of Posner-mediated neural processing [11, 15]. However, as we show later, our calculations on the tricalcium biphosphate dimers and subsequent analysis shown in additional sections (See Sections 6.7 and 6.5) suggest that while the symmetry of the molecule and its coupling constant values are certainly relevant, the longevity of the singlet state is primarily dictated by the number of coupled nuclear spins, i.e., the number of  $^{31}\text{P}$  atoms.

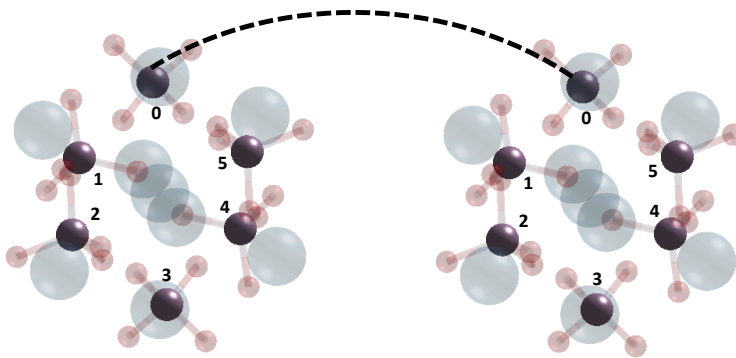


Figure 6.1: A pair of  $^{31}\text{P}$  nuclei, namely the pair labeled  $(0, 0)$ , entangled and initialized in the singlet state in two separate but identical Posner molecules. The separation between the molecules, although arbitrary, is large enough for intermolecular interactions between the  $^{31}\text{P}$  nuclear spins to be negligible. The entanglement between the nuclear spins has been depicted by a dotted line.

Using an  $S_6$  molecular point group symmetry for the Posner molecule, which renders

the six  $^{31}\text{P}$  nuclei magnetically equivalent, a singlet relaxation time of 37 minutes has been calculated previously by Player et al. [16]. The authors of that work, while refining the original estimate of 21 days for the entanglement lifetime of nuclear spin states [11, 15], acknowledge that the singlet state may relax even faster due to various interactions present in realistic scenarios. Here, we calculate the singlet probability for a pair of  $^{31}\text{P}$  nuclear spins due to their coherent evolution in the presence of dominant relaxation mechanisms. Our approach closely follows the above reference [16], but is extended to explicitly include spin relaxation in the calculation. Unlike the above work, however, which analyzed only a couple of symmetric structures, while using coupling constants from Ref. [11] (calculated for a different  $S_6$ -symmetric structure), we aim to explore the full ensemble of symmetric and asymmetric structures. To this end, and because the  $J$ -coupling constants are expected to be different for each structural configuration of the molecule, we estimate the coupling constants for all investigated structures through first principles calculations. We contend that our calculations and findings are more directly relevant to investigations of the viability of Fisher’s proposal, than earlier studies.

Lastly, given that the structures of the calcium phosphate monomer,  $\text{Ca}_3(\text{PO}_4)_2$ , and the dimer,  $\text{Ca}_6(\text{PO}_4)_4$ , are more conclusively known [14, 206], we also performed similar calculations on these structures and found extremely long-lived singlet states, irrespective of the symmetry of the molecule, for the case of the dimer. Their presence *in vivo* has not yet been considered, but is something that invites thorough future investigation.

## 6.1 Computational methodology

The calculation of the coupling constants between the  $^{31}\text{P}$  nuclei is a critical part of the study, and was done using the ORCA program [225]. More specifically, we used the B3LYP exchange-correlation functional, along with basis sets specifically built for the calculation of NMR coupling constants. For the P and O atoms, we used the pcJ-2 basis set [226]



(the largest such basis set that we could afford within computational constraint limitations), whereas the pcseg-2 basis set [227] was used for the Ca atoms, because the pcJ-n basis sets are not supported for atoms beyond Ar. Both these basis sets are polarization consistent. The chemical shielding tensors needed for including the chemical shift anisotropy effect were calculated using Gaussian [228] using the cc-pV5Z basis set. Following the calculation of the scalar coupling constants and the chemical shielding tensors, we simulated the spin dynamics of the  $^{31}\text{P}$  nuclear pairs, and calculated the singlet probabilities and the concurrences. The matrix representations of the various operators needed for this calculation were constructed using the QuTiP [229] library. A singlet state consisting of corresponding  $^{31}\text{P}$  nuclei in separate but identical Posner molecules was evolved through time, much like in Ref. [16]. For the molecular dynamics (MD) simulations, we used the LAMMPS software [230]. Following the work of Demichelis et al. [209], we placed the Posner molecule in a box of length 56 Å, with  $\sim 4000$  water molecules. The force fields introduced in Ref. [209] were used. The canonical NVT ensemble was utilized at a temperature of 300 K, with a timestep of 0.1 fs. The atoms were initially given a Gaussian-distributed velocity corresponding to a temperature of 300 K, and the initial linear momentum of the Posner molecule was set to zero. Following the MD simulation that proceeded for a total of 340790000 timesteps (equivalent to 34.07 ns), the trajectory was analyzed to calculate the rotational correlation constant,  $\tau_c$ , and the translational diffusion constant of the molecule. The Visual Molecular Dynamics (VMD) software [223] was used for calculating the point group symmetries of relevant molecular structures.

## 6.2 Setting up the spin Hamiltonian

We consider the coherent evolution of the six  $^{31}\text{P}$  nuclear spins in each Posner molecule subject to the spin Hamiltonian  $\hat{H}_0$ , where:

$$\hat{H}_0 = \omega_0 \sum_k \hat{I}_{k,z} + 2\pi \sum_{j < k} \sum_k J_{jk} \hat{I}_j \cdot \hat{I}_k . \quad (6.1)$$

Here,  $\omega_0 = -\gamma_k(1 - \sigma)B$  is the Larmor frequency of the  $^{31}\text{P}$  nucleus;  $\sigma$  is the isotropic chemical shielding constant;  $\hat{I}_k$  is the spin angular momentum operator for nucleus  $k$ ;  $\hat{I}_{k,z}$  is the  $z$ -component of the spin angular momentum operator; and  $J_{jk}$  is the scalar coupling constant between nuclear spins indexed  $j$  and  $k$ . The first term accounts for the Zeeman interactions, whereby differences in the chemical shielding will be assumed to be negligible in the low magnetic field considered. The second term corresponds to the intramolecular scalar spin-spin coupling interactions, characterized by the coupling constants  $J_{jk}$ . Since the evolution of the singlet probability and entanglement of pairs of spins are strongly dependent on the scalar coupling constants, it is critical to obtain accurate values of  $J_{jk}$ . Moreover, the coupling constants differ for each molecular structure. Here, the  $J_{jk}$  values have been derived from DFT calculations for every molecular geometry using the pcJ-n basis set [226], built specifically for the calculation of these interaction constants, for P and O atoms. The pcseg-n basis [227] set, optimized for the calculation of nuclear magnetic shielding, was used for the Ca atoms. We remark that the values obtained by us are appreciably different from those reported, and used, in earlier studies [11, 16]. Our use of an optimized method and of a more accurate and specialized basis set for each atom gives us confidence in the preciseness of constants employed for the calculations reported here.

Molecular motion modulates the spin Hamiltonian, which induces spin relaxation. Here, we discuss possible relaxation pathways such as intra- and intermolecular dipole-dipole interactions, chemical shielding anisotropy (CSA), dipolar coupling with the solvent, and spin-rotation relaxation. The first of these (i.e. intramolecular dipole-dipole interactions) is expected to be the dominant relaxation pathway for rapidly and independently rotating dilute Posner molecules in the geomagnetic field ( $\sim 50 \mu\text{T}$ ). Based on a simple estimate of spin-lattice relaxation times due to the modulation of the dipolar coupling by translational and rotational diffusion, the (concentration-dependent) intermolecular dipolar relaxation is expected to be slower than the intramolecular relaxation for concentrations of up to 7 mol/L (!). The CSA contribution is generally relevant in strong magnetic fields and can be consid-

ered negligible in the geomagnetic field, as is the case here (our estimates suggest a marked influence of CSA relaxation only for fields larger than 1 T). Any dipolar coupling with the solvent is expected to average out to zero in the presence of rapid, independent tumbling motion of the molecule. Finally, spin-rotation relaxation, which is thought to be the dominant relaxation mechanism for pyrophosphates [231, 232], is neglected here under the assumption that the standard deviation in the angular velocity is expected to be much smaller for the larger Posner molecule. Of all these pathways then, the intermolecular contribution is clearly negligible at reasonable concentrations, and the dominant relaxation is induced by the 15 pair-wise intramolecular dipolar nuclear spin couplings, the detailed form of which can be found in the following section.

### 6.2.1 Intramolecular dipole-dipole interactions between $^{31}\text{P}$ nuclear spins

The dominant relaxation mechanism considered here is the intramolecular dipole-dipole interactions. As highlighted in the main text, the intermolecular dipole-dipole interactions, dipolar coupling with the solvent, and spin-rotation relaxation have all been considered to be negligible and not included in our calculations. The chemical shielding anisotropy (CSA) contribution, although negligible in the geomagnetic field, has been included. The intramolecular dipole-dipole interactions for the 15  $^{31}\text{P}$  pairs is given by:

$$\hat{H}_{iDD}(t) = - \sum_{j < k} \sum_k \frac{\mu_0 \gamma_j \gamma_k \hbar}{4\pi |\mathbf{r}_{jk}|^3} \left( \hat{I}_j \cdot \hat{I}_k - \frac{3}{|\mathbf{r}_{jk}|^2} \left( \hat{I}_j \cdot \mathbf{r}_{jk} \right) \left( \hat{I}_k \cdot \mathbf{r}_{jk} \right) \right) \quad (6.2)$$

where  $\theta$  is the angle made by the vector  $\mathbf{r}_{jk}$  joining the two nuclear spins with the  $z$ -axis. Here,  $\gamma_k$  is the gyromagnetic ratio of the  $^{31}\text{P}$  nucleus,  $\hat{I}_k$  is the spin angular momentum operator for nucleus  $k$ , and  $\hat{I}_{k,z}$  is the  $z$ -component of the spin angular momentum operator.

### 6.3 Calculation and evolution of the singlet state

We calculate and evolve the singlet state as follows. Indexing the  $^{31}\text{P}$  nuclear spins in two separate Posner molecules,  $A$  and  $B$ , from  $0_{(A,B)}$  through  $5_{(A,B)}$ , we assume that, without loss of generality, the system is initialized in a state with spins  $0_A$  and  $0_B$  in the maximally entangled singlet state, while the ten other spins are uncorrelated. We represent this singlet state as  $|S_{0_A,0_B}\rangle = \frac{1}{\sqrt{2}}(|\alpha_{0_A}\beta_{0_B}\rangle - |\beta_{0_A}\alpha_{0_B}\rangle)$ , where  $|\alpha\rangle$  is the spin-up state, and  $|\beta\rangle$  is the spin-down state. Thus, the initial state density operator is proportional to the singlet projection operator, given as:

$$\begin{aligned}\hat{P}_{0_A,0_B} &= \sum_{\gamma \neq (0_A,0_B)} |S_{0_A,0_B}; \gamma\rangle \langle S_{0_A,0_B}; \gamma| \\ &= |S_{0_A,0_B}\rangle \langle S_{0_A,0_B}| \otimes \mathbb{1}.\end{aligned}\tag{6.3}$$

Here  $|S_{0_A,0_B}; \gamma\rangle = \frac{1}{\sqrt{2}}(|\alpha_{0_A}\beta_{0_B}\rangle - |\beta_{0_A}\alpha_{0_B}\rangle) \otimes |\gamma\rangle$ , and  $|\gamma\rangle$  is any of a set of states such that  $\sum_{\gamma \neq (0_A,0_B)} |\gamma\rangle \langle \gamma| = \mathbb{1}$ , *i.e.*, it assembles the maximally mixed spin state of the other 10 nuclear spins. The singlet probability  $p_{0_A,0_B}(t)$  is given by  $\text{Tr}[\hat{\rho}(t)\hat{P}_{0_A,0_B}]$  with  $\hat{\rho}(0) = \hat{P}_{0_A,0_B}/\text{Tr}(\hat{P}_{0_A,0_B})$ . To obtain the evolution of  $p_{0_A,0_B}(t)$  through time, we solve the Liouville-Neumann equation [233]:

$$\frac{d\hat{\rho}(t)}{dt} = -i\hat{L}\hat{\rho}(t),\tag{6.4}$$

where the Liouvillian superoperator  $\hat{L}$  is given by  $\hat{H}_0 + i\hat{\Gamma}$ , with the relaxation superoperator  $\hat{\Gamma}$  given, in the extreme narrowing limit applicable to fast rotational motion, by  $-\langle \hat{H}_1(t)\hat{H}_1(t) \rangle \tau_c$  [16]. Here, double hats denote the commutator superoperator of the operators in question, and  $\tau_c$  is the rotational correlation constant of the molecule.

To validate the form of the relaxation superoperator, we have calculated the rotational correlation constant of the molecule from molecular dynamics (MD) simulations. Closely following the work by Demichelis et al. [209], we simulated the Posner molecule in a box of water molecules and followed its trajectory over 34 ns (*i.e.*, at the simulation limits of computational resources available), using LAMMPS [230]. Details about the simulation have

been provided earlier (See Section 6.1). A value of  $\tau_c \sim 177$  ps was obtained by analyzing the rotational correlation function in 3 dimensions. Thus, we find a slower rotational dynamics (by roughly a factor of 3) compared to the previous estimate by Player et al. [16], which uses the approximate Stokes-Einstein-Debye relation. The value derived here is still well within the extreme narrowing limit, thus justifying the form of  $\hat{\Gamma}$ . Details about the calculation of the two-qubit concurrence [16, 224],  $\mathcal{C}_{0_A,0_B}$ , can be found in the following section.

### 6.3.1 Calculation of concurrence

In addition to the evolution of the singlet state between pairs of  $^{31}\text{P}$  nuclear spins, we also study the evolution of the two-qubit concurrence for a given pair. This acts as a measure of entanglement, and is calculated as [16, 224]:

$$\mathcal{C}_{0_A,0_B} = \max(0, \lambda_1 - \lambda_2 - \lambda_3 - \lambda_4) \tag{6.5}$$

where  $\lambda_i$  are the eigenvalues of the matrix  $\hat{\rho}(t) (\sigma_y \otimes \sigma_y) \hat{\rho}(t) (\sigma_y \otimes \sigma_y)$  in decreasing order, with  $\sigma_y$  being the second Pauli matrix.  $\hat{\rho}(t)$  is already known after having solved the Liouville-von Neumann equation (Eq. 6.4).

## 6.4 Application of the framework to the Posner molecule

With the above computational framework for spin relaxation calculations in hand, we build upon our previous work [14] detailed in Chapter 5, wherein we demonstrated that the Posner molecule exists as an asymmetric dynamic ensemble. *Ab initio* molecular dynamics (AIMD) simulations of eight transition state structures of the molecule formed the core of that previous contribution. Here, we examine the singlet probability and concurrence for not only the above transition state structures, but also for the time-averaged structures of each of the eight AIMD simulations. Additionally, to cover a wider range of possibly relevant structures, we also calculate here the singlet probability for the energetically most favorable structures

from each simulation, and the time-averaged configurations for structures associated with high-symmetries, as shown in Fig. 6.2. Lastly, we also use  $k$ -means clustering to further generate statistically relevant structures — both for the entire simulation and for the high-symmetry cases only — and calculate the singlet probabilities and concurrence for all of them. This thorough examination gives us over 100 unique structures to analyze.

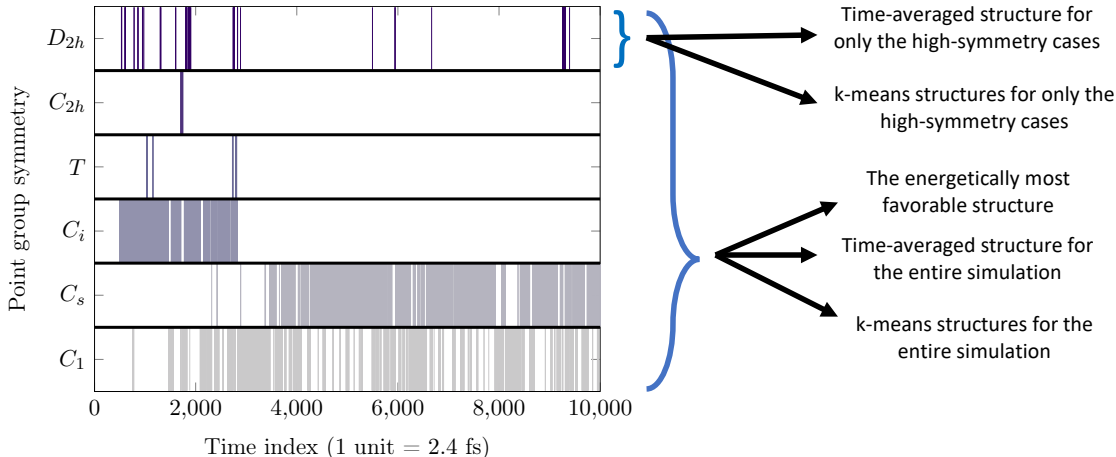


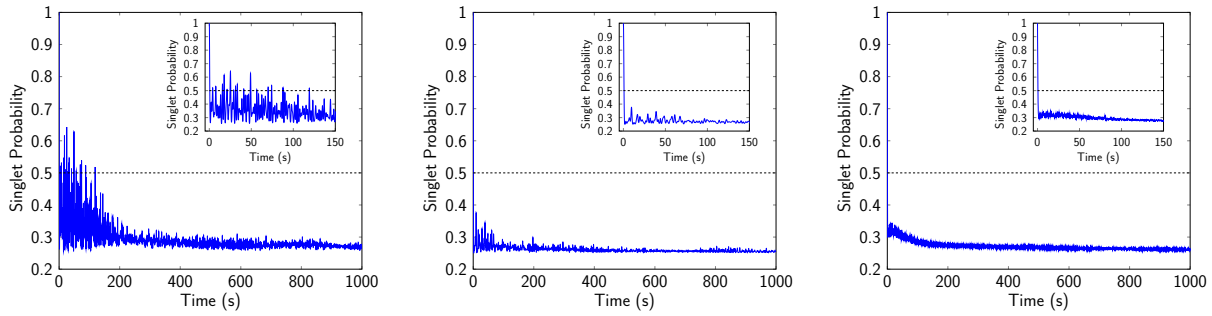
Figure 6.2: Illustration of the methodology for obtaining different configurations for spin dynamics calculations, starting from the AIMD structures presented in Ref. [14]. Here, we only show the type of structures obtained from one AIMD simulation (out of the eight that were performed). Overall, our approach gave us 102 unique structures. The graph on the left shows the evolution of the molecular point-group symmetry during a dynamic simulation of a transition-state structure of the Posner molecule.

We show the time evolution of the singlet probability and concurrence for two representative cases in Fig. 6.3 — namely the longest-lived singlet state (Figs. 6.3a and 6.3d), and the energetically most stable structure as per our dynamical analysis [14] (Figs. 6.3b and 6.3e). Given that the Posner molecule is expected to exist as a dynamic ensemble, we also show the singlet probability and the concurrence averaged over all 102 cases described above (Figs. 6.3c and 6.3f). We immediately observe that, in general, the singlet probabilities decay at a

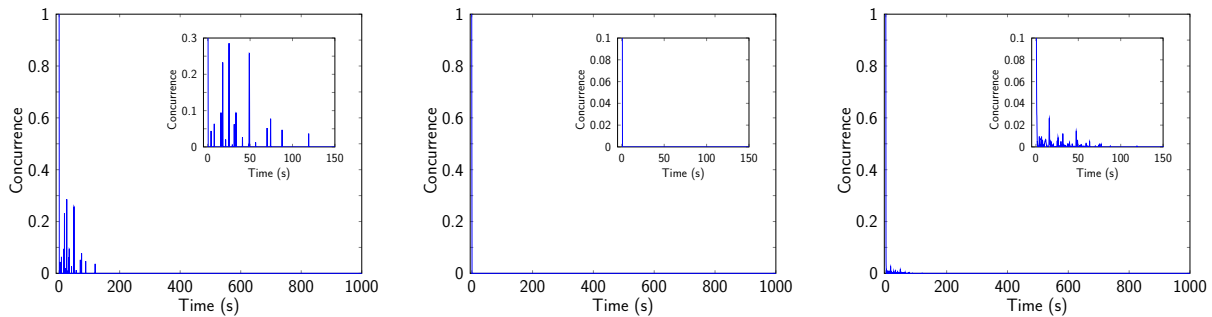
rate much faster than what may be necessary for neural processing [11, 15], and fall below the  $1/2$  entanglement threshold within a second. Correspondingly, the concurrence plots also suggest that the system loses entanglement within a second. Note that the plots presented in this study are for a model incorporating spin relaxation (in contrast with those presented in Player et al.’s work [16]), although spin relaxation is a minor contributor to the decay of the singlet probability on the timescales shown. For a majority of the cases, as shown in Fig. 6.4, the trend of Fig. 6.3b is followed. Overall, it is important to emphasize that the singlet probability rapidly decays below the  $1/2$  threshold within a second, regardless of the symmetry of the Posner molecule. Moreover, in cases where the singlet state is longer-lived, it is not entangled throughout, *i.e.*, the singlet probability decays quickly and then refocuses sporadically. This has major implications on the viability of the molecule as a quantum information processor, because any information processing will have to be done only at the instances when the system is entangled, *i.e.*, when the singlet probability is greater than  $1/2$ . In other words, the molecule may only act as a biological qubit for a very short periods of time, or only at specific time instances.

The longest time for which a singlet state was sustained in the presence of relaxation was a recurrence at 119 seconds (Fig. 6.3a), observed in one of the structures obtained using  $k$ -means clustering of the high-symmetry phase of a dynamic simulation ( $D_{2h}$  point group symmetry). Note that this time is defined as the last instance when the singlet probability was above the threshold of  $1/2$ , and that it does not correspond to the the singlet lifetime. A comprehensive overview of the relevant singlet probability parameters for the structures examined in this study is provided in Fig. 6.4. It is clear that, for 95% of the cases, the singlet state loses entanglement in less than a second. While a few structures do show recurrence of entanglement at time scales of tens of seconds, we reiterate that the molecule may act as a biological qubit at only the instances when the probability breaches the  $1/2$  — threshold, and not throughout.

Additionally, we also consider the transfer of entanglement from one pair of  $^{31}\text{P}$  nuclear



(a) The longest-lived singlet state occurs for a  $k$ -means structure of high symmetry. (b) The singlet probability for the energetically most stable structure. [14] (c) Averaged singlet probability for all 102 cases considered in the study.



(d) Concurrence values for even the longest-lived singlet state are extremely low. (e) Concurrence for the energetically most favorable structure. (f) Averaged concurrence for all 102 cases considered in the study.

Figure 6.3: The short-lived nature of the singlet probability and concurrence for the Posner molecule, shown for three representative structures. Insets show zoomed in regions of the plots. (a) and (d) correspond to the structure with the longest-lived singlet state — a  $k$ -means structure with  $D_{2h}$  symmetry; (b) and (e) correspond to the energetically most stable structure with no symmetry in our dynamical study [14]; (c) and (f) are the average singlet probability and concurrence for all 102 structures considered. Contrary to previous studies [11, 15, 16], the plots above suggest that the system is not suitable for quantum information processing at biologically relevant time scales.



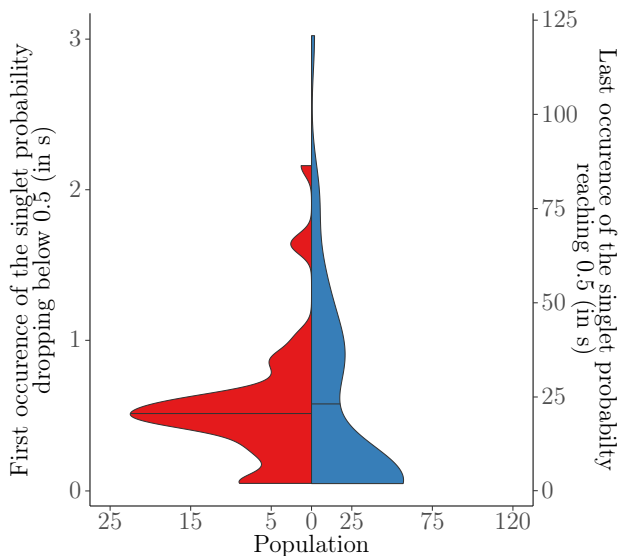


Figure 6.4: The first and last instances of the singlet probability crossing the threshold of  $1/2$ . The number of structures for each case, with different scales, has been represented on the  $x$ -axis. Note that the  $y$ -axes have different scales. A total of 102 structures have been considered, obtained from methods depicted in Fig. 6.2. The 50% quantile line has been shown in each case, and confirms that a majority of the structures are unable to maintain the singlet state for more than a second.

spins to another, owing to their interactions via the  $J$ -coupling constants. We show here the results for the configuration of the molecule that has the longest-lived singlet state in our study (see Fig. 6.5). Due to the large number of nuclear spin pairs between two Posner molecules, we only show the data for a few representative  $^{31}\text{P}$  nuclear spin pairs. The notation  $ij$  corresponds to spin pair comprising of the  $i^{\text{th}}$  spin in the first Posner molecule, and the  $j^{\text{th}}$  spin in the second Posner molecule. Each row represents the spin pair that was initialized in the singlet state (all other spins were left uncorrelated). The columns represent the spin pair for which the singlet probability is being calculated. The  $y$  axis (limits from 0.2 to 1) in each plot represents the singlet probability, and the  $x$  axis denotes time (a period of 1000 seconds is covered). Unsurprisingly, we observe that there is no marked transfer of the

singlet probability, and no transfer of entanglement in any case. The singlet probabilities remain low ( $\sim 0.25$ ) throughout, except for when the same nuclear spin pair is considered that was initialized in the singlet state. Note that this represents the best-case scenario because the structure considered had the longest-lived singlet state. We argue that for any other structural configuration of the Posner molecule considered in this study, the transfer of coherence between nuclear spin pairs will only be poorer. This further reinforces our claim that the Posner molecule, in any of its diverse structural configurations, fails to maintain long-lived entanglement amongst its  $^{31}\text{P}$  nuclear spins.

The above analysis suggests that the Posner molecule might not maintain long-lived singlet states for more than a second. However, Fig. 6.3a suggests that in a hypothetical high symmetry configuration, the molecule may sustain the nuclear singlet state for a longer duration, albeit only at specific instances when the singlet probability refocuses. Thus, to better understand the effect of symmetry on the longevity of the nuclear spin singlet state in the Posner molecule, we plotted the first and last instances when the singlet probability crosses the  $1/2$  threshold against the point group symmetry of the molecule or, more specifically, the number of symmetry operations associated with the point group. This has been depicted in Fig. 6.6.

Contrary to the expectation that the entanglement lifetime would be longer for structures that have higher symmetry, we find that the singlet state in the Posner molecule is, on average, short-lived (up to a few seconds at best) irrespective of the symmetry. We would also like to mention in passing that in addition to the 102 structures described above arising out of our AIMD simulations and subsequent analyses, we considered the two specific Posner molecule configurations explored in Ref. [11] and Ref. [16]. These configurations were not found to be energetically or structurally relevant in our dynamical simulations [14]. However, for these structures too, we found that the singlet probability falls below the  $1/2$  threshold within a second, and without any refocusing. On the other hand, if we make use of the  $J$ -coupling constants as suggested in Ref. [11] for one of these structures, our calculation broadly

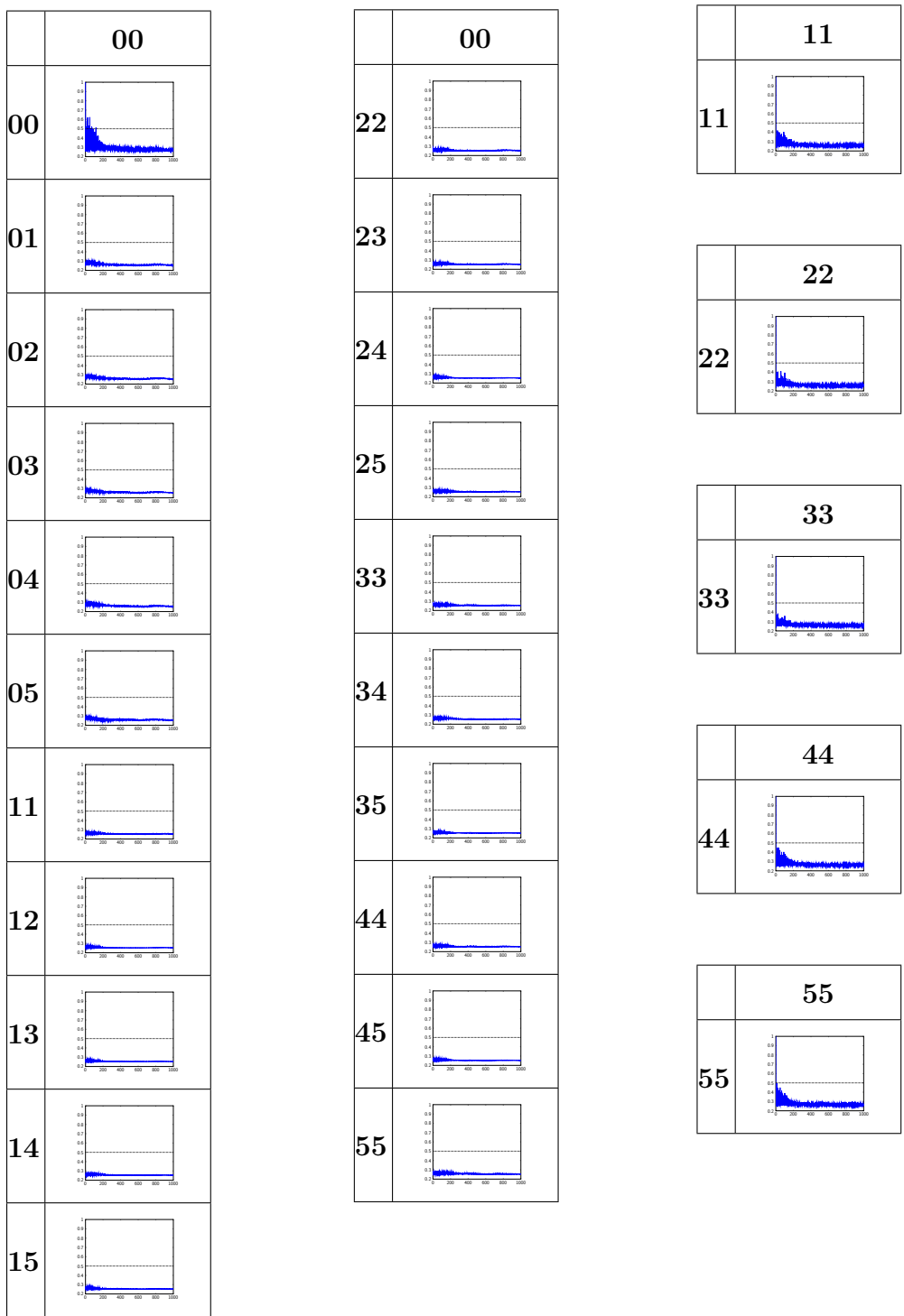
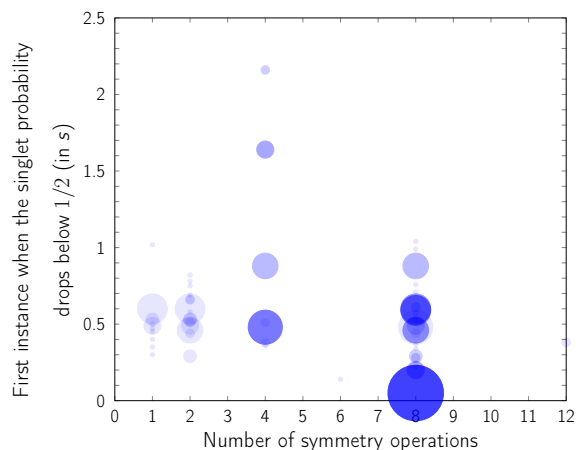
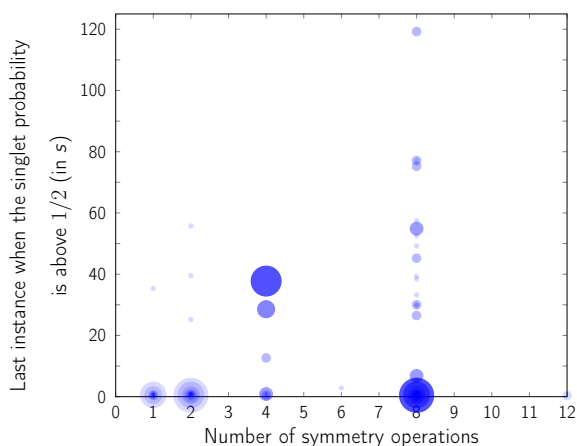


Figure 6.5: Transfer of entanglement between nuclear spin pairs in a Posner molecule. The 6 nuclear spins in each Posner are indexed from 0 through 5.



(a) First instances of the singlet probability dropping below  $1/2$  versus the number of symmetry operations in molecular point group.



(b) Last instances of the singlet probability being above  $1/2$  versus the number of symmetry operations in the molecular point group.

Figure 6.6: The symmetry of the molecule does not seem to play a major role in maintaining entanglement in the system, and Posner molecules generally have short entanglement lifetimes ( $< 1$  s) irrespective of their point-group symmetry. The marker size in each plot is proportional to the number of data points at the location, whereas darker areas represent overlapping of markers.

reproduces the results from Ref. [16], albeit with minor differences due to slightly different values of the chemical shielding tensor and the rotational correlation time. A comparison of the singlet probabilities in the above cases has been depicted in Fig. 6.7. Note that this comparison has only been done for two specific molecular configurations of the Posner molecule, and the results should not be generalized to other structures. Our observation above is consistent with the fact that, on average, symmetric molecules are expected to have a better entanglement yield. However, the values of the  $J$ -coupling constants matter in the sense that it is possible for a molecular configuration to have a wide range of entanglement yields, depending on the calculated values of those constants. Therefore, it is important to be able to calculate these constants accurately.

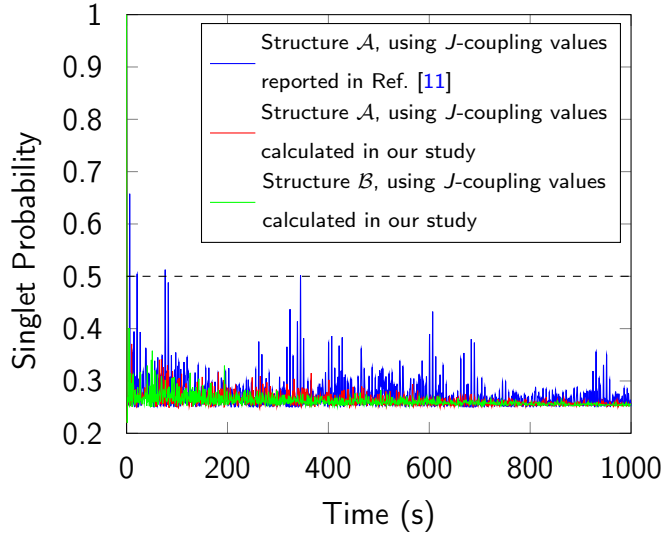


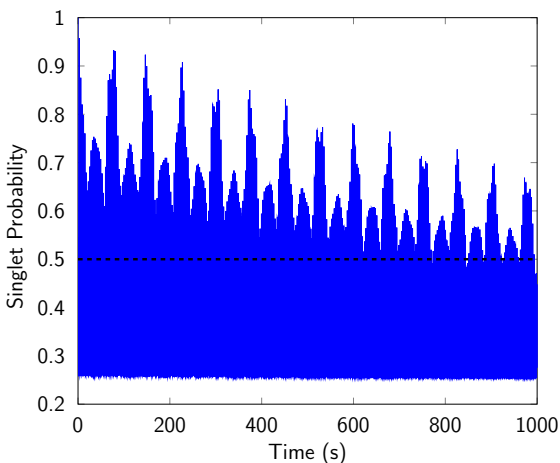
Figure 6.7: A comparison of the singlet probabilities for two  $S_6$  structures —  $\mathcal{A}$ , taken from Ref. [16], and  $\mathcal{B}$ , taken from Ref. [11] — with coupling constants as reported in Ref. [11] and as calculated in our study.

Overall, we observe that the singlet state between a pair of  $^{31}\text{P}$  nuclear spins in separate Posner molecules generally loses entanglement within a second. Only certain hypothetical or energetically unfavorable configurations of the molecule are found to preserve the state for more than a second. This is significantly shorter than previously suggested [11, 15, 16]. Commensurate with these findings, the concurrence values are also observed to drop rapidly within the same period of time. Notably, these findings do not preclude the molecule from being relevant for biological processes taking place at time scales for which the nuclear spin coherences are indeed maintained. However, due to the small diffusion constant of the molecule, it is unable to traverse neuronally relevant length-scales within its short entanglement lifetime, and so it might not be suitable for entanglement mediated neural signal processing, as previously suggested [15]. Specifically, we estimated the translational diffusion properties of the molecule by analyzing its trajectory in a hydrated environment (details in Section 6.1) and found the diffusion constant to be  $\sim 1.01 \times 10^{-9} \text{ m}^2/\text{s}$ . This implies that it would take the Posner molecule approximately 14 hours to traverse the length of a neuronal

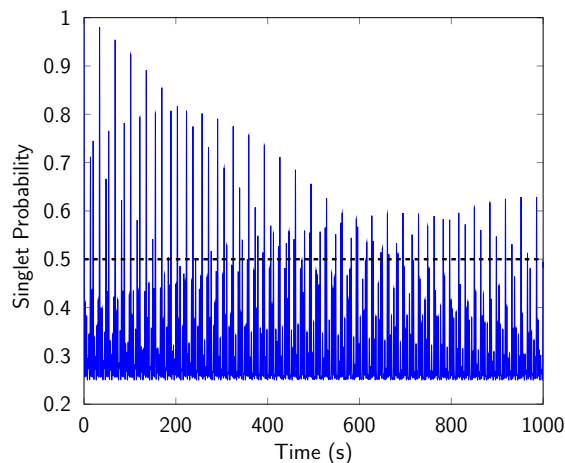
cell axon ( $\sim 1$  cm), much longer than the aforementioned entanglement lifetimes. We also note that the above estimated speeds are markedly slower than the average speed of nerve impulses [234].

## 6.5 Exploratory calculations on calcium phosphate dimers

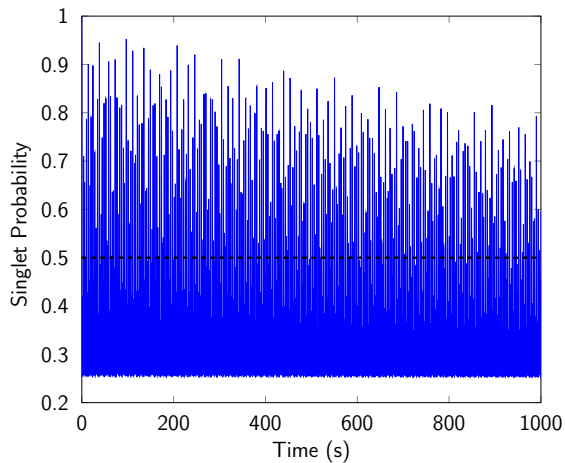
Surprisingly, exploratory calculations on the tricalcium biphosphate dimer,  $\text{Ca}_6(\text{PO}_4)_4$ , revealed that the singlet state in the dimer is exceedingly long-lived, irrespective of its structure. As reported in earlier studies [14, 206], although the dimer also exists in multiple configurations, its energetically favorable structures are known more conclusively. We were able to identify six stable structures for the dimer [14], although many more may exist. Again, as for the Posner molecules, we initialized a pair of  $^{31}\text{P}$  nuclei in two identical, spatially separated dimers in a singlet state, and then evaluated the singlet probability over time. Remarkably, even in the presence of relaxation, the singlet state in tricalcium biphosphate dimers is extremely long-lived (of the order of  $10^3$  seconds, and with significant refocusing) regardless of the symmetry of the molecule. This has been depicted in Fig. 6.8. The coupling constants used for these calculations have been shown in Table 6.1.



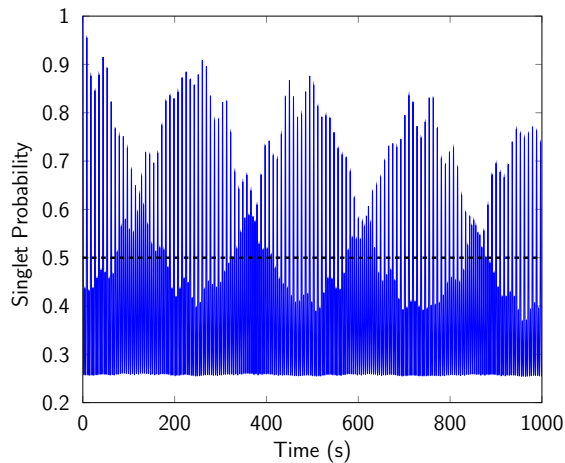
(a) Singlet probability for a dimer structure with a  $C_2$  symmetry



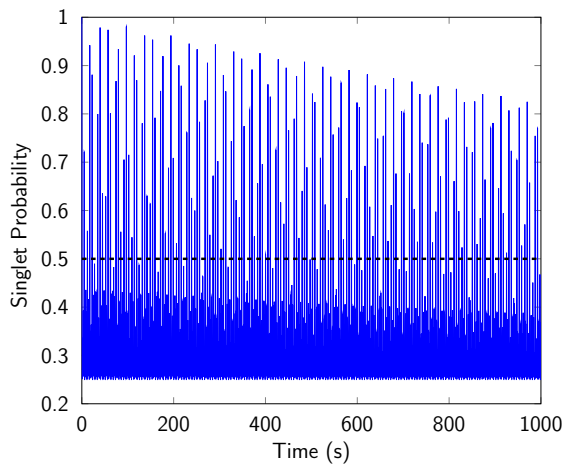
(b) Singlet probability for a dimer structure with a  $S_4$  symmetry



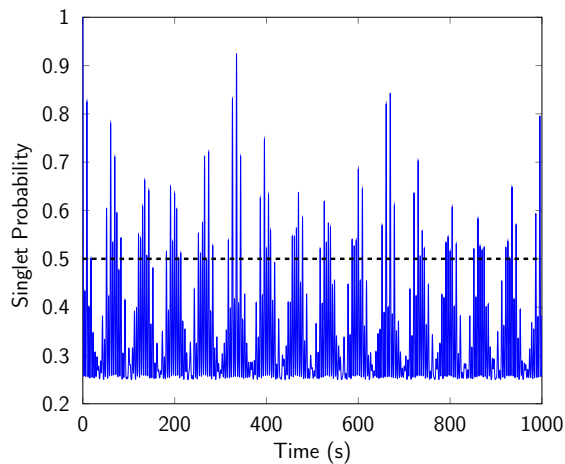
(c) Singlet probability for a dimer structure with a  $C_2$  symmetry



(d) Singlet probability for a dimer structure with a  $C_s$  symmetry



(e) Singlet probability for a dimer structure with a  $C_{2v}$  symmetry



(f) Singlet probability for a dimer structure with a  $T_d$  symmetry

Figure 6.8: Singlet probabilities for the six stable dimer structures explored in our previous study [14]. Long-lived singlet states are observed irrespective of the symmetry of the dimer, unlike the Posner molecule, potentially making it more suitable for quantum information processing. For clarity, the plots (a) through (f) have been arranged in decreasing order of the stability of the dimer structure

<b>Coupling constants (in Hz)</b>	<b>Structure corresponding to Fig. 6.8a</b>	<b>Structure corresponding to Fig. 6.8b</b>	<b>Structure corresponding to Fig. 6.8c</b>	<b>Structure corresponding to Fig. 6.8d</b>	<b>Structure corresponding to Fig. 6.8e</b>	<b>Structure corresponding to Fig. 6.8f</b>
$J_{ab}$	-0.394	-0.193	-0.200	0.142	-0.163	0.147
$J_{ac}$	-0.415	-0.139	-0.209	0.147	-0.161	0.154
$J_{ad}$	-0.163	-0.136	-0.267	0.152	-0.374	0.135
$J_{bc}$	-0.046	-0.143	-0.404	0.140	0.042	0.144
$J_{bd}$	-0.082	-0.142	-0.218	0.124	-0.162	0.150
$J_{cd}$	0.221	-0.189	-0.065	0.148	-0.161	0.142

Table 6.1: The  $J$ -coupling constants for each of the 6 dimer structures considered in this study. All values are in Hz. The coordinates of the  $^{31}\text{P}$  atoms corresponding to subscripts  $a, b, c, d$  are shown in Table 6.2.

<b>Figure corresponding to the structure</b>	<b>Coordinates (in Å) of <math>^{31}\text{P}</math> atom <math>a</math></b>	<b>Coordinates (in Å) of <math>^{31}\text{P}</math> atom <math>b</math></b>	<b>Coordinates (in Å) of <math>^{31}\text{P}</math> atom <math>c</math></b>	<b>Coordinates (in Å) of <math>^{31}\text{P}</math> atom <math>d</math></b>
Fig. 6.8a	[-2.82, 0.51, 0.06]	[0.47, 1.25, -3.39]	[0.44, 0.54, 3.21]	[1.98, -2.20, -0.01]
Fig. 6.8b	[1.34, -1.75, 2.03]	[-1.31, 1.69, 2.11]	[-1.74, -1.29, -2.09]	[1.71, 1.36, -2.08]
Fig. 6.8c	[-0.97, -0.24, 2.92]	[0.99, -2.86, -1.96]	[-2.69, 1.36, -1.58]	[2.77, 1.87, 0.30]
Fig. 6.8d	[2.95, -1.15, 1.05]	[-2.48, -1.75, 1.46]	[-0.28, 3.24, 0.81]	[-0.20, -0.34, -3.35]
Fig. 6.8e	[-3.42, -0.27, 0.06]	[0.88, 1.60, -2.80]	[0.99, 1.67, 2.73]	[1.51, -3.08, 0.01]
Fig. 6.8f	[-2.57, 0.28, 2.14]	[0.25, 2.80, -1.83]	[2.84, -0.47, 1.73]	[-0.52, -2.62, -2.04]

Table 6.2: The coordinates of the  $^{31}\text{P}$  atoms corresponding to each figure in Fig. 6.8



It is also interesting to study whether coherence is transferred from one  $^{31}\text{P}$  nuclear spin pair to another as the singlet state evolves over time. Below, we show this for all nuclear spin pairs for the dimer structure with a  $C_2$  point-group symmetry (see Fig. 6.9). Each row represents the spin pair that was initialized in the singlet state (all other spins were left uncorrelated). The columns represent the spin pair for which the singlet probability is being calculated. The  $y$  axis (limits from 0.2 to 1) in each plot represents the singlet probability, and the  $x$  axis denotes time (a period of 1000 seconds is covered). Even though the singlet state is long-lived for each individual pair of  $^{31}\text{P}$  nuclear spins, we see that, in some cases, coherence is indeed transferred to other spins pairs, suggesting that more than one nuclear spin pair might have long entanglement lifetimes. We expect a similar behavior for all other dimer structures. We provide an explanation for the exceptional longevity of the singlet state in the dimer, over the Posner molecule, in the following section (see Section 6.6). Despite these fascinating observations, we remark that the tricalcium biphosphate dimer does not appear to have been observed experimentally.

In view of the dimers' ability to maintain coherences for exceptionally long times, it is interesting to compare the formation energies per monomer unit of the trimer (Posner molecule) and the dimer. For the dimer configurations studied, the formation energy per monomer unit ranged from  $-88.700$  eV to  $-89.2007$  eV. For the trimer, the value ranges from  $-88.332$  eV to  $-90.517$  eV. In comparison, thermal energy at room temperature is  $0.026$  eV. Thus, the dimer appears to be roughly as stable as the Posner molecule and is expected to exist as an independent, stable entity without coalescing into Posner molecules. These observations suggests that the nuclear spin entanglement in tricalcium biphosphate dimers could be worth exploring both theoretically and experimentally.

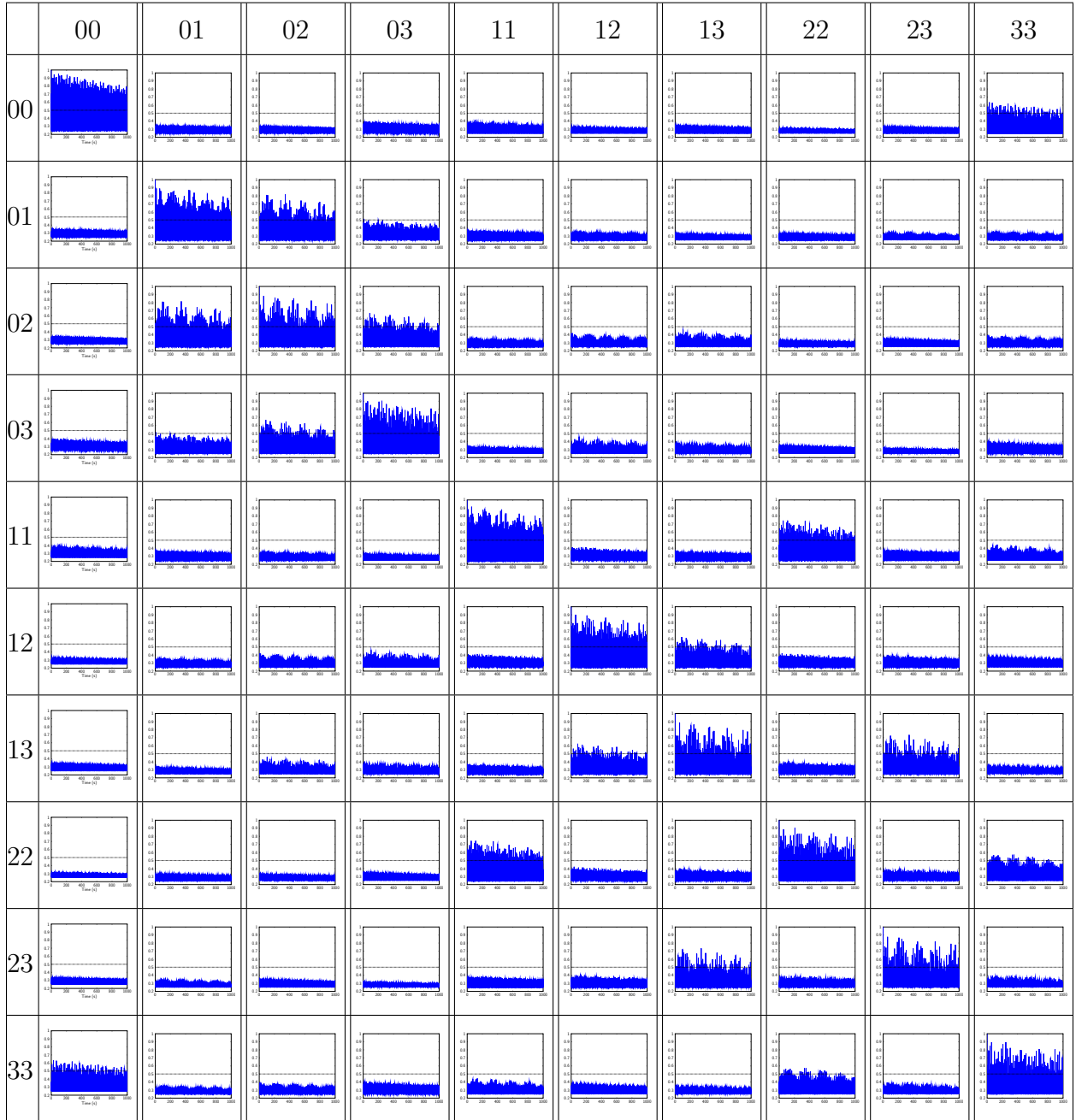


Figure 6.9: Transfer of entanglement between nuclear spin pairs in a tricalcium biphosphate dimer with a  $C_2$  point-group symmetry. The 4 nuclear spins in each dimer are indexed from 0 through 3. The notation  $ij$  corresponds to spin pair comprising of the  $i^{th}$  spin in the first dimer molecule, and the  $j^{th}$  spin in the second dimer molecule.

## 6.6 The effect of the number of coupled nuclear spins on the spin dynamics of a system

In general, we expect a spin system with a lesser number of coupled nuclear spins, such as the tricalcium biphosphate dimer, to be more favorable for maintaining long-lived singlet states than a spin system with a larger number of coupled nuclear spins, such as the Posner molecule. This conclusion can be derived from the following line of reasoning. Let there be  $n$  distinct spin energy levels in a molecule. Then,  $n = 2^{n_P}$  in a molecule with no symmetry, with  $n_P$  being the number of  $^{31}\text{P}$  atoms in the molecule. To get the total number of unique, positive frequencies contributing to coherences in one molecule, we count the number of pairs of energy levels, i.e.  $\sum_{i=1}^{n-1} i = \frac{n(n-1)}{2} = N$ .

Every frequency that could contribute to disentanglement of the singlet state by destructive interference in the singlet probability oscillations, is a result of a unique pair of frequencies from the above  $N$  frequencies across both molecules. Adding them up, we get:

$$z = \frac{1}{2}(N(N - 1)) + N + N.$$

Here,  $z$  is the total number of oscillation frequencies potentially contributing to the disentanglement of the spin singlet state. The first term on the right-hand side corresponds to combinations of unique pairs of different frequencies from the two molecules, the second term corresponds to oscillations within each molecule independent of the other, i.e., pairing up frequencies in one molecule to zero frequencies in the other molecule, and the last term corresponds to the combination of identical frequencies from both molecules. While symmetry and accidental degeneracies associated with specific choices of coupling constants will inevitably introduce redundant frequencies close to one another, and some others close to zero,  $z$  provides an upper limit to the number of oscillation frequencies. Written in terms of the number of distinct spin energy levels  $n$ , we have

$$z = \frac{1}{8}(n^4 - 2n^3 + 7n^2 - 6n).$$

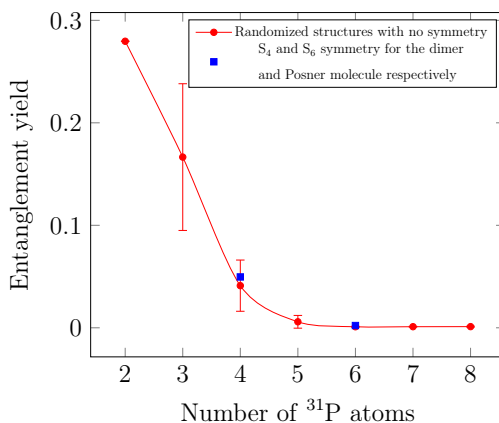


Figure 6.10: The entanglement yield monotonically decreases with the number of coupled nuclear spins. Note that the error bars and the data on the  $S_4$  and  $S_6$  – symmetric dimer and Posner structures respectively show that for individual structures, a different set of coupling constants result in different yields for a given number of  $^{31}\text{P}$  atoms.

In Fig. 6.10, we plot the entanglement yield for systems with different numbers of  $^{31}\text{P}$  atoms. The entanglement yield has been calculated as  $k \int_0^T \max(p_s(t) - 0.5, 0) e^{-kt} dt$ . Here,  $k = 1/300 \text{ s}^{-1}$  is related to the sampling duration,  $T = 1000\text{s}$  is the total duration over which  $p_s(t)$  was evaluated, and  $p_s(t)$  is the singlet probability over time. Note that these have been calculated in the absence of spin relaxation. Including spin relaxation would have required the structural information for each system, but we do not anticipate the trend to change appreciably even after its inclusion. We performed 50 simulations for each system size, and the  $J$ -coupling constants for each of the above simulation were chosen randomly from a normal distribution such that  $\sqrt{\sum_{i=1}^{n_P} J_{ij}^2} = 1 \text{ Hz}$ , where  $n_P$  is the number of  $^{31}\text{P}$  atoms.

Clearly, we see that a system with lesser number of coupled nuclear spins is much more adept at maintaining long-lived singlet states than a system with a larger number of coupled nuclear spins. This is in line with our results and our argument above. We reiterate that the accurate calculation of  $J$ -coupling constants remains crucial because the above discussion only suggests that a smaller coupled nuclear spin system would be better at maintaining long-

lived singlet states. To calculate the longevity of the singlet state, we still need accurate values of the coupling constants for a given structural configuration of the molecule.

Additionally, from Fig. 6.10, it is also evident that, on average, symmetric configurations (represented as blue dots on the plot) are expected to have better entanglement yields. For the same structure, it is possible to move across the error bar by simply altering the coupling constants. Since the values of the coupling constants are linked to the symmetry of the molecule, the above observation confirms the importance of these features when studying the spin dynamics of a given system with a dynamic ensemble of structures.

From the above discussion, and considering systems composed from dimers – with no symmetry (16 distinct energy levels per cluster) and with  $S_4$  symmetry (13 energy levels) – and from Posner molecules – with no symmetry (64 energy levels) and with  $S_6$  symmetry (44 energy levels) – the number of unique positive frequencies contributing to the coherent evolution of the singlet probability are 7380, 3159, 2035152, and 448877, respectively. While some of these might be close to degenerate or zero or not significantly contribute to the singlet probability, these numbers illustrate that destructive interference of coherent contributions will be vastly more likely in larger spin systems, regardless of cluster symmetry. This is in line with our results. We confirm the above argument by evaluating the entanglement yield, in the absence of spin relaxation, for randomly coupled systems with different number of  $^{31}\text{P}$  atoms and obtain the same trend. These calculations corroborate the insight that the preservation or recurrence of entangled states is primarily related to the number of coupled nuclei, and only secondarily influenced by the symmetry of the molecule and the actual  $J$ -coupling constants, which impact the evolution through exact and accidental degeneracies of energy levels. Regardless of these observations, we maintain that accurate calculations to determine the  $J$ -coupling constants for every molecular configuration are critical to evaluate the longevity of the spin singlet state of molecules in comparison to other structures of the same family, i.e. with the same number of coupled nuclear spins, and to assess effects of spin relaxation.

## 6.7 Calculations on the calcium phosphate monomer

Given the structure of the calcium phosphate monomer,  $\text{Ca}_3(\text{PO}_4)_2$ , [14, 203, 206] we can calculate the singlet probability for a pair of  $^{31}\text{P}$  nuclei in two spatially-separated calcium phosphate monomers (with the remaining uncorrelated nuclear spins serving as background). Unsurprisingly, and as can be seen in Fig. 6.11, the singlet probability is very well-behaved, i.e., it decays extremely slowly and has well-defined oscillations at a single frequency. However, this is to be expected since the monomer only has one unique scalar coupling constant, which suggests that the singlet probability — which is dominated by  $J$ -coupling constants — will recur at a single frequency. This is unlike the Posner molecule wherein the singlet probability recurs at multiple frequencies as determined by the various  $J$ -coupling constants, leading to destructive interference and a significantly faster relaxation of the singlet state [16].

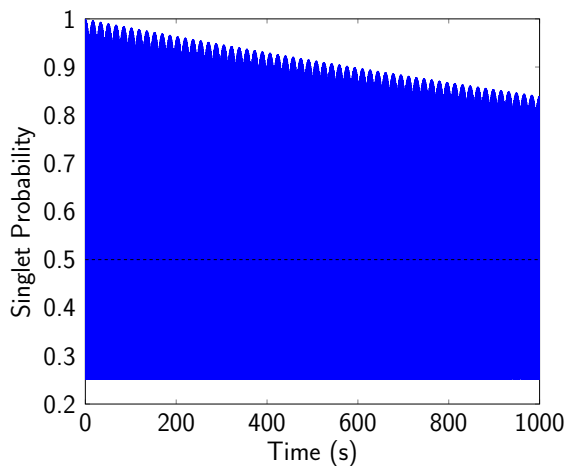


Figure 6.11: Singlet probability for the calcium phosphate monomer

However, these findings related to the entanglement behavior of the monomers is not expected to be of practical relevance due to energetic considerations. For the monomer, the formation energy was calculated to be  $-84.244$  eV, whereas the formation energy of the Posner molecule per monomer unit ranged from  $-88.332$  eV to  $-90.517$  eV. Clearly, the

Posner molecule is much more energetically stable, suggesting that two monomers would very likely coalesce to form a lumped, aggregate molecule, which may or may not result in the formation of calcium phosphate dimers and trimers (Posner molecules).

## 6.8 Concluding remarks

Our comprehensive study on the spin dynamics of the singlet state in pairs of Posner molecules, performed without any assumptions on the structure or the coupling constants of the molecule, shows that the singlet state is short-lived ( $< 1$  second) irrespective of the structural symmetry of the molecule. This also indicates that accurate calculation of the  $J$ -coupling constants, instead, are crucial to the study of spin dynamics pertaining to the Posner molecule. Our results suggest that the Posner molecule might be unsuitable as a biological quantum information processor since entanglement between  $^{31}\text{P}$  nuclei in pairs of Posner molecules is not expected to last for more than a second. It may be possible that coherence is transferred from one pair of  $^{31}\text{P}$  nuclei to the other, but as shown in earlier studies [16] and, to a greater extent, in our SI, this does not increase the singlet probability yield over time in any way. Moreover, recent findings on  $^{31}\text{P}$ - $^{31}\text{P}$  singlet lifetimes in common organic phosphorus compounds of interest (*e.g.*, adenosine diphosphate [235], nicotinamide adenine dinucleotide [235], tetrabenzyle pyrophosphate [231], pyrophosphate [232]), show that the singlet lifetime ranges from less than half a second in large diphosphates and pyrophosphates to few tens of seconds in small, highly symmetric pyrophosphates. Additionally, the latter study suggests that singlet lifetimes may be reduced further in a more realistic biological environment, and identifies spin-rotation relaxation as the dominant relaxation pathway [232]. While our model neglects spin-rotation relaxation (due to the larger size of the Posner molecule), it will be interesting to see how our results differ after its inclusion. The singlet lifetimes reported in the above studies are of the same order as that of the Posner molecule in the current study and suggest that, without conclusive evidence of the presence of isolated

Posner molecules *in vivo*, the longevity of the singlet state reported in this study is comparable to that found in other phosphorus compounds *in vitro*. Additionally, while the current study assumed a weak net external magnetic field, it would be interesting to observe the singlet probability in the presence of stronger magnetic fields, and to see whether that has any effect on increasing the singlet longevity. Finally, we observe long-lived ( $\sim 10^2$ – $10^3$  seconds) singlet states for the tricalcium biphosphate dimer, regardless of the structural symmetry of the molecule. This fascinating result is explained on the basis of the fact that any system with a smaller number of coupled nuclear spins is expected to better maintain entanglement within the singlet state, than a system with a larger number of coupled nuclear spins. This leads us to the conclusion that while the symmetry of the molecule and its coupling constants are critical for evaluating the longevity of the singlet state given a molecule, the behavior of the coherent oscillations is largely dictated by the system size. The fact that the dimers appear to be as energetically stable as the Posner molecule might suggest that the dimer could be a better candidate for a naturally occurring quantum information processor than the Posner molecule. However, confirmation of its presence *in vivo* is necessary.



## CHAPTER 7

# Electronic structure prediction of multi-million atom systems

### 7.1 Introduction

Over the past several decades, Density Functional Theory (DFT) calculations based on the Kohn-Sham formulation [163, 172] have emerged as a fundamental tool in the prediction of electronic structure. Today, they stand as the de facto workhorse of computational materials simulations [236, 237, 238, 239], offering broad applicability and versatility. Although formulated in terms of orbitals, the fundamental unknown in Kohn Sham Density Functional Theory (KS-DFT) is the electron density, from which many ground state material properties — including structural parameters, elastic constants, magnetic properties, phonons/vibrational spectra, etc., may be inferred. The ground state electron density is also the starting point for calculations of excited state phenomena, including those related to optical and transport properties [240, 241].

The importance of being able to routinely predict the electronic structure of generic bulk materials, especially, metallic and semiconducting systems with a large number of representative atoms within the simulation cell, cannot be overemphasized. Computational techniques that can perform such calculations accurately and efficiently have the potential to unlock insights into a variety of material phenomena and can lead to the guided design of new materials with optimized properties. Examples of materials problems where such computational techniques can push the state-of-the-art include elucidating the core structure

of defects at realistic concentrations, the electronic and magnetic properties of disordered alloys and quasicrystals [242, 243, 244, 245], and the mechanical strength and failure characteristics of modern, compositionally complex refractory materials [246, 247]. Moreover, such techniques are also likely to carry over to the study of low dimensional matter and help unlock the complex electronic features of emergent materials such as van-der-Waals heterostructures [248] and moiré superlattices [249]. Notably, a separate direction of work has also explored improving Density Functional Theory predictions themselves, by trying to learn the Hohenberg-Kohn functional or exchange correlation potentials [113, 250, 251]. This direction of work will not have much bearing on the discussion that follows below.

For physical reasons, the predicted electron density is expected to obey transformations consistent with overall rotation and translation of the material system. Moreover, it should remain invariant under permutation of atomic indices. To ensure such properties, several authors have employed equivariant-neural networks [109, 252, 253, 254, 255]. An alternative to such approaches, which is sufficient for scalar valued quantities such as electron density, is to employ invariant descriptors [110, 111, 252, 253]. We adopt this latter approach in this work and show through numerical examples that using invariant features and predicting electron density as a scalar valued variable indeed preserves the desired transformation properties.

A key challenge in building surrogate models of the ground state electron density from KS-DFT calculations is the process of data generation itself, which can incur significant offline cost [256]. In recent work [116], we have demonstrated how this issue can be addressed for chiral nanomaterials [42]. For such forms of matter, the presence of underlying structural symmetries allows for significant dimensionality reduction of the predicted fields, and the use of specialized algorithms for ground state KS-DFT calculations [4, 5, 138]. However, such strategies cannot be adopted for bulk materials with complex unit cells, as considered here. For generic bulk systems, due to the confining effects of periodic boundary conditions, small unit-cell simulations alone cannot represent a wide variety of configurations. To obtain ML models that can work equally well across scales and for a variety of configurations (e.g. defects

[257, 258]), data from large systems is also essential. However, due to the aforementioned cubic scaling of KS-DFT calculations, it is relatively inexpensive to generate a lot of training data using small sized systems (say, a few tens of atoms), while larger systems (a few hundred atoms) are far more burdensome, stymieing the data generation process. Previous work on electron density prediction [111, 112] has been made possible by using data from large systems exclusively. However, this strategy is likely to fail when complex systems such as multi-principal element alloys are dealt with, due to the large computational cells required for such systems. This is especially true while studying compositional variations in such systems since such calculations are expected to increase the overall computational expense of the process significantly.

In this work, we propose a machine-learning model that accurately predicts the ground state electron density of bulk materials at any scale, while quantifying the associated uncertainties. Once trained, our model significantly outperforms conventional KS-DFT-based computations in terms of speed. To address the high cost of training data generation associated with KS-DFT simulations of larger systems — a key challenge in developing effective ML surrogates of KS-DFT — we adopt a transfer learning (TL) approach [123]. Thus, our model is first trained using a large quantity of cheaply generated data from simulations of small systems, following which, a part of the model is retrained using a small amount of data from simulations of a few large systems. This strategy significantly lowers the training cost of the ML model, without compromising its accuracy. Along with the predicted electron density fields, our model also produces a detailed spatial map of the uncertainty, that enables us to assess the confidence in our predictions for very large scale systems (thousands of atoms and beyond), for which direct validation via comparison against KS-DFT simulations data is not possible. The uncertainty quantification (UQ) properties of our models are achieved through the use of Bayesian Neural Networks (BNNs), which systematically obtain the variance in prediction through their stochastic parameters, and tend to regularize better than alternative approaches [259, 260, 261]. They allow us to systematically judge the

generalizability of our ML model, and open the door to Active Learning approaches [262] that can be used to further reduce the work of data generation in the future.

To predict the electron density at a given point, the ML model encodes the local atomic neighborhood information in the form of descriptors, that are then fed as inputs to the BNN. Our neighborhood descriptors are rather simple: they include distance and angle information from nearby atoms in the form of scalar products and avoid choosing the basis set and “handcrafted” descriptors adopted by other workers [103, 263, 264, 265, 266]. Additionally, we have carried out a systematic algorithmic procedure to select the optimal set of descriptors, thus effectively addressing the challenge associated with the high dimensionality of the descriptor-space. To sample this descriptor space effectively, we have employed thermalization, i.e., *ab initio* molecular dynamics (AIMD) simulations at various temperatures, which has allowed us to carry out accurate predictions for systems far from training. Overall, our ML model reduces the use of heuristics adopted by previous workers in notable ways, making the process of ML based prediction of electronic structure much more systematic. Notably, the point-wise prediction of the electronic fields via the trained ML model, make this calculation scale linearly with respect to the system size, enabling a wide variety of calculations across scales.

## 7.2 Computational Framework

### 7.2.1 *Ab Initio* Molecular Dynamics

To generate training data for the model, *Ab Initio* Molecular Dynamics (AIMD) simulations were performed using the finite-difference based SPARC code [267, 268, 269]. We used the GGA PBE exchange-correlation functional [270] and ONCV pseudopotentials [271]. For aluminum, a mesh spacing of 0.25 Bohrs was used while for SiGe, a mesh spacing of 0.4 Bohrs was used. These parameters are more than sufficient to produce accurate energies and forces for the pseudopotentials chosen, as was determined through convergence tests. A tolerance

of  $10^{-6}$  was used for self-consistent field (SCF) convergence and the Periodic-Pulay [272] scheme was deployed for convergence acceleration. These parameters and pseudopotential choices were seen to produce the correct lattice parameters and bulk modulus values for the systems considered here, giving us confidence that the DFT data being produced is well rooted in the materials physics.

For AIMD runs, a standard NVT-Nosé Hoover thermostat [273] was used, and Fermi-Dirac smearing at an electronic temperature of 631.554 K was applied. The time step between successive AIMD steps was 1 femtosecond. The atomic configuration and the electron density of the system were captured at regular intervals, with sufficient temporal spacing between snapshots to avoid the collection of data from correlated atomic arrangements. To sample a larger subspace of realistic atomic configurations, we performed AIMD simulations at temperatures ranging from 315 K to about twice the melting point of the system, i.e. 1866 K for Al and 2600 K for SiGe. Bulk disordered SiGe alloy systems were generated by assigning atoms randomly to each species, consistent with the composition.

We also generate DFT data for systems with defects and systems under strain, in order to demonstrate the ability of our ML model to predict unseen configurations. To this end, we tested the ML model on monovacancies and divacancies, edge and screw dislocations, and grain boundaries. For vacancy defects, we generated monovacancies by removing an atom from a random location, and divacancies by removing two random neighboring atoms before running AIMD simulations. Edge and screw dislocations for aluminum systems were generated using AtomsK [274]. Further details can be found in Fig. 7.6. Grain boundary configurations were obtained based on geometric considerations of the tilt angle — so that an overall periodic supercell could be obtained, and by removing extra atoms at the interface. For aluminum, we also tested an isotropic lattice compression and expansion of up to 5%; these systems were generated by scaling the lattice vectors accordingly (while holding the fractional atomic coordinates fixed).

### 7.2.2 Machine learning map for charge density prediction

Our ML model maps the coordinates  $\{\mathbf{R}_I\}_{I=1}^{N_a}$  and species (with atomic numbers  $\{Z_I\}_{I=1}^{N_a}$ ) of the atoms, and a set of grid points  $\{\mathbf{r}_i\}_{i=1}^{N_{\text{grid}}}$  in a computational domain, to the electron density values at those grid points. Here,  $N_a$  and  $N_{\text{grid}}$  refer to the number of atoms and the number of grid points, within the computational domain, respectively. We compute the aforementioned map in two steps. First, given the atomic coordinates and species information, we calculate atomic neighborhood descriptors for each grid point. Second, a neural network is used to map the descriptors to the electron density at each grid point. These two steps are discussed in more detail subsequently.

### 7.2.3 Atomic neighborhood descriptors

In this work, we use a set of scalar product-based descriptors to encode the local atomic environment. The scalar product-based descriptors for the grid point at  $\mathbf{r}_i$  consist of distance between the grid point and the atoms at  $\mathbf{R}_I$ ; and the cosine of angle at the grid point  $\mathbf{r}_i$  made by the pair of atoms at  $\mathbf{R}_I$  and  $\mathbf{R}_J$ . Here  $i = 1, \dots, N_{\text{grid}}$  and  $I, J = 1, \dots, N_a$ . We refer to the collections of distances i.e.,  $\|\mathbf{r}_i - \mathbf{R}_I\|$  as set I descriptors, and the collections of the cosines of the angles i.e.,  $\frac{(\mathbf{r}_i - \mathbf{R}_I) \cdot (\mathbf{r}_i - \mathbf{R}_J)}{\|\mathbf{r}_i - \mathbf{R}_I\| \|\mathbf{r}_i - \mathbf{R}_J\|}$  are referred to as set II descriptors.

Higher order scalar products such as the scalar triple product, and the scalar quadruple product which involve more than two atoms at a time can also be considered. However, these additional scalar products are not included in the descriptor set in this work since they do not appear to increase the accuracy of predictions.

Since the predicted electron density is a scalar valued variable, invariance of the input features is sufficient to ensure equivariance of the predicted electron density under rotation, translation, and permutation of atomic indices (as mentioned in [252, 253]). Since the features of our ML model are scalar products and are sorted, they are invariant with respect to rotation, translation, and permutation of atomic indices. Details on the proof that our

descriptor space is indeed equivariant can be found in [177].

#### 7.2.4 Selection of optimal set of descriptors

As has been pointed out by previous work on ML prediction of electronic structure [110, 111], the nearsightedness principle [275, 276] and screening effects [277] indicate that the electron density at a grid point has little influence from atoms sufficiently far away. This suggests that only descriptors arising from atoms close enough to a grid point need to be considered in the ML model, a fact which is commensurate with our findings in Fig. 7.1. Using an excessive number of descriptors can increase the time required for descriptor-calculation, training, and inference, is susceptible to curse of dimensionality, and affect prediction performance [278, 279]. On the other hand, utilizing an insufficient number of descriptors can result in an inadequate representation of the atomic environments and lead to an inaccurate ML model.

Based on this rationale, we propose a procedure to select an optimal set of descriptors for a given atomic system. We select a set of  $M$  ( $M \leq N_a$ ) nearest atoms from the grid point to compute the descriptors and perform a convergence analysis to strike a balance between the aforementioned conditions to determine the optimal value of  $M$ . It is noteworthy that the selection of optimal descriptors has been explored in previous works, in connection with Behler-Parinello symmetry functions such as [280] and [281]. These systematic procedures for descriptor selection eliminate trial-and-error operations typically involved in finalizing a descriptor set. In [281], the authors have demonstrated for Behler-Parinello symmetry functions that using an optimal set of descriptors enhances the efficiency of machine learning models.

For  $M$  nearest atoms, we will have  $N_{\text{set I}}$  distance descriptors, and  $N_{\text{set II}}$  angle descriptors, with  $N_{\text{set I}} = M$  and  $N_{\text{set II}} \leq {}^M C_2$ . The total number of descriptors is  $N_{\text{desc}} = N_{\text{set I}} + N_{\text{set II}}$ . To optimize  $N_{\text{desc}}$ , we first optimize  $N_{\text{set I}}$ , till the error converges as shown in Fig. 7.1. Subsequently, we optimize  $N_{\text{set II}}$ . To do this, we consider a nearer subset of atoms of size  $M_a \leq M$ , and for each of these  $M_a$  atoms, we consider the angle subtended at the grid

point, by the atoms and their  $k$  nearest neighbors. This results in  $N_{\text{set II}} = M_a \times k$ , angle based descriptors, with  $M_a$  and  $k$  varied to yield the best results, as shown in Fig. 7.1. The pseudo-code for this process, as well as further details on feature convergence analysis are provided in [177].

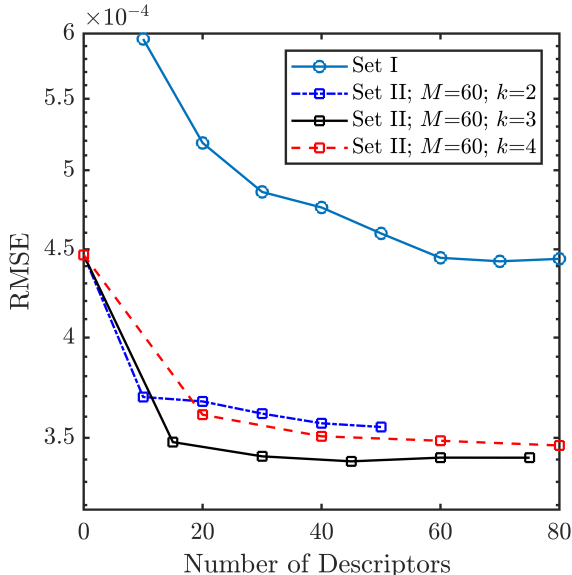


Figure 7.1: Convergence of error with respect to the number of descriptors, shown for aluminum. The blue line shows the convergence with respect to  $N_{\text{set I}}$ , while the other three lines show convergence with respect to  $N_{\text{set II}}$ . The optimal  $N_{\text{set I}}$  and  $N_{\text{set II}}$  are obtained where their test RMSE values converge.

### 7.2.5 Bayesian Neural Network

Bayesian Neural Networks (BNNs) have stochastic parameters in contrast to deterministic parameters used in conventional neural networks. They provide a mathematically rigorous and efficient way to quantify uncertainties in their prediction.

We use a Bayesian neural network to estimate the probability  $P(\rho|\mathbf{x}, \mathcal{D})$  of the output electron density  $\rho$  for a given input descriptor  $\mathbf{x} \in \mathbb{R}^{N_{\text{desc}}}$  and training data set  $\mathcal{D} = \{\mathbf{x}_i, \rho_i\}_{i=1}^{N_d}$ .



The probability is evaluated as:

$$P(\rho|\mathbf{x}, \mathcal{D}) = \int_{\Omega_w} P(\rho|\mathbf{x}, \mathbf{w})P(\mathbf{w}|\mathcal{D})d\mathbf{w}. \quad (7.1)$$

Here  $\mathbf{w} \in \Omega_w$  is the set of parameters of the network and  $N_d$  is the size of the training data set. Through this marginalization over parameters, a BNN provides a route to overcome modeling biases via averaging over an ensemble of networks. Given a prior distribution  $P(\mathbf{w})$  on the parameters, the posterior distribution of the parameters  $P(\mathbf{w}|\mathcal{D})$  are learned via the Bayes' rule as  $P(\mathbf{w}|\mathcal{D}) = P(\mathcal{D}|\mathbf{w})P(\mathbf{w})/P(\mathcal{D})$ , where  $P(\mathcal{D}|\mathbf{w})$  is the likelihood of the data.

This posterior distribution of parameters  $P(\mathbf{w}|\mathcal{D})$  is intractable since it involves the normalizing factor  $P(\mathcal{D})$ , which in turn is obtained via marginalization of the likelihood through a high dimensional integral. Therefore, it is approximated through techniques such as variational inference [259, 282, 283] or Markov Chain Monte Carlo methods [284]. In variational inference, as adopted here, a tractable distribution  $q(\mathbf{w}|\boldsymbol{\theta})$  called the ‘‘variational posterior’’ is considered, which has parameters  $\boldsymbol{\theta}$ . For instance, if the variational posterior is a Gaussian distribution the corresponding parameters are its mean and standard deviation,  $\boldsymbol{\theta} = (\boldsymbol{\mu}_\theta, \boldsymbol{\sigma}_\theta)$ . The optimal value of parameters  $\boldsymbol{\theta}$  is obtained by minimizing the statistical dissimilarity between the true and variational posterior distributions. The dissimilarity is measured through the KL divergence  $\text{KL} [q(\mathbf{w}|\boldsymbol{\theta}) || P(\mathbf{w}|\mathcal{D})]$ . This yields the following optimization problem:

$$\begin{aligned} \boldsymbol{\theta}^* &= \arg \min_{\boldsymbol{\theta}} \text{KL} [q(\mathbf{w}|\boldsymbol{\theta}) || P(\mathbf{w}|\mathcal{D})] \\ &= \arg \min_{\boldsymbol{\theta}} \int q(\mathbf{w}|\boldsymbol{\theta}) \log \left[ \frac{q(\mathbf{w}|\boldsymbol{\theta})}{P(\mathbf{w})P(\mathcal{D}|\mathbf{w})} P(\mathcal{D}) \right] d\mathbf{w}. \end{aligned} \quad (7.2)$$

This leads to the following loss function for BNN that has to be minimized:

$$\mathcal{F}_{\text{KL}}(\mathcal{D}, \boldsymbol{\theta}) = \text{KL} [q(\mathbf{w}|\boldsymbol{\theta}) || P(\mathbf{w})] - \mathbb{E}_{q(\mathbf{w}|\boldsymbol{\theta})}[\log P(\mathcal{D}|\mathbf{w})]. \quad (7.3)$$

This loss function balances the simplicity of the prior and the complexity of the data through its first and second terms respectively, yielding regularization [259, 260].

Once the parameters  $\boldsymbol{\theta}$  are learned, the BNNs can predict the charge density at any new input descriptor  $\mathbf{x}$ . In this work, the mean of the parameters ( $\boldsymbol{\mu}_\theta$ ) are used to make point estimate predictions of the BNN.

### 7.2.6 Uncertainty quantification

The variance in the output distribution  $P(\rho|\mathbf{x}, \mathcal{D})$  in Eq. 7.1 is the measure of uncertainty in the BNN's prediction. Samples from this output distribution can be drawn in three steps: In the first step, a  $j^{th}$  sample of the set of parameters,  $\widehat{\mathbf{w}}_{j=1, \dots, N_s}$ , is drawn from the variational posterior  $q(\mathbf{w}|\boldsymbol{\theta})$  which approximates the posterior distribution of parameters  $P(\mathbf{w}|\mathcal{D})$ . Here,  $N_s$  is the number of samples drawn from the variational posterior of parameters. In the second step, the sampled parameters are used to perform inference of the BNN ( $f_N$ ) to obtain the  $j^{th}$  prediction  $\widehat{\rho}_j = f_N^{\widehat{\mathbf{w}}_j}(\mathbf{x})$ . In the third step, the likelihood is assumed to be a Gaussian distribution:  $P(\rho|\mathbf{x}, \widehat{\mathbf{w}}_j) = \mathcal{N}(\widehat{\rho}_j, \sigma(\mathbf{x}))$ , whose mean is given by the BNN's prediction,  $\widehat{\rho}_j$ , and standard deviation by a heterogenous observation noise,  $\sigma(\mathbf{x})$ . A sample is drawn from this Gaussian distribution  $\mathcal{N}(\widehat{\rho}_j, \sigma(\mathbf{x}))$  that approximates a sample from the distribution  $P(\rho|\mathbf{x}, \mathcal{D})$ . The total variance of such samples can be expressed as:

$$\text{var}(\rho) = \sigma^2(\mathbf{x}) + \left[ \frac{1}{N_s} \sum_{j=1}^{N_s} (\widehat{\rho}_j)^2 - (\mathbb{E}(\widehat{\rho}_j))^2 \right]. \quad (7.4)$$

Here,  $\mathbb{E}(\widehat{\rho}_j) = \frac{1}{N_s} \sum_{j=1}^{N_s} f_N^{\widehat{\mathbf{w}}_j}(\mathbf{x})$ . The first term,  $\sigma^2(\mathbf{x})$ , in Eq. 7.4 is the aleatoric uncertainty that represents the inherent noise in the data and is considered irreducible. The second term (in the square brackets) in Eq. 7.4 is the epistemic uncertainty, that quantifies the modeling uncertainty.

In this work, the aleatoric uncertainty is learned via the BNN model along with the charge densities  $\rho$ . Therefore, for each input  $\mathbf{x}$ , the BNN learns two outputs:  $f_N^{\mathbf{w}}(\mathbf{x})$  and  $\sigma(\mathbf{x})$ . For a Gaussian likelihood, the noise  $\sigma$  is learned through the likelihood term of the

loss function Eq. 7.3 following [285] as:

$$\log P(\mathcal{D}|\mathbf{w}) = \sum_{i=1}^{N_d} -\frac{1}{2} \log \sigma_i^2 - \frac{1}{2\sigma_i^2} (f_N^{\mathbf{w}}(\mathbf{x}_i) - \rho_i)^2. \quad (7.5)$$

Here,  $N_d$  is the size of the training data set. The aleatoric uncertainty,  $\sigma$ , enables the loss to adapt to the data. The network learns to reduce the effect of erroneous labels by learning a higher value for  $\sigma^2$ , which makes the network more robust or less susceptible to noise. On the other hand, the model is penalized for predicting high uncertainties for all points through the  $\log \sigma^2$  term.

The epistemic uncertainty is computed by evaluating the second term of Eq. 7.4, via sampling  $\widehat{\mathbf{w}}_j$  from the variational posterior.

### 7.2.7 Transfer Learning using multi-scale data

Conventional DFT simulations for smaller systems are considerably cheaper than those for larger systems, as the computational cost scales cubically with the number of atoms present in the simulation cell. However, the ML models cannot be trained using simulation data from small systems alone. This is because, smaller systems are far more constrained in the number of atomic configurations they can adopt, thus limiting their utility in simulating a wide variety of materials phenomena. Additionally, the electron density from simulations of smaller systems differs from that of larger systems, due to the effects of periodic boundary conditions.

To predict accurately across all length scales while reducing the cost of training data generation via DFT simulations, we use a transfer learning approach here. Transfer learning is a machine learning technique where a network, initially trained on a substantial amount of data, is later fine-tuned on a smaller dataset for a different task, with only the last few layers being updated while the earlier layers remain unaltered [123]. The initial layers (called “frozen layers”) capture salient features of the inputs from the large dataset, while the re-trained layers act as decision-makers and adapt to the new problem.

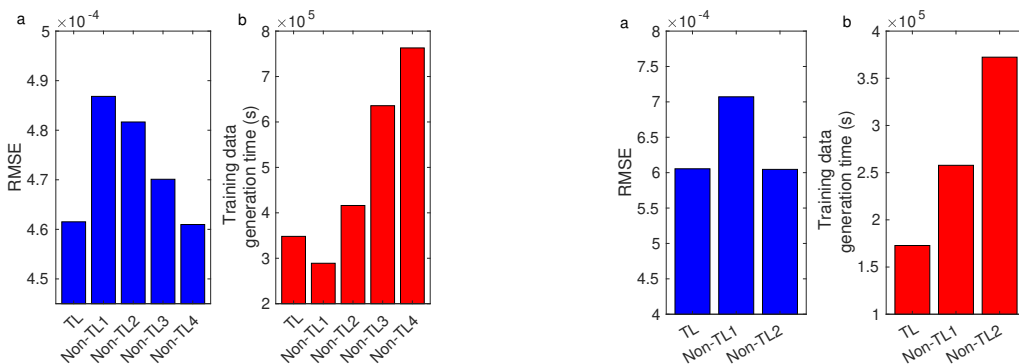


Figure 7.2: Comparison of (a) error and (b) training data generation time between models with and without transfer learning for aluminium (left) and SiGe (right) systems.

Transfer learning has been used in training neural network potentials, first on Density Functional Theory (DFT) data, and subsequently using datasets generated using more accurate, but expensive quantum chemistry models [286]. In contrast, in this work, transfer learning is employed to leverage the multi-scale aspects of the problem. Specifically, the present transfer learning approach leverages the statistical dissimilarity in data distributions between various systems and the largest system. This process is employed to systematically select the training data, ultimately reducing reliance on heuristics. This can be seen in Fig. 7.2 which depicts a comparison between a transfer learned (TL) model and various other models. This approach allows us to make electron density predictions across scales and system configurations, while significantly reducing the cost of training data generation.

In the case of aluminum, at first, we train the model using a large amount of data from DFT simulations of (smaller) 32-atom systems. Subsequently, we freeze the initial one-third layers of the model and re-train the remaining layers of the model using a smaller amount (40%) of data from simulations of (larger) 108-atom systems. Further training using data from larger bulk systems was not performed, since the procedure described above already provides good accuracy (Figs. 7.8, 7.16), which we attribute to the statistical similarity of the electron density of 108 atom systems and those with more atoms. A similar transfer learning procedure is used for the SiGe model, where we initially train with data from 64-

atom systems and subsequently retrain using data from 216-atom systems. Overall, due to the non-linear data generation cost using DFT simulations, the transfer learning approach reduces training data generation time by over 50%.

### 7.2.8 Postprocessing of ML predicted electron density

One way to test the accuracy of the ML models is to compute quantities of interest (such as the total ground state energy, exchange-correlation energy, and Fermi level) using the predicted electron density,  $\rho^{\text{ML}}$ . Although information about the total charge in the system is included in the prediction, it is generally good practice to first re-scale the electron density before postprocessing [119, 116], as follows:

$$\rho^{\text{scaled}}(\mathbf{r}) = \rho^{\text{ML}}(\mathbf{r}) \frac{N_e}{\int_{\Omega} \rho^{\text{ML}}(\mathbf{r}) d\mathbf{r}}. \quad (7.6)$$

Here,  $\Omega$  is the periodic supercell used in the calculations, and  $N_e$  is the number of electrons in the system. Using this scaled density, the Kohn-Sham Hamiltonian is set up within the SPARC code framework, which was also used for data generation via AIMD simulations [267, 268, 269]. A single step of diagonalization is then performed, and the energy of the system is computed using the Harris-Foulkes formula [287, 288]. The errors in predicting  $\rho^{\text{ML}}(\mathbf{r})$ , and the ground state energy thus calculated, can be seen in Fig. 7.8. More detailed error values can be found in [177].

## 7.3 Machine learning predictions

In this section, we present electron density predictions by the proposed machine learning (ML) model for two types of bulk materials — pure aluminum and alloys of silicon-germanium. These serve as prototypical examples of metallic and covalently bonded semi-conducting systems, respectively. These materials were chosen for their technological im-

portance and because the nature of their electronic fields is quite distinct, thus presenting distinct challenges to the ML model. Additionally, being metallic, the aluminum systems do not show simple localized electronic features often observed in insulators [276, 289], further complicating electron density prediction.

The overview of the present ML model is given in Fig. 7.3. The models are trained using a transfer learning approach, with thermalization used to sample a variety of system configurations. In the case of aluminum (Al), the model is trained initially on a 32-atom and subsequently on a 108-atom system. Corresponding system sizes for silicon germanium (SiGe) are 64 and 216 atoms respectively. Details of the ML model were provided in section 7.2.

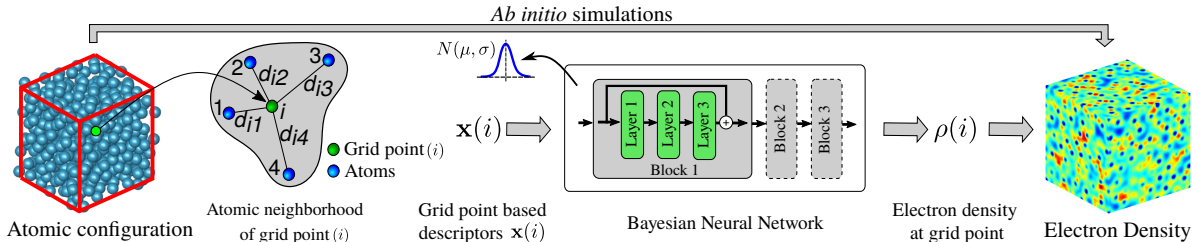


Figure 7.3: Overview of the present Machine Learning (ML) model. The first step is the training data generation via *ab initio* simulations shown by the arrow at the top. The second step is to generate atomic neighborhood descriptors  $\mathbf{x}(i)$  for each grid point,  $i$ , in the training configurations. The third step is to create a probabilistic map (Bayesian Neural Network with DenseNet like blocks consisting of skip connections) from atomic neighborhood descriptors  $\mathbf{x}(i)$  to the charge density at the corresponding grid point  $\rho(i)$ . The trained model is then used for inference which includes (i) descriptor generation for all grid points in the query configuration, (ii) forward propagation through the Bayesian Neural Network, and (iii) aggregation of the point-wise charge density  $\rho(i)$  to obtain the charge density field  $\rho$ .

We evaluate the performance of the ML models for a wide variety of test systems, which are by choice, well beyond the training data. This is ensured by choosing system sizes far beyond training, strained systems, systems containing defects, or alloy compositions

not included in the training. We assess the accuracy of the ML models by comparing predicted electron density fields and ground state energies against DFT simulations. In addition, we quantify the uncertainty in the model’s predictions. We decompose the total uncertainty into two parts: “aleatoric” and “epistemic”. The first is a result of inherent variability in the data, while the second is a result of insufficient knowledge about the model parameters due to limited training data. The inherent variability in the data might arise due to approximations and round-off errors incurred in the DFT simulations and calculation of the ML model descriptors. On the other hand, the modeling uncertainty arises due to the lack of or incompleteness in the data. This lack of data is inevitable since it is impossible to exhaustively sample all possible atomic configurations during the data generation process. Decomposing the total uncertainty into these two parts helps distinguish the contributions of inherent randomness and incompleteness in the data to the total uncertainty. In the present work, a “heteroscedastic” noise model is used to compute the aleatoric uncertainty, which captures the spatial variation of the noise/variance in the data.

### 7.3.1 Error Estimation

To evaluate the accuracy of the model, we calculated the Root Mean Squared Error (RMSE) for the entire test dataset, including systems of the same size as the training data as well as sizes bigger than training data. For aluminum, the RMSE was determined to be  $4.1 \times 10^{-4}$ , while for SiGe, it was  $7.1 \times 10^{-4}$ , which shows an improvement over RMSE values for Al available in [111]. The  $L^1$  norm per electron for Aluminum is  $2.63 \times 10^{-2}$  and for SiGe it is  $1.94 \times 10^{-2}$  for the test dataset. Additionally, the normalized RMSE is obtained by dividing the RMSE value by the range of respective  $\rho$  values for aluminum and SiGe. The normalized RMSE for aluminum and SiGe test dataset was found to be  $7.9 \times 10^{-3}$  for both materials. Details of training and test dataset can be found in [177]. However, briefly, the amount of data used in training for the two systems is as follows:

- Al: 127 snaps from 32 atom data and in addition 25 snaps from 108 atom data. The 108 atom data has  $90 \times 90 \times 90$  grid points, while the 32 atom system has  $60 \times 60 \times 60$  grid points.
- SiGe: 160 snaps of 64 atom data and in addition 30 snaps of 216 atom data. The 64 atom system has  $53 \times 53 \times 53$  grid points, while the 216 atom system has  $79 \times 79 \times 79$  grid points.

To assess the generalizability of the model, we evaluate the accuracy of the ML model using systems much larger than those used in training, but accessible to DFT. We consider two prototypical systems, an Aluminium system having 1372 atoms (Fig. 7.4) and a Silicon Germanium ( $\text{Si}_{0.5}\text{Ge}_{0.5}$ ) system having 512 atoms (Fig. 7.5). The model shows remarkable accuracy for both of these large systems. The RMSE is  $3.8 \times 10^{-4}$  and  $7.1 \times 10^{-4}$  for aluminum and SiGe respectively, which confirms the high accuracy of the model for system sizes beyond those used in training.

We now evaluate the performance of the ML model for systems containing extended and localized defects, although such systems were not used in training. We consider the following defects: mono-vacancies, di-vacancies, grain boundaries, edge, and screw dislocations for Al, and mono-vacancies and di-vacancies for SiGe. The electron density fields predicted by the ML models match with the DFT calculations extremely well, as shown in Figs. 7.6 and 7.7. The error magnitudes (measured as the  $L^1$  norm of the difference in electron density fields, per electron) are about  $2 \times 10^{-2}$  (see Fig. 7.8). The corresponding NRMSE is  $7.14 \times 10^{-3}$ . We show in Section 7.3.2, that the model errors and uncertainty can be both brought down significantly, by including a single snapshot with defects, during training.

Another stringent test of the generalizability of the ML models is performed by investigating  $\text{Si}_x\text{Ge}_{1-x}$  alloys, for  $x \neq 0.5$ . Although only equi-atomic alloy compositions (i.e.,  $x = 0.5$ ) were used for training, the error in prediction (measured as the  $L^1$  norm of the difference in electron density fields, per electron) is lower than  $3 \times 10^{-2}$  (see Fig. 7.8). The



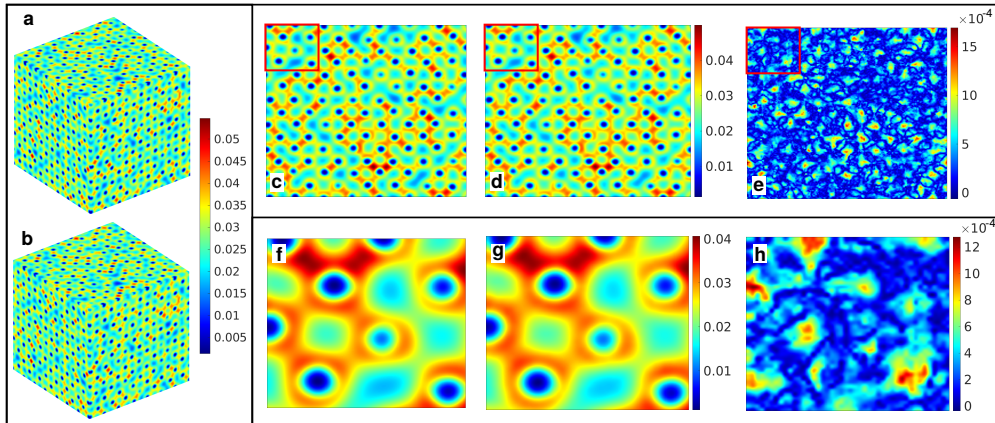


Figure 7.4: 1372 atom aluminum simulation cell at 631 K. Electron densities (a) calculated by DFT and (b) predicted by ML. The two-dimensional slice of (b) that has the highest mean squared error, as calculated by (c) DFT and predicted by (d) ML. (e) Corresponding absolute error in ML with respect to DFT. (f) - (h) Magnified view of the rectangular areas in (c) - (e) respectively. The unit for electron density is  $e \text{ Bohr}^{-3}$ , where  $e$  denotes the electronic charge.

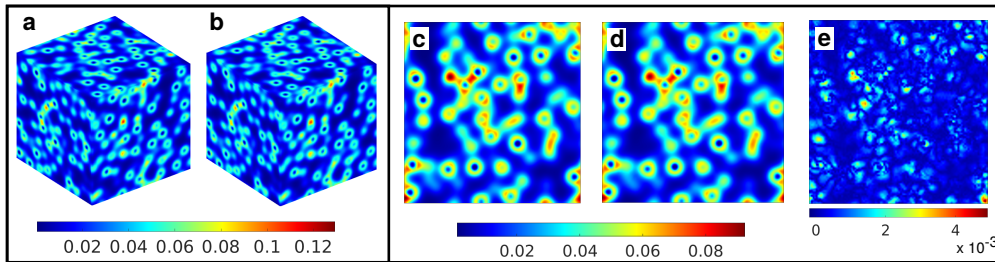


Figure 7.5: 512 atoms  $\text{Si}_{0.5}\text{Ge}_{0.5}$  simulation cell at 2300 K. Electron densities (a) calculated by DFT and (b) predicted by ML. The two-dimensional slice of (b) that has the highest mean squared error, as calculated by (c) DFT and predicted by (d) ML. (e) Corresponding absolute error in ML with respect to DFT. The unit for electron density is  $e \text{ Bohr}^{-3}$ , where  $e$  denotes the electronic charge.

corresponding RMSE is  $8.04 \times 10^{-4}$  and NRMSE is  $7.32 \times 10^{-3}$ . We would like to make a note that we observed good accuracy in the immediate neighborhood ( $x = 0.4$  to  $0.6$ ) of

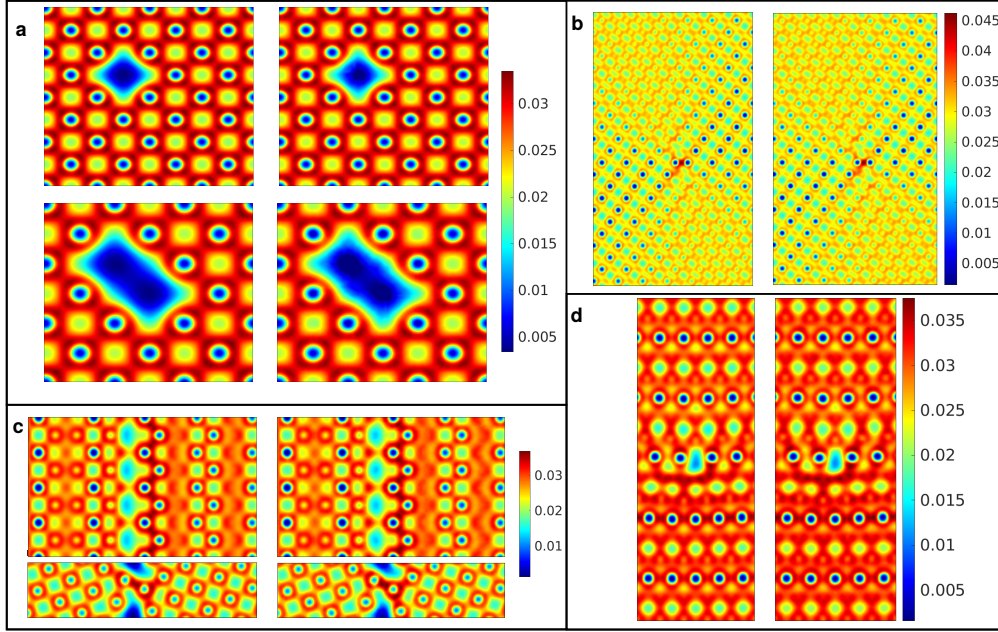


Figure 7.6: Electron density contours for aluminum systems with localized and extended defects — Left: calculated by DFT, Right: predicted by ML. (a) (Top) Mono-vacancy in 256 atom aluminum system, (Bottom) Di-Vacancy in 108 atom aluminum system, (b) (1 1 0) plane of a perfect screw dislocation in aluminum with Burgers vector  $\frac{a_0}{2}[110]$ , and line direction along  $[110]$ . The coordinate system was aligned along  $[1\bar{1}2]-[\bar{1}11]-[110]$ , (c) (Top) (0 1 0) plane, (bottom) (0 0 1) plane of a  $[001]$  symmetric tilt grain boundary ( $0^\circ$  inclination angle) in aluminum, (d) Edge dislocation in aluminum with Burgers vector  $\frac{a_0}{2}[110]$ . The coordinate system was aligned along  $[110]-[\bar{1}11]-[1\bar{1}2]$  and the dislocation was created by removing a half-plane of atoms below the glide plane. The unit for electron density is  $e \text{ Bohr}^{-3}$ , where  $e$  denotes the electronic charge.

the training data ( $x = 0.5$ ). Prediction for  $x = 0.4$  is shown in Fig. 6(ii). The prediction accuracy however decreases as we move far away from the training data composition. This generalization performance far away from the training data is expected. We have also carried out tests with aluminum systems subjected to volumetric strains, for which the results were similarly good.

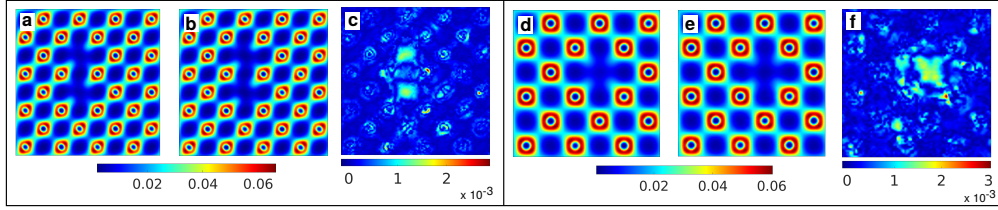


Figure 7.7: Electron density contours and absolute error in ML for SiGe systems with (a-c) Si double vacancy defect in 512 atom system (d-f) Ge single vacancy defect in 216 atom system. Densities (a,d) calculated by DFT, (b,e) predicted by ML, and (c,f) error in ML predictions. Note that the training data for the above systems did not include any defects. The unit for electron density is  $e \text{ Bohr}^{-3}$ , where  $e$  denotes the electronic charge.

Our electron density errors are somewhat lower than compared to the earlier works [110, 111], At the same time, thanks to the sampling and transfer learning techniques adopted by us, the amount of time spent on DFT calculations used for producing the training data is also smaller. To further put into context the errors in the electron density, we evaluate the ground state energies from the charge densities predicted by the ML model through a postprocessing step and compare these with the true ground state energies computed via DFT. Details on the methodology for postprocessing have been discussed in section 7.2.8, and a summary of our postprocessing results can be seen in Fig. 7.8. On average, the errors are well within chemical accuracy for all test systems considered and are generally  $\mathcal{O}(10^{-4})$  Ha atom $^{-1}$ , as seen in Fig. 7.8. Further details can regarding the energies can be seen in Tables 7.1 and 7.2.

Furthermore, not only are the energies accurate, but the derivatives of the energies, e.g., with respect to the supercell lattice parameter, are found to be quite accurate as well (see Fig. 7.9 and Table 7.3). This enables us to utilize the ML model to predict the optimum lattice parameter — which is related to the first derivative of the energy curve, and the bulk modulus — which is related to the second derivative of the energy curve, accurately. We observe that the lattice parameter is predicted accurately to a fraction of a percent,

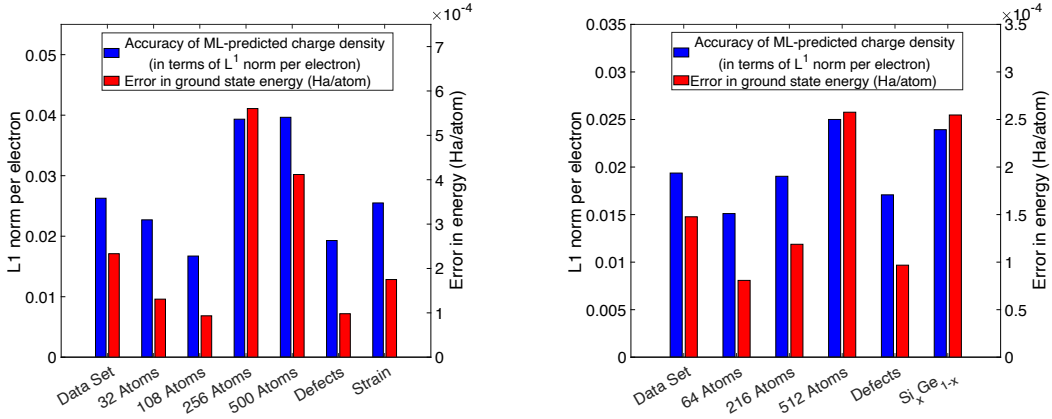


Figure 7.8: A comparison of the accuracy in the prediction of the charge density (in terms of the  $L^1$  norm per electron between  $\rho^{\text{DFT}}$  and  $\rho^{\text{scaled}}$ ), and the error (in Ha/atom) in the ground state total energy computed using  $\rho^{\text{DFT}}$  and  $\rho^{\text{scaled}}$ , for Al (left), and SiGe (right) systems.  $\rho^{\text{scaled}}$  is the scaled ML predicted electron density as given in Eq. 7.6. We observe that the errors are far better than chemical accuracy, i.e., errors below  $1 \text{ kcal mol}^{-1}$  or  $1.6$  milli-Hartree atom $^{-1}$ , for both systems, even while considering various types of defects and compositional variations. Note that for  $\text{Si}_x\text{Ge}_{1-x}$ , we chose  $x = 0.4, 0.45, 0.55, 0.6$ .

and the bulk modulus is predicted to within 1% of the DFT value (which itself is close to experimental values [17]). This demonstrates the utility of the ML models to predict not only the electron density but also other relevant physical properties.

Overall, the generalizability of our models is strongly suggestive that our use of thermalization to sample the space of atomic configurations, and the use of transfer-learning to limit training data generation of large systems are both very effective. We discuss uncertainties arising from the use of these strategies and due to the neural network model, in addition to the noise in the data, in the following sections.

Case	Accuracy of electron density (L <sup>1</sup> norm per electron)	Ground-state energy (Ha/atom)	Exch. Corr. energy (Ha/atom)	Fermi level (Ha)	Max error in eigenvalue (Ha)
Entire test data set	$2.62 \times 10^{-2}$	$2.33 \times 10^{-4}$	$4.36 \times 10^{-4}$	$4.61 \times 10^{-4}$	$4.58 \times 10^{-3}$
Al (32 atoms)	$2.27 \times 10^{-2}$	$1.30 \times 10^{-4}$	$1.07 \times 10^{-3}$	$9.80 \times 10^{-4}$	$4.10 \times 10^{-3}$
Al (108 atoms)	$1.67 \times 10^{-2}$	$9.33 \times 10^{-5}$	$9.82 \times 10^{-5}$	$1.13 \times 10^{-4}$	$1.87 \times 10^{-3}$
Al (256 atoms)	$3.93 \times 10^{-2}$	$5.60 \times 10^{-4}$	$4.18 \times 10^{-4}$	$2.03 \times 10^{-4}$	$6.67 \times 10^{-3}$
Al (500 atoms)	$3.96 \times 10^{-2}$	$4.11 \times 10^{-4}$	$2.41 \times 10^{-4}$	$5.04 \times 10^{-4}$	$8.52 \times 10^{-3}$
Al vacancy defects	$1.92 \times 10^{-2}$	$9.80 \times 10^{-5}$	$1.42 \times 10^{-4}$	$2.98 \times 10^{-4}$	$3.85 \times 10^{-3}$
Strain imposed Al	$2.54 \times 10^{-2}$	$1.75 \times 10^{-4}$	$8.91 \times 10^{-4}$	$6.64 \times 10^{-4}$	$3.11 \times 10^{-3}$

Table 7.1: Accuracy of the ML predicted electron density in terms of the L<sup>1</sup> norm per electron, calculated as  $\frac{1}{N_e} \times \int_{\Omega} |\rho^{\text{scaled}}(\mathbf{r}) - \rho^{\text{DFT}}(\mathbf{r})| d\mathbf{r}$ , for various test cases for an FCC aluminum bulk system ( $N_e$  is the number of electrons in the system). Also shown in the table are errors in the different energies as computed from  $\rho^{\text{scaled}}$ . The test data set for post-processing was chosen such that it covered examples from all system sizes, configurations, and temperatures. For calculating the relevant energies,  $\rho^{\text{scaled}}$  was used as the initial guess for the electron density, and a single Hamiltonian diagonalization step was performed. Energies were then computed.

### 7.3.2 Uncertainty quantification

The present work uses a Bayesian Neural Network (BNN) which provides a systematic route to uncertainty quantification (UQ) through its stochastic parameters as opposed to other methods for UQ, for instance ensemble averaging [290]. Estimates of epistemic and aleatoric uncertainties for the following systems are shown: a defect-free Al system with 1372 atoms (Fig. 7.10), a 256-atom Al system with a mono-vacancy (Fig. 7.12(a-d)), and a Si<sub>0.4</sub>Ge<sub>0.6</sub> alloy (Fig. 7.11). Note, for the results in Fig. 7.12(a-d) the training data does not contain any systems having defects, and for the results in Fig. 7.11 the training data contains only 50 – 50 composition.

Case	Accuracy of electron density (L <sup>1</sup> norm per electron)	Ground-state energy (Ha/atom)	Exch. Corr. energy (Ha/atom)	Fermi level (Ha)	Max error in eigenvalue (Ha)
Entire test data set	$1.93 \times 10^{-2}$	$1.47 \times 10^{-4}$	$9.34 \times 10^{-4}$	$1.43 \times 10^{-3}$	$7.29 \times 10^{-3}$
Si <sub>0.5</sub> Ge <sub>0.5</sub> (64 atoms)	$1.51 \times 10^{-2}$	$8.08 \times 10^{-5}$	$1.40 \times 10^{-3}$	$8.71 \times 10^{-4}$	$5.07 \times 10^{-3}$
Si <sub>0.5</sub> Ge <sub>0.5</sub> (216 atoms)	$1.90 \times 10^{-2}$	$1.18 \times 10^{-4}$	$2.50 \times 10^{-4}$	$3.08 \times 10^{-4}$	$4.99 \times 10^{-3}$
Si <sub>0.5</sub> Ge <sub>0.5</sub> (512 atoms)	$2.50 \times 10^{-2}$	$2.57 \times 10^{-4}$	$3.70 \times 10^{-4}$	$1.32 \times 10^{-3}$	$1.27 \times 10^{-2}$
Si <sub>0.5</sub> Ge <sub>0.5</sub> vacancy defects	$1.70 \times 10^{-2}$	$9.68 \times 10^{-5}$	$2.36 \times 10^{-4}$	$2.82 \times 10^{-3}$	$6.85 \times 10^{-3}$
Si <sub>x</sub> Ge <sub>1-x</sub> ( $x \neq 0.5$ )	$2.39 \times 10^{-2}$	$2.54 \times 10^{-4}$	$2.41 \times 10^{-3}$	$1.25 \times 10^{-3}$	$9.36 \times 10^{-3}$

Table 7.2: Accuracy of the ML predicted electron density in terms of L<sup>1</sup> norm per electron, calculated as  $\frac{1}{N_e} \times \int_{\Omega} |\rho^{\text{scaled}}(\mathbf{r}) - \rho^{\text{DFT}}(\mathbf{r})| d\mathbf{r}$ , for various test cases for Si<sub>0.5</sub>Ge<sub>0.5</sub> ( $N_e$  is the number of electrons in the system). Also shown in the table are errors in the different energies as computed from  $\rho^{\text{scaled}}$ . The test data set for post-processing was chosen such that it covered examples from all system sizes and temperatures. For calculating the relevant energies,  $\rho^{\text{scaled}}$  was used as the initial guess for the electron density, and a single Hamiltonian diagonalization step was performed. Energies were then computed. For Si<sub>x</sub>Ge<sub>1-x</sub>, we used  $x = 0.40, 0.45, 0.55, 0.60$ .

Material property	$2 \times 2 \times 2$ supercell	$3 \times 3 \times 3$ supercell
Lattice parameter (Bohr)	7.4294 (7.4281)	7.5208 (7.5188)
Bulk modulus (GPa)	92.2774 (92.7708)	75.7977 (76.3893)

Table 7.3: A comparison between the calculated lattice parameter and the bulk modulus for aluminum using  $\rho^{\text{ML}}$  and  $\rho^{\text{DFT}}$  (DFT values in parentheses). We observe that the predicted lattice parameter closely matches the value given by DFT calculations. The “true” optimized lattice parameter for Al, using a fine k-space mesh, is found to be 7.5098 Bohr while experimental values are about 7.6 Bohr [19]). The ML predicted value of the bulk modulus matches the DFT value very closely, which itself is very close to the experimental value of approximately 76 GPa [17], at room temperature.

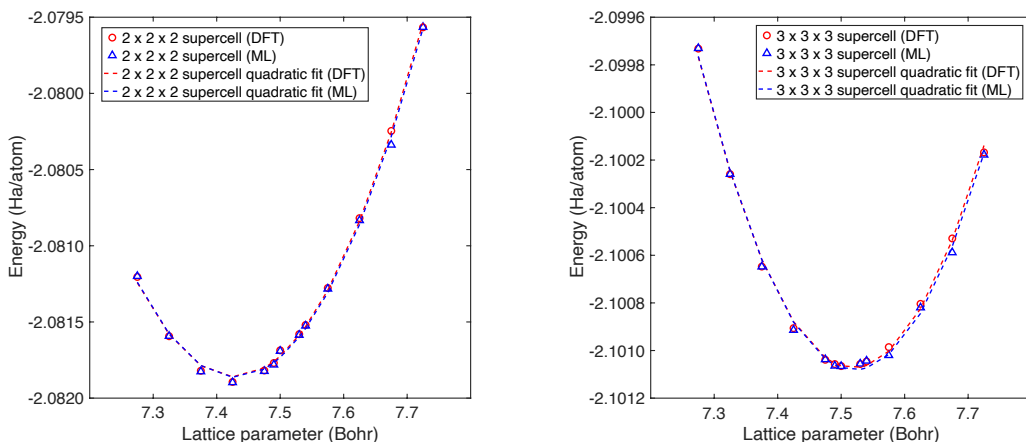


Figure 7.9: The energy curve with respect to different lattice parameters for a  $2 \times 2 \times 2$  (left) and  $3 \times 3 \times 3$  (right) supercell of aluminum atoms. Overall, we see excellent agreement in the energies (well within chemical accuracy). The lattice parameter (related to the first derivative of the energy plot) calculated in each case agrees with the DFT-calculated lattice parameter to  $\mathcal{O}(10^{-2})$  Bohr or better (i.e., it is accurate to a fraction of a percent). The bulk modulus calculated (related to the second derivative of the energy plot) from DFT data and ML predictions agree to within 1%. For the  $3 \times 3 \times 3$  supercell, the bulk modulus calculated via DFT calculations is 76.39 GPa, close to the experimental value of about 76 GPa [17]. The value calculated from ML predictions is 75.80 GPa.

In these systems, the aleatoric uncertainty has the same order of magnitude as the epistemic uncertainty. This implies that the uncertainty due to the inherent randomness in the data is of a similar order as the modeling uncertainty. The aleatoric uncertainty is significantly higher near the nuclei (Fig. 7.10 and Fig. 7.11) and also higher near the vacancy (Fig. 7.12). This indicates that the training data has high variability at those locations. The epistemic uncertainty is high near the nucleus (Fig. 7.10 and Fig. 7.11) since only a small fraction of grid points are adjacent to nuclei, resulting in the scarcity of training data for such points. For the system with vacancy, the aleatoric uncertainty is higher in most regions, as shown in Fig. 7.12(c). However, the epistemic uncertainty is significantly higher only at

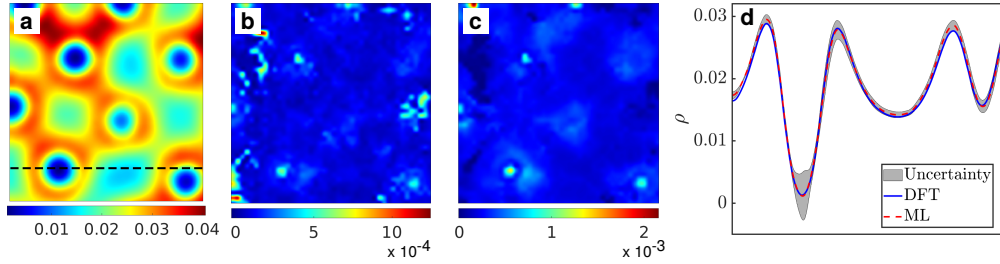


Figure 7.10: Uncertainty quantification for 1372 atom aluminum system. (a) ML prediction of the electron density, (b) Epistemic Uncertainty (c) Aleatoric Uncertainty (d) Total Uncertainty shown along the dotted line from the ML prediction slice. The uncertainty represents the bound  $\pm 3\sigma_{total}$ , where,  $\sigma_{total}$  is the total uncertainty. The unit for electron density is  $e \text{ Bohr}^{-3}$ , where  $e$  denotes the electronic charge.

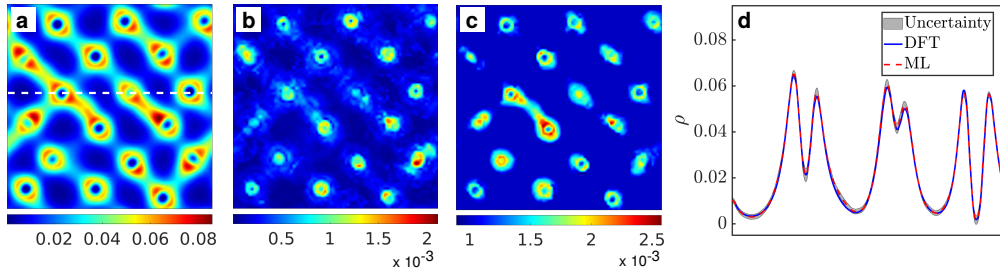


Figure 7.11: Uncertainty quantification for  $\text{Si}_{0.4}\text{Ge}_{0.6}$  system. (a) ML prediction of the electron density, (b) Epistemic Uncertainty (c) Aleatoric Uncertainty (d) Total Uncertainty shown along the dotted line from the ML prediction slice. The uncertainty represents the bound  $\pm 3\sigma_{total}$ , where,  $\sigma_{total}$  is the total uncertainty. The unit for electron density is  $e \text{ Bohr}^{-3}$ , where  $e$  denotes the electronic charge.

the vacancy (Fig. 7.12(b)), which might be attributed to the complete absence of data from systems with defects in the training.

To investigate the effect of adding data from systems with defects in the training, we added a single snapshot of 108 atom aluminum simulation with mono vacancy defect to the training data. This reduces the error at the defect site significantly and also reduces the uncertainty (Fig. 7.12(e)). However, the uncertainty is still quite higher at the defect site



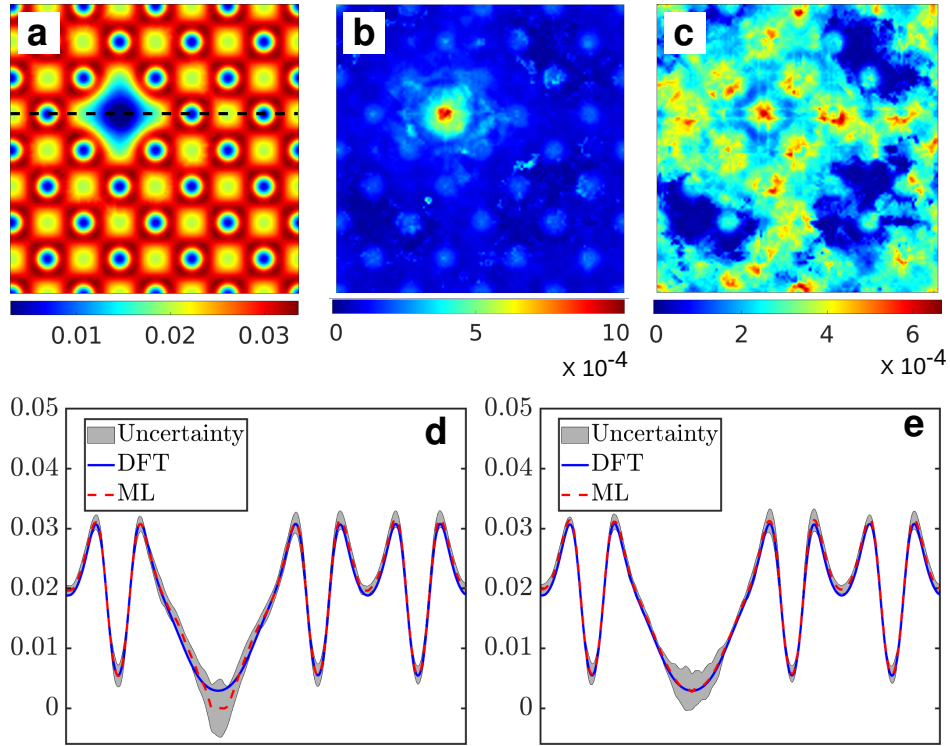


Figure 7.12: Uncertainty quantification for a 256 atom aluminum system with a mono vacancy defect. (a) ML prediction of the electron density shown on the defect plane, (b) Epistemic uncertainty (c) Aleatoric uncertainty (d) Uncertainty shown along the black dotted line from the ML prediction slice. The uncertainty represents the bound  $\pm 3\sigma_{total}$ , where,  $\sigma_{total}$  is the total uncertainty. Note that the model used to make the predictions in (a-d) is not trained on the defect data, as opposed to the model used for (e), where defect data from the 108 atom aluminum system was used to train the model. The uncertainty and error at the location of the defect reduce with the addition of defect data in the training, as evident from (d) and (e). The unit for electron density is  $e \text{ Bohr}^{-3}$ , where  $e$  denotes the electronic charge.

because the data is biased against the defect site. That is, the amount of training data available at the defect site is much less than the data away from it. Thus, this analysis distinguishes uncertainty from inaccuracy.

To investigate the effect of adding data from larger systems in training, we compare two models. The first model is trained with data from the 32-atom system. The second model uses a transfer learning approach where it is initially trained using the data from the 32-atom system and then a part of the model is retrained using data from the 108-atom system. We observe a significant reduction in the error and in the epistemic uncertainty for the transfer learned model as compared to the one without transfer learning. The RMSE on the test system (256 atom) decreases by 50% when the model is transfer learned using 108 atom data. The addition of the 108-atom system’s data to the training data decreases epistemic uncertainty as well since the 108-atom system is less restricted by periodic boundary conditions than the 32-atom system. Further, it is also statistically more similar to the larger systems used for testing [177]. These findings demonstrate the effectiveness of the Bayesian Neural Network in pinpointing atomic arrangements or physical sites where more data is essential for enhancing the ML model’s performance. Additionally, they highlight its ability to measure biases in the training dataset. The total uncertainty in the predictions provides a confidence interval for the ML prediction. This analysis provides an upper bound of uncertainty arising out of two key heuristic strategies adopted in our ML model: data generation through thermalization of the systems and transfer learning.

### **7.3.3 Computational efficiency gains and confident prediction for very large system sizes**

Conventional KS-DFT calculations scale as  $\mathcal{O}(N_a^3)$  with respect to the number of atoms  $N_a$ , whereas, our ML model scales linearly (i.e.,  $\mathcal{O}(N_a)$ ), as shown in Fig. 7.13. This provides computational advantage for ML model over KS-DFT with increasing number of atoms. For example, even with 500 atoms, the calculation wall times for ML model is 2 orders of magnitude lower than KS-DFT. The linear scaling behavior of the ML model with respect to the number of atoms can be understood as follows. As the number of atoms within the simulation domain increases, so does the total simulation domain size, leading to a linear

increase in the total number of grid points (keeping the mesh size constant, to maintain calculation accuracy). Since the machine learning inference is performed for each grid point, while using information from a fixed number of atoms in the local neighborhood of the grid point, the inference time is constant for each grid point. Thus the total ML prediction time scales linearly with the total number of grid points, and hence the number of atoms in the system.

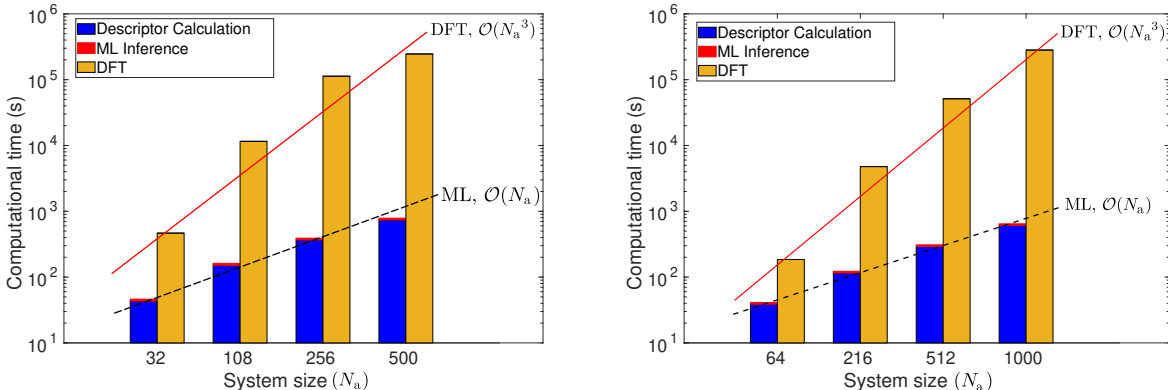


Figure 7.13: Computational time comparison between DFT calculations and prediction via trained ML model. (Top) Aluminum, (Bottom) SiGe. The DFT calculations scale  $\mathcal{O}(N_a^3)$  with respect to the system size (number of atoms  $N_a$ ), whereas, the present ML model scales linearly (i.e.,  $\mathcal{O}(N_a)$ ). The time calculations were performed using the same number of CPU cores and on the same system (Perlmutter CPU).

Taking advantage of this trend, the ML model can be used to predict the electronic structure for system sizes far beyond the reach of conventional calculation techniques, including systems containing millions of atoms, as demonstrated next. We anticipate that with suitable parallel programming strategies (the ML prediction process is embarrassingly parallel) and computational infrastructure, the present strategy can be used to predict the electronic structure of systems with hundreds of millions or even billions of atoms. Recently, there have been attempts at electronic structure predictions at million atom scales. In [291], a machine learning based potential is developed for germanium–antimony–tellurium alloys, effectively

working for device scale systems containing over half a million atoms. Another contribution comes from Fiedler et al. [112], where they present a model predicting electronic structure for systems containing over 100,000 atoms.

We show the electron densities, as calculated by our ML model, for a four million atom system of Al and a one million atom system of SiGe, in Figs. 7.14 and 7.15 respectively. In addition to predicting electron densities, we also quantify uncertainties for these systems. We found that the ML model predicts larger systems with equally high certainty as smaller systems [177]. The confidence interval obtained by the total uncertainty provides a route to assessing the reliability of predictions for these million atom systems for which KS-DFT calculations are simply not feasible. A direct comparison of ML obtained electron density with DFT for large systems is not done till date, mainly because simulating such systems with DFT is impractical. However, recent advancements in DFT techniques hold promise for simulating large-scale systems [96, 292, 293]. In future, it will be worthwhile to compare ML predicted electron density for large systems and the electron density obtained through DFT, utilizing these recently introduced DFT techniques.

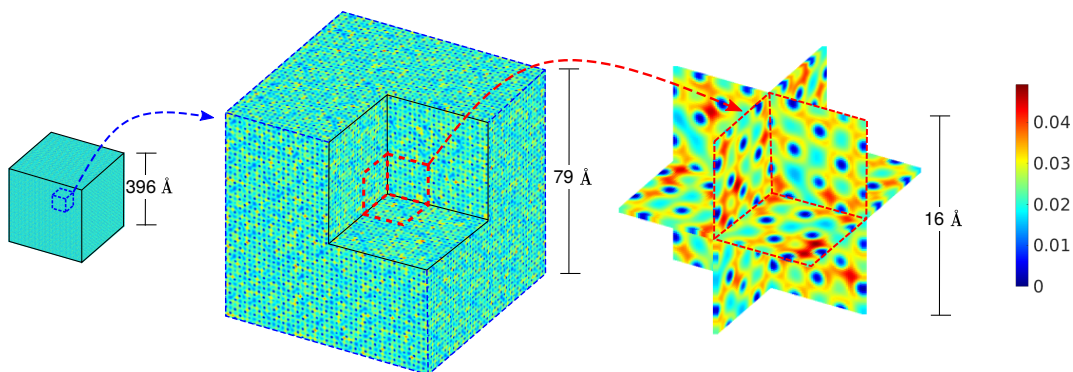


Figure 7.14: Prediction of electronic structure for aluminum system containing  $\approx 4.1$  million atoms. The unit for electron density is  $e \text{ Bohr}^{-3}$ , where  $e$  denotes the electronic charge.

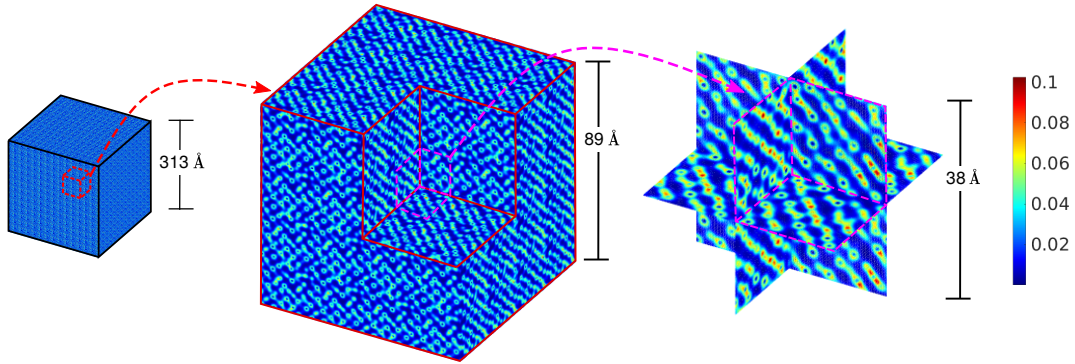


Figure 7.15: Prediction of electronic structure for  $\text{Si}_{0.5}\text{Ge}_{0.5}$  system containing  $\approx 1.4$  million atoms. The unit for electron density is  $e \text{ Bohr}^{-3}$ , where  $e$  denotes the electronic charge.

### 7.3.4 Reduction of training data generation cost via transfer learning

One of the key challenges in developing an accurate ML model for electronic structure prediction is the high computational cost associated with the generation of the training data through KS-DFT, especially for predicting the electron density for systems across length-scales. A straightforward approach would involve data generation using sufficiently large systems wherein the electron density obtained from DFT is unaffected by the boundary constraints. However, simulations of larger bulk systems are significantly more expensive than smaller systems. To address the computational burden of simulating large systems, strategies such as “fragmentation” have been used in electronic structure calculations [294, 295]. Further, certain recent studies on Machine Learning Interatomic Potentials suggest utilizing portions of a larger system for training the models [296, 297]. To the best of our knowledge, there is no corresponding work that utilizes fragmentation in ML modeling of the electron density. In this work, to address the issue, we employed a transfer learning (TL) approach. We first trained the ML model on smaller systems and subsequently trained a part of the neural network using data from larger systems. This strategy allows us to obtain an efficient ML model that requires fewer simulations of expensive large-scale systems compared to what would have been otherwise required without the TL approach. The effectiveness of the

TL approach stems from its ability to retain information from a large quantity of cheaper, smaller scale simulation data. We would like to note however, that the transfer learning approach is inherently bound by the practical constraints associated with simulating the largest feasible system size.

As an illustration of the above principles, we show in Fig. 7.16, the RMSE obtained on 256 atom data (system larger than what was used in the training data) using the TL model and the non-TL model. We also show the time required to generate the training data for both models. For the Al systems, we trained the TL model with 32-atom data first and then 108-atom data. In contrast, the non-TL model was trained only on the 108-atom data.

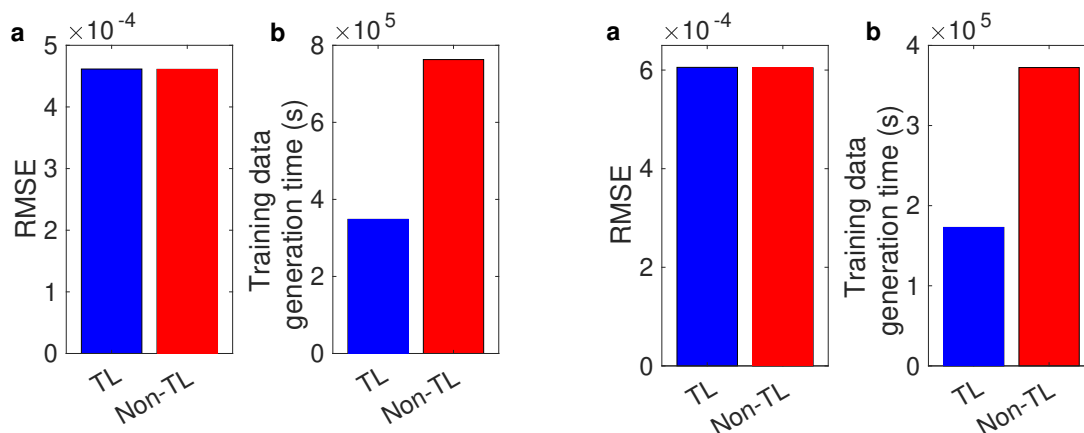


Figure 7.16: Models with Transfer Learning (TL) and without Transfer Learning (Non-TL) for aluminium (left) and SiGe (right): (a) Root mean square error (RMSE) on the test dataset and (b) Computational time to generate the training data. In the case of aluminum, the TL model is trained using 32 and 108 atom data. For SiGe, the TL model was trained using 64 and 216 atom data. In the case of aluminum, the non-TL model is trained using 108 atom data. Whereas, in the case of SiGe, the non-TL model is trained using 216 atom data.

The non-TL model requires significantly more 108-atom data than the TL model to achieve a comparable RMSE on the 256-atom dataset. Moreover, the TL model's training data generation time is approximately 55% less than that of the non-TL model. This repre-

sents a substantial computational saving in developing the ML model for electronic structure prediction, making the transfer learning approach a valuable tool to expedite such model development. Similar savings in training data generation time were observed for SiGe as shown in Fig. 7.16. In the case of SiGe, the TL model was first trained using 64 atom data and then transfer learned using 216 atom data.

## 7.4 Discussions

We have developed an uncertainty quantification (UQ) enabled machine learning (ML) model that creates a map from the descriptors of atomic configurations to the electron densities. We use simple scalar product-based descriptors to represent the atomic neighborhood of a point in space. These descriptors, while being easy to compute, satisfy translational, rotational, and permutational invariances. In addition, they avoid any handcrafting. We systematically identify the optimal set of descriptors for a given dataset. Once trained, our model enables predictions across multiple length scales and supports embarrassingly parallel implementation. As far as we can tell, our work is the first attempt to systematically quantify uncertainties in ML predicted electron densities across different scales relevant to materials physics. To alleviate the high cost of training data generation via KS-DFT, we propose a two-pronged strategy: i) we use thermalization to comprehensively sample system configurations, leading to a highly transferable ML model; and ii) we employ transfer learning to train the model using a large amount of inexpensively generated data from small systems while retraining a part of the model using a small amount of data from more expensive calculations of larger systems. The transfer learning procedure is systematically guided by the probability distributions of the data. This approach enables us to determine the maximum size of the training system, reducing dependence on heuristic selection. As a result of these strategies, the cost of training data generation is reduced by more than 50%, while the models continue to be highly transferable across a large variety of material configurations.

Our use of Bayesian Neural Networks (BNNs) allows the uncertainty associated with these aforementioned strategies to be accurately assessed, thus enabling confident predictions in scenarios involving millions of atoms, for which ground-truth data from conventional KS-DFT calculations is infeasible to obtain. Overall, our ML model significantly decreases the reliance on heuristics used by prior researchers, streamlining the process of ML-based electronic structure prediction and making it more systematic.

We demonstrate the versatility of the proposed machine learning models by accurately predicting electron densities for multiple materials and configurations. We focus on bulk aluminum and Silicon-Germanium alloy systems. The ML model shows remarkable accuracy when compared with DFT calculations, even for systems containing thousands of atoms. In the future, a similar model can be developed to test the applicability of the present descriptors and ML framework for molecules across structural and chemical space [298, 299, 300, 301]. As mentioned above, the ML model also has excellent generalization capabilities, as it can predict electron densities for systems with localized and extended defects, and varying alloy compositions, even when the data from such systems were not included in the training. It is likely that the ensemble averaging over model parameters in the BNNs, along with comprehensive sampling of the descriptor space via system thermalization together contribute to the model generalization capabilities. Our findings also show a strong agreement between physical parameters calculated from the DFT and ML electron densities (e.g. lattice constants and bulk moduli).

To rigorously quantify uncertainties in the predicted electron density, we adopt a Bayesian approach. Uncertainty quantification by a Bayesian neural network (BNN) is mathematically well-founded and offers a more reliable measure of uncertainty in comparison to non-Bayesian approaches such as the method of ensemble averaging. Further, we can decompose the total uncertainty into aleatoric and epistemic parts. This decomposition allows us to distinguish and analyze the contributions to the uncertainty arising from (i) inherent noise in the training data (i.e. aleatoric uncertainty) and (ii) insufficient knowledge about the model



parameters due to the lack of information in the training data (i.e. epistemic uncertainty). The aleatoric uncertainty or the noise in the data is considered irreducible, whereas the epistemic uncertainty can be reduced by collecting more training data. As mentioned earlier, the UQ capability of the model allows us to establish an upper bound on the uncertainty caused by two key heuristic strategies present in our ML model, namely, data generation via the thermalization of systems and transfer learning.

The reliability of the ML models is apparent from the low uncertainty of its prediction for systems across various length-scales and configurations. Furthermore, the magnitude of uncertainty for the million-atom systems is similar to that of smaller systems for which the accuracy of the ML model has been established. This allows us to have confidence in the ML predictions of systems involving multi-million atoms, which are far beyond the reach of conventional DFT calculations.

The ML model can achieve a remarkable speed-up of more than two orders of magnitude over DFT calculations, even for systems involving a few hundred atoms. As shown here, these computational efficiency gains by the ML model can be further pushed to regimes involving multi-million atoms, not accessible via conventional KS-DFT calculations.

In the future, we intend to leverage the uncertainty quantification aspects of this model to implement an active learning framework. This framework will enable us to selectively generate training data, reducing the necessity of extensive datasets and significantly lowering the computational cost associated with data generation. Moreover, we anticipate that the computational efficiencies offered via the transfer learning approach, are likely to be even more dramatic while considering more complex materials systems, e.g. compositionally complex alloys [302, 303].

## CHAPTER 8

### Conclusion and future directions

In summary, in Chapters 2 and 3, we have presented a novel spectral method, HelicES, for efficiently solving the Schrödinger equation for quasi-one-dimensional materials and structures. The basis functions in our method — helical waves — are natural analogs of plane-waves, and allow systematically convergent electronic structure calculations of materials such as nanowires, nanoribbons and nanotubes to be carried out. We have discussed various mathematical, algorithmic and implementation oriented issues of our technique. We have also used our method to carry out a variety of demonstrative calculations and studied its accuracy, computational efficiency, and convergence behaviors.

We anticipate that the method presented here will find utility in the discovery and characterization of new forms of low dimensional matter. It is particularly well suited for coupling with specialized machine learning techniques [116] and for the multiscale modeling of low dimensional systems [169]. Building self-consistency into the method, so as to enable *ab initio* calculations (e.g. using Hartree-Fock or Kohn-Sham Density Functional Theory [170]) remains the scope of ongoing and future work. An important first step in this direction is efficient solution of the associated electrostatics problem [10], towards which we have been making recent progress [168, 304], the details of which were elucidated in Chapter 4. Specifically, we developed a novel pseudo-spectral method to solve for the Hartree electrostatic potential and note that our framework may be used in other settings too, such as the Navier-Stokes equation in fluid dynamics, and the Cahn-Hilliard [305] and Allen-Cahn [306, 307] equations for phase separation in helical geometries. We showcase orders of mag-

nitide reduction in wall times using our framework which, in conjunction with HelicES, paves the way for a highly efficient self consistent density functional theory package. The full power of some of the techniques described in Chapters 2, 3, and 4 can be brought to bear upon complex materials problems, once a parallel, efficient, hardware optimized version of HelicES is available. Development of such a code constitutes yet another avenue of ongoing and future work.

Additionally, in Chapters 5 and 6, we comprehensively examine the structure and  $^{31}\text{P}$  nuclear spin entanglement lifetimes of calcium phosphate monomer, dimers, and trimers using *ab initio* methods. Our conclusion on the asymmetrical nature of the Posner molecule and its short-lived singlet state sheds new light on its viability as a biological quantum information processor. Moreover, our exploration into the space of calcium phosphate dimers — the first of its kind as far as we know — potentially opens up an entirely new field of research. However, we would like to note here again that experimental validation on the presence of these molecules *in vivo* remains of utmost importance.

Lastly, in Chapter 7, we conclude our set of studies by realizing the inherent limitations of density functional theory calculations with respect to the system size, and by developing a novel machine learning framework for the prediction of the electron density of multi-million atom systems. The use of transfer learning to drastically reduce training data requirement and, thus, alleviate a major bottleneck in this line of work was demonstrated. We also detail how uncertainty quantification can be utilized to explore systems inaccessible to conventional density functional theory calculations. Expanding this work to ternary and quaternary alloy systems constitutes a rich avenue of future work, while the descriptor and learning framework used here may be applicable to isolated systems as well — with the latter remaining unexplored for now.

## REFERENCES

- [1] M. P. Teter, M. C. Payne, D. C. Allan, Solution of Schrödinger's equation for large systems, *Physical Review B* 40 (1989) 12255–12263.
- [2] A. Knyazev, Toward the optimal preconditioned eigensolver: Locally optimal block preconditioned conjugate gradient method, *SIAM Journal on Scientific Computing* 23 (2) (2001) 517–541.
- [3] A. Mayer, Band structure and transport properties of carbon nanotubes using a local pseudopotential and a transfer-matrix technique, *Carbon* 42 (10) (2004) 2057–2066.
- [4] A. S. Banerjee, Ab initio framework for systems with helical symmetry: theory, numerical implementation and applications to torsional deformations in nanostructures, *Journal of the Mechanics and Physics of Solids* (2021) 104515.
- [5] H. M. Yu, A. S. Banerjee, Density functional theory method for twisted geometries with application to torsional deformations in group-iv nanotubes, *Journal of Computational Physics* 456 (2022) 111023.
- [6] A. A. Laturia, M. L. Van de Put, W. G. Vandenberghe, Generation of empirical pseudopotentials for transport applications and their application to group iv materials, *Journal of Applied Physics* 128 (3) (2020) 034306.
- [7] M. L. Van de Put, M. V. Fischetti, W. G. Vandenberghe, Scalable atomistic simulations of quantum electron transport using empirical pseudopotentials, *Computer Physics Communications* 244 (2019) 156–169.
- [8] J. Pask, N. Sukumar, S. Mousavi, Linear scaling solution of the all-electron coulomb problem insolids, *International Journal for Multiscale Computational Engineering* 10 (1) (2012).
- [9] D. Marx, J. Hutter, *Ab initio molecular dynamics: basic theory and advanced methods*, Cambridge University Press, 2009.
- [10] I. Nikiforov, B. Hourahine, B. Aradi, T. Frauenheim, T. Dumitrică, Ewald summation on a helix: A route to self-consistent charge density-functional based tight-binding objective molecular dynamics, *The Journal of Chemical Physics* 139 (9) (2013) 094110.
- [11] M. W. Swift, C. G. Van de Walle, M. P. A. Fisher, Posner molecules: from atomic structure to nuclear spins, *Phys. Chem. Chem. Phys.* 20 (2018) 12373–12380.
- [12] F. Weigend, R. Ahlrichs, Balanced basis sets of split valence, triple zeta valence and quadruple zeta valence quality for h to rn: Design and assessment of accuracy, *Phys. Chem. Chem. Phys.* 7 (18) (2005) 3297–3305.

- [13] F. Weigend, Accurate coulomb-fitting basis sets for h to rn, *Phys. Chem. Chem. Phys.* 8 (9) (2006) 1057–1065.
- [14] S. Agarwal, C. D. Aiello, D. R. Kattnig, A. S. Banerjee, The dynamical ensemble of the posner molecule is not symmetric, *The Journal of Physical Chemistry Letters* 12 (42) (2021) 10372–10379.
- [15] M. P. Fisher, Quantum cognition: The possibility of processing with nuclear spins in the brain, *Ann. Phys.* 362 (2015) 593–602.
- [16] T. C. Player, P. Hore, Posner qubits: spin dynamics of entangled  $\text{ca}_9(\text{po}_4)_6$  molecules and their role in neural processing, *J R Soc Interface* 15 (147) (2018) 20180494.
- [17] S. Raju, K. Sivasubramanian, E. Mohandas, The high temperature bulk modulus of aluminium: an assessment using experimental enthalpy and thermal expansion data, *Solid state communications* 122 (12) (2002) 671–676.
- [18] J. R. Chelikowsky, *Introductory Quantum Mechanics with MATLAB: For Atoms, Molecules, Clusters, and Nanocrystals*, John Wiley & Sons, 2019.
- [19] A. S. Cooper, Precise lattice constants of germanium, aluminum, gallium arsenide, uranium, sulphur, quartz and sapphire, *Acta Crystallographica* 15 (6) (1962) 578–582.
- [20] B. Bhushan, B. Bhushan, Baumann, *Springer handbook of nanotechnology*, Vol. 2, Springer, 2007.
- [21] G. Cao, *Nanostructures & nanomaterials: synthesis, properties & applications*, Imperial college press, 2004.
- [22] I. Kang, M. J. Schulz, J. H. Kim, V. Shanov, D. Shi, A carbon nanotube strain sensor for structural health monitoring, *Smart materials and structures* 15 (3) (2006) 737.
- [23] S. Chopra, K. McGuire, N. Gothard, A. Rao, A. Pham, Selective gas detection using a carbon nanotube sensor, *Applied Physics Letters* 83 (11) (2003) 2280–2282.
- [24] R. H. Baughman, C. Cui, A. A. Zakhidov, Z. Iqbal, J. N. Barisci, G. M. Spinks, G. G. Wallace, A. Mazzoldi, D. De Rossi, A. G. Rinzler, et al., Carbon nanotube actuators, *Science* 284 (5418) (1999) 1340–1344.
- [25] L. Kong, W. Chen, Carbon nanotube and graphene-based bioinspired electrochemical actuators, *Advanced materials* 26 (7) (2014) 1025–1043.
- [26] H. Sun, Y. Zhang, J. Zhang, X. Sun, H. Peng, Energy harvesting and storage in 1d devices, *Nature Reviews Materials* 2 (6) (2017) 1–12.
- [27] F. R. Fan, W. Tang, Z. L. Wang, Flexible nanogenerators for energy harvesting and self-powered electronics, *Advanced Materials* 28 (22) (2016) 4283–4305.

- [28] C. Xu, *Chiral Nanoprobes for Biological Applications*, John Wiley & Sons, 2022.
- [29] R. D. James, Objective structures, *Journal of the Mechanics and Physics of Solids* 54 (11) (2006) 2354–2390.
- [30] T. Giamarchi, *Quantum physics in one dimension*, Vol. 121, Clarendon press, 2003.
- [31] M. Bockrath, D. H. Cobden, J. Lu, A. G. Rinzler, R. E. Smalley, L. Balents, P. L. McEuen, Luttinger-liquid behaviour in carbon nanotubes, *Nature* 397 (6720) (1999) 598–601.
- [32] R. Egger, A. Zazunov, A. L. Yeyati, Helical luttinger liquid in topological insulator nanowires, *Physical review letters* 105 (13) (2010) 136403.
- [33] S. Zaitsev-Zotov, Y. A. Kumzerov, Y. A. Firsov, P. Monceau, Luttinger-liquid-like transport in long insb nanowires, *Journal of Physics: Condensed Matter* 12 (20) (2000) L303.
- [34] K. Arutyunov, D. Golubev, A. Zaikin, Superconductivity in one dimension, *Physics Reports* 464 (1-2) (2008) 1–70.
- [35] F. Qin, W. Shi, T. Ideue, M. Yoshida, A. Zak, R. Tenne, T. Kikitsu, D. Inoue, D. Hashizume, Y. Iwasa, Superconductivity in a chiral nanotube, *Nature communications* 8 (1) (2017) 1–6.
- [36] L. Krusin-Elbaum, D. Newns, H. Zeng, V. Derycke, J. Sun, R. Sandstrom, Room-temperature ferromagnetic nanotubes controlled by electron or hole doping, *Nature* 431 (7009) (2004) 672–676.
- [37] M. Liu, J. Wang, Giant electrocaloric effect in ferroelectric nanotubes near room temperature, *Scientific reports* 5 (1) (2015) 1–7.
- [38] D. Zhang, M. Hua, T. Dumitrica, Stability of polycrystalline and wurtzite si nanowires via symmetry-adapted tight-binding objective molecular dynamics, *The Journal of Chemical Physics* 128 (8) (2008) 084104.
- [39] J. Ding, X. Yan, J. Cao, Analytical relation of band gaps to both chirality and diameter of single-wall carbon nanotubes, *Physical Review B* 66 (7) (2002) 073401.
- [40] S. J. Tans, A. R. Verschueren, C. Dekker, Room-temperature transistor based on a single carbon nanotube, *Nature* 393 (6680) (1998) 49–52.
- [41] S. Li, Z. Yu, S.-F. Yen, W. Tang, P. J. Burke, Carbon nanotube transistor operation at 2.6 ghz, *Nano Letters* 4 (4) (2004) 753–756.

- [42] C. D. Aiello, J. M. Abendroth, M. Abbas, A. Afanasev, S. Agarwal, A. S. Banerjee, D. N. Beratan, J. N. Belling, B. Berche, A. Botana, J. R. Caram, G. L. Celardo, G. Cuniberti, A. Garcia-Etxarri, A. Dianat, I. Diez-Perez, Y. Guo, R. Gutierrez, C. Herrmann, J. Hihath, S. Kale, P. Kurian, Y.-C. Lai, T. Liu, A. Lopez, E. Medina, V. Mujica, R. Naaman, M. Noormandipour, J. L. Palma, Y. Paltiel, W. Petuskey, J. C. Ribeiro-Silva, J. J. Saenz, E. J. G. Santos, M. Solyanik-Gorgone, V. J. Sorger, D. M. Stemer, J. M. Ugalde, A. Valdes-Curiel, S. Varela, D. H. Waldeck, M. R. Wasielewski, P. S. Weiss, H. Zacharias, Q. H. Wang, A chirality-based quantum leap, *ACS Nano* 0 (0) (2022).
- [43] R. Naaman, D. H. Waldeck, Spintronics and chirality: Spin selectivity in electron transport through chiral molecules, *Annual Review of Physical Chemistry* 66 (1) (2015) 263–281.
- [44] H. Zhang, D. E. Liu, M. Wimmer, L. P. Kouwenhoven, Next steps of quantum transport in majorana nanowire devices, *Nature communications* 10 (1) (2019) 1–7.
- [45] R. M. Martin, *Electronic Structure: Basic Theory and Practical Methods*, 1st Edition, Cambridge University Press, 2004.
- [46] D. Marx, J. Hutter, *Ab initio molecular dynamics: basic theory and advanced methods*, 1st Edition, Cambridge University Press, 2009.
- [47] A. S. Banerjee, *Density functional methods for Objective Structures: Theory and simulation schemes*, Ph.D. thesis, University of Minnesota, Minneapolis (2013).
- [48] P. D’Arco, Y. Noel, R. Demichelis, R. Dovesi, Single-layered chrysotile nanotubes: A quantum mechanical ab initio simulation, *The Journal of chemical physics* 131 (20) (2009) 204701.
- [49] R. Dovesi, V. Saunders, C. Roetti, R. Orlando, C. Zicovich-Wilson, F. Pascale, B. Civalleri, K. Doll, N. Harrison, I. Bush, et al., *Crystal17* (2017).
- [50] C. T. White, D. H. Robertson, J. W. Mintmire, Helical and rotational symmetries of nanoscale graphitic tubules, *Physical Review B* 47 (1993) 5485–5488.
- [51] E. Chang, G. Bussi, A. Ruini, E. Molinari, First-principles approach for the calculation of optical properties of one-dimensional systems with helical symmetry: The case of carbon nanotubes, *Physical Review B* 72 (2005) 195423.
- [52] Y. Noel, P. D’arco, R. Demichelis, C. M. Zicovich-Wilson, R. Dovesi, On the use of symmetry in the ab initio quantum mechanical simulation of nanotubes and related materials, *Journal of Computational Chemistry* 31 (4) (2010) 855–862.
- [53] E. Chang, G. Bussi, A. Ruini, E. Molinari, Excitons in carbon nanotubes: An *Ab Initio* symmetry-based approach, *Physical Review Letters* 92 (2004) 196401.

- [54] R. M. Balabin, Communications: Intramolecular basis set superposition error as a measure of basis set incompleteness: Can one reach the basis set limit without extrapolation?, *The Journal of chemical physics* 132 (21) (2010) 211103.
- [55] M. Gutowski, G. Chalasiński, Critical evaluation of some computational approaches to the problem of basis set superposition error, *The Journal of chemical physics* 98 (7) (1993) 5540–5554.
- [56] S. Simon, M. Duran, J. Dannenberg, How does basis set superposition error change the potential surfaces for hydrogen-bonded dimers?, *The Journal of chemical physics* 105 (24) (1996) 11024–11031.
- [57] S. Ghosh, A. S. Banerjee, P. Suryanarayana, Symmetry-adapted real-space density functional theory for cylindrical geometries: Application to large group-IV nanotubes, *Physical Review B* 100 (12) (2019) 125143.
- [58] A. Sharma, P. Suryanarayana, Real-space density functional theory adapted to cyclic and helical symmetry: Application to torsional deformation of carbon nanotubes, *Physical Review B* 103 (3) (2021) 035101.
- [59] F. Gygi, G. Galli, Real-space adaptive-coordinate electronic-structure calculations, *Physical Review B* 52 (4) (1995) R2229.
- [60] A. S. Banerjee, P. Suryanarayana, Cyclic density functional theory: A route to the first principles simulation of bending in nanostructures, *Journal of the Mechanics and Physics of Solids* 96 (2016) 605–631.
- [61] Y. Saad, *Numerical Methods for Large Eigenvalue Problems*, Revised Edition, SIAM, 2011.
- [62] A. S. Banerjee, R. S. Elliott, R. D. James, A spectral scheme for kohn–sham density functional theory of clusters, *Journal of Computational Physics* 287 (2015) 226–253.
- [63] MATLAB, 9.7.0.1190202 (R2019b), the MathWorks Inc., Natick, Massachusetts (2019).
- [64] R. Broglia, G. Coló, G. Onida, H. Roman, *Solid State Physics of Finite Systems: Metallic Clusters, Fullerenes, Atomic Wires*, 1st Edition, *Advanced Texts in Physics*, Springer, 2004.
- [65] P. N. D’yachkov, D. Makaev, Linear augmented cylindrical wave method and its applications to nanotubes electronic structure, *Journal of Nanophotonics* 4 (1) (2010) 041680.
- [66] S. R. Hussain, S. Kharitonov, V. Pavelyev, Calculation of the band structure of a non-chiral semiconductor and metallic carbon nanotubes, in: *Journal of Physics: Conference Series*, Vol. 1096, IOP Publishing, 2018, p. 012109.



- [67] P. D’Yachkov, Cylindrical wave method for pure and doped nanotubes, in: *Nanodevices and Nanomaterials for Ecological Security*, Springer, 2012, pp. 87–100.
- [68] D. Makaev, P. D’yachkov, Linearized augmented cylindrical wave method for chiral nanotubes, in: *Doklady Physical Chemistry*, Vol. 419, Springer, 2008, pp. 47–52.
- [69] D. Jüstel, G. Friesecke, R. D. James, Bragg–von laue diffraction generalized to twisted x-rays, *Acta Crystallographica Section A: Foundations and Advances* 72 (2) (2016) 190–196.
- [70] G. Friesecke, R. D. James, D. Jüstel, Twisted x-rays: incoming waveforms yielding discrete diffraction patterns for helical structures, *SIAM Journal on Applied Mathematics* 76 (3) (2016) 1191–1218.
- [71] G. Chaplain, J. De Ponti, R. Craster, Elastic orbital angular momentum, *Physical Review Letters* 128 (6) (2022) 064301.
- [72] G. J. Chaplain, J. M. De Ponti, The elastic spiral phase pipe, *Journal of Sound and Vibration* 523 (2022) 116718.
- [73] P. Motamarri, M. R. Nowak, K. Leiter, J. Knap, V. Gavini, Higher-order adaptive finite-element methods for kohn–sham density functional theory, *Journal of Computational Physics* 253 (2013) 308–343.
- [74] K. Mohseni, T. Colonius, Numerical treatment of polar coordinate singularities, *Journal of Computational Physics* 157 (2) (2000) 787–795.
- [75] M.-C. Lai, A note on finite difference discretizations for Poisson equation on a disk, *Numerical Methods for Partial Differential Equations* 17 (3) (2001) 199–203.
- [76] M.-C. Lai, W.-C. Wang, Fast direct solvers for poisson equation on 2d polar and spherical geometries, *Numerical Methods for Partial Differential Equations: An International Journal* 18 (1) (2002) 56–68.
- [77] A. S. Posner, F. Betts, Synthetic amorphous calcium phosphate and its relation to bone mineral structure, *Acc. Chem. Res.* 8 (8) (1975) 273–281.
- [78] G. Treboux, P. Layrolle, N. Kanzaki, K. Onuma, A. Ito, Symmetry of posner’s cluster, *J. Am. Chem. Soc.* 122 (34) (2000) 8323–8324.
- [79] X. Yin, M. J. Stott, Biological calcium phosphates and posner’s cluster, *J. Chem. Phys.* 118 (8) (2003) 3717–3723.
- [80] L.-W. Du, S. Bian, B.-D. Gou, Y. Jiang, J. Huang, Y.-X. Gao, Y.-D. Zhao, W. Wen, T.-L. Zhang, K. Wang, Structure of clusters and formation of amorphous calcium phosphate and hydroxyapatite: from the perspective of coordination chemistry, *Cryst. Growth Des.* 13 (7) (2013) 3103–3109.

- [81] A. Dey, P. H. Bomans, F. A. Müller, J. Will, P. M. Frederik, The role of prenucleation clusters in surface-induced calcium phosphate crystallization, *Nat. Mater* 9 (2010) 1010–1014.
- [82] L. Wang, S. Li, E. Ruiz-Agudo, C. V. Putnis, A. Putnis, Posner’s cluster revisited: direct imaging of nucleation and growth of nanoscale calcium phosphate clusters at the calcite-water interface, *CrystEngComm* 14 (19) (2012) 6252–6256.
- [83] C. P. Weingarten, P. M. Doraiswamy, M. Fisher, A new spin on neural processing: quantum cognition, *Front. Hum. Neurosci.* 10 (2016) 541.
- [84] S. Goedecker, Linear scaling electronic structure methods, *Reviews of Modern Physics* 71 (4) (1999) 1085.
- [85] D. Bowler, T. Miyazaki, M. Gillan, Recent progress in linear scaling ab initio electronic structure techniques, *Journal of Physics: Condensed Matter* 14 (11) (2002) 2781.
- [86] E. Artacho, D. Sánchez-Portal, P. Ordejón, A. Garcia, J. M. Soler, Linear-scaling ab-initio calculations for large and complex systems, *physica status solidi (b)* 215 (1) (1999) 809–817.
- [87] C.-K. Skylaris, P. D. Haynes, A. A. Mostofi, M. C. Payne, Introducing onetep: Linear-scaling density functional simulations on parallel computers, *The Journal of chemical physics* 122 (8) (2005).
- [88] P. P. Pratapa, P. Suryanarayana, J. E. Pask, Spectral quadrature method for accurate o (n) electronic structure calculations of metals and insulators, *Computer Physics Communications* 200 (2016) 96–107.
- [89] L. Lin, M. Chen, C. Yang, L. He, Accelerating atomic orbital-based electronic structure calculation via pole expansion and selected inversion, *J. Phys.: Condens. Matter* 25 (2013) 295501.
- [90] L. Lin, C. Yang, J. C. Meza, J. Lu, L. Ying, W. E. Selin—an algorithm for selected inversion of a sparse symmetric matrix, *ACM Transactions on Mathematical Software (TOMS)* 37 (4) (2011) 1–19.
- [91] P. Motamarri, V. Gavini, Subquadratic-scaling subspace projection method for large-scale kohn-sham density functional theory calculations using spectral finite-element discretization, *Physical Review B* 90 (11) (2014) 115127.
- [92] L. Lin, J. Lu, L. Ying, R. Car, W. E, Fast algorithm for extracting the diagonal of the inverse matrix with application to the electronic structure analysis of metallic systems, *Communications In Mathematical Sciences* 7 (2009) 755.

- [93] A. S. Banerjee, L. Lin, W. Hu, C. Yang, J. E. Pask, Chebyshev polynomial filtered subspace iteration in the discontinuous galerkin method for large-scale electronic structure calculations 145 (15) (2016) 154101.
- [94] A. S. Banerjee, L. Lin, P. Suryanarayana, C. Yang, J. E. Pask, Two-level chebyshev filter based complementary subspace method: pushing the envelope of large-scale electronic structure calculations, *Journal of chemical theory and computation* 14 (6) (2018) 2930–2946.
- [95] A. Marek, V. Blum, R. Johanni, V. Havu, B. Lang, T. Auckenthaler, A. Heinecke, H.-J. Bungartz, H. Lederer, The elpa library: scalable parallel eigenvalue solutions for electronic structure theory and computational science, *Journal of Physics: Condensed Matter* 26 (21) (2014) 213201.
- [96] V. Gavini, S. Baroni, V. Blum, D. R. Bowler, A. Buccheri, J. R. Chelikowsky, S. Das, W. Dawson, P. Delugas, M. Dogan, et al., Roadmap on electronic structure codes in the exascale era, *Modelling and Simulation in Materials Science and Engineering* 31 (6) (2023) 063301.
- [97] W. Hu, H. An, Z. Guo, Q. Jiang, X. Qin, J. Chen, W. Jia, C. Yang, Z. Luo, J. Li, et al., 2.5 million-atom ab initio electronic-structure simulation of complex metallic heterostructures with dgdft, in: *SC22: International Conference for High Performance Computing, Networking, Storage and Analysis, IEEE, 2022*, pp. 1–13.
- [98] W. Hu, X. Qin, Q. Jiang, J. Chen, H. An, W. Jia, F. Li, X. Liu, D. Chen, F. Liu, et al., High performance computing of DGDFE for tens of thousands of atoms using millions of cores on sunway taihulight, *Science Bulletin* 66 (2) (2021) 111–119.
- [99] M. Dogan, K.-H. Liou, J. R. Chelikowsky, Real-space solution to the electronic structure problem for nearly a million electrons, *The Journal of Chemical Physics* 158 (24) (2023).
- [100] G. R. Schleder, A. C. Padilha, C. M. Acosta, M. Costa, A. Fazzio, From dft to machine learning: recent approaches to materials science—a review, *Journal of Physics: Materials* 2 (3) (2019) 032001.
- [101] H. J. Kulik, T. Hammerschmidt, J. Schmidt, S. Botti, M. A. Marques, M. Boley, M. Scheffler, M. Todorović, P. Rinke, C. Oses, et al., Roadmap on machine learning in electronic structure, *Electronic Structure* 4 (2) (2022) 023004.
- [102] G. Csányi, T. Albaret, M. Payne, A. De Vita, “learn on the fly”: A hybrid classical and quantum-mechanical molecular dynamics simulation, *Physical review letters* 93 (17) (2004) 175503.
- [103] J. Behler, M. Parrinello, Generalized neural-network representation of high-dimensional potential-energy surfaces, *Physical review letters* 98 (14) (2007) 146401.

- [104] A. Seko, A. Takahashi, I. Tanaka, Sparse representation for a potential energy surface, *Physical Review B* 90 (2) (2014) 024101.
- [105] H. Wang, L. Zhang, J. Han, E. Weinan, Deepmd-kit: A deep learning package for many-body potential energy representation and molecular dynamics, *Computer Physics Communications* 228 (2018) 178–184.
- [106] C. Chen, S. P. Ong, A universal graph deep learning interatomic potential for the periodic table, *Nature Computational Science* 2 (11) (2022) 718–728.
- [107] R. Freitas, Y. Cao, Machine-learning potentials for crystal defects, *MRS Communications* 12 (5) (2022) 510–520.
- [108] A. M. Lewis, A. Grisafi, M. Ceriotti, M. Rossi, Learning electron densities in the condensed phase, *Journal of Chemical Theory and Computation* 17 (11) (2021) 7203–7214.
- [109] P. B. Jørgensen, A. Bhowmik, Equivariant graph neural networks for fast electron density estimation of molecules, liquids, and solids, *npj Computational Materials* 8 (1) (2022) 183.
- [110] L. Zepeda-Núñez, Y. Chen, J. Zhang, W. Jia, L. Zhang, L. Lin, Deep density: circumventing the kohn-sham equations via symmetry preserving neural networks, *Journal of Computational Physics* 443 (2021) 110523.
- [111] A. Chandrasekaran, D. Kamal, R. Batra, C. Kim, L. Chen, R. Ramprasad, Solving the electronic structure problem with machine learning, *npj Computational Materials* 5 (1) (2019) 22.
- [112] L. Fiedler, N. A. Modine, S. Schmerler, D. J. Vogel, G. A. Popoola, A. P. Thompson, S. Rajamanickam, A. Cangi, Predicting electronic structures at any length scale with machine learning, *npj Computational Materials* 9 (1) (2023) 115.
- [113] F. Brockherde, L. Vogt, L. Li, M. E. Tuckerman, K. Burke, K.-R. Müller, Bypassing the kohn-sham equations with machine learning, *Nature communications* 8 (1) (2017) 872.
- [114] B. Deng, P. Zhong, K. Jun, J. Riebesell, K. Han, C. J. Bartel, G. Ceder, Chgnet as a pretrained universal neural network potential for charge-informed atomistic modelling, *Nature Machine Intelligence* 5 (9) (2023) 1031–1041.
- [115] T. W. Ko, S. P. Ong, Recent advances and outstanding challenges for machine learning interatomic potentials, *Nature Computational Science* (2023) 1–3.
- [116] S. Pathrudkar, H. M. Yu, S. Ghosh, A. S. Banerjee, Machine learning based prediction of the electronic structure of quasi-one-dimensional materials under strain, *Phys. Rev. B* 105 (2022) 195141.

- [117] G. Arora, A. Manzoor, D. S. Aidhy, Charge-density based evaluation and prediction of stacking fault energies in ni alloys from dft and machine learning, *Journal of Applied Physics* 132 (22) (2022).
- [118] B. Medasani, A. Gamst, H. Ding, W. Chen, K. A. Persson, M. Asta, A. Canning, M. Haranczyk, Predicting defect behavior in b2 intermetallics by merging ab initio modeling and machine learning, *npj Computational Materials* 2 (1) (2016) 1.
- [119] J. M. Alred, K. V. Bets, Y. Xie, B. I. Yakobson, Machine learning electron density in sulfur crosslinked carbon nanotubes, *Composites Science and Technology* 166 (2018) 3–9.
- [120] A. Grisafi, A. Fabrizio, B. Meyer, D. M. Wilkins, C. Corminboeuf, M. Ceriotti, Transferable machine-learning model of the electron density, *ACS central science* 5 (1) (2018) 57–64.
- [121] A. Fabrizio, A. Grisafi, B. Meyer, M. Ceriotti, C. Corminboeuf, Electron density learning of non-covalent systems, *Chemical science* 10 (41) (2019) 9424–9432.
- [122] J. A. Ellis, L. Fiedler, G. A. Popoola, N. A. Modine, J. A. Stephens, A. P. Thompson, A. Cangi, S. Rajamanickam, Accelerating finite-temperature kohn-sham density functional theory with deep neural networks, *Physical Review B* 104 (3) (2021) 035120.
- [123] F. Zhuang, Z. Qi, K. Duan, D. Xi, Y. Zhu, H. Zhu, H. Xiong, Q. He, A comprehensive survey on transfer learning, *Proceedings of the IEEE* 109 (1) (2020) 43–76.
- [124] J. P. Walter, M. L. Cohen, Wave-vector-dependent dielectric function for si, ge, gaas, and znse, *Physical Review B* 2 (6) (1970) 1821.
- [125] C. Fong, M. L. Cohen, Energy band structure of copper by the empirical pseudopotential method, *Physical Review Letters* 24 (7) (1970) 306.
- [126] M. Hoffmann-Ostenhof, T. Hoffmann-Ostenhof, R. Ahlrichs, J. Morgan, On the exponential fall off of wavefunctions and electron densities, in: K. Osterwalder (Ed.), *Mathematical Problems in Theoretical Physics*, Vol. 116 of *Lecture Notes in Physics*, Springer Berlin / Heidelberg, 1980, pp. 62–67.
- [127] R. Ahlrichs, M. Hoffmann-Ostenhof, T. Hoffmann-Ostenhof, J. D. Morgan, Bounds on the decay of electron densities with screening, *Physical Review A* 23 (5) (1981) 2106–2117.
- [128] R. Waldron, A helical coordinate system and its applications in electromagnetic theory, *The Quarterly Journal of Mechanics and Applied Mathematics* 11 (4) (1958) 438–461.
- [129] D. Hochberg, G. Edwards, T. W. Kephart, Representing structural information of helical charge distributions in cylindrical coordinates, *Physical Review E* 55 (3) (1997) 3765.

- [130] M. Abramowitz, I. A. Stegun, R. H. Romer, Handbook of mathematical functions with formulas, graphs, and mathematical tables (1988).
- [131] [NIST Digital Library of Mathematical Functions](http://dlmf.nist.gov/), <http://dlmf.nist.gov/>, Release 1.1.5 of 2022-03-15, f. W. J. Olver, A. B. Olde Daalhuis, D. W. Lozier, B. I. Schneider, R. F. Boisvert, C. W. Clark, B. R. Miller, B. V. Saunders, H. S. Cohl, and M. A. McClain, eds. (2022).  
URL <http://dlmf.nist.gov/>
- [132] L. J. Laslett, W. Lewish, Evaluation of the zeros of cross-product bessel functions, *Mathematics of Computation* 16 (78) (1962) 226–232.
- [133] Y. Saad, J. R. Chelikowsky, S. M. Shontz, Numerical methods for electronic structure calculations of materials, *SIAM Review* 52 (1) (2010) 3–54.
- [134] S. A. Orszag, Transform method for the calculation of vector-coupled sums: Application to the spectral form of the vorticity equation, *Journal of the Atmospheric Sciences* 27 (6) (1970) 890–895.
- [135] S. A. Orszag, Spectral methods for problems in complex geometries, *Journal of Computational Physics* 37 (1) (1980) 70–92.
- [136] J. Shen, T. Tang, L.-L. Wang, Spectral methods: algorithms, analysis and applications, Springer Series in Computational Mathematics, Springer Berlin, New York, 2011.
- [137] D. Gottlieb, S. Orszag, Numerical Analysis of Spectral Methods: Theory and Applications, SIAM-CBMS, Philadelphia, 1977.
- [138] S. Agarwal, A. S. Banerjee, Solution of the schrödinger equation for quasi-one-dimensional materials using helical waves, *Journal of Computational Physics* 496 (2024) 112551.
- [139] P. P. Teodorescu, N.-D. Stanescu, N. Pandrea, Numerical Analysis with Applications in Mechanics and Engineering, 1st Edition, John Wiley & Sons, 2013.
- [140] E. Bylaska, K. Tsemekhman, N. Govind, M. Valiev, Large-scale plane-wave-based density functional theory: Formalism, parallelization, and applications, *Computational methods for large systems: electronic structure approaches for biotechnology and nanotechnology* (2011) 77–116.
- [141] E. Cancès, R. Chakir, Y. Maday, Numerical analysis of the planewave discretization of some orbital-free and Kohn-Sham models, *ESAIM: Mathematical Modelling and Numerical Analysis* 46 (2012) 341–388.
- [142] H. J. Monkhorst, J. D. Pack, Special points for brillouin-zone integrations, *Physical review B* 13 (12) (1976) 5188.

- [143] I. I. Geru, Time-Reversal Symmetry, Springer, 2018.
- [144] D. Lemoine, The discrete bessel transform algorithm, The Journal of chemical physics 101 (5) (1994) 3936–3944.
- [145] H. Johansen, K. Sørensen, Fast hankel transforms, Geophysical Prospecting 27 (4) (1979) 876–901.
- [146] R. Bisseling, R. Kosloff, The fast hankel transform as a tool in the solution of the time dependent schrödinger equation, Journal of Computational Physics 59 (1) (1985) 136–151.
- [147] K. Key, Is the fast hankel transform faster than quadrature?, Geophysics 77 (3) (2012) F21–F30.
- [148] L. S. Blackford, A. Petitet, R. Pozo, K. Remington, R. C. Whaley, J. Demmel, J. Dongarra, I. Duff, S. Hammarling, G. Henry, et al., An updated set of basic linear algebra subprograms (blas), ACM Transactions on Mathematical Software 28 (2) (2002) 135–151.
- [149] G. W. Stewart, A krylov–schur algorithm for large eigenproblems, SIAM Journal on Matrix Analysis and Applications 23 (3) (2002) 601–614.
- [150] M. C. Payne, M. P. Teter, D. C. Allan, T. A. Arias, J. D. Joannopoulos, Iterative minimization techniques for *ab initio* total-energy calculations: molecular dynamics and conjugate gradients, Rev. Mod. Phys. 64 (1992) 1045–1097.
- [151] Y. Zhou, J. R. Chelikowsky, X. Gao, A. Zhou, On the “preconditioning” function used in planewave dft calculations and its generalization, Communications in Computational Physics 18 (1) (2015) 167–179.
- [152] A. Knyazev, Locally Optimal Block Preconditioned Conjugate Gradient, <https://github.com/lobpcg/blopex>, <https://www.mathworks.com/matlabcentral/fileexchange/48-locally-optimal-block-preconditioned-conjugate-gradient>, Accessed: 2022-07-21 (2022).
- [153] A. V. Knyazev, M. E. Argentati, I. Lashuk, E. Ovtchinnikov, Block locally optimal preconditioned eigenvalue solvers (BLOPEX) in HYPRE and PETSc, SIAM Journal on Scientific Computing 29 (5) (2007) 2224–2239.
- [154] J. A. Duersch, M. Shao, C. Yang, M. Gu, A robust and efficient implementation of lobpcg, SIAM Journal on Scientific Computing 40 (5) (2018) C655–C676.
- [155] A. S. Banerjee, L. Lin, W. Hu, C. Yang, J. E. Pask, Chebyshev polynomial filtered subspace iteration in the Discontinuous Galerkin method for large-scale electronic structure calculations, arXiv preprint arXiv:1606.03416 (2016).

- [156] Y. Zhou, J. R. Chelikowsky, Y. Saad, Chebyshev-filtered subspace iteration method free of sparse diagonalization for solving the Kohn–Sham equation, *Journal of Computational Physics* 274 (2014) 770–782.
- [157] A. Rohatgi, [Webplotdigitizer: Version 4.5](https://automeris.io/WebPlotDigitizer) (2021).  
URL <https://automeris.io/WebPlotDigitizer>
- [158] A. Mayer, J.-P. Vigneron, Accuracy-control techniques applied to stable transfer-matrix computations, *Physical Review E* 59 (4) (1999) 4659.
- [159] J. Pendry, A. MacKinnon, Calculation of photon dispersion relations, *Physical Review Letters* 69 (19) (1992) 2772.
- [160] H. Tamura, T. Ando, Conductance fluctuations in quantum wires, *Physical Review B* 44 (4) (1991) 1792.
- [161] M. L. Van de Put, A. A. Laturia, M. V. Fischetti, W. G. Vandenberghe, Efficient modeling of electron transport with plane waves, in: *2018 International Conference on Simulation of Semiconductor Processes and Devices (SISPAD)*, 2018, pp. 71–74.
- [162] N. Troullier, J. L. Martins, Efficient pseudopotentials for plane-wave calculations, *Physical Review B* 43 (3) (1991) 1993.
- [163] W. Kohn, L. J. Sham, Self-consistent equations including exchange and correlation effects, *Phys. Rev.* 140 (1965) A1133–A1138.
- [164] J. P. Perdew, Y. Wang, Accurate and simple analytic representation of the electron-gas correlation energy, *Physical Review B* 45 (1992) 13244–13249.
- [165] D. Zhang, R. D. James, T. Dumitrica, Electromechanical characterization of carbon nanotubes in torsion via symmetry adapted tight-binding objective molecular dynamics, *Physical Review B* 80 (11) (2009) 115418.
- [166] L. Yang, M. Anantram, J. Han, J. Lu, Band-gap change of carbon nanotubes: Effect of small uniaxial and torsional strain, *Physical Review B* 60 (19) (1999) 13874.
- [167] L. Yang, J. Han, Electronic structure of deformed carbon nanotubes, *Physical review letters* 85 (1) (2000) 154.
- [168] S. Agarwal, A. S. Banerjee, On the solution of the Poisson problem for twisted geometries, (In preparation) (2024).
- [169] Y. Hakobyan, E. Tadmor, R. James, Objective quasicontinuum approach for rod problems, *Physical Review B* 86 (24) (2012) 245435.
- [170] C. Le Bris (Ed.), *Computational Chemistry*, Vol. X of *Handbook of Numerical Analysis*, North-Holland, 2003.



- [171] J. C. Slater, G. F. Koster, Simplified lcao method for the periodic potential problem, *Physical Review* 94 (6) (1954) 1498.
- [172] P. Hohenberg, W. Kohn, Inhomogeneous electron gas, *Physical review* 136 (3B) (1964) B864.
- [173] C. D. Sherrill, H. F. Schaefer III, The configuration interaction method: Advances in highly correlated approaches, in: *Advances in quantum chemistry*, Vol. 34, Elsevier, 1999, pp. 143–269.
- [174] C. Møller, M. S. Plesset, Note on an approximation treatment for many-electron systems, *Physical review* 46 (7) (1934) 618.
- [175] H. G. Kümmel, A biography of the coupled cluster method, *International Journal of Modern Physics B* 17 (28) (2003) 5311–5325.
- [176] Y. Saad, J. R. Chelikowsky, S. M. Shontz, Numerical methods for electronic structure calculations of materials, *SIAM review* 52 (1) (2010) 3–54.
- [177] S. Pathrudkar, P. Thiagarajan, S. Agarwal, A. S. Banerjee, S. Ghosh, Electronic structure prediction of multi-million atom systems through uncertainty quantification enabled transfer learning, *arXiv preprint arXiv:2308.13096* (2023).
- [178] A. Damle, L. Lin, Disentanglement via entanglement: a unified method for wannier localization, *Multiscale Modeling & Simulation* 16 (3) (2018) 1392–1410.
- [179] M. S. Zöllner, A. Saghatchi, V. Mujica, C. Herrmann, Influence of electronic structure modeling and junction structure on first-principles chiral induced spin selectivity, *Journal of Chemical Theory and Computation* 16 (12) (2020) 7357–7371.
- [180] M. S. Zöllner, S. Varela, E. Medina, V. Mujica, C. Herrmann, Insight into the origin of chiral-induced spin selectivity from a symmetry analysis of electronic transmission, *Journal of chemical theory and computation* 16 (5) (2020) 2914–2929.
- [181] V. V. Maslyuk, R. Gutierrez, A. Dianat, V. Mujica, G. Cuniberti, Enhanced magnetoresistance in chiral molecular junctions, *The journal of physical chemistry letters* 9 (18) (2018) 5453–5459.
- [182] H. M. Yu, S. Sharma, S. Agarwal, O. Liebman, A. S. Banerjee, Carbon kagome nanotubes—quasi-one-dimensional nanostructures with flat bands, *RSC advances* 14 (2) (2024) 963–981.
- [183] L. M. Fraser, W. Foulkes, G. Rajagopal, R. Needs, S. Kenny, A. Williamson, Finite-size effects and coulomb interactions in quantum monte carlo calculations for homogeneous systems with periodic boundary conditions, *Physical Review B* 53 (4) (1996) 1814.

- [184] H. Takemoto, T. Ohyama, A. Tohsaki, Direct sum of coulomb potential without ambiguities of conditionally convergent series, *Progress of theoretical physics* 109 (4) (2003) 563–573.
- [185] P. P. Ewald, Die berechnung optischer und elektrostatischer gitterpotentiale, *Annalen der physik* 369 (3) (1921) 253–287.
- [186] D. S. Shamsirgar, J. Bagge, A.-K. Tornberg, Fast ewald summation for electrostatic potentials with arbitrary periodicity, *The Journal of Chemical Physics* 154 (16) (2021).
- [187] V. Gavini, J. Knap, K. Bhattacharya, M. Ortiz, Non-periodic finite-element formulation of orbital-free density functional theory, *Journal of the Mechanics and Physics of Solids* 55 (4) (2007) 669–696.
- [188] E. Y. Andrei, D. K. Efetov, P. Jarillo-Herrero, A. H. MacDonald, K. F. Mak, T. Senthil, E. Tutuc, A. Yazdani, A. F. Young, The marvels of moiré materials, *Nature Reviews Materials* 6 (3) (2021) 201–206.
- [189] L. Wang, E.-M. Shih, A. Ghiotto, L. Xian, D. A. Rhodes, C. Tan, M. Claassen, D. M. Kennes, Y. Bai, B. Kim, et al., Correlated electronic phases in twisted bilayer transition metal dichalcogenides, *Nature materials* 19 (8) (2020) 861–866.
- [190] Y. Cao, V. Fatemi, S. Fang, K. Watanabe, T. Taniguchi, E. Kaxiras, P. Jarillo-Herrero, Unconventional superconductivity in magic-angle graphene superlattices, *Nature* 556 (7699) (2018) 43–50.
- [191] R. Pons, A. Mielke, T. Stauber, Flat-band ferromagnetism in twisted bilayer graphene, *Physical Review B* 102 (23) (2020) 235101.
- [192] Y. Choi, H. Kim, Y. Peng, A. Thomson, C. Lewandowski, R. Polski, Y. Zhang, H. S. Arora, K. Watanabe, T. Taniguchi, et al., Correlation-driven topological phases in magic-angle twisted bilayer graphene, *Nature* 589 (7843) (2021) 536–541.
- [193] Y. Cao, V. Fatemi, A. Demir, S. Fang, S. L. Tomarken, J. Y. Luo, J. D. Sanchez-Yamagishi, K. Watanabe, T. Taniguchi, E. Kaxiras, et al., Correlated insulator behaviour at half-filling in magic-angle graphene superlattices, *Nature* 556 (7699) (2018) 80–84.
- [194] L. C. Andrews, *Special functions of mathematics for engineers*, Vol. 49, Spie Press, 1998.
- [195] K. Onuma, A. Ito, Cluster growth model for hydroxyapatite, *Chem. Mater.* 10 (11) (1998) 3346–3351.
- [196] A. Buckingham, I. Love, Theory of the anisotropy of nuclear spin coupling, *J. Magn. Reson.* 2 (3) (1970) 338–351.

- [197] F. A. Perras, D. L. Bryce, Symmetry-amplified j splittings for quadrupolar spin pairs: a solid-state nmr probe of homoatomic covalent bonds, *J. Am. Chem. Soc.* 135 (34) (2013) 12596–12599.
- [198] R. Annabestani, D. G. Cory, Dipolar relaxation mechanism of long-lived states of methyl groups, *Quantum Inf. Process.* 17 (1) (2018) 1–25.
- [199] D. A. Lidar, [Review of Decoherence-Free Subspaces, Noiseless Subsystems, and Dynamical Decoupling](#), John Wiley & Sons, Ltd, 2014, pp. 295–354. [arXiv:https://onlinelibrary.wiley.com/doi/pdf/10.1002/9781118742631.ch11](#). URL [https://onlinelibrary.wiley.com/doi/abs/10.1002/9781118742631.ch11](#)
- [200] Y. Feng, T. Theis, T.-L. Wu, K. Claytor, W. S. Warren, Long-lived polarization protected by symmetry, *J. Chem. Phys.* 141 (13) (2014) 134307.
- [201] E. Vinogradov, A. K. Grant, Long-lived states in solution nmr: Selection rules for intramolecular dipolar relaxation in low magnetic fields, *J. Magn. Reson.* 188 (1) (2007) 176–182.
- [202] G. Stevanato, S. S. Roy, J. Hill-Cousins, I. Kuprov, L. J. Brown, R. C. Brown, G. Pileio, M. H. Levitt, Long-lived nuclear spin states far from magnetic equivalence, *Phys. Chem. Chem. Phys.* 17 (8) (2015) 5913–5922.
- [203] G. Treboux, P. Layrolle, N. Kanzaki, K. Onuma, A. Ito, Existence of posner’s cluster in vacuum, *J. Phys. Chem. A* 104 (21) (2000) 5111–5114.
- [204] T.-J. Lin, C.-C. Chiu, Structures and infrared spectra of calcium phosphate clusters by ab initio methods with implicit solvation models, *Phys. Chem. Chem. Phys.* 20 (1) (2018) 345–356.
- [205] M. Swift, Private communication (2020).
- [206] N. Kanzaki, G. Treboux, K. Onuma, S. Tsutsumi, A. Ito, Calcium phosphate clusters, *Biomaterials* 22 (21) (2001) 2921–2929.
- [207] G. Mancardi, C. E. H. Tamargo, D. Di Tommaso, N. H. De Leeuw, Detection of posner’s clusters during calcium phosphate nucleation: a molecular dynamics study, *J. Mater. Chem. B* 5 (35) (2017) 7274–7284.
- [208] R. I. Ainsworth, D. D. Tommaso, J. K. Christie, N. H. de Leeuw, Polarizable force field development and molecular dynamics study of phosphate-based glasses, *J. Chem. Phys.* 137 (23) (2012) 234502.
- [209] R. Demichelis, N. A. Garcia, P. Raiteri, R. Innocenti Malini, C. L. Freeman, J. H. Harding, J. D. Gale, Simulation of calcium phosphate species in aqueous solution: force field derivation, *J. Phys. Chem. B* 122 (4) (2018) 1471–1483.

- [210] S. Agarwal, D. R. Kattnig, C. D. Aiello, A. S. Banerjee, The biological qubit: Calcium phosphate dimers, not trimers, *The Journal of Physical Chemistry Letters* 14 (10) (2023) 2518–2525.
- [211] G. Prandini, A. Marrazzo, I. E. Castelli, N. Mounet, N. Marzari, Precision and efficiency in solid-state pseudopotential calculations, *NPJ Comput. Mater.* 4 (1) (2018) 1–13.
- [212] K. Lejaeghere, G. Bihlmayer, T. Björkman, P. Blaha, S. Blügel, V. Blum, D. Caliste, I. E. Castelli, S. J. Clark, A. Dal Corso, et al., Reproducibility in density functional theory calculations of solids, *Science* 351 (6280) (2016).
- [213] T. N. Truong, E. V. Stefanovich, A new method for incorporating solvent effect into the classical, ab initio molecular orbital and density functional theory frameworks for arbitrary shape cavity, *Chem. Phys. Lett.* 240 (4) (1995) 253–260.
- [214] V. Barone, M. Cossi, Quantum calculation of molecular energies and energy gradients in solution by a conductor solvent model, *J. Phys. Chem. A* 102 (11) (1998) 1995–2001.
- [215] A. W. Lange, J. M. Herbert, A smooth, nonsingular, and faithful discretization scheme for polarizable continuum models: The switching/gaussian approach, *J. Chem. Phys.* 133 (24) (2010) 244111.
- [216] S. Grimme, J. Antony, S. Ehrlich, H. Krieg, A consistent and accurate ab initio parametrization of density functional dispersion correction (dft-d) for the 94 elements h-pu, *J. Chem. Phys.* 132 (15) (2010) 154104.
- [217] P. Pulay, Convergence acceleration of iterative sequences. the case of scf iteration, *Chem. Phys. Lett.* 73 (2) (1980) 393–398.
- [218] P. Pulay, Improved scf convergence acceleration, *J. Comput. Chem.* 3 (4) (1982) 556–560.
- [219] T. Van Voorhis, M. Head-Gordon, A geometric approach to direct minimization, *Mol. Phys.* 100 (11) (2002) 1713–1721.
- [220] W. F. Polik, J. Schmidt, Webmo: Web-based computational chemistry calculations in education and research, *Wiley Interdiscip. Rev. Comput. Mol. Sci.* e1554.
- [221] W. Smith, C. Yong, P. Rodger, Dl\_poly: Application to molecular simulation, *Mol. Simul.* 28 (5) (2002) 385–471.
- [222] I. Roohani, S. Cheong, A. Wang, How to build a bone?-hydroxyapatite or posners clusters as bone minerals, *Open Ceramics* (2021) 100092.
- [223] W. Humphrey, A. Dalke, K. Schulten, VMD – Visual Molecular Dynamics, *J. Mol. Graph.* 14 (1996) 33–38.

- [224] W. K. Wootters, Entanglement of formation of an arbitrary state of two qubits, *Physical Review Letters* 80 (10) (1998) 2245.
- [225] F. Neese, F. Wennmohs, U. Becker, C. Riplinger, The orca quantum chemistry program package, *The Journal of chemical physics* 152 (22) (2020) 224108.
- [226] F. Jensen, The basis set convergence of spin-spin coupling constants calculated by density functional methods, *Journal of Chemical Theory and Computation* 2 (5) (2006) 1360–1369.
- [227] F. Jensen, Segmented contracted basis sets optimized for nuclear magnetic shielding, *Journal of Chemical Theory and Computation* 11 (1) (2015) 132–138.
- [228] M. J. Frisch, G. W. Trucks, H. B. Schlegel, G. E. Scuseria, M. A. Robb, J. R. Cheeseman, G. Scalmani, V. Barone, G. A. Petersson, H. Nakatsuji, X. Li, M. Caricato, A. V. Marenich, J. Bloino, B. G. Janesko, R. Gomperts, B. Mennucci, H. P. Hratchian, J. V. Ortiz, A. F. Izmaylov, J. L. Sonnenberg, D. Williams-Young, F. Ding, F. Lipparini, F. Egidi, J. Goings, B. Peng, A. Petrone, T. Henderson, D. Ranasinghe, V. G. Zakrzewski, J. Gao, N. Rega, G. Zheng, W. Liang, M. Hada, M. Ehara, K. Toyota, R. Fukuda, J. Hasegawa, M. Ishida, T. Nakajima, Y. Honda, O. Kitao, H. Nakai, T. Vreven, K. Throssell, J. A. Montgomery, Jr., J. E. Peralta, F. Ogliaro, M. J. Bearpark, J. J. Heyd, E. N. Brothers, K. N. Kudin, V. N. Staroverov, T. A. Keith, R. Kobayashi, J. Normand, K. Raghavachari, A. P. Rendell, J. C. Burant, S. S. Iyengar, J. Tomasi, M. Cossi, J. M. Millam, M. Klene, C. Adamo, R. Cammi, J. W. Ochterski, R. L. Martin, K. Morokuma, O. Farkas, J. B. Foresman, D. J. Fox, *Gaussian~16 Revision C.01*, gaussian Inc. Wallingford CT (2016).
- [229] J. R. Johansson, P. D. Nation, F. Nori, Qutip: An open-source python framework for the dynamics of open quantum systems, *Computer Physics Communications* 183 (8) (2012) 1760–1772.
- [230] A. P. Thompson, H. M. Aktulga, R. Berger, D. S. Bolintineanu, W. M. Brown, P. S. Crozier, P. J. in't Veld, A. Kohlmeyer, S. G. Moore, T. D. Nguyen, et al., LAMMPS—a flexible simulation tool for particle-based materials modeling at the atomic, meso, and continuum scales, *Computer Physics Communications* 271 (2022) 108171.
- [231] D. E. Korenchan, J. Lu, M. H. Levitt, A. Jerschow, 31 p nuclear spin singlet lifetimes in a system with switchable magnetic inequivalence: experiment and simulation, *Physical Chemistry Chemical Physics* 23 (35) (2021) 19465–19471.
- [232] D. Korenchan, J. Lu, M. Sabba, L. Dagys, L. Brown, M. Levitt, A. Jerschow, Limits of the quantum cognition hypothesis: 31p singlet order lifetimes of pyrophosphate from experiment and simulation, chemrxiv. cambridge: Cambridge open engage; (preprint) (2022).

- [233] H.-P. Breuer, F. Petruccione, et al., *The theory of open quantum systems*, Oxford University Press on Demand, 2002.
- [234] M. Nuwer, N. Pouratian, *Monitoring of neural function: electromyography nerve conduction and evoked potentials*, in: Youmans and Winn neurological surgery, Elsevier, 2017.
- [235] S. J. DeVience, R. L. Walsworth, M. S. Rosen, Nmr of  $^{31}\text{P}$  nuclear spin singlet states in organic diphosphates, *Journal of Magnetic Resonance* 333 (2021) 107101.
- [236] T. Van Mourik, M. Bühl, M.-P. Gaigeot, *Density functional theory across chemistry, physics and biology* (2014).
- [237] P. Makkar, N. N. Ghosh, A review on the use of dft for the prediction of the properties of nanomaterials, *RSC advances* 11 (45) (2021) 27897–27924.
- [238] J. Hafner, C. Wolverton, G. Ceder, Toward computational materials design: the impact of density functional theory on materials research, *MRS bulletin* 31 (9) (2006) 659–668.
- [239] A. E. Mattsson, P. A. Schultz, M. P. Desjarlais, T. R. Mattsson, K. Leung, Designing meaningful density functional theory calculations in materials science—a primer, *Modelling and Simulation in Materials Science and Engineering* 13 (1) (2004) R1.
- [240] R. M. Martin, L. Reining, D. M. Ceperley, *Interacting electrons*, Cambridge University Press, 2016.
- [241] S. Datta, *Quantum transport: atom to transistor*, Cambridge university press, 2005.
- [242] S.-H. Wei, L. Ferreira, J. E. Bernard, A. Zunger, Electronic properties of random alloys: Special quasirandom structures, *Physical Review B* 42 (15) (1990) 9622.
- [243] M. Jaros, Electronic properties of semiconductor alloy systems, *Reports on Progress in Physics* 48 (8) (1985) 1091.
- [244] S. Fischer, S. Kaul, H. Kronmüller, Critical magnetic properties of disordered polycrystalline cr 75 fe 25 and cr 70 fe 30 alloys, *Physical Review B* 65 (6) (2002) 064443.
- [245] G. T. de Laissardière, D. Nguyen-Manh, D. Mayou, Electronic structure of complex hume-rothery phases and quasicrystals in transition metal aluminides, *Progress in Materials Science* 50 (6) (2005) 679–788.
- [246] O. N. Senkov, G. Wilks, J. Scott, D. B. Miracle, Mechanical properties of nb25mo25ta25w25 and v20nb20mo20ta20w20 refractory high entropy alloys, *Intermetallics* 19 (5) (2011) 698–706.
- [247] O. Senkov, G. Wilks, D. Miracle, C. Chuang, P. Liaw, Refractory high-entropy alloys, *Intermetallics* 18 (9) (2010) 1758–1765.

- [248] A. K. Geim, I. V. Grigorieva, Van der waals heterostructures, *Nature* 499 (7459) (2013) 419–425.
- [249] S. Carr, S. Fang, E. Kaxiras, Electronic-structure methods for twisted moiré layers, *Nature Reviews Materials* 5 (10) (2020) 748–763.
- [250] J. C. Snyder, M. Rupp, K. Hansen, K. R. Müller, K. Burke, Finding density functionals with machine learning, *Physical review letters* 108 (25) (2012) 253002.
- [251] B. Kanungo, P. M. Zimmerman, V. Gavini, Exact exchange-correlation potentials from ground-state electron densities, *Nature communications* 10 (1) (2019) 1–9.
- [252] N. Thomas, T. Smidt, S. Kearnes, L. Yang, L. Li, K. Kohlhoff, P. Riley, Tensor field networks: Rotation-and translation-equivariant neural networks for 3d point clouds, *arXiv preprint arXiv:1802.08219* (2018).
- [253] T. Koker, K. Quigley, L. Li, Higher order equivariant graph neural networks for charge density prediction, in: *NeurIPS 2023 AI for Science Workshop*, 2023.
- [254] J. Nigam, M. J. Willatt, M. Ceriotti, Equivariant representations for molecular hamiltonians and n-center atomic-scale properties, *The Journal of Chemical Physics* 156 (1) (2022).
- [255] O. Unke, M. Bogojeski, M. Gastegger, M. Geiger, T. Smidt, K.-R. Müller, Se (3)-equivariant prediction of molecular wavefunctions and electronic densities, *Advances in Neural Information Processing Systems* 34 (2021) 14434–14447.
- [256] Y. S. Teh, S. Ghosh, K. Bhattacharya, Machine-learned prediction of the electronic fields in a crystal, *Mechanics of Materials* 163 (2021) 104070.
- [257] C. Woodward, S. Rao, Flexible ab initio boundary conditions: Simulating isolated dislocations in bcc mo and ta, *Physical review letters* 88 (21) (2002) 216402.
- [258] V. Gavini, K. Bhattacharya, M. Ortiz, Vacancy clustering and prismatic dislocation loop formation in aluminum, *Physical Review B* 76 (18) (2007) 180101.
- [259] C. Blundell, J. Cornebise, K. Kavukcuoglu, D. Wierstra, Weight uncertainty in neural network, in: *International conference on machine learning*, *Proceedings of Machine Learning Research*, 2015, pp. 1613–1622.
- [260] P. Thiagarajan, P. Khairnar, S. Ghosh, Explanation and use of uncertainty quantified by bayesian neural network classifiers for breast histopathology images, *IEEE Transactions on Medical Imaging* 41 (4) (2021) 815–825.
- [261] P. Thiagarajan, S. Ghosh, Jensen-shannon divergence based novel loss functions for bayesian neural networks (2023). [arXiv:2209.11366](https://arxiv.org/abs/2209.11366).

- [262] B. Settles, Active learning literature survey (2009).
- [263] H. Huo, M. Rupp, Unified representation of molecules and crystals for machine learning, *Machine Learning: Science and Technology* 3 (4) (2022) 045017.
- [264] A. P. Bartók, R. Kondor, G. Csányi, On representing chemical environments, *Physical Review B* 87 (18) (2013) 184115.
- [265] M. Rupp, A. Tkatchenko, K.-R. Müller, O. A. Von Lilienfeld, Fast and accurate modeling of molecular atomization energies with machine learning, *Physical review letters* 108 (5) (2012) 058301.
- [266] F. Musil, A. Grisafi, A. P. Bartók, C. Ortner, G. Csányi, M. Ceriotti, Physics-inspired structural representations for molecules and materials, *Chemical Reviews* 121 (16) (2021) 9759–9815.
- [267] Q. Xu, A. Sharma, B. Comer, H. Huang, E. Chow, A. J. Medford, J. E. Pask, P. Suryanarayana, Sparc: Simulation package for ab-initio real-space calculations, *SoftwareX* 15 (2021) 100709.
- [268] Q. Xu, A. Sharma, P. Suryanarayana, M-sparc: Matlab-simulation package for ab-initio real-space calculations, *SoftwareX* 11 (2020) 100423.
- [269] S. Ghosh, P. Suryanarayana, Sparc: Accurate and efficient finite-difference formulation and parallel implementation of density functional theory: Isolated clusters, *Computer Physics Communications* 212 (2017) 189–204.
- [270] J. P. Perdew, K. Burke, M. Ernzerhof, Generalized gradient approximation made simple, *Physical review letters* 77 (18) (1996) 3865.
- [271] D. Hamann, Optimized norm-conserving vanderbilt pseudopotentials, *Physical Review B* 88 (8) (2013) 085117.
- [272] A. S. Banerjee, P. Suryanarayana, J. E. Pask, Periodic Pulay method for robust and efficient convergence acceleration of self-consistent field iterations, *Chemical Physics Letters* 647 (2016) 31–35.
- [273] D. J. Evans, B. L. Holian, The nose–hoover thermostat, *The Journal of chemical physics* 83 (8) (1985) 4069–4074.
- [274] P. Hirel, AtomsK: A tool for manipulating and converting atomic data files, *Computer Physics Communications* 197 (2015) 212–219.
- [275] W. Kohn, Density functional and density matrix method scaling linearly with the number of atoms, *Physical Review Letters* 76 (17) (1996) 3168.



- [276] E. Prodan, W. Kohn, Nearsightedness of electronic matter, *Proceedings of the National Academy of Sciences of the United States of America* 102 (33) (2005) 11635–11638.
- [277] N. W. Ashcroft, N. D. Mermin, *Solid state physics*, Cengage Learning, 2022.
- [278] V. Hamer, P. Dupont, An importance weighted feature selection stability measure, *J. Mach. Learn. Res.* 22 (1) (jan 2021).
- [279] I. Guyon, A. Elisseeff, An introduction to variable and feature selection, *J. Mach. Learn. Res.* 3 (null) (2003) 1157–1182.
- [280] M. Gastegger, L. Schwiedrzik, M. Bittermann, F. Berzsényi, P. Marquetand, wacsf—weighted atom-centered symmetry functions as descriptors in machine learning potentials, *The Journal of chemical physics* 148 (24) (2018).
- [281] G. Imbalzano, A. Anelli, D. Giofré, S. Klees, J. Behler, M. Ceriotti, Automatic selection of atomic fingerprints and reference configurations for machine-learning potentials, *The Journal of chemical physics* 148 (24) (2018).
- [282] G. E. Hinton, D. Van Camp, Keeping the neural networks simple by minimizing the description length of the weights, in: *Proceedings of the sixth annual conference on Computational learning theory*, 1993, pp. 5–13.
- [283] A. Graves, Practical variational inference for neural networks, *Advances in neural information processing systems* 24 (2011).
- [284] R. Zhang, C. Li, J. Zhang, C. Chen, A. G. Wilson, Cyclical stochastic gradient mcmc for bayesian deep learning, in: *International Conference on Learning Representations*, 2020.
- [285] A. Kendall, Y. Gal, What uncertainties do we need in bayesian deep learning for computer vision?, *Advances in neural information processing systems* 30 (2017).
- [286] J. S. Smith, B. T. Nebgen, R. Zubatyuk, N. Lubbers, C. Devereux, K. Barros, S. Tretiak, O. Isayev, A. E. Roitberg, Approaching coupled cluster accuracy with a general-purpose neural network potential through transfer learning, *Nature communications* 10 (1) (2019) 2903.
- [287] J. Harris, Simplified method for calculating the energy of weakly interacting fragments, *Physical Review B* 31 (4) (1985) 1770.
- [288] W. M. C. Foulkes, R. Haydock, Tight-binding models and density-functional theory, *Physical review B* 39 (17) (1989) 12520.
- [289] R. Resta, S. Sorella, Electron localization in the insulating state, *Physical Review Letters* 82 (2) (1999) 370.

- [290] A. T. Fowler, C. J. Pickard, J. A. Elliott, Managing uncertainty in data-derived densities to accelerate density functional theory, *Journal of Physics: Materials* 2 (3) (2019) 034001.
- [291] Y. Zhou, W. Zhang, E. Ma, V. L. Deringer, Device-scale atomistic modelling of phase-change memory materials, *Nature Electronics* 6 (10) (2023) 746–754.
- [292] P. Suryanarayana, P. P. Pratapa, A. Sharma, J. E. Pask, [Sqdf: Spectral quadrature method for large-scale parallel  \$o\(n\)\$  kohn–sham calculations at high temperature](https://doi.org/10.1016/j.cpc.2017.12.003), *Computer Physics Communications* 224 (2018) 288–298. doi:<https://doi.org/10.1016/j.cpc.2017.12.003>.  
URL <https://www.sciencedirect.com/science/article/pii/S0010465517304022>
- [293] S. Das, P. Motamarri, V. Subramanian, D. M. Rogers, V. Gavini, Dft-fe 1.0: A massively parallel hybrid cpu-gpu density functional theory code using finite-element discretization, *Computer Physics Communications* 280 (2022) 108473.
- [294] L.-W. Wang, B. Lee, H. Shan, Z. Zhao, J. Meza, E. Strohmaier, D. H. Bailey, Linearly scaling 3d fragment method for large-scale electronic structure calculations, in: *SC’08: Proceedings of the 2008 ACM/IEEE Conference on Supercomputing*, IEEE, 2008, pp. 1–10.
- [295] W. Yang, T.-S. Lee, A density-matrix divide-and-conquer approach for electronic structure calculations of large molecules, *The Journal of chemical physics* 103 (13) (1995) 5674–5678.
- [296] M. Herbold, J. Behler, Machine learning transferable atomic forces for large systems from underconverged molecular fragments, *Physical Chemistry Chemical Physics* 25 (18) (2023) 12979–12989.
- [297] M. Herbold, J. Behler, A hessian-based assessment of atomic forces for training machine learning interatomic potentials, *The Journal of Chemical Physics* 156 (11) (2022).
- [298] S. De, A. P. Bartók, G. Csányi, M. Ceriotti, Comparing molecules and solids across structural and alchemical space, *Physical Chemistry Chemical Physics* 18 (20) (2016) 13754–13769.
- [299] A. P. Bartók, S. De, C. Poelking, N. Bernstein, J. R. Kermode, G. Csányi, M. Ceriotti, Machine learning unifies the modeling of materials and molecules, *Science advances* 3 (12) (2017) e1701816.
- [300] V. L. Deringer, A. P. Bartók, N. Bernstein, D. M. Wilkins, M. Ceriotti, G. Csányi, Gaussian process regression for materials and molecules, *Chemical Reviews* 121 (16) (2021) 10073–10141.

- [301] A. Grisafi, D. M. Wilkins, G. Csányi, M. Ceriotti, Symmetry-adapted machine learning for tensorial properties of atomistic systems, *Physical review letters* 120 (3) (2018) 036002.
- [302] Y. Ikeda, B. Grabowski, F. Körmann, Ab initio phase stabilities and mechanical properties of multicomponent alloys: A comprehensive review for high entropy alloys and compositionally complex alloys, *Materials Characterization* 147 (2019) 464–511.
- [303] E. P. George, D. Raabe, R. O. Ritchie, High-entropy alloys, *Nature reviews materials* 4 (8) (2019) 515–534.
- [304] O. Liebman, S. Agarwal, A. Banerjee, Helical waves for self-consistent first principles calculations of chiral one-dimensional nanomaterials, *Bulletin of the American Physical Society* (2022).
- [305] J. W. Cahn, J. E. Hilliard, Free energy of a nonuniform system. i. interfacial free energy, *The Journal of chemical physics* 28 (2) (1958) 258–267.
- [306] S. M. Allen, J. W. Cahn, Ground state structures in ordered binary alloys with second neighbor interactions, *Acta Metallurgica* 20 (3) (1972) 423–433.
- [307] S. M. Allen, J. W. Cahn, A correction to the ground state of fcc binary ordered alloys with first and second neighbor pairwise interactions, *Scripta Metallurgica* 7 (12) (1973) 1261–1264.